Simulations and Modelling of Bacterial Flagellar Propulsion

Henry Shum

St Catherine's College

University of Oxford

A thesis submitted for the degree of

Doctor of Philosophy

Michaelmas 2011

To my brother and parents.

Acknowledgements

I would like to express my gratitude to my supervisor, Dr Eamonn Gaffney, who has given me not only sound guidance but also encouragement and confidence since the beginning of my DPhil studies. I would also like to thank other members of our cell motility group for their invaluable insight and support: Prof John Blake, Dr Jackson Kirkman-Brown, Dr David Smith and Mr Hermes Gadêlha.

Special thanks go to Prof Judy Armitage and Prof Dan Nicolau for many interesting and fruitful discussions, particularly about *Rhodobacter sphaeroides* and bacteria swimming in channels.

I am grateful to Prof Philip Maini and all those at the Mathematical Institute and at St Catherine's College who have given me great support throughout my studies. I would like to especially acknowledge the generous scholarship I received from my college.

The past few years have been full of rewarding and memorable experiences. I should thank conference organisers around the world for the numerous opportunities to travel and make contacts but most of all, I am grateful for my friends, who have been tremendously inspirational and have taught me so much along the way.

Finally, it would be difficult to overstate my appreciation and gratitude to my parents, who encouraged and made it possible for me to pursue this degree and have always done everything they could for me, and to my brother, to whom I also owe so much.

Simulations and Modelling of Bacterial Flagellar Propulsion

Henry Shum, St Catherine's College

A thesis submitted for the degree of Doctor of Philosophy

Michaelmas Term 2011

Motility of flagellated bacteria has been a topic of increasing scientific interest over the past decades, attracting the attention of mathematicians, physicists, biologists and engineers alike. Bacteria and other micro-organisms cause substantial damage through biofilm growth on submerged interfaces in water cooling systems, ship hulls and medical implants. This gives social and economic motivations for learning about how micro-organisms swim and behave in different environments. Fluid flows on such small scales are dominated by viscosity and therefore behave differently from the inertia-dominated flows that we are more familiar with, making bacterial motility a physically intriguing phenomenon to study as well.

We use the boundary element method (BEM) to simulate the motion of singly flagellated bacteria in a viscous, Newtonian fluid. One of our main objectives is to investigate the influence of external surfaces on swimming behaviour. We show that the precise shape of the cell body and flagellum can be important for determining boundary behaviour, in particular, whether bacteria are attracted or repelled from surfaces. Furthermore, we investigate the types of motion that may arise between two parallel plates and in rectangular channels of fluid and show how these relate to the plane boundary interactions.

As an extension to original models of flagellar propulsion in bacteria that assume a rotation of the rigid helical flagellum about an axis fixed relative to the cell body, we consider flexibility of the bacterial hook connecting the aforementioned parts of the swimmer. This is motivated by evidence that the hook is much more flexible than the rest of the flagellum, which we therefore treat as a rigid structure. Elastic dynamics of the hook are modelled using the equations for a Kirchhoff rod. In some regimes, the dynamics are well described by a rigid hook model but we find the possibility of additional modes of behaviour.

Contents

1 Introduction **1**

1.1 The role of bacteria 1

1.2 Bacterial physiology and locomotion 3

1.2.1 The motor and basal body 6

1.2.2 The hook and flagellar filament 9

1.3 Statement of mathematical problem 11

1.4 Historical development of mathematical and numerical analyses of flagellated micro-organisms 15

1.4.1 Resistive force theory (RFT) 15

1.4.2 Slender body theory (SBT) 20

1.4.3 Boundary element method (BEM) 23

1.4.4 Immersed boundary method (IBM) 24

2 Numerical methods **29**

2.1 The boundary integral equation 30

2.2 Boundary meshing 32

2.3 Quadrature Methods 36

2.3.1 Gaussian quadrature on standard intervals and triangles . . . 36

2.3.2 General intervals and triangles 38

2.3.3 Solving the boundary integral equation 39

3 Swimming and optimisation **41**

3.1 Model geometry 41

3.2 Solving instantaneous dynamics 45

3.3 Tracking bacterial trajectories 47

3.4 Stability of integration schemes 48

3.4.1 Heun's predictor–corrector 50

3.4.2 Backward Euler 50

3.4.3 Trapezoidal rule . . . 51
3.4.4 Implementing time stepping schemes . . . 51
3.5 Progressive and phase-averaged velocities . . . 52
3.6 Swimming speed and optimisation . . . 54
3.6.1 Optimisation results . . . 56
3.6.2 Discussion . . . 57
3.7 Summary . . . 61

4 Interactions with no-slip plane boundaries 63
4.1 Interpolation method for approximate swimmer dynamics . . . 66
4.2 Analysis of dynamics in different fluid geometries . . . 67
4.3 Half space . . . 70
4.4 Parallel plates . . . 76
4.5 Discussion of implications for bacterial trajectories . . . 76
4.6 Summary . . . 84

5 Swimming in channels 87
5.1 Methods for approximate trajectory analysis . . . 90
5.1.1 Edges of large channels . . . 90
5.1.2 Channels of finite cross-section . . . 94
5.2 Simulated trajectories in channels . . . 95
5.2.1 Trajectories in edges of large channels . . . 95
5.2.2 Long-term behaviour in fully enclosed channels . . . 99
5.2.3 Average swimming speeds and durations . . . 112
5.2.4 Discussion . . . 115
5.3 Summary . . . 121

6 A model for flexible hooks 125
6.1 Curves and rods . . . 125
6.2 The Kirchhoff rod . . . 127
6.3 Bacterial dynamics with a Kirchhoff hook . . . 130
6.4 Hook behaviour in free space . . . 133
6.5 Steady states of the hook . . . 135
6.5.1 Bend/twist ratio . . . 136
6.5.2 Hook length . . . 138
6.5.3 Boundary accumulation . . . 139
6.6 Discussion . . . 142

6.7 Conclusions 147

7 Discussion and future work **150**
7.1 Discussion 150
7.1.1 Swimming efficiency 150
7.1.2 Swimming near surfaces 151
7.1.3 Effect of hook stiffness 153
7.2 Future work 153

A Swimmer geometry and parameters **157**

B Convergence of numerical methods **161**

C Analysis of potentially periodic trajectories **167**
C.1 Identifying periodicity in a one-variable time series 167
C.2 Periodicity of channel trajectories 169
C.3 Comparing periodic orbits 170

Bibliography **176**

List of Figures

1.1 Illustration of three bacterial cell shapes. (a) Cocci are rarely reported to have flagella. (b) Rod-shaped bacteria are the most commonly studied type of flagellated bacterium. Examples include *E. coli*, *S. typhimurium* and *R. sphaeroides*. (c) Some rod-shaped bacteria, such as *C. crescentus*, are curved. Figure reproduced with permission from reference [25]. 3

1.2 Schematic diagram of the structure of the bacterial flagellum. The layers labelled IM and OM are the inner and outer membranes of the bacterial cell respectively. The main components of the flagellar apparatus are the filament, the motor and the hook connecting the filament to the rotor. Figure reproduced with permission from reference [37]. 4

1.3 Superposition of three frames taken from a movie of swimming *R. sphaeroides* courtesy of Howard Berg's laboratory website [10]. The organism, with a clearly visible flagellum, moves from left to right in a clockwise circular arc over a period of roughly two seconds. The curved path is due to the presence of nearby surfaces, such as a cover slip, an effect that will be discussed in chapter 4. Movies such as this give support to modelling the bacterial flagellum, at least for monotrichous species, as a rotating rigid helix during periods of steady swimming. Furthermore, the directional persistence of steadily swimming cells in movies indicates that Brownian motion is not a leading order effect and may be neglected here. 5

1.4 A schematic of the empirically deduced torques produced by bacterial motors operating at various frequencies. In each of the three species presented, the torque is approximately independent of frequency at low rotation rates and drops to zero with increasing frequency at high rotation rates. The straight lines passing through the origin show the estimated linear relationship between the rotation rate and the torque required to turn the helical flagellum at such a rate (see main text for further details). The marked intersections between the motor curve and flagellum load line for *C. crescentus* and *V. alginolyticus* indicate the frequencies and estimated motor torques corresponding to the respective freely swimming cells. For *E. coli* the load line refers to a single filament and not the flagellar bundle. Figure reproduced with permission from reference [84]. 8

1.5 A two-dimensional representation of the resistive force theory approximation. The local velocity of a slender filament of circular cross-section can be separated into components tangential and perpendicular to the filament, $\mathbf{v}_{\mathrm{T}}$ and $\mathbf{v}_{\mathrm{N}}$, resulting in drag forces $\mathbf{f}_{\mathrm{T}}$ and $\mathbf{f}_{\mathrm{N}}$ respectively. Drag anisotropy means that $\mathbf{f}$ and $\mathbf{v}$ need not lie in the same direction. The generalisation to three dimensions, incorporating binormal components of the velocity vector field, is straightforward. 17

1.6 In slender body theory, Stokeslets and higher order singularities are distributed along the centreline $\mathbf{X}(s)$ with the aim of matching the resulting velocities at surface points $\mathbf{x}(s_0, \varphi)$ to the appropriate boundary velocities of the flagellum. To leading order this involves removing the φ-dependence and matching the surface velocities to the required centreline velocity at $\mathbf{X}(s_0)$ for each $s_0 \in [0, L]$. 23

1.7 A schematic of the two distinct meshes in an immersed boundary method. The immersed boundary is described by the nodes $\mathbf{X}_k$. The fluid equations are solved on the rectangular grid of points $\mathbf{x}_{i,j}$ considering body forces that are derived from the boundary forces $\mathbf{F}_k^{\mathrm{hyd}}$. 26

2.1 Mapping between real space and ξ–η parameter space for describing quadratic triangular elements, where the edge nodes $\mathbf{x}^4$, $\mathbf{x}^5$ and $\mathbf{x}^6$ are equidistant from the corner nodes on their respective edges, giving $\alpha = \beta = \gamma = 0.5$. 35

2.2 Splitting a triangular element for accurate quadrature of singular integrands. If an integrand has singular behaviour at a point X that is (a) in the interior or (b) on an edge of triangle ABC, then the triangle is divided into smaller elements as shown with X as a vertex of each sub-triangle. 38

3.1 Illustration of model bacterium in the body reference frame. As depicted, a_1^{B}, a_2^{B} and a_3^{B} are the lengths of the semi-principal axes of the cell body in the $\mathbf{e}_1^{\mathrm{B}}$, $\mathbf{e}_2^{\mathrm{B}}$ and $\mathbf{e}_3^{\mathrm{B}}$ body-fixed directions respectively. The flagellum axis coincides with $\mathbf{e}_1^{\mathrm{B}}$. The flagellum has radius a^{T} and begins a short distance $d^{\mathrm{gap}} = 0.05\,\bar{a}$ (not labelled) from the pole of the cell body, growing into a helix over the starting region of length $\sim 2/k_{\mathrm{E}}$. The helix has amplitude a and wavelength λ (wavenumber $k = 2\pi/\lambda$). The length of the flagellum is L, measured along the curved centreline, and the number of turns (including the starting region) is N_λ. The lengthscale used for non-dimensionalisation is $\bar{a} = (a_1^{\mathrm{B}}\, a_2^{\mathrm{B}}\, a_3^{\mathrm{B}})^{1/3}$, which is the radius required for a sphere of volume equal to that of the bacterium's body. The tail director basis vectors, $\mathbf{e}_j^{\mathrm{T}}$, $j = 1, 2, 3$, are related to the body basis vectors by the rotation ϕ^{T} about the common axis, which we also take to be the motor axis $\mathbf{e}^{\mathrm{M}} \equiv \mathbf{e}_1^{\mathrm{B}} \equiv \mathbf{e}_1^{\mathrm{T}}$. The position of the bacterium relative to a fixed reference frame is described by the vector $\mathbf{x}^{\mathrm{B}}$, which tracks the pole of the cell body nearer the flagellum (not labelled in this figure). 42

3.2 Construction and surface discretisation of bacterial flagellum. (a) The tip of the filament, with circular rings indicating the cross-sections at arc lengths s^k, $k = 1, 2, 3, 4$ (see main text for details). (b) The normal and binormal vectors are $\mathbf{n}^k$ and $\mathbf{b}^k$ respectively at the point $\mathbf{X}^k$ on the flagellar centreline, used to determine the cross-section in which to place surface nodes $\mathbf{x}_j^k$. Curved lines (blue) in (a) and (b) joining the surface nodes show the edges of the actual triangular elements used in computation while the shaded surfaces in this figure, which are composed of flat triangles connecting mesh nodes, is for visualisation purposes only. 44

3.3 Contour plots of swimming efficiency as a function of flagellum wavelength, $\lambda/\bar{a}$, and total length, $L/\bar{a}$. Top row: power efficiency; bottom row: torque efficiency. Left column: swimming in unbounded fluid; right column: swimming parallel to boundary at distance $h/\bar{a} = 2$, with the same colour scale as the corresponding plot in unbounded fluid. Dots indicate the optimal parameter values in each case. Bacterium shapes are illustrated for the four corners of parameter space in (a). Figure originally published by Shum et al. [114]. 58

4.1 Bacterial configuration relative to a plane boundary (wall). Averaging over variations in tail phase, the bacterium's configuration is specified by the height above the wall, h, and the inclination angle, θ, of its axis relative to the wall. 69

4.2 A small region of the phase plane showing stable spiral dynamics for a swimmer near a plane boundary. The bacterium has the following parameter values: $a_1^{\mathrm{B}}/a_2^{\mathrm{B}} = 2$, $L/\bar{a} = 10$, $ak = 1$, $N_\lambda = 2$ (see §3.1 or appendix A for descriptions of geometrical parameters of the model bacterium). Blue curves indicate pathlines generated using the interpolation method. A trajectory obtained using a full tracking simulation with the BEM is shown by the green curve and exhibits oscillations at the frequency of motor revolutions. The thick, black curve is a temporally smoothed plot of this trajectory. The region below the dashed line is excluded due to entailing intersections between the bacterium and the wall. Figure modified from Shum et al. [114] . 71

4.3 Variations in stable junction height ($h^*/\bar{a}$, solid lines) and radius of curvature of the stable orbit ($R/\bar{a}$, dashed lines) with geometrical parameters: (a) number of turns on flagellum, (b) cell body aspect ratio, (c) helix pitch angle, (d) flagellum length, (e) flagellum thickness, (f) flagellum starting region length. The base morphology uses the parameter values: $N_\lambda = 2$, $a_1^{\mathrm{B}}/a_2^{\mathrm{B}} = 2$, $ak = 1$, $L/\bar{a} = 10$, $a^{\mathrm{T}}/\bar{a} = 0.05$, $k/k_{\mathrm{E}} = 1$. Some tail parameters are inter-related; $\lambda/\bar{a}$ varies as necessary in (a) and (c), and N_λ varies in (d) and (f). Dots in (a) and (b) mark limits beyond which the bacterium descends into the wall. Figure originally published by Shum et al. [114]. 73

4.4 Phase plane diagrams for bacteria of flagellar length L swimming near a no-slip plane boundary. (a) $L = 7.5\,\bar{a}$, (b) $L = 6.5\,\bar{a}$, and (c) $L = 5\,\bar{a}$. A bifurcation takes place over this range of parameters. There is a stable state in (a) and as long as the bacterium is not initially inclined too sharply either away from or towards the wall, the swimmer will reach the stable state. However, the stable point is absent in (c) and even trajectories that are initially approaching the boundary are deflected away. Case (b) is an intermediary, with some trajectories reaching the stable state and others approaching but being deflected back into the bulk fluid. 74

4.5 Examples of the three types of bacterial trajectories near plane surfaces, (i) descent into the wall, (ii) stable circular orbiting, and (iii) escape into the bulk medium. In (a), the junction height is plotted against time and the model bacteria shown to the scale of the junction height axis. The top-down view of the trajectories are shown in (b). The characteristic behaviour observed is consistent over a wide range of initial conditions and is determined by the shape of the bacterium. The cell body aspect ratios and flagellum lengths used in these examples are (i) $a_1^{\mathrm{B}}/a_2^{\mathrm{B}} = 1$, $L/\bar{a} = 5$; (ii) $a_1^{\mathrm{B}}/a_2^{\mathrm{B}} = 2$, $L/\bar{a} = 10$; and (iii) $a_1^{\mathrm{B}}/a_2^{\mathrm{B}} = 2$, $L/\bar{a} = 5$. The other parameter values used in these simulations were fixed at: $\lambda = \lambda_0 \approx 3.58$, $ak = 1$, $a^{\mathrm{T}}/\bar{a} = 0.05$, $k/k_E = 1$. λ_0 was chosen such that $N_\lambda = 2$ for $L/\bar{a} = 10$. Figure originally published by Shum et al. [114]. 77

4.6 Phase diagram showing regions of descent, stable orbits and escape from walls as cell body aspect ratio and flagellum length are varied. The colour scale indicates non-dimensionalised stable height above wall, $h^*/\bar{a}$. The dotted line between the region of escape and the region of descent is only hypothesised as these parameters were not explored. Bacterium shapes are illustrated for the points at the four corners of parameter space. The fixed parameters are the same as those quoted for Fig. 4.5. Figure originally published by Shum et al. [114]. 78

4.7 Free space (a) power efficiency and (b) torque efficiency with varying flagellar length and cell aspect ratio as in Fig. 3.3 with boundary behaviour from Fig. 4.6 overlaid. Thick lines separate regions where the behaviour of such swimmers near a plane boundary is characterised by stable orbits, escape from the wall, and descent into the influence of close-range surface interactions. As in Fig. 4.6, the boundary between the regions of escape and descent is only hypothesised as these parameters were not explored. A dot in (a) marks the location of the power optimum. Figure originally published by Shum et al. [114]. . . 78

4.8 Phase plane diagrams for bacteria of flagellar length L swimming between parallel plates of separation $H/\bar{a} = 15$. (a) $L = 7.5\,\bar{a}$, (b) $L = 6.5\,\bar{a}$, and (c) $L = 5\,\bar{a}$. A bifurcation takes place over this range of parameters corresponding to the bifurcation seen in the half space geometry (Fig. 4.4). In all cases, the central point ($\theta = 0, h = 0$) is an unstable steady state. In (a), there is practically global attraction to the stable states, of which there is one close to each plate. These stable points are absent in (c) and trajectories instead converge to a limit cycle that oscillates from one plate to the other. Case (b) is an intermediary, with some trajectories leading to the stable states and others attracted to the limit cycle. 79

4.9 Phase plane diagrams for bacteria of flagellar length L swimming between parallel plates of separation $H/\bar{a} = 5$. (a) $L = 7.5\,\bar{a}$, (b) $L = 6.5\,\bar{a}$, and (c) $L = 5\,\bar{a}$. The narrow gap constrains the bacterium to swim in or close to the centre in all cases. However, the central configuration is only a stable state in (a). In both (b) and (c), limit cycles can be seen around this point but are greatly reduced compared with those in Fig. 4.8 where the plate separation is larger. Moreover, we observe that a bifurcation has taken place with the boundary accumulating swimmer, (a). Instead of having two stable points close to the plates and an unstable point in the centre, there is only a single, stable steady state when the plate separation is small. 80

5.1 Visualisation of the mesh used for the BEM hydrodynamic model of bacterial swimming in a square channel. Because the far field of a force-free swimmer decays with the square of the distance relative to the size of the swimmer, accurate results can be obtained using a channel mesh extending only a few body lengths behind and ahead of the swimmer. 88
5.2 Visualisation of the mesh used for the BEM hydrodynamic model of bacterial swimming near an edge of an infinitely large square channel. Only the part of the channel within $25\,\bar{a}$ of the edge and within about $20\,\bar{a}$ behind and ahead of the bacterium is meshed. 89
5.3 The breakdown of the channel by proximity to walls. This diagram concerns the space near the $\bar{y} = \bar{z} = 0$ edge of a channel of large cross-sectional extent. The vertical and horizontal walls at this edge are shown in thick, solid lines. Dashed lines indicate the division of the fluid space into Regions 1–4 and other regions that we do not explicitly analyse. The dynamics in the marked half space and free space regions can be inferred from previous work. The space between the walls and the enumerated regions is largely excluded because the finite volume occupied by the cell intersects or closely approaches the walls when the tracked junction position, $\mathbf{x}^{\mathrm{B}}$, is in this region. 92
5.4 Three channel trajectories relaxing to an edge accumulating periodic orbit in (*a*) the cross-sectional view and (*b*) the top–down view, with starting points indicated by dots in (*a*). Only two of the channel walls were meshed, as described in §5.1.1, with the horizontal wall at height $\bar{z}/\bar{a} = 0$ and the vertical wall being the plane $\bar{y}/\bar{a} = 0$, indicated by a straight black line in (*b*). In both (*a*) and (*b*), the vertical scale is 10 times as fine as the horizontal scale to allow the structure of the orbit to be more clearly seen. The thick, black curve in (*a*) marks the periodic orbit, which is nearly constant in $\bar{z}$, reached by all three shown trajectories. 98

5.5 Real parts of the eigenvalues, λ, of the Jacobian matrix $\mathbf{J}^{\text{chan}}$ evaluated in the parallel, central position of a square channel as the width of the channel is varied. The eigenvalues are scaled by the rate $\bar{t}^{-1}$. In each case, two pairs of complex conjugate eigenvalues were found. The distinct real parts are plotted and marked with crosses for a boundary accumulator and with open circles for a boundary escaper. Since at least one pair of complex eigenvalues has positive real part, there is no evidence of stability of the central position within the parameter range tested. 101

5.6 Relaxation to periodic orbits for a boundary escaping bacterium in a square channel of width $20\,\bar{a}$. (a) Thick, black curves indicate two periodic orbits in the cross-sectional view, while four sample trajectories that converge to these two states are shown in thinner curves of different colours. The initial conditions of these four trajectories are marked by dots. (b) Top–down view of channel showing the computed tracks once the bacteria have relaxed to periodic orbits. (c) Time series of the transient phase of the same trajectories in (a) and (b). Note that only a small proportion of random initial conditions evolve to a periodic orbit without colliding into walls so these are not representative of generic trajectories. The extent of the channel is marked with straight, black lines in (a) and (b). 103

5.7 Comparison between approximate solution using the interpolation method (solid curves) and time stepping simulation of the full system (dashed curves) for a boundary escaping bacterium in a channel of size $H_y = H_z = 15\,\bar{a}$. (a) The cross-sectional view with the extent of the channel marked by straight, black lines and the starting point of the trajectory indicated by a dot. (b) The time series of the horizontal position, y. 104

5.8 Relaxation to periodic orbits for a boundary escaping bacterium in a square channel of width $30\,\bar{a}$. (a) Thick, black curves indicate two periodic orbits in the cross-sectional view, while four sample trajectories that converge to these two states are shown in thinner curves of different colours. The initial conditions of these four trajectories are marked by dots. (b) Top–down view of channel showing the computed tracks once the bacteria have relaxed to periodic orbits. (c) Time series of the transient phase of the same trajectories in (a) and (b). The extent of the channel is marked with straight, black lines in (a) and (b). 105

5.9 Relaxation to periodic orbits for a boundary escaping bacterium in a rectangular channel of size $H_y = 25\,\bar{a}$, $H_z = 20\,\bar{a}$. (a) A thick, black curve indicates the periodic orbit in the cross-sectional view, while two sample trajectories that converge to this state are shown in thin curves of different colours with the starting points marked by dots. (b) Top–down view of channel showing the computed tracks once the bacteria have relaxed to periodic orbits. (c) Time series of the transient phase of the trajectories in (a) and (b). The extent of the channel is marked with straight, black lines in (a) and (b). 106

5.10 Sample trajectories for a boundary escaping bacterium in a square channel of width $5\,\bar{a}$ in (a) the cross-sectional view, and (b) the top–down view of channel. Collisions severely limit the extent of tracks. The extent of the channel is marked with straight, black lines. 107

5.11 Relaxation to periodic orbits for a boundary accumulating bacterium in a square channel of width $20\,\bar{a}$. (a) Isolated, thick, black regions indicate the projections of the four periodic orbits in the cross-sectional view. These periodic orbits are related to each other by rotations about the axis of the channel. One trajectory that accumulates at each edge is shown in thin curves of different colours with starting points marked by dots. (b) Top–down view of channel showing the computed tracks once the bacteria have relaxed to periodic orbits. (c) Time series of the transient phase of the same trajectories in (a) and (b). The extent of the channel is marked with straight, black lines in (a) and (b). . . . 108

5.12 Behaviour of a boundary accumulating bacterium in a square channel of width $20\,\bar{a}$. (a) The projections in the channel cross-section of four trajectories starting from different initial conditions are shown in different colours. (b) Top–down view of the channel showing a section of the tracks in (a). The bacterium here has a flagellar length of $L/\bar{a} = 6.5$, which differs from the length $L/\bar{a} = 7.5$ used in all other presented examples of boundary accumulating swimmers in this section. The shorter length increases the preferred distance from walls, reducing close contact and allowing longer trajectories to be computed. Similar behaviour could be found in slightly smaller channels using the flagellar length $L/\bar{a} = 7.5$ but collisions could not be avoided at edges as they are in this figure. The extent of the channel is marked with straight, black lines. 109

5.13 Relaxation to periodic orbits for a boundary accumulating bacterium in a channel of size $H_y = 20\,\bar{a}$, $H_z = 10\,\bar{a}$. (a) Large, black dots mark stable steady states in the cross-sectional view, while one trajectory that accumulates at each of these is shown in thinner, solid curves of different colours. The starting points of these trajectories are marked by dots. In addition, one trajectory computed using precise velocity evaluations rather than phase-averaged interpolation is shown in a dashed curve. (b) Top–down view of channel showing two computed tracks once the bacteria have relaxed to the steady states (solid lines) of the phase-averaged system and a solution of the full system (dashed curve). (c) Time series of the transient phase of the same trajectories in (a) and (b). The extent of the channel is marked with straight, black lines in (a) and (b). 110

5.14 Histograms showing the frequency distributions of track durations, $T_{\text{collision}}$, for swimming in square channels of varying size. A total of 200 trajectories starting from random initial conditions were computed for each channel size with (a) a boundary accumulating swimmer, and (b) a boundary escaping swimmer. Most of the trajectories in the category for durations greater than $500\,\bar{t}$ evolve to periodic orbits and hence do not have finite track durations. 113

5.15 Average channel progression speeds, $\bar{U}_x$, in square channels of different sizes for (a) a boundary accumulating swimmer, and (b) a boundary escaping swimmer. Speeds of long-term trajectories are plotted with dots while the average speed of trajectories lasting less than $500\,\bar{t}$ before collision are marked with open circles. Error bars indicate the standard deviations computed from samples of 200 runs, combining both colliding and non-colliding trajectories. The speeds are expressed as fractions of the respective free space phase-averaged swimming speed, U_0, of the bacterium. 116

5.16 An example of how a population of bacteria in a rectangular channel might spontaneously separate into different regions according to the direction of travel. This effect is due to edge accumulation only being stable at two edges for a given swimming direction (Fig. 5.13). 119

6.1 Comparison between (a) the rigid hook model and (b) the current, flexible hook. The alignment angle between the body axis, $\mathbf{e}_1^{\mathrm{B}}$, and the flagellum axis, $\mathbf{e}_1^{\mathrm{T}}$, is denoted ψ. Since the shapes of the flagella differ near the cell body, the rigid model is not simply the limiting case where stiffness is taken to be very large in the flexible hook model. In both models we assume the motor axis is aligned with the major axis of the cell, i.e. $\mathbf{e}^{\mathrm{M}} = \mathbf{e}_1^{\mathrm{B}}$. 132

6.2 Illustrations of bacterial shape A (left) and B (right). See table 6.1 for geometry parameters used. 133

6.3 Evolution of alignment angle ψ showing transient hook behaviour at different levels of stiffness. The steady state alignment angles are plotted as dashed lines (see Fig. 6.5). (a) $k^{\mathrm{H}} = 0.4$, (b) $k^{\mathrm{H}} = 0.5$, (c) $k^{\mathrm{H}} = 1$. Time is non-dimensionalised by the timescale $\bar{t} = 16\pi^2\bar{a}^3\mu/\tau^{\mathrm{M}}$, where $\bar{a}$ is the body's volumetric radius, μ is the dynamic viscosity of the fluid and τ^{M} is the magnitude of the motor torque. 134

6.4 Exemplar swimmers (a) with a stable hook state and (b) with an unstable steady hook state. The initial configurations (right) are out of equilibrium but a steady state is soon reached in the stable case. The paths of the junction point $\mathbf{x}^{\mathrm{B}}$ are shown as solid curves. The trajectories correspond to cases (c) and (a) respectively from Fig. 6.3. 135

6.5 Variations in steady state (a) alignment angle, (b) stability and (c) swimming speed with hook stiffness. Solid curves indicate data for bacterial shape A while dashed curves correspond to shape B. Swimming speeds in (c) are plotted relative to the speeds, U_{R}, calculated using the previous rigid hook model with the equivalent geometrical parameters. 137
6.6 Variations in alignment angle (solid curve) and swimming speed (dashed curve) with hook length $L^{\mathrm{H}}/\bar{a}$. The lengthscale $\bar{a}$ is the volumetric radius of the cell body and the alignment angles and swimming speeds are shown normalised by the values ψ_0 and U_0 respectively for our standard swimmer A with hook length $L^{\mathrm{H}}/\bar{a} = 0.2$. 138
6.7 Time series of (a) junction height, h, and (b) hook alignment angle, ψ, as a bacterium with hook stiffness $k^{\mathrm{H}} = 1$ approaches a stable orbit above a plane boundary. The stable accumulation height of the rigid hook model equivalent, $h^*/\bar{a} \approx 0.94$ is indicated by a horizontal dashed line in (a) and the value of the stable alignment angle $\psi^* \approx 0.13$ in free space is marked by a horizontal dashed line in (b). 140
6.8 Swimming behaviour of bacterial shape A near a plane boundary with varying hook stiffness. (a) Curves marked with dots indicate the minimum and maximum alignment angles observed after transience compared with the free space stable angle shown by the unmarked, thick curve. (b) The minimum and maximum swimming heights over a revolution of the motor during stable boundary swimming after transience (curves marked with dots) and the minimum separation distance between the wall and the swimmer (curve marked with crosses). Using the rigid hook model, this swimmer would have a stable swimming height of $h^*/\bar{a} \approx 0.94$. The dashed lines on the left hand side mark the stiffness value for which the swimmer was found to collide with the wall below and no boundary accumulating trajectory could be obtained. 141

6.9 Swimming behaviour of bacterial shape B near a plane boundary with varying hook stiffness. (a) Curves marked with dots indicate the minimum and maximum alignment angles observed after transience compared with the free space stable angle shown by the unmarked, thick curve. (b) The minimum and maximum swimming heights over a revolution of the motor during stable boundary swimming after transience (curves marked with dots) and the minimum separation distance between the wall and the swimmer (curve marked with crosses). Using the rigid hook model, this swimmer would have a stable swimming height of $h^*/\bar{a} \approx 0.92$. The dashed lines on the left and right hand sides mark stiffness values for which the swimmer was found to escape from the wall and no boundary accumulating trajectory could be obtained. 143

6.10 Trajectories of two geometrically identical swimmers near plane boundaries. Swimmer (i) has hook stiffness $k^{\mathrm{H}} = 0.7$ and swimmer (ii) has hook stiffness $k^{\mathrm{H}} = 2$. The 3-D trajectories are shown in thick, blue curves while projections of the trajectories onto the x–y plane are shown in thin, green curves. The heights of the swimmers above the wall are also indicated at regular time intervals by vertical lines from the x–y plane. The bacteria are shown at their respective starting positions. Note the much smaller radius of curvature of swimmer (ii) once the steady circular orbit is reached. 144

A.1 Illustration of model bacterium in the body reference frame (repeated from Fig. 3.1 for convenience). Refer to table A.1 and §3.1 for further details. 160

B.1 Convergence of the BEM with increasing mesh refinement for a sphere of radius $\bar{a}$ translating in free space under a prescribed force $\mathbf{F}$. The relative error is defined as $\epsilon_{\mathrm{rel}} := \|\mathbf{U} - \mathbf{U}_0\|/\|\mathbf{U}_0\|$, where $\mathbf{U}$ is the computed velocity and $\mathbf{U}_0 = \mathbf{F}/(6\pi\mu\bar{a})$ is the analytical velocity determined by the formula for Stokes' drag. The two sets of data correspond to an octahedral and an icosahedral arrangement of mesh nodes before refinement. We generally use the second icosahedral level of refinement in simulations of swimming bacteria. 162

B.2 Comparison of the BEM with analytical result for a sphere of radius $\bar{a}$ translating under a prescribed force $\mathbf{F}$ towards a no-slip plane boundary at $z/\bar{a} = 0$. The vertical speed U_z is computed using the half space Green's function (dashed curve marked with open circles) and by explicitly meshing a portion of the boundary of size $20\,\bar{a} \times 20\,\bar{a}$ underneath the sphere (dotted curve marked with crosses). An analytical expression for the correction factor to Stokes' drag due to the presence of a plane boundary was given by Brenner [23]. This gives us the analytical speed of the sphere, shown with a solid, unmarked curve. Elements of the sphere mesh are adaptively refined based on proximity to the wall and likewise the elements on the wall are refined based on proximity to the sphere. 163

B.3 Convergence of the BEM for a bacterium swimming in free space using different levels of flagellum mesh refinement determined by the mesh parameters N_s and N_TN, described in §3.1. The progressive speed, $\bar{U}$, is defined in §3.5 and is scaled by the value U_0 at the highest refinement level with $N_\mathrm{s} = 10$. Reliable results are achieved with $N_\mathrm{s} \geq 6$ and $N_\mathrm{TN} \geq 200$ for this swimmer geometry, which is described by the parameters: $a_1^\mathrm{B}/a_2^\mathrm{B} = 1.4$, $N_\lambda = 1.5$, $L/\bar{a} = 10$, $ak = 1$, $a^\mathrm{T}/\bar{a} = 0.05$. The interpretations of model geometry parameters are summarised in appendix A. 164

B.4 Comparison of results using the rigid hook model of this thesis, abbreviated (S), the BEM of Phan-Thien et al. [99], abbreviated (P), and the SBT analysis of Higdon [64], abbreviated (H). $\bar{U}/V$ is the progressive speed non-dimensionalised by the linear wavespeed of the flagellum. The radius of the spherical cell body considered for this data set is denoted by $A \equiv \bar{a}$. The solid curves are predictions from (H). On the curve labelled $L/A = 5$, the solutions of (P) are represented by open circles while diamonds show the results of (S). On the curve labelled $L/A = 10$, the results of (P) are marked by closed triangles while those of (S) are open squares. This figure was reproduced with permission from reference [99] with new data overlaid. 165

B.5 Convergence of the swimming velocity for a bacterium in a channel as the length of the meshed channel section, L_x, is varied. The channel has dimensions $H_y = H_z = 10\,\bar{a}$ and the bacterium is aligned with the channel and placed at $y/\bar{a} = 0$ with three different heights: $z/\bar{a} = 0$ ("centre"), $z/\bar{a} = -2$ ("midway") and $z/\bar{a} = -4$ ("boundary") as illustrated in (a). The relative error is defined as $\epsilon_{\text{rel}} := \|\mathbf{U} - \mathbf{U}_0\|/\|\mathbf{U}_0\|$, where $\mathbf{U}$ is the computed instantaneous velocity and $\mathbf{U}_0$ is the instantaneous velocity in the case of the greatest meshed channel section length, $L_x = 100\,\bar{a}$. 166

C.1 A periodic orbit found for a trajectory in a square channel of size $30\,\bar{a}$ (see Fig. 5.8). (a) Time series of $\tilde{x}_j^1 \equiv \tilde{y}_j$ (blue curve) and $\tilde{x}_j^2 \equiv \tilde{z}_j$ (green curve), (b) $\tilde{x}_j^3 \equiv \tilde{\eta}_j$ (cyan curve) and $\tilde{x}_j^4 \equiv \tilde{\zeta}_j$ (red curve). (c) Periodograms I_k of the discrete Fourier transform for each of the components of the trajectory. Colours correspond to the curves in (a) and (b) and the vertical scale is logarithmic. Strong peaks are evident at some multiples of the fundamental frequency $k = N_\tau = 5$ and the error computed for this data set was $\varepsilon_{\tau,N_\tau} = 2.5 \times 10^{-5}$. 174

C.2 Comparison of periodic orbits from different trajectories and evaluation of rotational symmetry. (a) A periodic orbit and its three rotational images are plotted (all lying under the cyan curve) for a boundary escaping swimmer in a square channel of width $20\,\bar{a}$. The periodic orbit of another trajectory is also plotted (black curve). (b) A periodic orbit and its three rotational images are plotted for a boundary escaping swimmer in a square channel of width $30\,\bar{a}$. This orbit has rotational symmetry of order two. 175

Chapter 1

Introduction

1.1 The role of bacteria

Since Antonie van Leeuwenhoek first observed bacteria under a microscope more than 300 years ago, we have come to learn how widespread and important these organisms are in their many roles in nature. They have evolved many unique metabolic pathways and adaptations to thrive in almost any habitat on Earth and are critical for maintaining nutrient cycles by fixing atmospheric carbon and nitrogen, for example. The versatility and diversity of this group of organisms are well demonstrated by the estimate that 10,000 bacterial types can be found in a 100 g sample of soil [123].

Most experimental studies of bacteria involve pure cultures of planktonic cells. This nutrient-rich, controlled environment allows the strains to grow well without contamination or interaction with other microbes. However, there is evidence that bacteria in naturally occuring environments behave very differently as a result of the complexity of the habitat [32]. In particular, Lock et al. [87] found that more bacteria exist in sessile colonies than in planktonic form in the river ecosystems that were studied. These colonies are termed biofilms and form macroscopic, gel-like masses that often grow on solid surfaces immersed in water.

Initially, a few planktonic bacteria adhere to a surface through pili and polymers protruding from the bacterial surface. These cells divide and exude polysaccharides that form a matrix around the developing microcolony. Planktonic bacteria are also

more likely to adhere to this matrix and join the community. A mature biofilm provides a protected environment for its inhabitants by reducing the contact with antibacterial chemicals and organisms [32]. This makes it particularly difficult to combat biofilm growth.

Many industrial systems are faced with the problem of undesirable biofilm formation. For example, the surfaces of water-cooled heat exchangers need regular cleaning because bacterial biofilms that gradually build up can drastically reduce the efficiency of heat transfer by preventing convection at the exchange surface [46]. Other types of impact include increased drag due to biofouling on hulls of ships and bacterial-induced corrosion of metals. It was estimated that the costs due to heat exchanger fouling alone in the UK exceeded £300 million per annum over 30 years ago [42].

Medical implants are also highly susceptible to biofilm colonisation and are thought to be related to roughly half of all nosocomial infections [108]. Compared with most of the body's natural tissue surfaces, the surfaces of implants are ineffective against bacteria and consequently, large biofilm populations have been seen on a wide variety of implanted devices [32]. While these biofilms are often not problematic themselves, they act as reservoirs where potentially harmful microbes grow before being released into the body. This can lead to chronic infections as the source of the pathogens is difficult to eradicate.

Motility is an important aspect of bacterial behaviour, as a factor in the pathogenicity of certain strains as well as being crucial to the dispersal of populations that leads to the colonisation of new surfaces [45, 73]. The most common method of bacterial locomotion not requiring a solid substrate is flagellar propulsion, which is the focus of this thesis.

1.2 Bacterial physiology and locomotion

Most bacteria that swim using external flagella are rod-shaped. Some species, such as *Caulobacter crescentus* and *Vibrio cholerae*, have curved bodies (Fig. 1.1). Embedded in the cell membrane is a rotary motor, which turns the long, helical flagellum in the surrounding fluid (Fig. 1.2). Monotrichous bacteria are those with a single flagellum, typically at a pole of the rod-shaped cell. When turned, the flagellum acts as a propellor driving the cell forward. The motion of *Rhodobacter sphaeroides*, a monotrichous bacterium, is illustrated in Fig. 1.3. Peritrichous bacteria, such as *Escherichia coli* and *Salmonella typhimurium*, have multiple flagella emerging from all over the cell surface. When all flagella turn in the same sense, the filaments tend to bundle together behind the cell and push the bacterium forward much like a single flagellum. Lophotrichous bacteria similarly form flagellar bundles but their flagella instead all emerge from a specific region at a pole of the cell body.

Motors of some bacteria can operate in either direction and occasionally switch to the reverse direction. When this happens in peritrichous bacteria, the filaments do not turn coherently and the flagellar bundle disassociates, leading to an unpredictable rotation of the cell. This action, known as "tumbling", randomises the subsequent direction of motion and is an integral part of the strategy many bacterial species use to respond to gradients in environmental stimuli. In the monotrichous *R. sphaeroides*,

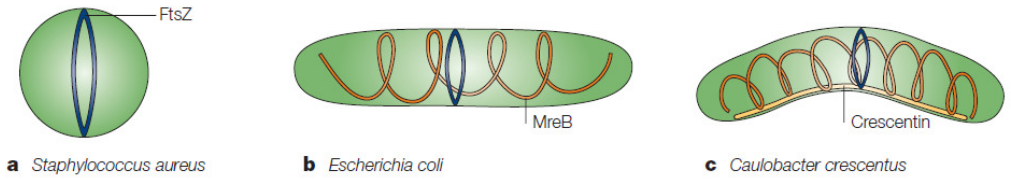

Figure 1.1: Illustration of three bacterial cell shapes. (a) Cocci are rarely reported to have flagella. (b) Rod-shaped bacteria are the most commonly studied type of flagellated bacterium. Examples include *E. coli*, *S. typhimurium* and *R. sphaeroides*. (c) Some rod-shaped bacteria, such as *C. crescentus*, are curved. Figure reproduced with permission from reference [25].

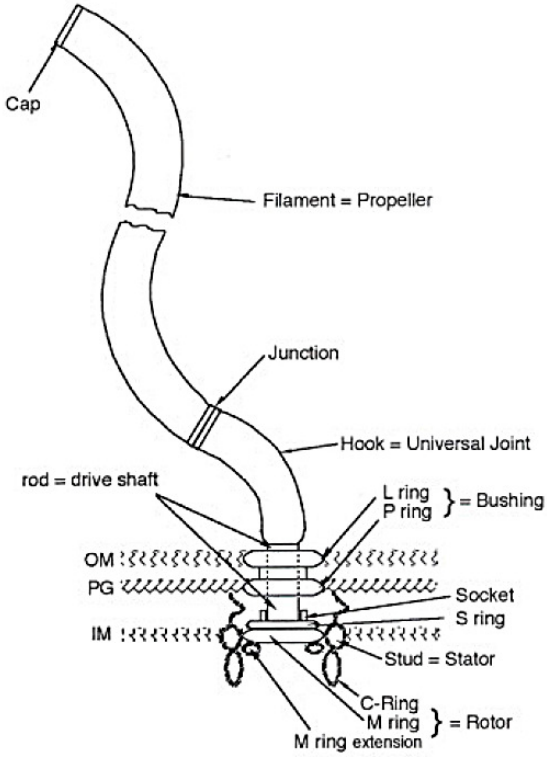

Figure 1.2: Schematic diagram of the structure of the bacterial flagellum. The layers labelled IM and OM are the inner and outer membranes of the bacterial cell respectively. The main components of the flagellar apparatus are the filament, the motor and the hook connecting the filament to the rotor. Figure reproduced with permission from reference [37].

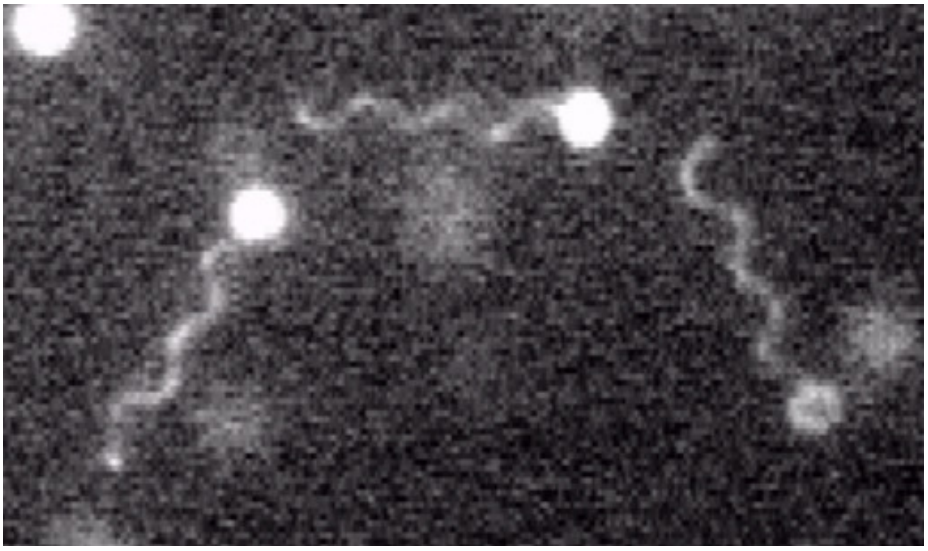

Figure 1.3: Superposition of three frames taken from a movie of swimming *R. sphaeroides* courtesy of Howard Berg's laboratory website [10]. The organism, with a clearly visible flagellum, moves from left to right in a clockwise circular arc over a period of roughly two seconds. The curved path is due to the presence of nearby surfaces, such as a cover slip, an effect that will be discussed in chapter 4. Movies such as this give support to modelling the bacterial flagellum, at least for monotrichous species, as a rotating rigid helix during periods of steady swimming. Furthermore, the directional persistence of steadily swimming cells in movies indicates that Brownian motion is not a leading order effect and may be neglected here.

the motor does not reverse but occasionally stops [4]. This is analogous to the "tumbling" of peritrichous cells as the cell reorientates due to coiling of the flagellar filament during the periods of stopped motor activity [5].

By regulating the frequency of reorientation based on perceived changes in the environment, bacteria can swim preferentially towards or away from a chemical or light source, for example. The process of migrating towards or away from regions of higher chemical concentrations is known as chemotaxis, while the equivalent response to gradients in light intensity is known as phototaxis. Although each reorientation is random and does not guarantee a favourable new direction of motion, the underlying temporal regulation in bacterial chemotaxis has proven to be a very successful strategy and has inspired optimisation algorithms for general numerical applications [94].

1.2.1 The motor and basal body

The bacterial motor is a structure about 45 nm in diameter spanning the cytoplasmic membrane, cell wall and outer membrane (Fig. 1.2) [35, 49]. Much is known about the structure of the various rings of proteins that make up the basal body, which depends on the species under consideration. It is widely accepted that the motor is driven by the flow of ions, H^+ in many species but Na^+ in others, across the cytoplasmic membrane through the motor. The ion concentration gradient is maintained by other processes that pump the ions back out of the cell. However, the precise details of the motor torque generation mechanism are still the subject of investigations [118, 100].

A variety of experimental techniques have been used to investigate the relationship between motor torque generation and rotation frequency. The findings of many such studies are well summarised by Sowa & Berry [118]. One example is the work by Sowa et al. [119] on the marine bacterium, *Vibrio alginolyticus*, in which cells were immobilised on a glass surface. Beads of sizes 0.46–1.65 μm in diameter were allowed to attach to the flagella, which continued to be driven by the motors of

these immobilised cells. The oscillatory motion of the beads was tracked with sub-millisecond and nanometer resolution using phase-contrast imaging. From this data, the motor frequency was deduced. By virtue of the governing Stokes flow equations, a linear relationship can be assumed between the rotational frequency and the torque required to drive the flagellum. The rotational drag coefficient was estimated for the combined flagellum and bead, allowing the motor torque to be calculated from each observation.

Since a range of bead sizes was used, data could be collected with different values of the drag coefficient. This had the effect of altering the observed motor frequency, allowing a curve to be generated to describe the torque that the motor was capable of exerting at different frequencies. This curve is shown in Fig. 1.4 along with results of experiments on two other bacterial species. For all three species, the motor produces a nearly constant torque from stationary up to a "knee" frequency of hundreds of revolutions per second. Above this frequency, the torque output drops roughly linearly and relatively rapidly.

The relevance of the motor response curve to locomotion is that it determines the frequency of flagellum rotation, and consequently the swimming speed, when the bacterium is placed in a given medium. Because the angular momentum of the swimmer is negligible in Stokes flow, the flagellum accelerates effectively instantaneously so that the total torque from viscous drag along the filament balances the torque applied by the motor.

To estimate the viscous torque acting on the flagellum at different frequencies, we can assume that the shape of the flagellum is constant. This is not strictly true; we will see shortly that the elastic properties of filaments can lead to nonlinear deformations with stress. However, as long as the range of frequencies considered is not too large, this is a fair approximation. Linearity of the Stokes flow equations dictates that the torque required to turn the flagellum is proportional to the frequency. The load curve,

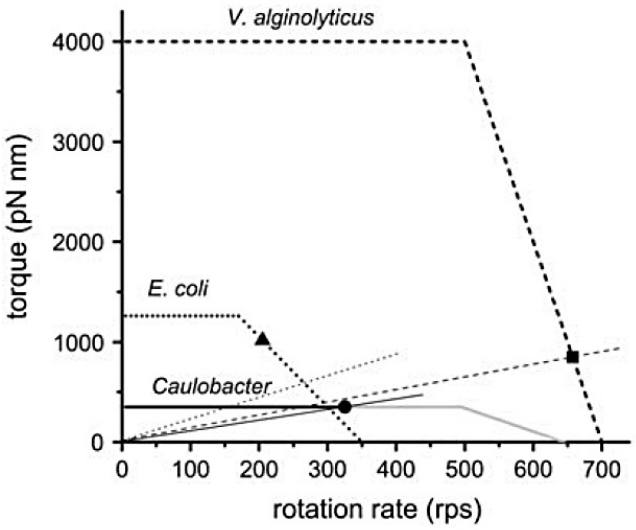

Figure 1.4: A schematic of the empirically deduced torques produced by bacterial motors operating at various frequencies. In each of the three species presented, the torque is approximately independent of frequency at low rotation rates and drops to zero with increasing frequency at high rotation rates. The straight lines passing through the origin show the estimated linear relationship between the rotation rate and the torque required to turn the helical flagellum at such a rate (see main text for further details). The marked intersections between the motor curve and flagellum load line for *C. crescentus* and *V. alginolyticus* indicate the frequencies and estimated motor torques corresponding to the respective freely swimming cells. For *E. coli* the load line refers to a single filament and not the flagellar bundle. Figure reproduced with permission from reference [84].

which defines the relationship between the rotation frequency and viscous torque for a given flagellum, is therefore a straight line with a gradient dependent on the flagellum shape. The intersection of this load curve with the motor response curve gives the observed motor frequency of the swimmer as this is the point at which the motor produces the torque required to balance the viscous load on the flagellum.

Experimental data suggest that some bacteria, namely *E. coli* and *V. alginolyticus*, swim in watery media with the motor operating in the high frequency range where the torque drops with frequency (Fig. 1.4). *C. crescentus* is an example in which the motor frequency while swimming in a watery medium was within the plateau region, i.e., below the "knee" frequency. Changing the viscosity of the medium affects the slope of the load curve, so it is possible to alter the intersection point and change the motor frequency. This is often exploited by experimentalists to reduce the motor speed and allow better imaging [5].

1.2.2 The hook and flagellar filament

Connected to the rotor of the bacterial motor is a polymeric filament about 20 nm in diameter and 50 nm long in *E. coli* [36] and about 100 nm long in *R. sphaeroides* [57]. This structure, called the hook, is highly curved in most species, often seen bent to a right angle [36]. There are some exceptions, such as *R. sphaeroides* and *V. alginolyticus*, which have straight hooks [117, 80]. The hook acts as a flexible coupling, transmitting the torque from the motor to the filament, which are generally not coaxial. The mechanism of hook length regulation is still not fully understood but the standard deviation within a culture is about 10% and there is evidence that this control is important for proper motility [66, 128].

Most of the flagellum is accounted for by the flagellar filament, which is roughly of the same thickness as the hook but can grow to 15 μm in length [93]. The filament is made up of flagellin proteins with 11 protofilaments twisting around each other leaving

a hollow core running through the centre. The filament itself forms a helical shape under normal conditions. Different conformations of the helical superstructure can be identified. Calladine [26] proposed a simple model explaining these observations based on the hypothesis that each subunit can exist in one of two states affecting the positions of its sites of binding with neighbours. By considering the elastic energy in forcing the subunits into a given lattice configuration, favourable arrangements can be found. A modification of this model used by Darnton & Berg [34] gave 12 predicted filament conformations, which correspond to the possible numbers of the 11 protofilaments in a particular state. The resulting conformations range from straight to highly coiled and most have been seen experimentally. An alternative model also based on elastic interactions between subunits was proposed by Srigiriraju & Powers [121], who outlined predicted phase transitions in response to applied moments.

These models illustrate the complexity of bacterial flagella despite the relative simplicity of the components and structure and the common purpose of achieving motility. In fact there are many subtle differences between flagella of different species, resulting in a variety of possible sets of polymorphisms. For instance, Shah et al. [111] reported that the flagella of *R. sphaeroides* show unique characteristics among bacterial filaments, including the range of polymorphic transitions displayed under varying conditions and the common occurence of an open-coil form under physiological conditions. A systematic survey of 18 strains of bacteria showed that many species could be categorised into three families of flagellar polymorphisms but there were also exceptions [52]. Thus, it is clearly a simplification to treat all flagella as the same.

Nonetheless, if we consider only steadily swimming monotrichous bacteria, it is consistently observed that the flagellum is turned like a corkscrew, maintaining an approximately helical shape (Fig. 1.3). Flagellar bundles in species with multiple flagella also appear to propagate helical waves during swimming, though the interactions between filaments and kinematics of each filament are not fully

understood.

1.3 Statement of mathematical problem

The focus of this DPhil work will be an analysis of a simple model for a rod-shaped bacterium propelled by a single, polar flagellum. *R. sphaeroides* and *V. alginolyticus* are two species to which this model may reasonably apply. The flagellum is approximately helical and extends directly behind the cell body during periods of steady swimming. Filament elasticity, with its complex polymorphisms, will not be considered but a model for an elastic hook will be presented in chapter 6. Elsewhere it is assumed that the shape of the hook is fixed as the bacterium swims and hence the flagellum rotates rigidly about the cell body axis.

For simplicity, the model developed in the present work assumes that the surface of the bacterium body and flagellum is smooth (i.e. free of pili and other irregularities) and deformations and all non-hydrodynamic effects, such as electrostatic interactions and Brownian motion, are neglected. Before proceeding with the hydrodynamic formulation, the neglect of Brownian motion should be justified.

Microscopic objects drift and turn randomly due to molecular scale collisions with the fluid particles. Swimming would be a waste of energy and resources if thermal noise completely randomised the overall trajectory. By comparing Brownian effects to directed propulsion, Dusenbery [44] found that the minimum length of an organism expected to benefit from active motility is roughly $0.6\,\mu\text{m}$. The ratio of diffusion coefficients of motile to non-motile cells was found to vary with the sixth power of the body length. Hence, Brownian motion quickly becomes irrelevant as the size surpasses the minimum requirement. Brownian rotation of the cell, which makes controlled motility more difficult, is reduced in part by the stabilising effect of a flagellum extending from the cell body [91]. For *R. sphaeroides* with a length of $1.73\,\mu\text{m}$ [115], it would be justified to neglect Brownian motion, as further indicated

from inspection of bacterial swimming movies such as those produced by Berg's laboratory (Fig. 1.3) [10].

In flagellar propulsion, motility is achieved as a consequence of the fluid–structure interaction between the organism and the surrounding medium. Thus, for a prescribed swimming stroke, the cell trajectories and associated flow fields can be calculated by solving a fluid dynamics problem with boundary conditions determined by the geometry of the swimmer. For a *V. alginolyticus* cell of length $L = 2\,\mu\text{m}$ swimming at a speed of $U = 100\,\mu\text{m}\,\text{s}^{-1}$ [90] in a fluid with the viscosity and density of water, with $\mu = 10^{-3}\,\text{Pa}\,\text{s}$ and $\rho = 1000\,\text{kg}\,\text{m}^{-3}$ respectively, the Reynolds number is $\text{Re} = \rho UL/\mu = 2 \times 10^{-4}$. Considering fluid flow around the flagellar filament, the lengthscale is the flagellar diameter, $d = 32\,\text{nm}$, and the characteristic flow speed is the linear speed of a point on the flagellum, which is in the shape of a helix of radius $r = 0.14\,\mu\text{m}$ rotating at frequency $\omega = 1000\,\text{Hz}$. This results in an even smaller Reynolds number $\text{Re} = \rho\omega rd/\mu \approx 4.5 \times 10^{-6}$. The Reynolds number is of a similar order of magnitude for other bacterial species as well. Thus, we can be confident that fluid inertia is negligible and the fluid around the swimmer is well described by the equations of Stokes flow,

$$-\nabla p + \mu\nabla^2\mathbf{u} = \mathbf{0}, \quad \nabla\cdot\mathbf{u} = 0, \tag{1.1}$$

where p is the generalised pressure field, $\mathbf{u}$ is the velocity field and μ is the dynamic viscosity of the fluid. The generalised pressure is the usual fluid pressure field possibly modified by the addition of a scalar potential field, the gradient of which describes a conservative body force. For example, a constant gravitational body force may be included in this way without introducing an additional term in (1.1). Linearity of these equations greatly improves both analytical and numerical tractability, but a world without inertia is unfamiliar to human experience and results can sometimes seem counter-intuitive.

Defining a reference point $\mathbf{x}_0$ and a set of basis vectors $\mathbf{e}_i$, $i = 1, 2, 3$ associated

with the swimmer, the deformation of the swimmer configuration can be decomposed into a rigid body motion, consisting of the translation of $\mathbf{x}_0$ and rotation of $\mathbf{e}_i$, and the deformation relative to this rigid motion, which we define as the swimming stroke. If the translational velocity is $\mathbf{U}$, the rotational velocity is $\boldsymbol{\Omega}$ and the velocity due to the swimming stroke is $\mathbf{u}_\mathrm{s}$, then the instantaneous velocity at a given point $\mathbf{x}$ on the surface of the swimmer can be expressed as

$$\mathbf{u}(\mathbf{x}) = \mathbf{U} + \boldsymbol{\Omega} \times (\mathbf{x} - \mathbf{x}_0) + \mathbf{u}_\mathrm{s}(\mathbf{x}), \quad \mathbf{x} \text{ on surface of swimmer.} \tag{1.2}$$

If the swimmer has approximately the same density as the surrounding fluid, then we can neglect the inertia of the swimmer as we have done for the fluid. This can be justified by considering the effect of the inertia of a sphere translating in one dimension, $I = 4\pi r^3 \rho v/3$, where r is the sphere radius and v is the speed. The Stokes drag formula gives the drag force $\mathrm{d}I/\,\mathrm{d}t = F = -6\pi\mu r v$, leading to an exponentially decaying velocity with decay constant $9\mu/(2\rho r^2) = 4.5 \times 10^6\,\mathrm{s}^{-1}$ for a sphere of radius $1\,\mu\mathrm{m}$ in a watery medium. Hence, such an object stops within a microsecond and its inertia can be neglected on the timescale of interest, which is of the order of milliseconds for a motor frequency of hundreds of Hertz. A similar calculation shows that angular momentum is also negligible. The sum of all forces and torques on the swimmer can therefore be taken to be zero. We write

$$\mathbf{F}^\mathrm{visc} + \mathbf{F}^\mathrm{ext} = \mathbf{0}, \quad \mathbf{M}^\mathrm{visc} + \mathbf{M}^\mathrm{ext} = \mathbf{0}, \tag{1.3}$$

where $\mathbf{F}^\mathrm{visc}$ is the total viscous force over the entire swimmer, $\mathbf{M}^\mathrm{visc}$ is the torque resulting from the viscous force distribution, and any other effects, such as sedimentation due to the swimmer being denser than the surrounding fluid, or gravitational torques due to non-uniform mass density within the organism, are encapsulated by the external force and torque, $\mathbf{F}^\mathrm{ext}$ and $\mathbf{M}^\mathrm{ext}$, respectively.

The task of determining swimming speed and cellular trajectories given a flagellar waveform characterised by the swimming stroke $\mathbf{u}_\mathrm{s}$ and external forces and torques

$\mathbf{F}^{\text{ext}}$, $\mathbf{M}^{\text{ext}}$ then reduces to the determination of $\mathbf{U}$ and $\boldsymbol{\Omega}$ that allow (1.1) to be solved subject to the boundary conditions (1.2) and constraints (1.3). The swimming stroke is time dependent but the absence of inertia means that the velocity $\mathbf{U}$ and angular velocity $\boldsymbol{\Omega}$ depend only on the instantaneous swimming stroke velocity and geometrical configuration of the swimmer's boundary. By using a suitable time-stepping algorithm we can obtain the cell trajectory and orientation as functions of time.

In our models of bacterial cells, we will impose $\mathbf{F}^{\text{ext}} = \mathbf{0}$ and $\mathbf{M}^{\text{ext}} = \mathbf{0}$. This either implies that there is no gravity acting or that the swimmer is neutrally buoyant and the centre of volume coincides with the centre of mass so that gravity does not cause sedimentation or reorientation of the cell. Unicellular organisms are typically 5–10% denser than water. Balancing this excess gravitational force with Stokes drag gives a sedimentation velocity of the order of tens of nanometres per second whereas typical swimming speeds are tens or hundreds of microns per second. There is also experimental evidence that the flow fields around a bacterium are consistent with those of force-free swimmers [40]. Neglecting gravity is therefore justified in the situations we will be investigating. It is interesting to note that since viscous drag scales with the particle radius whereas the gravitational force scales with volume, it is not appropriate to neglect gravity for the much larger *Volvex carteri*, which is a flagellated organism 200 μm in radius, even though the excess density is as low as 0.3% [41].

We will first give some consideration to the notion of swimming efficiency and explore how morphology might be optimised within the limited scope of our geometrical model. A comparison will be made between two scenarios: swimming in bulk fluid and swimming near a no-slip plane boundary. We will then examine the effects of such a boundary on the trajectories of the bacteria. The most important feature to note is whether or not flagellated swimmers are hydrodynamically attracted

to boundaries. We will extend the analysis to swimming between two parallel planes and inside a rectangular prism of fluid bounded by no-slip walls. The aims are to predict the types of trajectories that arise from confinement in channels of different sizes and probe the possible effects of this confinement on the speed of propagation along the channel.

Finally, an extension of the model will be implemented to allow elastic deformations of the flagellar hook. This gives extra degrees of freedom for the swimming stroke velocity $\mathbf{u}_s$ within the mathematical formulation of the swimming problem described above. The implications of hook flexibility will be investigated to determine when it may be neglected and when it is dynamically important.

1.4 Historical development of mathematical and numerical analyses of flagellated micro-organisms

1.4.1 Resistive force theory (RFT)

In the 1950s Gray & Hancock [60] calculated the propulsive forces and resulting velocity from planar bending waves along the flagellum of a sea-urchin spermatozoon. The technique they pioneered became known as resistive force theory and gives a linear relationship between the viscous drag per unit length acting on a section of a slender filament and the velocity of this section relative to the ambient fluid. This is an approximation to only logarithmic accuracy in the slenderness ratio of the filament but remains popular because its simplicity allows it to be used to capture the hydrodynamics within more complex frameworks including elastic deformations, for example [54].

In formulating resistive force theory, the filament in question is assumed to be thin, with a circular cross-section. Thus one can firstly consider an average force per unit length acting on the filament centreline, rather than a force per unit area acting

over the surface. In addition, the cross-sectional symmetry also entails there are only two independent, non-trivial coefficients C_{N} and C_{T} relating forces to velocities for the filament in the normal and tangential directions, since the binormal and normal are interchangeable. Decomposing the local filament centreline velocity into its tangential, normal and binormal directions, i.e. $\mathbf{v} = \mathbf{v}_{\mathrm{N}} + \mathbf{v}_{\mathrm{T}} + \mathbf{v}_{\mathrm{B}}$, with an analogous expression for the local viscous force per unit length acting on the filament, $\mathbf{f} = \mathbf{f}_{\mathrm{N}} + \mathbf{f}_{\mathrm{T}} + \mathbf{f}_{\mathrm{B}}$, then resistive force theory formally states that in an otherwise quiescent fluid the local viscous drag forces and filament velocities are related by

$$\mathbf{f}_{\mathrm{T}} = -C_{\mathrm{T}}\mathbf{v}_{\mathrm{T}}, \quad \mathbf{f}_{\mathrm{N}} = -C_{\mathrm{N}}\mathbf{v}_{\mathrm{N}}, \quad \mathbf{f}_{\mathrm{B}} = -C_{\mathrm{N}}\mathbf{v}_{\mathrm{B}}. \tag{1.4}$$

Simple kinematical and symmetry arguments based on linearity are sufficient to demonstrate that a linear, symmetric tensor relates viscous drag to velocity for a sufficiently long, straight cylinder and thus, via a suitable choice of axes, the above equations emerge. However, the power of resistive force theory is the possibility of applying these local relationships to any slender body with circular cross-section so that the viscous drag on a moving and deforming slender body can be estimated by summing contributions from short segments, as long as the thickness of the body is small compared to the radius of curvature of its centreline. For a filament of length L, the net viscous force and torque on the filament are given by

$$\begin{aligned}
\mathbf{F}^{\mathrm{fil}} &:= \int_0^L \mathbf{f}(s)\,\mathrm{d}s \\
&= -C_{\mathrm{N}}\int_0^L \mathbf{v}_{\mathrm{N}}(s)\,\mathrm{d}s - C_{\mathrm{N}}\int_0^L \mathbf{v}_{\mathrm{B}}(s)\,\mathrm{d}s - C_{\mathrm{T}}\int_0^L \mathbf{v}_{\mathrm{T}}(s)\,\mathrm{d}s, \qquad (1.5)\\
\mathbf{M}^{\mathrm{fil}} &:= \int_0^L \mathbf{x}(s)\times\mathbf{f}(s)\,\mathrm{d}s \\
&= -C_{\mathrm{N}}\int_0^L \mathbf{x}(s)\times\mathbf{v}_{\mathrm{N}}(s)\,\mathrm{d}s - C_{\mathrm{N}}\int_0^L \mathbf{x}(s)\times\mathbf{v}_{\mathrm{B}}(s)\,\mathrm{d}s - C_{\mathrm{T}}\int_0^L \mathbf{x}(s)\times\mathbf{v}_{\mathrm{T}}(s)\,\mathrm{d}s. \qquad (1.6)
\end{aligned}$$

Assuming the bacterium is neutrally buoyant and no other non-hydrodynamic forces are present, the force and moment equations (1.3) dictate that the viscous forces and

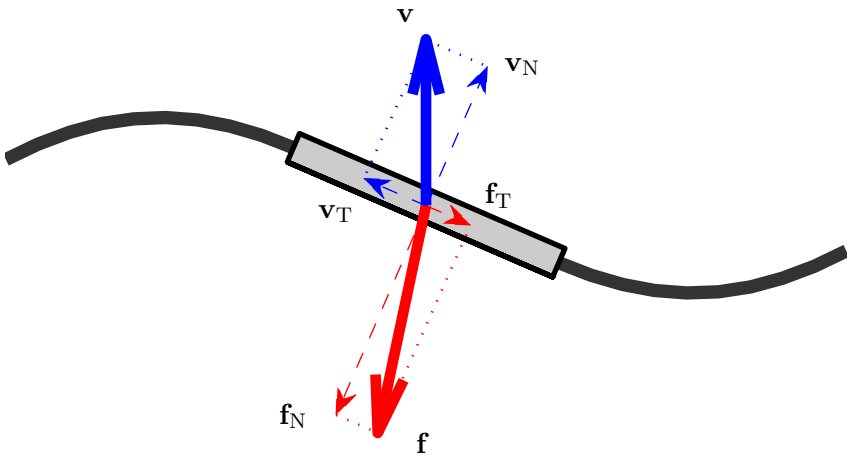

Figure 1.5: A two-dimensional representation of the resistive force theory approximation. The local velocity of a slender filament of circular cross-section can be separated into components tangential and perpendicular to the filament, $\mathbf{v}_\mathrm{T}$ and $\mathbf{v}_\mathrm{N}$, resulting in drag forces $\mathbf{f}_\mathrm{T}$ and $\mathbf{f}_\mathrm{N}$ respectively. Drag anisotropy means that $\mathbf{f}$ and $\mathbf{v}$ need not lie in the same direction. The generalisation to three dimensions, incorporating binormal components of the velocity vector field, is straightforward.

torques on the flagellum must balance those acting on the cell body. This is sufficient to determine the translational and rotational velocities of the cell body and thus the cell's swimming trajectory.

Critical to the prospect of locomotion is that $C_\mathrm{N} \neq C_\mathrm{T}$. To see why, consider an element of length δl of the flagellum undergoing some cyclic motion with period T while the body is held stationary. The time-average contribution to the net force by this element is

$$\begin{aligned}\langle \delta\mathbf{F} \rangle &= -\frac{C_\mathrm{N}\delta l}{T}\int_0^T \mathbf{v}_\mathrm{N}(t)\,\mathrm{d}t - \frac{C_\mathrm{N}\delta l}{T}\int_0^T \mathbf{v}_\mathrm{B}(t)\,\mathrm{d}t - \frac{C_\mathrm{T}\delta l}{T}\int_0^T \mathbf{v}_\mathrm{T}(t)\,\mathrm{d}t \\ &= -\delta l(C_\mathrm{N}\langle \mathbf{v}_\mathrm{N}\rangle + C_\mathrm{N}\langle \mathbf{v}_\mathrm{B}\rangle + C_\mathrm{T}\langle \mathbf{v}_\mathrm{T}\rangle). \end{aligned} \tag{1.7}$$

While $\langle \mathbf{v}_\mathrm{N}\rangle$, $\langle \mathbf{v}_\mathrm{B}\rangle$ and $\langle \mathbf{v}_\mathrm{T}\rangle$ need not be zero for a general periodic motion, the net displacement,

$$\mathbf{x}(T) - \mathbf{x}(0) = T\langle \mathbf{v}\rangle = T(\langle \mathbf{v}_\mathrm{N}\rangle + \langle \mathbf{v}_\mathrm{B}\rangle + \langle \mathbf{v}_\mathrm{T}\rangle),$$

is zero by assumption. Hence, the condition $C_\mathrm{N} = C_\mathrm{T}$ leads to a vanishing average

force contribution from each element of the flagellum. This means on average no force is required to hold the body stationary, i.e. there is no locomotion.

Application of RFT requires the evaluation of the resistance coefficients C_{N} and C_{T}, which is based on the flow fields around slender filaments in very viscous fluids. Hancock [61] explored such problems using two forms of singular solutions to the Stokes flow equations. The first is known as a Stokeslet and represents a point forcing of the fluid. In particular, the flow field $\mathbf{u}$ at location $\mathbf{x}$ due to a point forcing of strength $\mathbf{F}$ acting at point $\mathbf{X}$ in an infinite domain is given by

$$u_i(\mathbf{x}) = S_{ij}(\mathbf{x}, \mathbf{X})F_j, \quad S_{ij} = \frac{1}{8\pi\mu}\left(\frac{\delta_{ij}}{R} + \frac{R_i R_j}{R^3}\right) \tag{1.8}$$

where $\mathbf{R} := \mathbf{x} - \mathbf{X}$ and $R := \|\mathbf{R}\|$. Throughout this thesis, we use the notation $\|\mathbf{v}\| := \sqrt{v_1^2 + v_2^2 + ... + v_n^2}$ for the Euclidean norm of an n-dimensional vector $\mathbf{v}$, and δ_{ij} is the Kronecker delta.

The second singular solution is the potential dipole, or point source dipole. The flow field due to a potential dipole of strength $\mathbf{d}$ placed at point $\mathbf{X}$ in an infinite fluid is

$$u_i(\mathbf{x}) = D_{ij}(\mathbf{x}, \mathbf{X})d_j, \quad D_{ij} = \frac{1}{4\pi}\left(-\frac{\delta_{ij}}{R^3} + 3\frac{R_i R_j}{R^5}\right). \tag{1.9}$$

Taking advantage of the linearity of Stokes flow, Hancock [61] constructed asymptotically accurate expressions for the flow fields near a moving slender filament by placing these two types of singularity along its centreline with appropriately chosen weightings. By calculating the viscous stresses on the filament, the approximate relationship between viscous drag and local velocity can be deduced. Guided by these reults, Gray & Hancock [60] used

$$C_{\mathrm{T}} = \frac{2\pi\mu}{\ln(2\lambda/r) - 1/2}, \quad C_{\mathrm{N}}/C_{\mathrm{T}} = 2, \tag{1.10}$$

where r is the filament radius and λ is the wavelength of the flagellar beat pattern. The result $C_{\mathrm{N}}/C_{\mathrm{T}} = 2$ is the limiting value as the slenderness parameter

$\epsilon := r/\lambda \to 0$. However, due to the logarithmic dependence of both C_{T} and C_{N} on the slenderness parameter, this approximation is somewhat crude even for flagella, for which we typically have values $\epsilon = 10^{-3}$–10^{-2}. Improvements in the formulas for the resistance coefficients have been proposed by various authors, for example Lighthill [85] suggested $C_{\mathrm{T}} = 2\pi\mu/\log(0.18\lambda/r)$ and $C_{\mathrm{N}} = 4\pi\mu/(\log(0.18\lambda/r) + 1/2)$ for infinitely long filaments of constant radius either in the form of travelling helical waves or planar bending waves of small amplitude where in both cases it was assumed that the flagellum was moving in a zero-thrust state, i.e., the flagellum was not generating any net thrust to propel an attached load. Many authors have found the ratio $C_{\mathrm{N}}/C_{\mathrm{T}} \sim 1.7 - 1.8$ to be most appropriate [72].

The formalism of resistive force theory was extensively applied in numerous models of singly flagellated swimmers [30, 109, 31]. Such studies allowed estimates of the swimming speeds, viscous forces, energy dissipation, efficiencies and other physical quantities given the observed flagellar waveform. Lauga et al. [82] more recently used RFT with coefficients modified by the presence of a plane boundary [75] to explain the migration of flagellated bacteria towards boundaries and the circular paths that ensue close to the boundary. The analytical work assumed a spherical cell body close to the boundary so that lubrication approximations could be applied and only the special case in which the swimmer is parallel to the boundary was considered. The expressions obtained indicated that the swimmer both translates and rotates towards the wall as it swims. Estimates were also given for the curvature of the path assuming a trajectory parallel to and at a given distance from the wall. We will expand on this work using numerical techniques that are much less restrictive and show that there may exist a stable configuration at which the swimmer no longer drifts closer to the wall. This stable state then gives rise to the observed persistent, circular paths.

Resistive force theory has been shown to be remarkably consistent with more sophisticated theoretical methods as well as experiment when the flagellum propels a

small load, as is often the case for spermatozoa [72, 50]. However, it is recognised that using this simple approximation based on resistance coefficients leads to much greater errors when the filament must provide a substantial thrust to overcome the drag on an attached cell body, as with bacteria for instance [72, 120, 28]. It is likewise unable to take into consideration hydrodynamic interactions with other nearby swimmers or surfaces without losing its advantage of tractability.

1.4.2 Slender body theory (SBT)

Many of the values of coefficients used in RFT were derived from results of a more accurate set of mathematical techniques that grew into slender body theory. As in Hancock's [61] pioneering analysis, line distributions of Stokes flow singularities are sought to satisfy the no-slip boundary condition around the body subject to required force and torque balance constraints. Cox [33] and Batchelor [8] used matched asymptotic expansions in the logarithm of the filament aspect ratio to relate the disturbance velocities to the local force densities. Keller & Rubinow [76] used the results of Cox to improve upon existing analyses by characterising the full three-dimensional trajectories rather than assuming propagation in one linear direction. For instance, it was shown that helical wave motion of the flagellum leads to a trajectory that is helical with a small radius.

As a consequence of the logarithmic dependence on the slenderness ratio, high accuracy requires many terms in the asymptotic expansions, which are complex and cumbersome. Lighthill [85] greatly simplified the process of solving filament dynamics by determining an expression for the relationship between the Stokeslet strength and the potential dipole strength, and giving an integral equation relating the Stokeslet distribution to the velocity at a given cross-section of the filament.

Discretisation of the integral equation leads to an algebraic system of equations that can be solved numerically. Not only can this be applied to general motions of

flexible filaments but the error in this formulation is linear, rather than logarithmic, in the slenderness parameter. Further developments were made by Johnson [71], who explored the accuracy of singularity representations of the flow field for curvilinear prolate ellipsoids and more general cross-sections. Flagellar end effects were incorporated and higher order accuracy was achieved by considering additional types of singularities.

This led to a canonical slender body theory in common use today which takes the form of the integral relation

$$u_i(\mathbf{x}) = \int_0^L S_{ij}(\mathbf{x}, \mathbf{X}(s)) f_j(s)\, \mathrm{d}s + \int_0^L D_{ij}(\mathbf{x}, \mathbf{X}(s)) g_j(s)\, \mathrm{d}s \tag{1.11}$$

between the flow field and the singularity weights along the flagellum centreline, parameterised by $\mathbf{X}(s)$; see Fig. 1.6. For a curvilinear filament with circular cross-section radius $r = \epsilon\eta(s)$, for $s \in [-1, 1]$ a non-dimensional arc-length parameter, one finds that the no-slip boundary conditions necessitate

$$\mathbf{g} = -\epsilon^2 \frac{\eta^3(s)}{2\eta'(s)} \frac{s}{1-s^2} \mathbf{f}$$

whereupon (1.11) reduces to an integral equation for the singularity strengths, $\mathbf{f}$ (with an implicit assumption that $\eta'(s) = 0$ only has one simple root at $s = 0$). This can be readily solved numerically, providing all the required information for exploring cellular trajectories and behaviors in terms of a given flagellar waveform. The cell body can also be incorporated in the analysis through additional singularities. Flagellated swimmers with spherical bodies were considered in this way by Higdon [63, 64]. A comparison between resistive force theory and slender body theory indicated good agreement between the two in cases where the cell body is small or absent but discrepancies grow when the cell body is significant, as is typically the case for bacteria [72, 120].

It should be noted that, while the helical beat pattern is typical of bacterial propulsion, all of the studies mentioned above deal with a eukaryotic flagellum. The

key difference here, from the point of view of hydrodynamics, is that the bacterial flagellum revolves with respect to the cell body as it is turned by a motor in the basal structure. In contrast, eukaryotic flagella (e.g. in spermatozoa) bend to give rise to propagating waves without rotating relative to the body except for very limited flagellar torsion. This results in a different velocity distribution around the surface of a given cross-section of the flagellum, although the motion of the centreline could be identical. The distinction was made clear in the review by Brennen & Winet [22] but there seems to be no consideration of the prokaryotic flagellum prior to that. This is quite understandable, given that quantitative comparisons with observations of spermatozoa were only just becoming possible at the time and bacteria are an order of magnitude smaller. Indeed, the idea that bacteria rotate their flagella was not proposed until 1966 [39] and a decade passed before this view became widely accepted. In any case, Brennen & Winet suggest that this bacterial rotation would make little difference to the overall motion of the organism. The correction would consist of an additional rotlet distribution along the flagellum and on the cell body. These torques would be small compared with the torque due to the helical wave motion and rotational motions decay faster than translations in viscous fluid. Hence, results from SBT considering helical motion of eukaryotic flagella are expected to apply almost equally well to prokaryotic flagella undergoing the equivalent motion.

A more important detail is that, for many flagellated organisms, a spherical cell body is a poor geometrical approximation. The possible influence of cell geometry on flagellar motility in spermatozoa was recognised as early as 1977 [56]. However, it is very difficult if not impossible to extend SBT analytically in the spirit of Higdon [63] to account for more general or realistic cell shapes. Furthermore, SBT is not suitable if there is close proximity between non-neighbouring parts of the flagellum or between the flagellum and another swimmer or external surface. Such cases call for direct numerical solution of the three-dimensional Stokes flow problem. One technique that

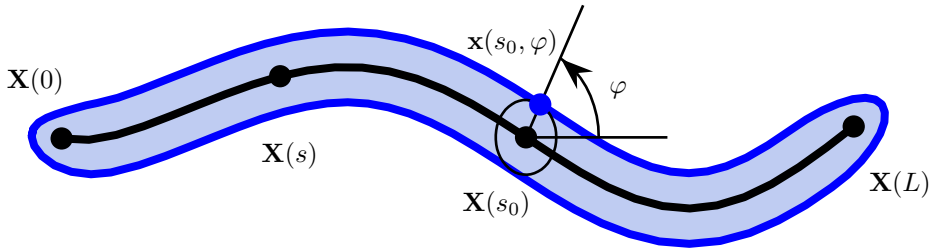

Figure 1.6: In slender body theory, Stokeslets and higher order singularities are distributed along the centreline $\mathbf{X}(s)$ with the aim of matching the resulting velocities at surface points $\mathbf{x}(s_0, \varphi)$ to the appropriate boundary velocities of the flagellum. To leading order this involves removing the φ-dependence and matching the surface velocities to the required centreline velocity at $\mathbf{X}(s_0)$ for each $s_0 \in [0, L]$.

is commonly used for simulations of cell locomotion is the boundary element method.

1.4.3 Boundary element method (BEM)

The boundary element method is a technique for solving partial differential equations where a Green's function is available. This is the method we will be implementing and will be discussed in more detail in chapter 2. Like SBT, this method is based on an integral equation relating the fluid velocity field to singularity distribution strengths. However, instead of a line distribution, the singularities act over a closed surface bounding the fluid, which constitutes the body of the swimmer in the case of modelling bacteria. The boundary integral equation gives an exact representation of the solution to the Stokes equations with no assumption about the slenderness of the body. It is therefore suitable for simulating the dynamics of cells with general body shapes, though most studies related to bacteria use cell bodies that are spherical, ellipsoidal or cylindrical with hemispherical caps on either end.

Phan-Thien et al. [99] used a BEM to analyse the motion of an ellipsoidal cell body propelled by a rotating helical flagellum. Good agreement was found when compared to Higdon's SBT results for optimising swimming in unbounded fluids [64]. More recently, Fujita & Kawai [53] have drawn the same conclusions with quantitatively

very similar results in their own BEM study. The applicability of these hydrodynamic models was tested by Goto et al. [59], who found quantitative agreement in swimming speeds between experimental observations and BEM simulations.

Ramia et al. [107] extended investigations to consider the interactions between two adjacent swimmers and between a swimmer and plane walls. This gave the first theoretical confirmation of Berg's [11] observations that bacteria swim with curved trajectories near surfaces and also demonstrated the tendency for cells to swim towards solid surfaces. However, despite its numerical flexibility boundary element studies to date have only considered up to two interacting swimmers or one swimmer in a confined domain. This limitation is partly due to high computational demands in larger problems but also because of the complexity in analysing the dynamics of even these systems. In addition, only rigidly rotating helical flagella have been considered.

One reason for this is the nontrivial formulation of constitutive relations that would govern the response of a deformable bacterium body or flagellum to the viscous stresses it experiences. However, there have been simulations of other types of swimmers with prescribed shape deformations and boundary fluid velocities that do not coincide with boundary motion [70, 2]. Nonetheless, the limited scope of studies to date reveals numerous areas where novel developments in the computational simulation of bacteria can be pursued.

1.4.4 Immersed boundary method (IBM)

An alternative, and in some ways complementary, approach to the boundary element method is the immersed boundary method. This was first used in the 1970s by Peskin [97] to model the flow of blood and structural response of the walls and valves in a human heart but is a general method for fluid–structure interactions. Unlike the techniques described above, it is valid at arbitrary Reynolds number and handles elastically deforming boundaries naturally. For detailed reviews of the immersed

boundary method, please see references [98, 92] and those therein.

Many variations of this method can be devised but the key idea is that the Eulerian grid on which the fluid equations are solved is separate from the Lagrangian mesh that describes the moving fluid–structure interface, or immersed boundary. Boundary conditions on the immersed boundary are translated into forcing terms on the interior fluid grid points. One advantage of this is that standard, efficient techniques can be used to solve the fluid equations on simple grids with simple boundary conditions.

The solid body is immersed in the fluid domain and it is typically assumed that some properties of the solid, such as density, are indistinguishable from those of the fluid. This means that the dynamics of the material points of the solid can be identified with the motion of the fluid that occupies the same space. Essentially, the boundary is treated as a collection of marked fluid points. The solid-like properties of this structure are enforced by the addition of elastic restoring forces between nodes of the immersed boundary. The general strategy is summarised as follows:

1. Suppose at a given time step we have the positions of the N boundary nodes $\mathbf{X}_k$, $k = 1, 2, ..., N$. Based on these, we compute the elastic forces between each pair of nodes $\mathbf{F}_{kl}^{\text{elast}}(\mathbf{X}_k, \mathbf{X}_l)$.

2. Since there is no inertia associated with the boundary (the inertia of the solid object is carried by the fluid in the space it occupies), we require the total force acting on each node to be zero. This means the hydrodynamic force exerted on the fluid at this node is equal to the sum of pairwise elastic boundary forces acting on this node, $\mathbf{F}_k^{\text{hyd}} = \sum_{l \neq k} \mathbf{F}_{kl}^{\text{elast}}$.

3. We then distribute these boundary forces onto the M Eulerian fluid grid points $\mathbf{x}_i$, $i = 1, 2, ..., M$, covering the computation fluid domain. This is achieved using a suitable regularised delta function $D_i(\mathbf{x}) = D(\|\mathbf{x} - \mathbf{x}_i\|)$ to obtain the fluid forces $\mathbf{f}_i = \sum_{k=1}^{N} D_i(\mathbf{X}_k)\mathbf{F}_k^{\text{hyd}}$. The boundary force $\mathbf{F}_k^{\text{hyd}}$ typically only

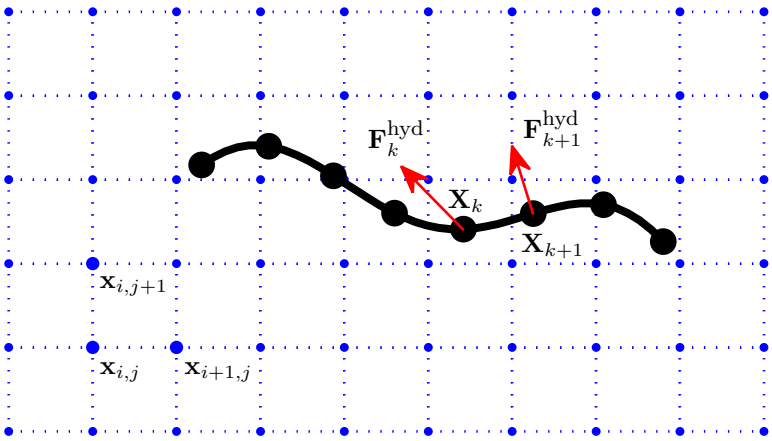

Figure 1.7: A schematic of the two distinct meshes in an immersed boundary method. The immersed boundary is described by the nodes $\mathbf{X}_k$. The fluid equations are solved on the rectangular grid of points $\mathbf{x}_{i,j}$ considering body forces that are derived from the boundary forces $\mathbf{F}_k^{\text{hyd}}$.

contributes to the grid force $\mathbf{f}_i$ at grid nodes within a few grid spacings of $\mathbf{X}_k$. Note that it would, of course, be more natural to use two or three indices to label grid points in a two- or three-dimensional fluid domain respectively but the current notation is used without loss of generality.

4. Solving a discretisation of the fluid flow equations with these forcing terms gives the flow field and hence the positions of the immersed boundary nodes at the next time step.

At this point, a few brief comments are warranted. Step 3 above has the effect of diffusing the fluid–structure interface since the boundary forces no longer act purely at boundary points. The choice of the spreading function D has implications both for the computational performance and for the accuracy in preserving the desired boundary condition. Usually the support of D_i will be limited to a small region in the neighborhood of $\mathbf{x}_i$. While this spreading can be utilised to efficiently simplify

the representation of the immersed object [24], it generally degrades the resolution of boundaries.

The Eulerian grid must therefore be sufficiently fine to resolve the local flow near the immersed boundary. At the same time, it must be sufficiently extensive to cover an appropriate fluid domain. Due to the long range of hydrodynamic interactions in the viscous limit, distant boundaries are particularly important when simulating microswimmers. Solving the Navier–Stokes equations generally requires a finite grid domain and the imposed boundary conditions on this domain will affect the motion of any swimmer placed inside. Although this may be desirable when modelling a finite chamber for comparison with an experimental set-up, this spatial dependence within the domain means that it is difficult to distinguish between wall effects and the dynamics of the swimmer in isolation. An unbounded domain, which is naturally accommodated by techniques involving singular solutions of Stokes flow, is more suitable in the latter case.

Another issue is the precise elastic interaction between boundary points. A one-dimensional immersed object may be reasonably described by a bead and spring model with a Hookian potential encouraging a preferred separation between successive nodes and preferred angle between successive pairs of nodes. When dealing with a general two- or three-dimensional object, it is less obvious how to define the forces acting on the interfacial nodes in a way that accurately reflects the structural response of the material. Elastic cross-links can certainly be used to provide structural reinforcement to an object of arbitrary shape but care must be exercised to verify that the resulting body behaves like the object it is intended to model.

Apart from the relative ease of implementing an IBM, there is the advantage that solving the fluid equations is somewhat independent of the size and complexity of the boundaries immersed within. Hence, multiple swimmers and arbitrary surfaces may be placed in the same fluid volume and the computational cost increases only for the

steps of computing the forces acting on the fluid and updating the positions of the swimmers. These steps are inexpensive and increase only linearly with the combined size of the immersed boundaries. For moderate numbers of simple swimmers, most of the computational effort is in solving the fluid equations and the number of swimmers has little impact on overall computation speed. To demonstrate this, nine swimming bacterial cells have been simulated in three-dimensional space [67]. Nonetheless, this is still far too few to guide and test how individual bacterial behaviors manifest at the population level, and simulating a sufficiently large domain for many bacteria with this technique is currently unfeasible. In addition, a geometrically accurate simulation of a peritrichous bacterium remains elusive even via the immersed boundary method.

Chapter 2

Numerical methods

The modern numerical technique known as the boundary element method has been growing in popularity since it was developed for early electronic computers in the 1960s and 1970s. In fact, the study of the equations on which this method is based has a much longer history. The original motivation came from potential theory, which describes electrostatics, gravity and diffusion, but many analogous results were subsequently found and applied in other areas of physics, such as acoustics, elasticity and fluid mechanics. An overview of some of the key figures in the development of BEMs and from the 18th century onwards was given by Cheng & Cheng [29].

The first textbook on BEMs was written by Brebbia in 1978 [21]. Other useful references include Banerjee & Butterfield [6] and Pozrikidis [104, 105], who also made available an extensive library of computational subroutines for implementing the BEM for solutions of Laplace's equation, Helmholtz's equation and Stokes flow. Implementing a BEM can be divided into four parts: deriving the relevant boundary integral equation, discretising the domain boundary into mesh elements, approximating the boundary integral by quadrature on the boundary mesh and solving the discretised boundary integral equation. We now consider each of these tasks in turn.

2.1 The boundary integral equation

The forced, incompressible Stokes equations are

$$\left.\begin{aligned} -\nabla p + \mu\nabla^2\mathbf{u} + \mathbf{b} = \nabla\cdot\boldsymbol{\sigma} + \mathbf{b} = \mathbf{0}, \\ \nabla\cdot\mathbf{u} = 0, \end{aligned}\right\} \tag{2.1}$$

where $\mathbf{b}$ and $\boldsymbol{\sigma}$ are the applied force and Cauchy stress tensor fields respectively, and the other quantities are as defined in §1.3. It can be shown [105] that if a flow is unforced throughout the interior of its domain V, then it can be represented by integrals over the boundary ∂V as

$$\begin{aligned} u_j(\mathbf{X}) = &-\int_{\partial V} f_i(\mathbf{x}) S_{ij}(\mathbf{x},\mathbf{X})\,\mathrm{d}S(\mathbf{x}) \\ &+\int_{\partial V} u_i(\mathbf{x}) T_{ijk}(\mathbf{x},\mathbf{X})\hat{n}_k(\mathbf{x})\,\mathrm{d}S(\mathbf{x}), \end{aligned} \tag{2.2}$$

where S_{ij} are the ij-components of the Stokeslet Green's function (1.8), $\mathbf{f}$ is the traction vector acting on the boundary enclosing the fluid, $\hat{\mathbf{n}}$ is the unit normal vector directed into the fluid and T_{ijk} expresses the stress tensor associated with a Stokeslet of strength $\mathbf{F}$ at point $\mathbf{X}$ as defined by

$$\sigma_{ik}(\mathbf{x}) = -p\delta_{ik} + \mu\left(\frac{\partial u_i}{\partial x_k} + \frac{\partial u_k}{\partial x_i}\right) = T_{ijk}(\mathbf{x},\mathbf{X})F_j, \quad T_{ijk} = -\frac{3R_iR_jR_k}{4\pi R^5}, \tag{2.3}$$

where $\mathbf{R} := \mathbf{x} - \mathbf{X}$ and $R := \|\mathbf{R}\|$ as in §1.4.1. This formula for T_{ijk} again pertains to unbounded three-dimensional fluid domains. In some applications, it will be helpful to use a Green's function that respects the boundary conditions of other fluid domains. In particular, when we examine swimming near a plane boundary, we will replace S_{ij} in (2.2) with the half space Stokeslet found by Blake [17]. This constructs a solution with no flow on the plane boundary without the need to include the plane in the boundary integral. The stress T_{ijk} can similarly be modified but we will remove this term completely, as we shall see shortly.

Equation (2.2) is analogous to the Somigliana identity for describing deformations of an elastic body [99]. The first integral on the right-hand side is known as the single-

layer potential while the second is the double-layer potential. Taking the limit as $\mathbf{X}$ approaches the boundary, we find the boundary integral equation

$$\frac{1}{2}u_j(\mathbf{X}) = -\int_{\partial V} f_i(\mathbf{x})S_{ij}(\mathbf{x},\mathbf{X})\,\mathrm{d}S(\mathbf{x}) + \int_{\partial V}^{PV} u_i(\mathbf{x})T_{ijk}(\mathbf{x},\mathbf{X})\hat{n}_k(\mathbf{x})\,\mathrm{d}S(\mathbf{x}), \quad (2.4)$$

for a point $\mathbf{X}$ on the boundary. The superscript PV indicates the principal value of the integral, which is the limit of the same integral excluding a small region of the domain around the singular point at $\mathbf{x} = \mathbf{X}$ as the size of this exclusion region tends to zero. This result requires the surface ∂V to have continuous normal vector and velocity distributions. We see that the fluid velocity and the traction over the boundary surface are connected and so one quantity determines the other.

It should be noted that the double-layer potential can be removed in the special case where the boundary is composed of disjoint closed surfaces each restricted to rigid body motions. This reduces the boundary integral equation to

$$u_j(\mathbf{X}) = -\int_{\partial V} f_i(\mathbf{x})S_{ij}(\mathbf{x},\mathbf{X})\,\mathrm{d}S(\mathbf{x}), \quad (2.5)$$

which holds for points $\mathbf{X}$ in the interior of the fluid domain as well as on the boundary.

The single-layer representation (2.5) can also be used to describe the flow field in the presence of more general types of boundary motion as long as volume is conserved, i.e. $\int_{\partial V} u_j\hat{n}_j\,\mathrm{d}S = 0$. The density $\mathbf{f}$ would then correspond to an interfacial traction jump, rather than simply the traction from one side of the boundary [104]. The single-layer equation is convenient because of its direct relation to physical quantities and because the integral is relatively straightforward to compute numerically. However, (2.5) will commonly be solved as a Fredholm integral equation of the first kind for the traction density. These problems are known to give rise to ill-conditioned matrix systems, which may present numerical difficulties. An alternative formulation is to remove the single-layer potential, leaving the double-layer potential equation

$$u_j(\mathbf{X}) = -\frac{1}{2}q_j(\mathbf{X}) + \int_{\partial V}^{PV} q_i(\mathbf{x})T_{ijk}(\mathbf{x},\mathbf{X})\hat{n}_k(\mathbf{x})\,\mathrm{d}S(\mathbf{x}), \quad (2.6)$$

where q_j is the double-layer density, which does not represent an observable physical quantity. The resulting second-kind Fredholm integral equation is well-posed but the singular integral is more difficult to evaluate accurately. Furthermore, there are restrictions on the types of flow that can be expressed in this form. This can be corrected with additional terms, as in the completed double layer boundary integral method [103, 102].

Ingber & Mammoli [69] compared the direct formulation (2.4), the double-layer formulation (2.6) and a third formulation expressing the traction vector at a test point in terms of boundary integrals of the velocity and traction fields. It was found that using (2.4) directly gave the best results in most cases despite the higher condition numbers associated with first-kind Fredholm integral equations. We will consider only the reduced expression, the single-layer formulation (2.5), due to its ease of implementation since we will be restricting boundaries to rigid body motions.

2.2 Boundary meshing

To calculate the surface force distribution in a general problem where analytical solutions are unknown, a numerical approach is needed. Quadrature methods will be used to compute the contributions to the integral in equation (2.5) from a finite number of surface elements. One important aspect of the boundary element method is therefore generating a mesh to discretise the boundary. The simplest discretisation involves approximating the surface by a tesselation of N_E flat triangles, with the nodes of the triangles on the desired boundary. The surface force could be taken as a constant $\mathbf{f}^n$ on triangle n so the problem would then be to solve for the $3N_\mathrm{E}$ independent components of force.

Instead of flat triangles of constant force density, we will use curved triangles and fit a quadratically varying force density on each triangle. This higher order interpolation method is able to approximate the curvature of the boundary with

fewer nodes and therefore yields greater accuracy for a given mesh size. It is also possible to implement methods of order higher than quadratic to achieve even greater gains but these will not be considered in the current work [27]. Following the scheme described by Pozrikidis [105], the curved triangles are defined by the three vertices and an additional point along each of the three edges. The surface of the triangle is mapped to a right-angled isosceles in ξ–η parameter space (Fig. 2.1). If the ith node of the triangle is at the point $\mathbf{x}^i$ and we denote the distance between nodes i and j by $d_{ij} \equiv \|\mathbf{x}^i - \mathbf{x}^j\|$, then the nodes are mapped to (ξ, η)–coordinates as follows:

$$\begin{aligned} &\mathbf{x}^1 \to (0,0), && \mathbf{x}^2 \to (1,0), && \mathbf{x}^3 \to (0,1), \\ &\mathbf{x}^4 \to (\alpha,0), && \mathbf{x}^5 \to (\gamma, 1-\gamma), && \mathbf{x}^6 \to (0,\beta), \end{aligned}$$

where

$$\alpha = \frac{d_{41}}{d_{24}+d_{41}}, \qquad \beta = \frac{d_{61}}{d_{36}+d_{61}}, \qquad \gamma = \frac{d_{53}}{d_{25}+d_{53}}. \tag{2.7}$$

A general point on the triangle is given by the expression

$$\mathbf{x}(\xi,\eta) = \sum_{k=1}^{6} \mathbf{x}^k \phi^k(\xi,\eta), \tag{2.8}$$

where ϕ^k are the cardinal interpolation functions defined by

$$\left.\begin{aligned} \phi^2(\xi,\eta) &= \frac{1}{1-\alpha}\xi\left(\xi - \alpha + \frac{\alpha-\gamma}{1-\gamma}\eta\right), \\ \phi^3(\xi,\eta) &= \frac{1}{1-\beta}\eta\left(\eta - \beta + \frac{\beta+\gamma-1}{\gamma}\xi\right), \\ \phi^4(\xi,\eta) &= \frac{1}{\alpha(1-\alpha)}\xi(1-\xi-\eta), \\ \phi^5(\xi,\eta) &= \frac{1}{\gamma(1-\gamma)}\xi\eta, \\ \phi^6(\xi,\eta) &= \frac{1}{\beta(1-\beta)}\eta(1-\xi-\eta), \\ \phi^1(\xi,\eta) &= 1 - \phi^2 - \phi^3 - \phi^4 - \phi^5. \end{aligned}\right\} \tag{2.9}$$

The surface metric at a point on the surface is given by

$$h_{\mathrm{S}} = \left\| \frac{\partial \mathbf{x}}{\partial \xi} \times \frac{\partial \mathbf{x}}{\partial \eta} \right\| \tag{2.10}$$

and the unit normal at this point is

$$\hat{\mathbf{n}}(\xi,\eta) = \frac{1}{h_{\mathrm{S}}}\left(\frac{\partial \mathbf{x}}{\partial \xi} \times \frac{\partial \mathbf{x}}{\partial \eta}\right). \tag{2.11}$$

To compute the integral of a function f over a curved triangular element E, we use ξ and η as the variables of integration following the relation

$$\int_E f(\mathbf{x})\,\mathrm{d}S(\mathbf{x}) = \int_0^1 \int_0^{1-\xi} f(\mathbf{x}(\xi,\eta)) h_{\mathrm{S}}(\xi,\eta)\,\mathrm{d}\eta\,\mathrm{d}\xi. \tag{2.12}$$

Standard quadrature techniques can then be implemented as will be described in §2.3.

The surface force density $\mathbf{f}$ appears in many of our boundary integrals. Therefore, we must be able to define its value at all quadrature points. To do this, we approximate $\mathbf{f}$ with a quadratic expansion over each element using the same interpolation functions as before. In general, the constants α, β and γ defined in (2.7) will not be the same for all elements so we make the distinctions by writing the kth interpolation function over triangle n as ϕ^{nk}. Denoting the i-component of the force density at node k of triangle n by f_i^{nk}, the force density at a point on the surface element E_n is approximated by

$$f_i^n(\xi,\eta) \equiv f_i(\mathbf{x}(\xi,\eta)) \approx \sum_{k=1}^{6} f_i^{nk}\phi^{nk}(\xi,\eta), \tag{2.13}$$

with no implied summation over index n. To simplify notation later on, it will be advantageous to use the variable $\mathbf{x}$ rather than the ξ–η parameterisation. Hence we write $\phi^{nk}(\mathbf{x}) \equiv \phi^{nk}(\mathbf{x}(\xi,\eta)) = \phi^{nk}(\xi,\eta)$, giving

$$f_i(\mathbf{x}) \approx \sum_{k=1}^{6} f_i^{nk}\phi^{nk}(\mathbf{x}), \quad \mathbf{x} \in E_n. \tag{2.14}$$

To keep track of which nodes belong to which elements, we use a connectivity array C of size $N_{\mathrm{E}} \times 6$. The global index, m, of the point corresponding to node k of the six-node, curved element n is stored as $C_{nk} = m$. Thus, element n is made up of the global nodes C_{nk}, $k = 1, 2, \ldots, 6$.

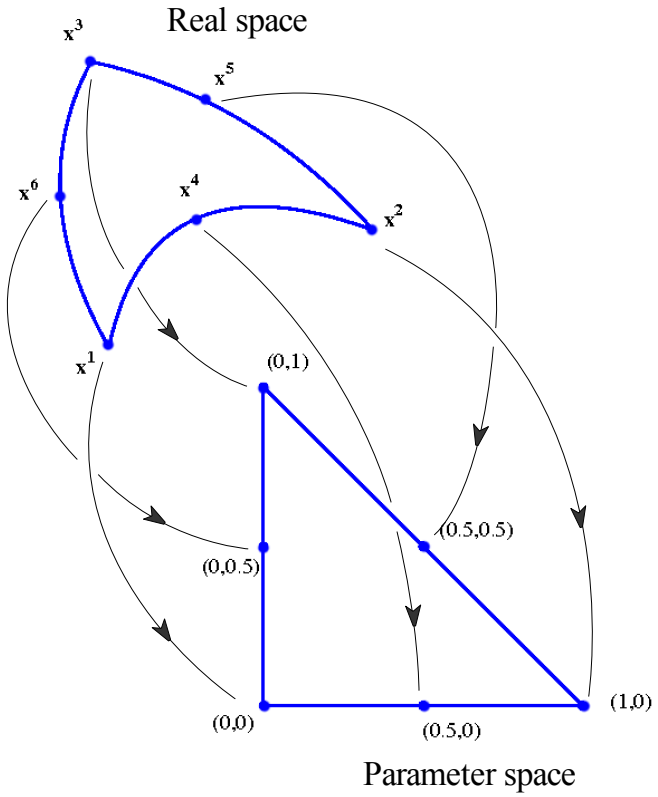

Figure 2.1: Mapping between real space and ξ–η parameter space for describing quadratic triangular elements, where the edge nodes $\mathbf{x}^4$, $\mathbf{x}^5$ and $\mathbf{x}^6$ are equidistant from the corner nodes on their respective edges, giving $\alpha = \beta = \gamma = 0.5$.

2.3 Quadrature Methods

2.3.1 Gaussian quadrature on standard intervals and triangles

To numerically compute integrals over the range $[-1, 1]$ in one dimension, we evaluate the function at N_Q points denoted x^q and use appropriate weightings w^q for each evaluation to approximate the integral by

$$\int_{-1}^{1} f(x)\,\mathrm{d}x \approx \sum_{q=1}^{N_\mathrm{Q}} f(x^q)w^q. \tag{2.15}$$

Similarly, we define the standard triangle $\Delta = \{(\xi, \eta)|\xi \geq 0, \eta \geq 0, \xi + \eta \leq 1\}$ and approximate the integral of a function over Δ by

$$\int_{\Delta} f(\xi, \eta)\,\mathrm{d}S \approx \frac{1}{2}\sum_{q=1}^{N_\mathrm{Q}} f(\xi^q, \eta^q)w^q, \tag{2.16}$$

where ξ^q and η^q are the coordinates of the qth quadrature point and w^q is the weighting of this point. In both one and two dimensions, the sum of all w^q is fixed to give the correct length of the interval or area of the triangle when the integrand is identically unity. The abscissas and weights can be chosen to give exact results for functions f that are polynomials up to a given degree. In the one dimensional case, the Gauss-Legendre abscissas and weights result in quadrature that is accurate to order $p = (2N_\mathrm{Q} - 1)$ in this sense. Tables of x^q and w^q can be found in Abramowitz & Stegun [1]. Tables of suitable ξ^q, η^q and w^q for triangular quadrature schemes of various orders have been given by e.g. Dunavant [43].

A complication arises when the integrand is singular or nearly singular on the domain of integration. The Gauss-Legendre method, which is based on polynomials, becomes inaccurate and a different approach is needed. Special quadratures have been developed for integrands of specific forms of singular behaviour (see e.g. [101]). In particular, we will be computing the integrals of the Stokeslet Green's function (1.8), which has an $O(1/r)$ singularity, where r is the distance from the evaluation point to the Stokeslet location.

Suppose that the singular point of the integrand lies on a vertex of a triangular element of aspect ratio close to unity. Without loss of generality we can choose this singular vertex to correspond to the $\xi = \eta = 0$ vertex in parameter space. Then the singularity is $O(1/r)$, where $r = \sqrt{\xi^2 + \eta^2}$. The quadrature is performed using a coordinate transformation to regularise the integral. With our assumptions, the integrand can be expressed in the form

$$f(\xi, \eta) = \frac{g(\xi, \eta)}{r} + h(\xi, \eta), \tag{2.17}$$

where g and h are regular functions on the triangle Δ. Using polar coordinates we write the surface integral as

$$\begin{aligned} \int_0^1 \int_0^{1-\xi} f(\xi, \eta)\, \mathrm{d}\eta\, \mathrm{d}\xi &= \int_0^{\frac{\pi}{2}} \int_0^{R(\theta)} f(\xi, \eta) r\, \mathrm{d}r\, \mathrm{d}\theta, \\ &= \int_0^{\frac{\pi}{2}} \int_0^{R(\theta)} \left[g(\xi, \eta) + r h(\xi, \eta) \right] \mathrm{d}r\, \mathrm{d}\theta, \end{aligned} \tag{2.18}$$

where the variables are related by

$$\xi = r \cos\theta, \qquad \eta = r \sin\theta, \tag{2.19}$$

and $R(\theta) = 1/(\cos\theta + \sin\theta)$. This integral can be computed accurately using two successive one dimensional Gauss-Legendre quadratures, since the integrand is no longer singular.

If $\mathbf{x}^0$ is on an edge or in the interior of the triangle, we can split the triangle so that each sub-triangle is either regular or satisfies the assumptions above. An example of each case is shown in Fig. 2.2. If the singular point is near but not on the element, it is more difficult to devise a quadrature rule to efficiently account for this type of behaviour. Nevertheless, adequate accuracy can still be obtained with suitable mesh refinement and in practice we will not need to calculate the flow velocity at such close proximity to the boundary except exactly at the mesh nodes.

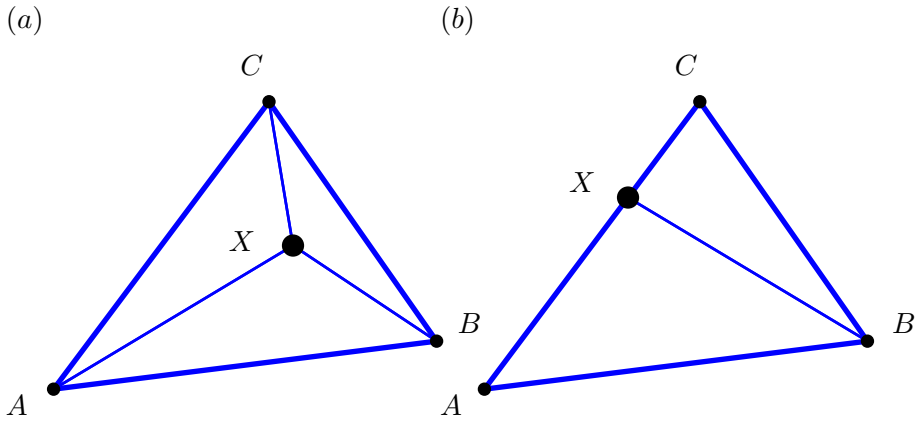

Figure 2.2: Splitting a triangular element for accurate quadrature of singular integrands. If an integrand has singular behaviour at a point X that is (a) in the interior or (b) on an edge of triangle ABC, then the triangle is divided into smaller elements as shown with X as a vertex of each sub-triangle.

2.3.2 General intervals and triangles

Equations (2.15) and (2.16) can of course be used for more general intervals and triangles of integration as follows:

$$\int_a^b f(x)\,\mathrm{d}x \approx \frac{(b-a)}{2}\sum_{q=1}^{N_\mathrm{Q}} f(x^q)w_\mathrm{L}^q, \tag{2.20}$$

$$\int_E f(\mathbf{x})\,\mathrm{d}S \approx \frac{1}{2}\sum_{q=1}^{N_\mathrm{Q}} f(\mathbf{x}^q)h_\mathrm{S}(\xi^q,\eta^q)w_\mathrm{T}^q, \tag{2.21}$$

where $x^q = (a+b)/2 + y^q\cdot(b-a)/2$, y^q and w_L^q are the standard abscissas and weights for the chosen linear quadrature scheme and w_T^q are the weights for quadrature on a triangle. Each contribution to the quadrature is scaled by h_S, defined in (2.10), to reflect the transformation from the standard element $(\xi^q,\eta^q)\to\mathbf{x}^q$ given by (2.8). For weakly singular surface integrals (as discussed above) we use

$$\int_E f(\mathbf{x})\,\mathrm{d}S \approx \frac{1}{4}\sum_{q=1}^{N_\mathrm{Q}}\sum_{p=1}^{N_\mathrm{Q}} f(\mathbf{x}^{pq})h_\mathrm{S}(\xi^{pq},\eta^{pq})w_L^p w_L^q, \tag{2.22}$$

where $\xi^{pq} := \xi(r^p,\theta^q)$ and $\eta^{pq} := \eta(r^q,\theta^p)$ are given by (2.19) and $\mathbf{x}^{pq} := \mathbf{x}(\xi^{pq},\eta^{pq})$ is given by (2.8) as before.

Regardless of which scheme we use, the quadrature may be represented as

$$\int_E f(\mathbf{x})\,\mathrm{d}S \approx Q_E[f] \equiv \sum_{q=1}^{N_\mathrm{Q}} f(\mathbf{x}^q) w^q, \tag{2.23}$$

where the quadrature points $\mathbf{x}^q$ and weighting factors w^q are chosen according to whether singular or non-singular quadrature is required on E, as discussed in §2.3.1. Hence in a given mesh, different elements may have different quadrature rules assigned. We will use N_E^n, w^{nq}, ξ^{nq}, etc. to denote the quantities for element n in the following section.

2.3.3 Solving the boundary integral equation

The two main approaches to solving the boundary integral equation are the collocation and Galerkin methods. Collocation methods have proved dominant in applications to micro-organism swimming and will be use in the present work. The strategy is to choose a finite set of N_N collocation points on the boundary mesh on which to enforce the numerical approximation of the boundary integral equation (2.5). Using the interpolation and quadrature methods outlined above, we obtain

$$u_j^m = u_j(\mathbf{x}^m) = -\sum_{n=1}^{N_\mathrm{E}} \sum_{q=1}^{N_\mathrm{Q}^n} \left(\sum_{k=1}^{6} f_i^{nk} \phi^{nk}(\mathbf{x}^{nq}) \right) S_{ij}(\mathbf{x}^{nq}, \mathbf{x}^m) w^{nq}, \tag{2.24}$$

for the velocity at the mth mesh node. By relabelling the interpolation functions ϕ^{nk} and tractions f_i^{nk} so that k refers to the node index in the list of all mesh nodes and defining $\phi^{nk} \equiv 0$ if node k does not belong to element n, we can rewrite this as

$$u_j^m = -\sum_{k=1}^{N_\mathrm{N}} f_i^k \left(\sum_{n=1}^{N_\mathrm{E}} \sum_{q=1}^{N_\mathrm{Q}^n} \phi^{nk}(\mathbf{x}^{nq}) S_{ij}(\mathbf{x}^{nq}, \mathbf{x}^m) w^{nq} \right). \tag{2.25}$$

For a given mesh, the contents of the large parentheses are computable, resulting in a matrix-coefficient linear equation relating the vector of velocity components to the vector of traction components. In the Dirichlet problem, where we know the fluid velocity everywhere on the boundary, we invert the matrix to obtain the traction

distribution. The Neumann problem is even simpler, as the solution is given explicitly by (2.25).

Problems for which analytical solutions are known, such as the viscous drag force on a translating sphere, can be used to test the accuracy and convergence of our numerical methods. These test cases are presented in appendix B.

For a general object in Stokes flow, we will know neither the velocity nor the traction distribution but aim to obtain these by satisfying additional conditions. Naturally, this is model-dependent and will be discussed for our application to swimming bacteria in the following chapter.

Chapter 3

Swimming and optimisation

3.1 Model geometry

The model for the bacterium, illustrated in Fig. 3.1, consists of two rigid bodies: an ellipsoid representing the cell body and a thin cylinder with hemispherical ends, curved into a helical shape with an amplitude envelope as suggested by Higdon [64] so that the tip of the flagellum assumed to be attached to the cell body lies on the axis of the helix. The growth rate of this amplitude envelope is modulated by the parameter k_{E} and the region over which the amplitude grows to its full value is referred to as the starting region, which has length roughly $2/k_{\mathrm{E}}$.

We maintain a small separation (of the order of a flagellum radius) between the body and the flagellum to avoid singularities in the solution due to a mismatch in velocities between two approaching surfaces. In reality, the rotation of the shaft relative to the surrounding stator proteins in the motor does entail large velocity gradients but these effects are on the molecular scale of the separation between these structures. We assume that the error in neglecting the precise fluid flow in the vicinity of the motor can be treated as an internal process of the motor, which we do not model.

This model is similar to that used by Phan-Thien et al. [99] but we discretise the surface with curved elements as described in §2.2 rather than flat triangles. We now detail the procedure for constructing the model bacterium mesh.

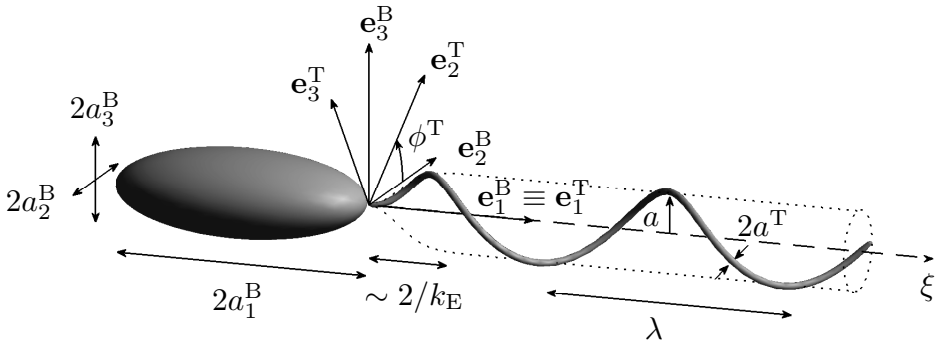

Figure 3.1: Illustration of model bacterium in the body reference frame. As depicted, a_1^{B}, a_2^{B} and a_3^{B} are the lengths of the semi-principal axes of the cell body in the $\mathbf{e}_1^{\mathrm{B}}$, $\mathbf{e}_2^{\mathrm{B}}$ and $\mathbf{e}_3^{\mathrm{B}}$ body-fixed directions respectively. The flagellum axis coincides with $\mathbf{e}_1^{\mathrm{B}}$. The flagellum has radius a^{T} and begins a short distance $d^{\mathrm{gap}} = 0.05\,\bar{a}$ (not labelled) from the pole of the cell body, growing into a helix over the starting region of length $\sim 2/k_{\mathrm{E}}$. The helix has amplitude a and wavelength λ (wavenumber $k = 2\pi/\lambda$). The length of the flagellum is L, measured along the curved centreline, and the number of turns (including the starting region) is N_λ. The lengthscale used for non-dimensionalisation is $\bar{a} = (a_1^{\mathrm{B}}\, a_2^{\mathrm{B}}\, a_3^{\mathrm{B}})^{1/3}$, which is the radius required for a sphere of volume equal to that of the bacterium's body. The tail director basis vectors, $\mathbf{e}_j^{\mathrm{T}}$, $j = 1, 2, 3$, are related to the body basis vectors by the rotation ϕ^{T} about the common axis, which we also take to be the motor axis $\mathbf{e}^{\mathrm{M}} \equiv \mathbf{e}_1^{\mathrm{B}} \equiv \mathbf{e}_1^{\mathrm{T}}$. The position of the bacterium relative to a fixed reference frame is described by the vector $\mathbf{x}^{\mathrm{B}}$, which tracks the pole of the cell body nearer the flagellum (not labelled in this figure).

To generate a mesh for a sphere, the triangular faces of a regular octahedron or icosahedron are repeatedly subdivided and the new nodes from each subdivision are projected onto the sphere surface, as implemented in the routines `trgl_octa` and `trgl_icos` from Pozrikidis' software library, *BEMLIB*. The mesh is then stretched into the desired ellipsoid. This approach was used in previous BEM works on micro-swimmers, where further details can be found [99, 116]. Isoparametric, quadratic triangular elements are used rather than linear elements for greater accuracy in approximating the curved surfaces and surface distributions. Typically there will be $N_{\mathrm{BE}} = 80$ ('B' in subscripts and superscripts denotes variables related to the body) such elements over the cell body, requiring $N_{\mathrm{BN}} = 162$ nodes. An illustration of the model and explanation of geometrical parameters used throughout are given in Fig. 3.1 and appendix A.

The flagellum is likewise discretised with quadratic triangular surface elements. We first set the directors $\mathbf{e}_j^{\mathrm{T}}$, $j = 1, 2, 3$, defining the reference frame of the tail (we will use 'T' in subscripts and superscripts to denote variables related to the tail). The centreline is written as $\mathbf{X}(\xi) = X_1(\xi)\mathbf{e}_1^{\mathrm{T}} + X_2(\xi)\mathbf{e}_2^{\mathrm{T}} + X_3(\xi)\mathbf{e}_3^{\mathrm{T}}$, where the shape functions in the tail-fixed reference frame are parameterised by

$$\left.\begin{aligned} X_1(\xi) &= \xi, \\ X_2(\xi) &= a\big(1 - \mathrm{e}^{-k_{\mathrm{E}}^2\xi^2}\big)\cos(k\xi), \\ X_3(\xi) &= a\big(1 - \mathrm{e}^{-k_{\mathrm{E}}^2\xi^2}\big)\sin(k\xi), \end{aligned}\right\} \tag{3.1}$$

$\xi \in [0, \xi_{\max}]$. We begin by forming a cap at the $\xi = 0$ end of the flagellum as follows.

1. Using the parametric equations for the flagellum centreline (3.1), divide the cap into four segments by finding ξ^k such that the arc lengths measured from the tip are $s^k := \int_0^{\xi^k} \|\,\mathrm{d}\mathbf{X}/\,\mathrm{d}\xi\|\,\mathrm{d}\xi = (1 - \cos(k\pi/8)) \cdot L^{\mathrm{cap}}$, $k = 1, 2, 3, 4$, where L^{cap} is the prescribed length of the cap.

2. Assuming a spheroidal variation of filament radius with arc length, the cross sectional radii at ξ^k are given by $a_k^{\mathrm{T}} = a^{\mathrm{T}} \cdot \sin(k\pi/8)$.

3. Place one mesh node at the tip, $\mathbf{X}(0)$.

4. Distribute N_{s} nodes around the circumference of the cross-section at each ξ_k for $k = 2, 3, 4$, using the formula $\mathbf{x}_j^k = \mathbf{X}(\xi^k) + a_k^{\mathrm{T}}(\mathbf{n}^k \cos\phi_j^k + \mathbf{b}^k \sin\phi_j^k)$, $j = 1, ..., N_{\mathrm{s}}$, where $\mathbf{n}^k$ and $\mathbf{b}^k$ are the local Frenet-Serret normal and binormal vectors and the azimuths are given by $\phi_j^k = (2\pi/N_{\mathrm{s}})(j + k/2)$. The $k/2$ term in the last expression serves to stagger the positions of the nodes between successive cross-sections.

5. Similarly, place $N_{\mathrm{s}}/2$ nodes around the circumference of the cross-section $k = 1$.

6. Assign each node to appropriate surface elements as illustrated in Fig. 3.2(a).

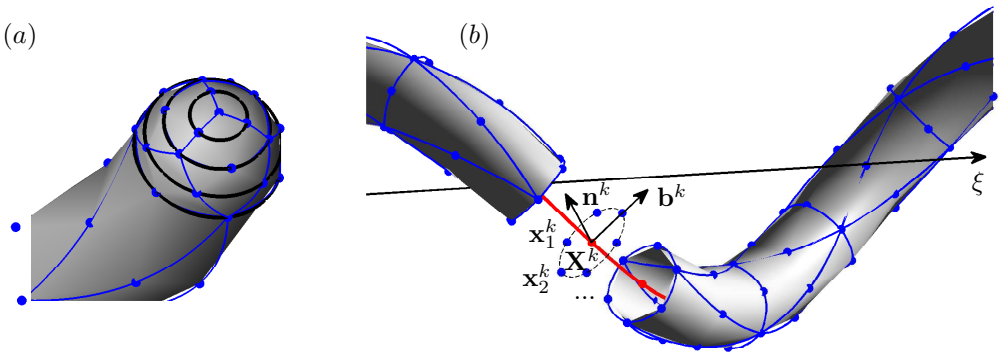

Figure 3.2: Construction and surface discretisation of bacterial flagellum. (a) The tip of the filament, with circular rings indicating the cross-sections at arc lengths s^k, $k = 1, 2, 3, 4$ (see main text for details). (b) The normal and binormal vectors are $\mathbf{n}^k$ and $\mathbf{b}^k$ respectively at the point $\mathbf{X}^k$ on the flagellar centreline, used to determine the cross-section in which to place surface nodes $\mathbf{x}_j^k$. Curved lines (blue) in (a) and (b) joining the surface nodes show the edges of the actual triangular elements used in computation while the shaded surfaces in this figure, which are composed of flat triangles connecting mesh nodes, is for visualisation purposes only.

The cap at the $\xi = \xi_{\max}$ end of the flagellum and the length of the filament between the two caps are constructed in a similar way with N_c cross-sections of constant filament radius, a^T, distributed uniformly in arc length between the caps. N_s is twice the number of quadratic triangular elements with edges lying around each cross-section. The value $N_s = 6$ is used in all referenced simulations as this was found to be optimal in balancing accuracy with computational speed (see appendix B). The total number of elements (N_{TE}) and nodes (N_{TN}) on the flagellum varies greatly, as the required mesh depends on the thickness, length and curvature of the filament. The mesh discretisation parameters are chosen to yield approximately equilateral trianglular elements.

The total numbers of elements and nodes are denoted $N_E := N_{BE} + N_{TE}$ and $N_N := N_{BN} + N_{TN}$ respectively. The number of degrees of freedom in the model, and thus the computational load, is dictated by N_N. Simulations span an approximate range $250 < N_N < 1000$.

For all simulations reported here, the body–flagellum junction will be at a pole

of the body (as depicted in Fig. 3.1). This is the most common configuration for monotrichous bacteria, although the flagellum can emerge from the side of the cell in *R. sphaeroides* [4].

The reference point of the bacterium is taken to be the pole of the cell nearer the flagellum, and will be referred to as the junction position, $\mathbf{x}^{\mathrm{B}}$. Since the relative motion of the flagellum with respect to the cell body is confined to rotations about its axis, the entire instantaneous configuration may be described in the stationary reference frame by the junction position, $\mathbf{x}^{\mathrm{B}}$, two body orientation vectors, $\mathbf{e}_1^{\mathrm{B}}$ and $\mathbf{e}_2^{\mathrm{B}}$, and the phase of the tail relative to the body, ϕ^{T}. We choose $\mathbf{e}_1^{\mathrm{B}}$ to be the unit vector pointing from the body towards the flagellum, along the principal axis of the body about which the flagellum turns. These configuration specifying variables, $\mathbf{x}^{\mathrm{B}}$, $\mathbf{e}_1^{\mathrm{B}}$, $\mathbf{e}_2^{\mathrm{B}}$ and ϕ^{T} are shown in Fig. 3.1. Note that the two body orientation vectors contain only three independent degrees of freedom between them due to orthonormality constraints.

3.2 Solving instantaneous dynamics

Our model supposes that the motion of the bacterium can be described by a translational velocity, $\mathbf{U}$, and rotational velocity, $\mathbf{\Omega}$, about the junction point $\mathbf{x}^{\mathrm{B}}$. The flagellum additionally rotates about the motor axis, $\mathbf{e}^{\mathrm{M}} \equiv \mathbf{e}_1^{\mathrm{T}} \equiv \mathbf{e}_1^{\mathrm{B}}$, relative to the body at a rate

$$\omega^{\mathrm{M}} := \frac{\mathrm{d}\phi^{\mathrm{T}}}{\mathrm{d}t}. \tag{3.2}$$

The two structures themselves remain rigid during motion.

Writing the relative position of a point as $\tilde{\mathbf{x}} = \mathbf{x} - \mathbf{x}^{\mathrm{B}}$, the surface velocity distribution can be expressed as

$$\mathbf{u}(\mathbf{x}) = \begin{cases} \mathbf{U} + \mathbf{\Omega} \times \tilde{\mathbf{x}}, & \mathbf{x} \in B, \\ \mathbf{U} + (\mathbf{\Omega} + \omega^{\mathrm{M}}\mathbf{e}^{\mathrm{M}}) \times \tilde{\mathbf{x}}, & \mathbf{x} \in T, \end{cases} \tag{3.3}$$

where B denotes the surface of the cell body and T denotes the surface of

the flagellum. Some additional equations are needed to determine the unknown quantities, $\mathbf{U}$, $\mathbf{\Omega}$ and ω^{M}.

Assuming that the bacterium is swimming in the absence of external forces such as gravity (valid for neutrally buoyant cells), the total force acting on the combined surfaces of the body and flagellum is zero. A $3 \times 3N_{\mathrm{N}}$ matrix of linear coefficients $\mathbb{A}$ can be generated to express this condition as

$$\int_{B \cup T} \mathbf{f} \, \mathrm{d}S \approx \mathbb{A}\bar{\mathbf{f}} = \mathbf{0}, \tag{3.4}$$

where $\bar{\mathbf{f}}$ is a column vector of length $3N_{\mathrm{N}}$ containing the force distribution evaluated at all surface nodes.

Similarly, no net torque acts on the bacterium, i.e.

$$\int_{B \cup T} \tilde{\mathbf{x}} \times \mathbf{f} \, \mathrm{d}S \approx \mathbb{M}\bar{\mathbf{f}} = \mathbf{0}, \tag{3.5}$$

where $\mathbb{M}$ is a $3 \times 3N$ matrix of contributions from each traction component to the total torque on the swimmer.

However, there will be a net torque acting on the flagellum, which will be balanced by an opposite torque acting on the body. Two of the torque components cannot be predetermined but the torque in the direction of the motor axis $\mathbf{e}^{\mathrm{M}}$ can be specified (assuming this is mediated by the motor), leading to an additional torque balance equation

$$\mathbf{e}^{\mathrm{M}} \cdot \int_{T} \tilde{\mathbf{x}} \times \mathbf{f} \, \mathrm{d}S \approx \mathbb{m}\bar{\mathbf{f}} = -\tau^{\mathrm{M}}, \tag{3.6}$$

where $\tau^{\mathrm{M}}\mathbf{e}^{\mathrm{M}}$ is the torque exerted on the flagellum by the motor and $\mathbb{m}$ is a $1 \times 3N$ matrix expressing the contributions from each traction component to the viscous torque exerted on the flagellum in the direction of the motor axis. In most simulations we will prescribe a constant motor torque but it is also possible to fix the rotation rate, ω^{M}, and determine the torque from the prescribed motion.

The discrete boundary-integral equation (2.25) can be expressed symbolically as

$$\begin{bmatrix} \\ \mathbb{U} \\ \\ \end{bmatrix} \begin{bmatrix} \mathbf{U} \\ \boldsymbol{\Omega} \\ \omega^{\mathrm{M}} \end{bmatrix} = \begin{bmatrix} \\ \mathbb{G} \\ \\ \end{bmatrix} \begin{bmatrix} \\ \bar{\mathbf{f}} \\ \\ \end{bmatrix}, \tag{3.7}$$

where $\mathbb{U}$ is a $3N_{\mathrm{N}} \times 7$ matrix defining the velocity distribution in terms of bulk velocities and $\mathbb{G}$ is a $3N_{\mathrm{N}} \times 3N_{\mathrm{N}}$ matrix that assigns suitable quadrature weights to the Green's function for each pair of nodes. In conjunction with discretised versions of the seven scalar force and torque balance equations above we have the following dense, $(3N_{\mathrm{N}}+7)$-dimensional linear algebraic problem, which is solved using standard LU decomposition subroutines from *Numerical Recipes in Fortran 77* [106]:

$$\left[\begin{array}{c|c} -\mathbb{G} & \mathbb{U} \\ \hline \mathbb{A} & \\ \mathbb{M} & \mathbf{0} \\ \mathbb{m} & \end{array}\right] \left[\begin{array}{c} \bar{\mathbf{f}} \\ \hline \mathbf{U} \\ \boldsymbol{\Omega} \\ \omega^{\mathrm{M}} \end{array}\right] = - \left[\begin{array}{c} \mathbf{0} \\ \hline \mathbf{0} \\ \mathbf{0} \\ \tau^{\mathrm{M}} \end{array}\right]. \tag{3.8}$$

To verify our numerical code, we compared our computed velocities for swimmers of different geometries with the results of previous SBT and BEM studies of equivalent swimmers. Agreement with Higdon's SBT results [64] was to within 4% and similar agreement was found with the BEM results of Phan-Thien et al. [99] except in a few cases where discrepancies were up to twice as large. Some of these tests are included in appendix B.

3.3 Tracking bacterial trajectories

The boundary element scheme provides a method for obtaining instantaneous velocities for a given configuration of the model swimmer. Since the velocities are precisely the rates of change of the configuration, the solution evolves as a system of

ordinary differential equations (ODEs). Standard algorithms for numerical solution of initial value problems for ODEs can be used to track the trajectories. A general state in an ODE system can be written as a vector, $\mathbf{x}$. For the model bacterium, this vector contains three position coordinates, three Euler angles and the motor phase angle. The velocity is correspondingly given by $\mathbf{v}(\mathbf{x}) = \dot{\mathbf{x}}$. The values at a particular time step n are indicated by a subscript.

3.4 Stability of integration schemes

Ordinary differential equations commonly appear in mathematical models of biological, chemical and physical systems, to name a few broad areas. Numerical approaches are usually required to solve the equations so this is a very important topic of numerical analysis. Basic concepts and algorithms can be found in many texts, such as *Numerical recipes in Fortran 77: the art of scientific computing* [106] and *Introduction to numerical analysis* [122]. We briefly review the issue of stability in numerical integration of differential equations as this will be relevant in some of the later sections of this thesis.

Consider the initial value problem

$$\dot{x} = \lambda x, \quad x(0) = x_0, \tag{3.9}$$

where λ is a constant complex number. This has the exact solution

$$x(t) = x_0 \mathrm{e}^{\lambda t}. \tag{3.10}$$

Suppose that we have an algorithm for advancing by one time step $\delta t > 0$ at a time to construct an approximate solution ξ_j, $j = 0, 1, 2, \ldots$ from the starting point $\xi_0 = x_0$. Commonly, when applied to the test case (3.9), the algorithm leads to a recursive rule

$$\xi_{j+1} = g(\lambda \delta t)\xi_j, \quad \text{or} \quad \xi_j = [g(\lambda \delta t)]^j x_0, \quad j = 0, 1, 2, \ldots, \tag{3.11}$$

where the function g is specific to the method employed. Since the exact solution converges to zero if λ has a negative real part, it would be desirable for the numerical method to exhibit this behaviour as well. For this to be the case, we require $|g(\lambda\delta t)| < 1$. If this condition is satisfied for any δt whenever $\Re(\lambda) < 0$, then the method is termed *absolutely stable* or *A-stable*.

In the simple case of Euler's method, we have

$$\xi_{n+1} = \xi_n + \dot{x}\delta t, \quad \text{giving} \quad g = (1 + \lambda\delta t). \tag{3.12}$$

If λ is real and negative, then the solution tends to zero only for $0 < \delta t < 2/|\lambda|$, so the Euler method is not A-stable. In fact, all explicit methods, which find the next state of the system using only information about the current state and not future states, are unstable in this sense.

A method that is not A-stable is susceptible to growing errors that soon dominate the solution unless the step size is sufficiently small. However, such methods need not always be avoided since, aside from the issue of stability, demands on the accuracy of the numerical solution also require step sizes to be controlled. It is only when a system of equations is stiff that stability becomes important [106].

Stiff dynamics are characterised by widely separated timescales such that one variable may vary rapidly while another is nearly constant. The analysis above can be repeated for ODE systems, where λ is replaced by a square matrix $\mathbf{A}$. The exact solution approaches the zero vector as $t \to \infty$ if all eigenvalues of $\mathbf{A}$ have negative real parts. The numerical solution will likewise converge to the zero vector if the condition obtained in the scalar case is met for all eigenvalues of $\mathbf{A}$. This means that the step size is limited by the shortest timescale of the problem if the integration method is not A-stable.

A stiff system will be encountered in chapter 6 where we will incorporate the dynamics of a flexible bacterial hook. Because the timescale of elastic relaxation is much shorter than the period of the bacterial motor, we will require stable methods

to solve the equations on the longer timescale. We now introduce methods that will be used in our simulations for tracking the dynamics of the swimming bacterium.

3.4.1 Heun's predictor–corrector

Heun's predictor–corrector algorithm is a second order method that was used by Smith et al. [116] for hydrodynamic simulations of swimming spermatozoa. The predictor step involves calculating the instantaneous velocities $\mathbf{v}_n = \mathbf{v}(\mathbf{x}_n)$ at time step n. The tentative configuration at the next time step $\bar{\mathbf{x}}_{n+1} = \mathbf{x}_n + \delta t \cdot \mathbf{v}_n$ is used to calculate the velocity $\bar{\mathbf{v}}_{n+1} = \mathbf{v}(\bar{\mathbf{x}}_{n+1})$, which is an estimate of the true velocity at the next time step. The corrected velocity, or difference quotient, is then defined by $\mathbf{v}_n^* := \frac{1}{2}(\mathbf{v}_n + \bar{\mathbf{v}}_{n+1})$. This is used to make the corrected step, resulting in the new configuration, $\mathbf{x}_{n+1} = \mathbf{x}_n + \delta t \cdot \mathbf{v}_n^*$.

This method is explicit and therefore not A-stable. However, it is efficient and useful when applied to non-stiff differential equations such as the system we will construct with the flagellum constrained to rotate about an axis fixed with respect to the cell body.

3.4.2 Backward Euler

The backward Euler rule is a first order implicit method in which the difference quotient is the future velocity, i.e.

$$\mathbf{x}_{n+1} = \mathbf{x}_n + \delta t \cdot \mathbf{v}_n^*, \quad \mathbf{v}_n^* = \mathbf{v}_{n+1}. \tag{3.13}$$

In order to solve the implicit equation (3.13), we begin with an initial estimate for the difference quotient, $\hat{\mathbf{v}}_n$. Using $\hat{\mathbf{v}}_n = \mathbf{v}_n$ leads to an Euler step identical to the predictor in §3.4.1. The vector error associated with using this estimate is defined by

$$\boldsymbol{\varepsilon}(\hat{\mathbf{v}}_n) = \mathbf{v}(\mathbf{x}_n + \delta t \cdot \hat{\mathbf{v}}_n) - \hat{\mathbf{v}}_n, \tag{3.14}$$

which vanishes when $\hat{\mathbf{v}}_n = \mathbf{v}_n^*$. Using the multidimensional Newton–Raphson

method [106], we iteratively approach a root of the equation, allowing us to proceed to the next time step.

This method is L-stable, which means that it is A-stable and has the additional property that $|g(\lambda\delta t)| \to 0$ as $|\lambda\delta t| \to \infty$ whenever $\Re(\lambda) < 0$. Loosely, this means that the numerical solution of the test equation (3.9) will tend to zero rapidly even if the step size is large compared with the timescale of the exact decay, while a general A-stable method may take many steps to converge.

3.4.3 Trapezoidal rule

The trapezoidal rule is another implicit method. It is a second order A-stable method but is not L-stable. The difference quotient is given by

$$\mathbf{v}_n^* = \tfrac{1}{2}(\mathbf{v}_n + \mathbf{v}_{n+1}). \tag{3.15}$$

Note that this is almost the same as the predictor–corrector rule, which simply replaces the unknown future value $\mathbf{v}_{n+1}$ with the explicit estimate, $\hat{\mathbf{v}}_{n+1}$. However, this is a crucial difference that severely limits the maximum feasible size of time steps in stiff systems using explicit methods.

The vector error associated with assuming the trial difference quotient $\hat{\mathbf{v}}_n$ is defined by

$$\boldsymbol{\varepsilon}(\hat{\mathbf{v}}_n; \mathbf{v}_n) = \frac{\mathbf{v}_n + \mathbf{v}(\mathbf{x}_n + \delta t \cdot \hat{\mathbf{v}}_n)}{2} - \hat{\mathbf{v}}_n. \tag{3.16}$$

Again, the multidimensional Newton–Raphson method can be used to locate a root given a suitable initial estimate.

3.4.4 Implementing time stepping schemes

The integration schemes described above are the basis for following the motion of our model bacterium. When we consider the rigid hook model, i.e., the flagellum is restricted to rotations about a fixed axis relative to the cell body, the predictor–

corrector method is used. Introducing flexibility of the connecting hook leads to a stiff system and requires implicit methods. This will be discussed in chapter 6.

Our BEM code was developed to incrementally update the swimmer configuration. That is, we perform finite rotations on the node positions and orientation vectors at each time step without explicitly computing the corresponding Euler angles or the tail phase. The update $\mathbf{x} \to \mathbf{x} + \delta t \cdot \mathbf{v}^*$, where $\mathbf{v}^*$ corresponds to $(\mathbf{U}^*, \boldsymbol{\Omega}^*, \omega^{\mathrm{M}*})$, is executed according to these steps:

1. Translate all mesh nodes and position vector $\mathbf{x}^{\mathrm{B}}$ by $\mathbf{U}^* \delta t$.

2. Rotate all mesh nodes and orientation vector $\mathbf{e}_2^{\mathrm{B}}$ about the point $\mathbf{x}^{\mathrm{B}}$ by the axial rotation vector $\mathbf{R}_{\parallel}^{\mathrm{B}} := (\boldsymbol{\Omega}^* \cdot \mathbf{e}^{\mathrm{M}})\, \delta t\, \mathbf{e}^{\mathrm{M}}$.

3. Rotate all mesh nodes and orientation vectors $\mathbf{e}_1^{\mathrm{B}}$, $\mathbf{e}_2^{\mathrm{B}}$ about the point $\mathbf{x}^{\mathrm{B}}$ by the transverse rotation vector $\mathbf{R}_{\perp}^{\mathrm{B}} := \boldsymbol{\Omega}^* \delta t - \mathbf{R}_{\parallel}^{\mathrm{B}}$.

4. Rotate flagellum mesh nodes about the point $\mathbf{x}^{\mathrm{B}}$ by the motor rotation vector $\omega^{\mathrm{M}*} \delta t \mathbf{e}^{\mathrm{M}}$.

The main reason for using this procedure is that it is natural to compute the rotational velocity vector $\boldsymbol{\Omega}^*$ in the stationary reference frame using the boundary element method. This could be converted into rates of change of the Euler angles for the standard approach of solving a system of ODEs, though the Euler angle representation suffers from a singularity.

3.5 Progressive and phase-averaged velocities

The bacterium experiences fluctuations in velocity as the flagellum turns through each revolution. Rather than considering an instantaneous velocity, which depends on the phase of the flagellum and has a large lateral component, it will be more useful to find the net motion over a cycle. Consider the case with a high degree of symmetry where

the body is a spheroid, the flagellum is aligned with the body axis and the swimmer is in unbounded fluid. In the reference frame of the flagellum, the boundary conditions are constant since there is no distinction as the cell body rotates. The swimming velocities are therefore constant in the reference frame rotating with the tail basis and the average velocity in the stationary reference frame over a complete period of motion can be determined from data at one instant. The tail basis rotates with constant angular velocity $\mathbf{\Omega}^{\mathrm{T}}$ equal to the sum of the body rotation and motor revolution vectors, i.e., $\mathbf{\Omega}^{\mathrm{T}} = \mathbf{\Omega}^{\mathrm{B}} + \omega^{M}\mathbf{e}^{\mathrm{M}}$. We therefore define the progressive velocity, $\bar{\mathbf{U}}$, as the projection of the instantaneous translational velocity, $\mathbf{U}$, in this direction of mean progress [99], i.e.,

$$\bar{\mathbf{U}} := \bar{U}\,\frac{\mathbf{\Omega}^{\mathrm{T}}}{\|\mathbf{\Omega}^{\mathrm{T}}\|}, \quad \bar{U} := \frac{\mathbf{U}\cdot\mathbf{\Omega}^{\mathrm{T}}}{\|\mathbf{\Omega}^{\mathrm{T}}\|}. \tag{3.17}$$

Note that for a given cell body position and orientation, the instantaneous body rotational velocity vector, $\mathbf{\Omega}$, and hence the direction of progressive motion, depends on the initial flagellar phase.

When symmetry is broken, for example by the presence of a no-slip boundary, one computation is no longer sufficient to deduce the trajectory for all time and the progressive velocity defined above no longer exactly describes the mean motion. Indeed, a suitable timescale must be set on which to consider mean motion, since we anticipate that the velocities will vary as the swimmer moves relative to the wall. We use the same approach as Phan-Thien et al. [99], which is to calculate the arithmetic mean of several instantaneous velocities for the same head position but varying flagellum phases,

$$\widehat{\mathbf{U}} = \frac{1}{N_\phi}\sum_{j=1}^{N_\phi}\mathbf{U}(\mathbf{x}^{\mathrm{B}},\mathbf{e}_1^{\mathrm{B}},\mathbf{e}_2^{\mathrm{B}},\phi^{\mathrm{T}}=2\pi j/N_\phi) \approx \frac{1}{2\pi}\int_0^{2\pi}\mathbf{U}(\mathbf{x}^{\mathrm{B}},\mathbf{e}_1^{\mathrm{B}},\mathbf{e}_2^{\mathrm{B}},\phi^{\mathrm{T}})\,\mathrm{d}\phi^{\mathrm{T}}, \tag{3.18}$$

where $\mathbf{U}(\mathbf{x}^{\mathrm{B}},\mathbf{e}_1^{\mathrm{B}},\mathbf{e}_2^{\mathrm{B}},\phi^{\mathrm{T}})$ denotes the velocity computed for the swimmer by the BEM with position $\mathbf{x}^{\mathrm{B}}$, orientation vectors $\mathbf{e}_1^{\mathrm{B}}$ and $\mathbf{e}_2^{\mathrm{B}}$, and motor phase ϕ^{T}. We use $N_\phi = 4$, 8 or 16, depending on the rate of convergence of the computed mean. Other phase-

averaged quantities such as the cell body rotation rate and torque may be computed similarly.

The phase-averaged velocity, $\widehat{\mathbf{U}}$, is slightly different from the progressive velocity, $\overline{\mathbf{U}}$. In free space for instance, the phase-averaged velocity must be along the axis of symmetry while the progressive velocity will be at a slight angle to this due to the component of $\mathbf{\Omega}^{\mathrm{T}}$ perpendicular to the motor axis. $\widehat{\mathbf{U}}$ is the average velocity over one period of motion assuming the swimmer does not appreciably change in position or orientation on this timescale. Alternatively, $\widehat{\mathbf{U}}$ can be thought of as the ensemble average velocity over configurations with a fixed body position and orientation but unspecified tail phase. Calculations for free space kinematics by Keller & Rubinow [76] indicate that periodic fluctuations in the orientation scale with the square of the ratio of flagellar helix radius to curvilinear length, while fluctuations in the position of a particular point scale with the same ratio multiplied by the helical pitch. Although we can expect discrepancies to increase near a wall, $\widehat{\mathbf{U}}$ and $\overline{\mathbf{U}}$ are essentially the same and both are good indicators for the net movement of the organism. It is convenient to describe the mean motion in a phase-independent manner, which is the main motivation for defining the phase-averaged velocity. We will use $\widehat{\mathbf{U}}$ to quantify swimming efficiency in the remainder of this chapter and to investigate the motion near boundaries in later chapters.

3.6 Swimming speed and optimisation

The studies of Phan-Thien et al. [99] and Fujita & Kawai [53] addressed the question of optimising swimming speed in bulk fluid using power efficiency as the objective function. While this may have some relevance, particularly in the design of artificial micro-swimmers, there are a host of other factors that would affect biological fitness of bacteria in nature [130]. Even if the sole desire were to make the fastest possible swimmer, there would be several conditions to consider. In particular, there are

constraints on the output of the flagellar motor. A bacterium with body and flagellum shape giving the most power-efficient propulsion may not achieve the greatest speed if the motor cannot achieve the required torque and frequency combination. In light of the constant torque produced by motors at all but the fastest speeds of biological relevance, we will also examine the alternative optimisation criterion of torque-efficiency, which selects the fastest swimmer for a given motor torque. The result will be contrasted with the power-optimum and with examples from observation, allowing an assessment of whether optimisation studies are robust to the influence of additional biology in the choice of objective functions.

The power efficiency is defined as a ratio of the power needed to push a sphere of the same volume as the cell to the required mechanical power of the swimming motion giving the same mean speed, i.e.

$$\eta^{\mathrm{P}} := \frac{6\pi\mu\bar{a}\hat{U}^2}{P}, \tag{3.19}$$

where $P = \tau^M\hat{\omega}^{\mathrm{M}}$ is the average power required to produce the motion by turning the flagellum with the motor torque τ^{M} at the phase-averaged motor frequency $\hat{\omega}^{\mathrm{M}}$ and $\bar{a} = (a_1^{\mathrm{B}}\, a_2^{\mathrm{B}}\, a_3^{\mathrm{B}})^{1/3}$ is the volumetric radius of the cell body. Since power consumption is proportional to the square of speed, relative swimming speeds for a given power level are proportional to the square roots of the power efficiencies.

The torque efficiency can be defined as the reciprocal of the ratio of the motor torque to the torque required to rotate a sphere of the same volume as the cell body to achieve an equatorial surface speed equal to the mean swimming speed, i.e.

$$\eta^{\tau} := \frac{8\pi\mu\bar{a}^2\hat{U}}{\tau^{\mathrm{M}}}. \tag{3.20}$$

Consider the problem of optimisation over N geometrical parameters. The strategy we will follow is to first evaluate the power or torque efficiency on a regular grid in parameter space using the methods outlined in §3.2 and §3.5 to solve the dynamics of the system. The efficiencies will be computed in both free space and in

close proximity to a no-slip plane boundary. We will then use the MATLAB function `interpn` to produce an N-dimensional cubic spline interpolation of the sampled efficiency data, which can then be maximised with `fmincon` within the bounds of the sampled parameter range.

Variations in power efficiency with the geometrical parameters dictating the number of turns on the flagellum, N_λ, helix pitch angle, ak, starting region length, k/k_E, flagellum radius, $a^\mathrm{T}/\bar{a}$, flagellum length, $L/\bar{a}$, and body aspect ratio, $a_1^\mathrm{B}/a_2^\mathrm{B}$, have been described in the past [64, 99, 53] (see appendix A for descriptions of parameters). To arrive at an optimal geometry, the efficiency was optimised over each parameter in turn, which is essentially one iteration of a direction set method for optimisation. By interpolating a grid of parameter space instead of just one parameter at a time, we can obtain a better estimate for the local optimum.

Power efficiency appears to increase monotonically as flagellum radius decreases [99] so we will not look for an optimal value. In examples of monotrichous bacteria given by Brennen & Winet [22], we find $a^\mathrm{T}/\bar{a} \approx 0.01$–$0.04$. However, we will set a slightly higher value of $a^\mathrm{T}/\bar{a} = 0.05$ to allow greater computational accuracy without the excessive mesh refinement needed for highly curved surfaces. In addition, we will fix the value $k/k_\mathrm{E} = 1$ since it was found that efficiency is insensitive to the starting region length within a realistic range applicable to a bacterial model. Finally, only axisymmetric spheroids will be considered, i.e. $a_2^\mathrm{B} = a_3^\mathrm{B}$, since this is a good approximation for rod-shaped bacteria. Thus, we will optimise swimming efficiency over four parameters: number of turns on flagellum, N_λ, pitch angle, ak, flagellar length, $L/\bar{a}$ and cell body aspect ratio, $a_1^\mathrm{B}/a_2^\mathrm{B}$.

3.6.1 Optimisation results

In order to aid visualisation of the effects of individual parameters, we first consider optimising over two parameters: wavelength, $\lambda/\bar{a}$, and flagellar length, $L/\bar{a}$. This is

equivalent to optimising over N_λ and $L/\bar{a}$ since these parameters are inter-related. Fig. 3.3(a) shows the free space variation in power efficiency with these two parameters while imposing $ak = 1$ and $a_1^{\mathrm{B}}/a_2^{\mathrm{B}} = 2$. We find power efficiency is within about 10% of the maximum value in the region $3.5 < \lambda/\bar{a} < 5.5$, $6 < L/\bar{a} < 11$.

The torque-optimised shape is quite different from this. As Fig. 3.3(c) shows, there is a greater preference for short, small wavelength flagella. Considering variations in only these two parameters, the optimal region is roughly $1 < \lambda/\bar{a} < 2$ and $1.5 < L/\bar{a} < 5$. The power optimum is about half as torque efficient as the torque optimum, which has a power efficiency of about one fifth of the optimum.

Corresponding power and torque optimisation results for bacteria oriented parallel to the boundary at a distance $h/\bar{a} = 2$ are shown in Fig. 3.3(b,d). This separation distance is typical for swimmers that are attracted to boundaries, as we shall see in chapter 4. The overall efficiencies are slightly reduced near the boundary but the locations of the optima do not change significantly. Even upon inclusion of all four geometrical parameters, the configurations optimised for free space swimming and those optimised for boundary swimming do not differ greatly and are almost equally efficient. Results of geometrical optimisation in each case are listed in table 3.1 and comparisons with experimental measurements are shown in table 3.2. The free space power efficiency is optimised by the values $N_\lambda \approx 1.5$, $L/\bar{a} \approx 9$, $ak \approx 0.9$ and $a_1^{\mathrm{B}}/a_2^{\mathrm{B}} \approx 1.7$. This agrees well with the corresponding figures given by Phan-Thien et al. [99], $N_\lambda \approx 1.5$, $L/\bar{a} \approx 10$, $ak \approx 1$ and $a_1^{\mathrm{B}}/a_2^{\mathrm{B}} \approx 1.4$.

3.6.2 Discussion

A significant difference can be seen between bacterial shapes that optimise power and torque efficiency respectively. Visually comparing these with a selection of measured bacterial strains, we find some examples that are close to the computed power optimum and others that resemble the torque optimum, though the flagella

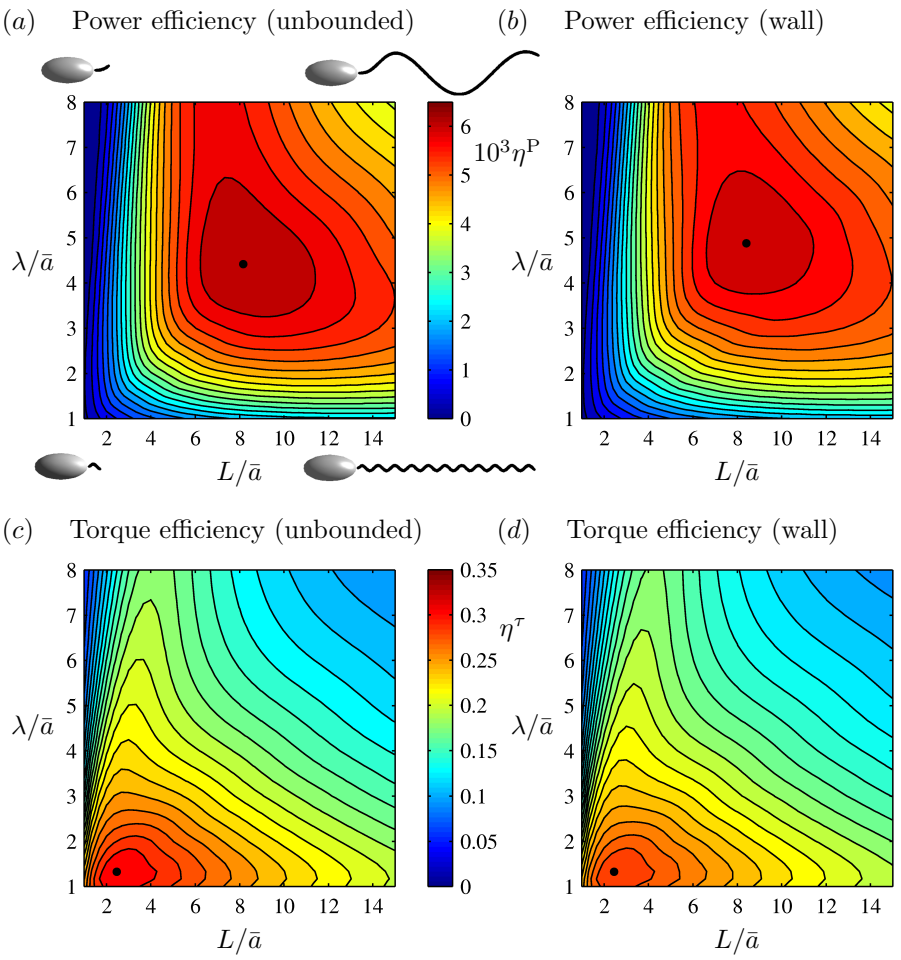

Figure 3.3: Contour plots of swimming efficiency as a function of flagellum wavelength, $\lambda/\bar{a}$, and total length, $L/\bar{a}$. Top row: power efficiency; bottom row: torque efficiency. Left column: swimming in unbounded fluid; right column: swimming parallel to boundary at distance $h/\bar{a} = 2$, with the same colour scale as the corresponding plot in unbounded fluid. Dots indicate the optimal parameter values in each case. Bacterium shapes are illustrated for the four corners of parameter space in (a). Figure originally published by Shum et al. [114].

Table 3.1: Optimal geometries and corresponding efficiencies. Results of power (P) and torque (T) efficiency optimisation for swimming in free space (F) and parallel to boundary (B) at distance $h/\bar{a} = 2$. Optimisations were performed over two parameters (2) and four parameters (4). Parameters marked with asterisks (*) were fixed at these values. $\eta_{\mathrm{F}}^{\mathrm{P}}$ and η_{F}^{τ} are the efficiencies in free space while $\eta_{\mathrm{B}}^{\mathrm{P}}$ and η_{B}^{τ} are the efficiencies for the same configuration near a boundary. Table originally published by Shum et al. [114].

Case	N_λ	$\lambda/\bar{a}$	$L/\bar{a}$	ak	$a_1^{\mathrm{B}}/a_2^{\mathrm{B}}$	$10^3\eta_{\mathrm{F}}^{\mathrm{P}}$	$10\eta_{\mathrm{F}}^{\tau}$	$10^3\eta_{\mathrm{B}}^{\mathrm{P}}$	$10\eta_{\mathrm{B}}^{\tau}$
P-F-2	1.33	4.41	8.17	1.00*	2.00*	6.32	1.78	6.21	1.74
P-B-2	1.24	4.87	8.42	1.00*	2.00*	6.27	1.67	6.26	1.63
T-F-2	1.34	1.32	2.46	1.00*	2.00*	1.38	3.14	1.21	2.94
T-B-2	1.33	1.32	2.45	1.00*	2.00*	1.37	3.14	1.21	2.94
P-F-4	1.49	4.68	9.14	0.87	1.67	6.43	1.79	6.25	1.74
P-B-4	1.28	5.16	8.76	0.90	1.88	6.36	1.69	6.32	1.65
T-F-4	1.28	1.40	2.14	0.68	3.88	1.05	3.65	0.95	3.47
T-B-4	1.27	1.37	2.09	0.69	4.21	1.00	3.65	0.91	3.47

Table 3.2: Comparison of optimal with observed geometries. Illustrations (not to same scale) and computed efficiencies of the four-parameter free space optimal geometries and approximate geometries of experimentally observed monotrichous bacteria. In all cases, the flagellum radius was fixed at $a^{\mathrm{T}} = 0.05\,\bar{a}$ and efficiencies are divided by their respective free space optima.

Species	Shape	$\eta_{\mathrm{F}}^{\mathrm{P}}/\eta_{\mathrm{max}}^{\mathrm{P}}$	$\eta_{\mathrm{F}}^{\tau}/\eta_{\mathrm{max}}^{\tau}$	Source of parameters
R. sphaeroides		0.49	0.65	[5]
P. phosphoreum		0.95	0.44	[22]
P. aeruginosa		0.85	0.51	[22]
V. cholera		0.44	0.54	[22]
C. crescentus		0.78	0.47	[84]
V. alginolyticus		0.67	0.70	[90]
P-F-4	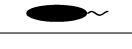	1.00	0.49	
T-F-4		0.16	1.00	

are all considerably longer than that of the torque optimum. In terms of efficiency, most species are moderately to highly power efficient but only moderately torque efficient at best. In general, based on the limited data available, power efficiency appears to be better optimised by bacteria than torque efficiency.

However, it would be inappropriate and overly simplistic to conclude that bacteria have evolved to optimise power efficiency of swimming. The wide variation between species is already evidence that bacteria do not all have the same optimisation criterion. As noted previously, the optimum appears to be broad, allowing deviations from the optimum without significantly impacting power efficiency. Hence other considerations may also play a role in determining morphology and swimming is robust to variations within a population and over the lifetime of an individual.

Conversely, the fact that the monotrichous bacteria included in the dataset do not achieve high torque efficiency does not rule out the biological relevance of this quantity. There may be specific environmental conditions for which torque efficiency becomes more important. For example, in a highly viscous fluid the motor torque may limit swimming speed, while this may not be the case in a watery medium because the free swimming motor frequency is above the plateau region of the motor torque–frequency curve [84]. A much deeper analysis of bacterial strains, their natural habitats and morphologies would be required to form sound conclusions about the role of swimming efficiencies in measuring bacterial fitness.

The methods of analysis employed here can also be applied to optimise other objective functions. This would be of use to engineers designing artificial micro-swimmers propelled in the fashion of bacteria. In this case, we are free to identify the factors and constraints of the optimisation task.

Moving from free space to near-surface swimming, for both power and torque optima there was a slight reduction in the number of helical turns and total length of the flagellum while the helical pitch angle and cell body aspect ratio increased slightly.

However, these modifications afforded an increase in efficiency of no more than about 1%. This suggests that no adaptation in shape is required for a bacterium to be an effective swimmer near surfaces if it swims well in bulk fluid, taking into account either power or torque efficiency. However, behaviour near surfaces is more complicated and characterised by more than a swimming efficiency ratio. We will demonstrate the range of swimming trajectories and the influence of bacterial geometry in the following chapter.

3.7 Summary

Our approach to investigating bacterial locomotion was to use the boundary element method to numerically solve the Stokes flow equations considering an idealised, prolate spheroidal cell body with a single helical flagellum turned about its axis by a motor torque. By treating the cell body and the flagellar filament as rigid structures, we were able to limit the dynamics of the bacterium to three translational and four rotational degrees of freedom. In free space, the average motion of the bacterium is a straight line characterised by a single direction vector and swimming speed. The computed speed was used to compare the effectiveness of swimmers of different shapes for a given power consumption or for a given motor torque in a novel study of optimisation over multi-dimensional parameter sets.

Among reported measurements of different bacterial species there are close matches to both the computed power optimum and to the torque optimum. However, many factors as well as population variability can influence the shapes in a given sample. This alone could account for apparent matches and it would be premature to suggest that a particular species has evolved to optimise a particular quantity. Nevertheless, we have demonstrated a method for optimising the geometrical design of a flagellated micro-swimmer according to an objective function based on swimming velocities and the distribution of stresses acting on the swimmer, from which

quantities such as power consumption can be derived.

Chapter 4

Interactions with no-slip plane boundaries

There is a growing interest in developing our understanding of how micro-organisms swim through confined environments, such as in narrow channels or porous media [16, 55]. This would be relevant in a wide range of scenarios. Bacteria moving through a host organism or in microdevices inevitably experience the effects of solid boundaries. Behaviour near surfaces is important for initiating biofilm formation [95] and modulating bacterial transport in bioremediation of contaminated groundwater [113]. It also affects the foraging patterns of organisms that feed on nutrients diffusing from surfaces. In such cases it would be beneficial to remain close to the surface so these organisms may exhibit features that encourage this. As an example, the marine bacterium *V. alginolyticus* adopts a run-and-reverse swimming strategy rather than run-and-tumble when it is near a large source of food. It has been found that backward swimming increases their residence time near solid surfaces [89]. On the other hand, tumbling could result in the bacterium swimming away from the surface, which is potentially a source of nutrients. Understanding how swimmers are affected by surfaces can even help us achieve certain aims, such as sorting a population of cells by size [68].

Theoretical studies on swimming near no-slip plane boundaries date back as early as 1974 with Katz [74], where the swimmer was an infinite waving sheet. RFT and

SBT have been extended to half space domains [18, 75], leading to SBT studies on flagellar motility near surfaces [116]. These techniques can be used reliably for separation distances of the order of the length of the slender body but distributions of force must be placed on the surface, rather than the centreline, to accurately satisfy the boundary conditions when the wall separation is of the order of the slender body width [7]. This leads to a boundary integral or boundary element method, which was used by Ramia et al. [107] to determine the kinematics of swimmers in unbounded fluid, near a plane boundary, between two parallel plane boundaries and near another swimmer. The path followed by a swimmer near a single plane boundary was shown to be circular, as is commonly observed under the microscope. This effect has been explained [82] and reported in a number of numerical studies. However, any long-timescale simulations have invariably had to terminate as the swimmer approached and crashed into the boundary (as reported by Ramia et al. [107], for example). This is due to the known hydrodynamic attraction of these types of swimmers to boundaries [13].

Short-ranged interactions between the swimmer and the boundary (e.g. van der Waals or electrostatic forces) have been hypothesised to play an important role in trapping micro-swimmers near surfaces [51]. These extra interaction potentials may be used in simulations to create a finite preferred separation from the boundary [83], with the additional numerical benefit of reducing errors and instabilities by preventing close contact.

However, two different kinds of "trapping" at surfaces were documented by Vigeant et al. [125]: cells can swim freely but at a fixed distance from the surface for extended periods of time or they can actually adhere to the surface and become immobilised. The study suggested that electrostatic and van der Waals forces may only be responsible for the latter kind of entrapment, whereas hydrodynamic interactions alone are sufficient to draw cells to swim along surfaces. In this case, the

extra forces one would add to a numerical model would tend to attract the swimmer rather than keep it from colliding with the boundary.

To understand static surface interactions between bacteria and substrates, Klein et al. [79] measured the equilibrium forces acting on single cells of *Staphylococcus aureus* held in optical traps at varying distances from glass surfaces. With bare glass, the cell was pulled out of the optical trap and adhered to the surface when it was brought to within 100 nm but there was no discernible interaction beyond this distance. Measurements were also taken using glass that had been coated with a protein, β-casein. Under this condition, no noticeable interactions were found until a separation distance of 60 nm, below which a repulsive force was measured and found to increase exponentially as the cell was brought closer to the substrate.

Evidently, close-range surface interactions depend on the details of the substrate material. Focussing on the hydrodynamics of bacterial motility, we will not consider any additional surface interactions in the current work. Instead, we limit the application of our model to situations in which the bacterium is sufficiently far from walls. We set this threshold distance to 35 nm, a distance at which the repulsive forces from β-casein coated glass were appreciable in Klein's experiment. This is in fact a very small separation distance, about twice the flagellum diameter. Using a lengthscale appropriate for *R. sphaeroides* [5], we find the non-dimensionalised cutoff distance $d_{\min} = 0.05\bar{a}$, where $\bar{a}$ is the volumetric radius of the cell body. We refer to instances in which the cell body or flagellum approaches this threshold as collisions; non-hydrodynamic surface forces may be required to resolve swimming behaviour beyond this point and we do not consider this further.

As mentioned above, long-range attraction of swimmers towards the boundary can be explained by hydrodynamics. Without the addition of repulsive surface interactions, few examples of stable trajectories at a finite separation from a boundary (i.e. not colliding) have been reported. The SBT simulation study by Smith et al. [116]

found that a spermatozoan swimmer employing planar or "elliptical helicoid" beat patterns could achieve stable trajectories near boundaries. We will see that a finite equilibrium separation can also exist for bacterial swimmers propelled by a rotating helical flagellum. In this chapter, we explore surface accumulation for monotrichous bacteria and characterise the geometrical aspects of swimmers that encourage or prevent stable surface motility.

4.1 Interpolation method for approximate swimmer dynamics

The trajectory of a swimming bacterium will clearly depend on its initial configuration. To characterise the complete behaviour of a bacterium of given shape, we would need to test a large number of initial configurations. This is a computationally expensive and inelegant endeavour and it is not clear a priori how long each simulation must be to show the long-term behaviour. Instead, we will simplify the analysis by examining just a few quantities of interest.

Solving the boundary element problem gives us the velocities

$$\left.\begin{aligned} \mathbf{U} &= f_{\mathbf{U}}(\mathbf{x}^{\mathrm{B}}, \mathbf{e}_1^{\mathrm{B}}, \mathbf{e}_2^{\mathrm{B}}, \phi^{\mathrm{T}}), \\ \boldsymbol{\Omega} &= f_{\boldsymbol{\Omega}}(\mathbf{x}^{\mathrm{B}}, \mathbf{e}_1^{\mathrm{B}}, \mathbf{e}_2^{\mathrm{B}}, \phi^{\mathrm{T}}), \\ \omega^{\mathrm{M}} &= f_{\omega^{\mathrm{M}}}(\mathbf{x}^{\mathrm{B}}, \mathbf{e}_1^{\mathrm{B}}, \mathbf{e}_2^{\mathrm{B}}, \phi^{\mathrm{T}}). \end{aligned}\right\} \tag{4.1}$$

It should be noted that the two orientation vectors $\mathbf{e}_1^{\mathrm{B}}$ and $\mathbf{e}_2^{\mathrm{B}}$ together represent only three independent degrees of freedom, due to orthonormality. By considering the phase-averaged velocities instead of instantaneous velocities, we remove ω^{M} and dependence on ϕ^{T}. Further simplifications can also be made by considering the symmetry of the fluid geometry. For example, the configuration of a swimmer near a plane boundary is specified up to symmetry by its distance from the wall and inclination angle relative to the wall. This will be discussed further below. For generality, we write the configuration state as a single vector, $\mathbf{x} = (x_1, x_2, ..., x_N)$,

where N is the number of variables required to uniquely specify the state up to symmetry. We can then express the problem in the standard form of an autonomous ODE system,

$$\dot{x}_i = f_i(x_1, x_2, ..., x_N), \quad i = 1, 2, ..., N. \tag{4.2}$$

It is reasonable to expect that the velocities depend smoothly on the bacterium's position and orientation in space. Therefore, we approximate f_i by interpolation using lists of values of the functions pre-evaluated on a grid in configuration space. Typically, we use around 10 different values in each dimension of configuration space, depending on the extent and resolution required. Since solving the boundary element problem is computationally expensive, interpolation is an attractive means of rapidly solving the bacterial swimming ODEs over long timescales for many initial conditions. This approach allows us to look for general long-term behaviour. Only an approximate agreement should be expected between this trajectory and that computed by tracking of the full system since, apart from errors arising from the interpolant approximation, phase-averaging removes details of the short-timescale fluctuations, which inevitably perturb the exact path. Results will be verified by carrying out some simulations of the full system as well.

4.2 Analysis of dynamics in different fluid geometries

When N is small, it is possible and instructive to visualise the phase space of the ODE system. For example, the two-dimensional system of swimming near a plane boundary can be visualised with a quiver plot after computing the velocities on a grid of points in the phase plane. MATLAB's built-in functions can be used to find nullclines and streamlines, which are equivalent to pathlines here. Doing this, we shall see that in some cases, the system possesses a steady state. The approximate solution gives a good estimate for the location of the steady state but this estimate can be improved

by applying Newton's method [106] to find roots of the ODE system. Assuming a suitable starting point can be supplied, this method is much quicker than obtaining a grid of function evaluations for interpolation. In this way, we can track the evolution of the steady state as the shape of the bacterium is incrementally adjusted.

We now detail the use of symmetry to reduce the dimensionality of the configuration phase space. In the most general fluid environment, an axisymmetric bacterium's configuration is specified by its position vector and three angles of orientation, giving $N = 6$. We will consider only axisymmetric bacterial shapes, which means the phase-averaged velocities are invariant to rotations about the body axis, reducing the dimensionality by one. In certain fluid geometries, the velocities transform in a known manner with translations and rotations of the configuration. Hence, we need only consider the dependence on a further reduced set of variables. It should be noted that reducing the dimensionality of the problem in this way is not an approximation as the full dynamics can be recovered by considering the necessary coordinate transformations.

The simplest case, swimming in unbounded fluid, is translationally invariant and the velocities transform with the reference frame of the swimmer when rotated. Therefore, the rotational velocity is constant and the translational velocity precesses around the axis of rotation, resulting in helical trajectories in the fixed reference frame. Such trajectories were analysed in detail by Keller & Rubinow [76]. With axisymmetric bodies, the phase-averaged rotational and translational velocities must lie along the axis of the swimmer so the phase-averaged trajectory is a straight line in this direction.

When the symmetry is broken by a plane boundary, the velocities will depend on the position and orientation of the body relative to the plane. Restricting attention to axisymmetric bodies, the configuration is described by two components of the bacterium's full state: the height, h, of the junction position above the no-slip plane

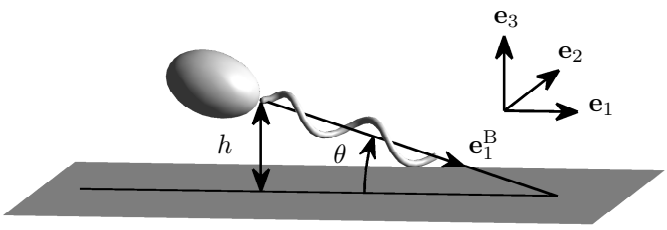

Figure 4.1: Bacterial configuration relative to a plane boundary (wall). Averaging over variations in tail phase, the bacterium's configuration is specified by the height above the wall, h, and the inclination angle, θ, of its axis relative to the wall.

boundary and the angle of inclination, θ, of the bacterium with respect to this plane (see Fig. 4.1). The phase of the flagellum is irrelevant as we will only consider phase-averaged quantities here. By symmetry, translations by a vector parallel to the plane and rotations about the plane's normal direction only change the perspective of the observer. Hence, for a spheroidal cell body and coaxial flagellum, we have the autonomous system

$$\left.\begin{aligned} \dot{\theta}(t) &= f_\theta(\theta(t), h(t)), \\ \dot{h}(t) &= f_h(\theta(t), h(t)), \end{aligned}\right\} \tag{4.3}$$

where $\dot{h} \equiv \widehat{U}_3$ is the phase-averaged vertical velocity and $\dot{\theta}$ is equal to the component of the phase-averaged rotation vector in the direction of the axis of inclination. This formulation makes the assumption that the time-averaged behaviour is well approximated by the phase-averaged behaviour, i.e., $\bar{\dot{\theta}} \approx \widehat{\dot{\theta}}$ and $\bar{\dot{h}} \approx \widehat{\dot{h}}$. With this assumption, we can infer the dynamics on timescales longer than a motor revolution from phase-averaged velocities, which are easily computable as given in (3.18).

When the bacterium is between two parallel plane walls, the configuration is again described by h and θ, where these quantities are relative to one of the walls. The same phase plane analysis can be carried out to investigate the dynamics in this domain geometry, which is appropriate for modelling the space between a microscope slide and coverslip or in the central region of a rectangular capillary tube.

Although expressions for the Green's function between parallel no-slip plane boundaries are known [86], these are cumbersome and we instead use the free space Green's function and explicitly mesh a finite portion of the planes, imposing the no-slip condition through the BEM. In the case of a single plane boundary, explicitly meshing a portion of the plane was compared with using the known half space Green's function [17]. Relative differences in velocity were of the order of 0.1%. The half space Green's function approach was used for the presented results to avoid the unnecessary burden of increasing the mesh size. One further fluid geometry, a rectangular prism bounded by four no-slip walls, will be discussed in §5 and requires explicit wall meshing.

4.3 Half space

The far-field flow due to a bacterium swimming in free space is equivalent to that due to a force dipole. The rationale for this is that the cell body pushes the fluid forward with some force and the flagellum exerts an equal and opposite force on the fluid at a location behind the effective position of the force from the body. A force dipole induces a flow field that decays with the square of the distance from the singularity point [9]. Near a no-slip plane boundary, the flow is the sum of this force dipole field and a disturbance field that satisfies the Stokes flow equations throughout the half space and cancels out the flow from the force dipole on the plane to satisfy the boundary conditions. The method of images can be used to construct the required disturbance field from a combination of singular solutions located at the reflection of the original force dipole with respect to the plane boundary. The leading order term in the image field is also a force dipole. Hence, for a swimmer of size $\bar{a}$ at a distance h from the wall, the influence of the wall is at most $O(\bar{a}^2/h^2)$, assuming h is large compared with the size of the swimmer. Walls further than about 10 μm from the swimmer may therefore be neglected in terms of hydrodynamics. It follows that the

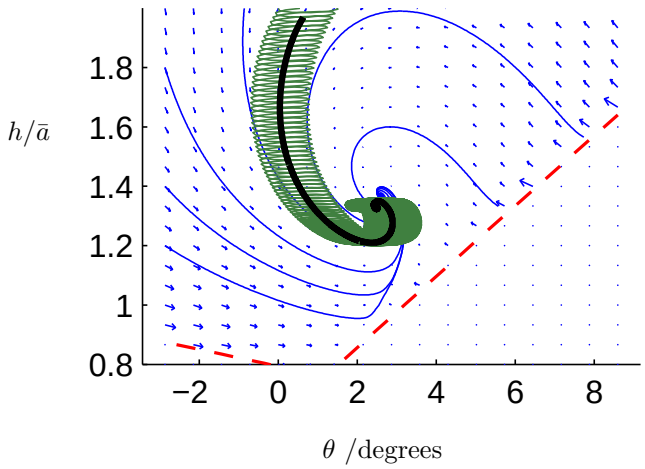

Figure 4.2: A small region of the phase plane showing stable spiral dynamics for a swimmer near a plane boundary. The bacterium has the following parameter values: $a_1^{\mathrm{B}}/a_2^{\mathrm{B}} = 2$, $L/\bar{a} = 10$, $ak = 1$, $N_\lambda = 2$ (see §3.1 or appendix A for descriptions of geometrical parameters of the model bacterium). Blue curves indicate pathlines generated using the interpolation method. A trajectory obtained using a full tracking simulation with the BEM is shown by the green curve and exhibits oscillations at the frequency of motor revolutions. The thick, black curve is a temporally smoothed plot of this trajectory. The region below the dashed line is excluded due to entailing intersections between the bacterium and the wall. Figure modified from Shum et al. [114]

.

dynamics of a swimmer in a general confined environment are well approximated by motion near a single no-slip plane boundary as long as all but one boundary of the fluid domain are far away and the nearby boundary is flat where it is close to the swimmer.

Performing time stepping simulations of the full dynamics with a variety of bacterial shapes initially parallel to and far from the wall, we noticed a tendency for many swimmers to turn and swim towards the boundary. The separation distance from the boundary converged to a constant average value, which was irrespective of the initial conditions for a given bacterial shape. Looking at the phase portrait of the approximate system, we see that this is to be expected since there is a stable spiral attracting trajectories to the steady state (Fig. 4.2).

At the steady state, the swimmer is inclined at a small angle away from the wall. Due to the chirality of the rotating helical flagellum and the symmetry breaking from the plane boundary, the bacterium must constantly turn about the axis normal to the wall, leading to circular orbits as commonly observed under the microscope. This stable, long-term behaviour is referred to as boundary accumulation since it implies that a population of such swimmers will eventually aggregate close to surfaces.

The effects of changing the geometrical parameters of the bacterial shape are shown in Fig. 4.3. All of the parameters affect the accumulation height and orbit curvature to some degree. The values examined for each parameter reflect a physiologically plausible range of morphologies. Within these ranges, it was found that the radius of curvature is positively correlated with the accumulation height. This is reasonable since the curvature is a result of the wall interaction, which diminishes as the separation distance increases. There was one notable exception: as the pitch angle ak increases, the stable height increases monotonically but the radius of curvature rises to a local maximum at $ak \approx 1$ before decreasing.

Two parameters of particular interest are the aspect ratio of the cell body and the length of the flagellum. There may be considerable variations in these quantities within a population as cells grow. We see from Fig. 4.3(b) that the body aspect ratio has a significant impact on boundary accumulation. Elongation tends to repel the swimmer further from walls and in this figure, below a threshold value of $a_1^{\mathrm{B}}/a_2^{\mathrm{B}} \approx 1.5$ the bacterium descends into the boundary.

Flagellum length has the opposite effect on accumulation; longer flagella encourage closer proximity to the boundary (Fig. 4.3(d)). The effect is only moderate above $L/\bar{a} = 10$ but as the length is decreased below this threshold, the stable configuration is rapidly pushed further from the boundary. Examining the phase portraits for different flagellar lengths, we see that the stable configuration is lost in a bifurcation event (Fig. 4.4).

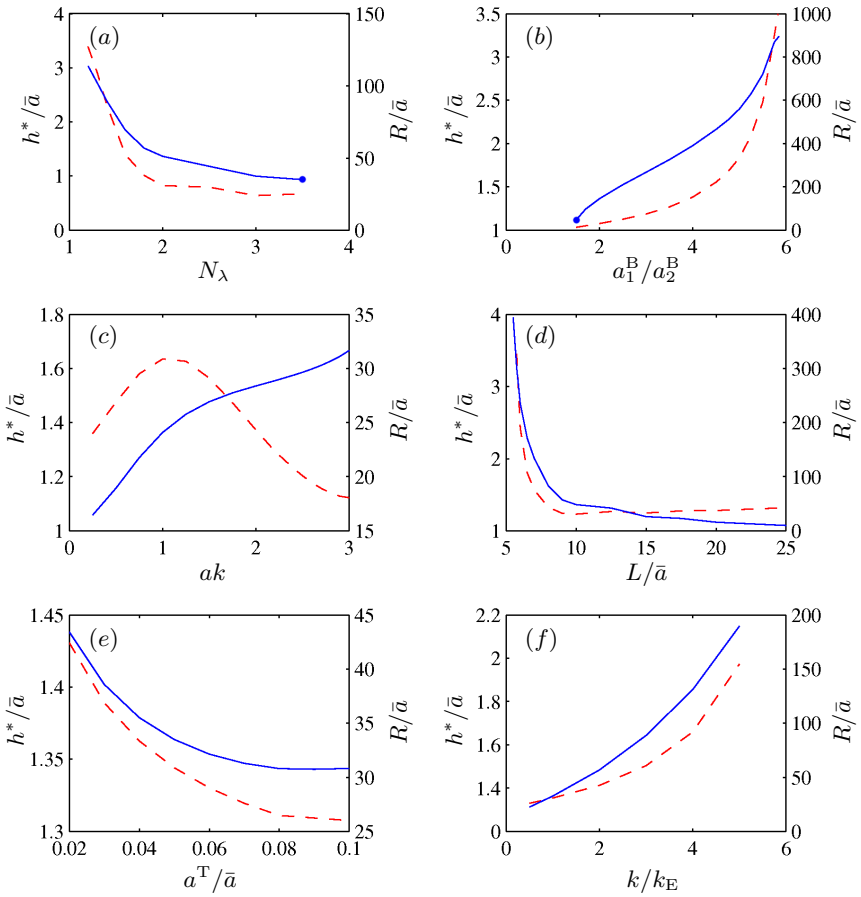

Figure 4.3: Variations in stable junction height ($h^*/\bar{a}$, solid lines) and radius of curvature of the stable orbit ($R/\bar{a}$, dashed lines) with geometrical parameters: (a) number of turns on flagellum, (b) cell body aspect ratio, (c) helix pitch angle, (d) flagellum length, (e) flagellum thickness, (f) flagellum starting region length. The base morphology uses the parameter values: $N_\lambda = 2$, $a_1^{\mathrm{B}}/a_2^{\mathrm{B}} = 2$, $ak = 1$, $L/\bar{a} = 10$, $a^{\mathrm{T}}/\bar{a} = 0.05$, $k/k_{\mathrm{E}} = 1$. Some tail parameters are inter-related; $\lambda/\bar{a}$ varies as necessary in (a) and (c), and N_λ varies in (d) and (f). Dots in (a) and (b) mark limits beyond which the bacterium descends into the wall. Figure originally published by Shum et al. [114].

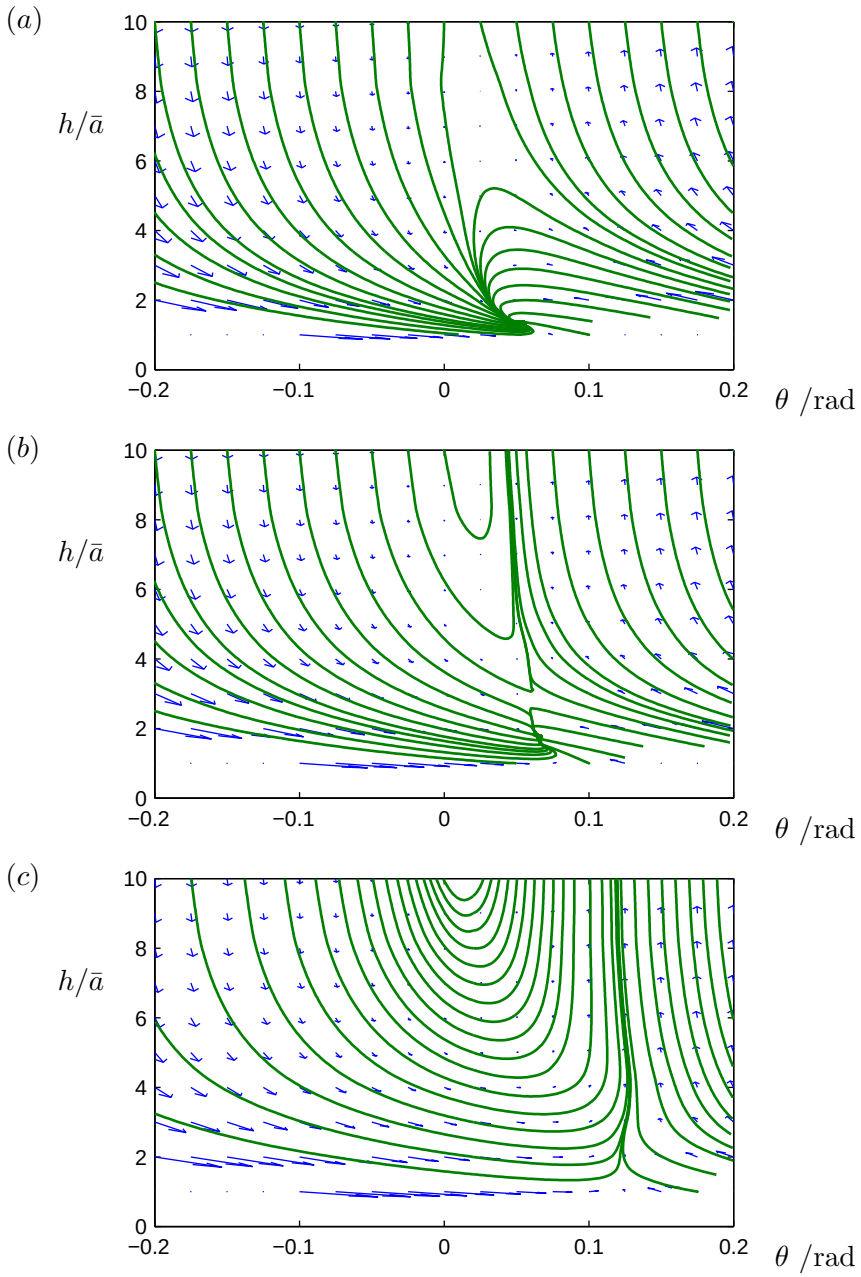

Figure 4.4: Phase plane diagrams for bacteria of flagellar length L swimming near a no-slip plane boundary. (a) $L = 7.5\,\bar{a}$, (b) $L = 6.5\,\bar{a}$, and (c) $L = 5\,\bar{a}$. A bifurcation takes place over this range of parameters. There is a stable state in (a) and as long as the bacterium is not initially inclined too sharply either away from or towards the wall, the swimmer will reach the stable state. However, the stable point is absent in (c) and even trajectories that are initially approaching the boundary are deflected away. Case (b) is an intermediary, with some trajectories reaching the stable state and others approaching but being deflected back into the bulk fluid.

Initially, the steady state has a large basin of attraction (Fig. 4.4(a)). For any given height, there is an inclination angle below which the bacterium will collide with the boundary and another threshold angle above which the bacterium can escape from the wall. Apart from these extremes in initial orientations, all trajectories approach a single steady state. However, decreasing the flagellum length reveals a new regime in which approaching swimmers are attracted and remain close to the boundary only if the angle of incidence is sharp enough (Fig. 4.4(b)). Shallow approaches are deflected away and the cell escapes from boundary effects. If the flagellum length is decreased further, the stable state disappears and all approaching trajectories are deflected away from the boundary (Fig. 4.4(c)).

In summary, three outcomes can be distinguished:

1. descent into the boundary,

2. stable circular orbiting close to the boundary, and

3. escape from the boundary.

Fig. 4.5 illustrates each of these types of trajectories. The timescale used in this figure is

$$\bar{t} = 16\pi^2\bar{a}^3\mu/\tau^{\mathrm{M}}, \tag{4.4}$$

which is the period of revolution of a sphere of radius $\bar{a}$ under the action of a constant torque of magnitude τ^{M} in the viscous fluid. This period typically allows about ten motor revolutions of the model bacterium, depending on the cell and flagellum shape. The data in Fig. 4.5(a) therefore correspond to approximately 1000 revolutions, or 1 s of swimming for an organism like *V. alginolyticus*.

Fig. 4.6 shows a phase diagram of the long-term behaviour for bacteria with different aspect ratios and flagellar lengths. The boundaries of the regions in the phase diagram are overlaid on plots of swimming efficiencies, as calculated previously in §3.6, in Fig. 4.7. We see that power-efficient swimmers can exhibit any of the

three types of behaviour, though peak efficiency is obtained in the region of stable swimmers. In contrast, torque efficiency strongly favours bacterial shapes that tend to escape from walls.

4.4 Parallel plates

By the reasoning given in §4.3, we would expect the behaviour near each of two parallel plates to resemble the behaviour in a half space geometry as long as there is sufficient separation between the two plates. The phase plane diagrams in Fig. 4.8 confirm that this is indeed the case. With a plate separation of $H/\bar{a} = 15$, we see the same transition from a stable state in the phase plane to escaping as flagellum length decreases. However, when a cell swims away from one plane it necessarily swims towards the other and is repeatedly deflected from wall to wall. This appears as a limit cycle in the phase plane (Fig. 4.8(c)). By symmetry, the configuration parallel and exactly midway between the plates is a fixed point. However, this configuration was found to be unstable whereas the limit cycle is stable under these conditions.

As the plate separation decreases, both walls influence the swimming dynamics and another bifurcation is observed. The stable nodes by the two walls in the boundary accumulating case are replaced by a single stable spiral point, which is the parallel, midway configuration that was unstable for larger plate separations. This point is still unstable for boundary escapers but the greatly suppressed limit cycle in such cases may be almost indistinguishable from a steady central position (Fig. 4.9).

4.5 Discussion of implications for bacterial trajectories

The hydrodynamic model we have developed predicts that boundary accumulation is dependent on cell and flagellum shape. In some regions of parameter space, the

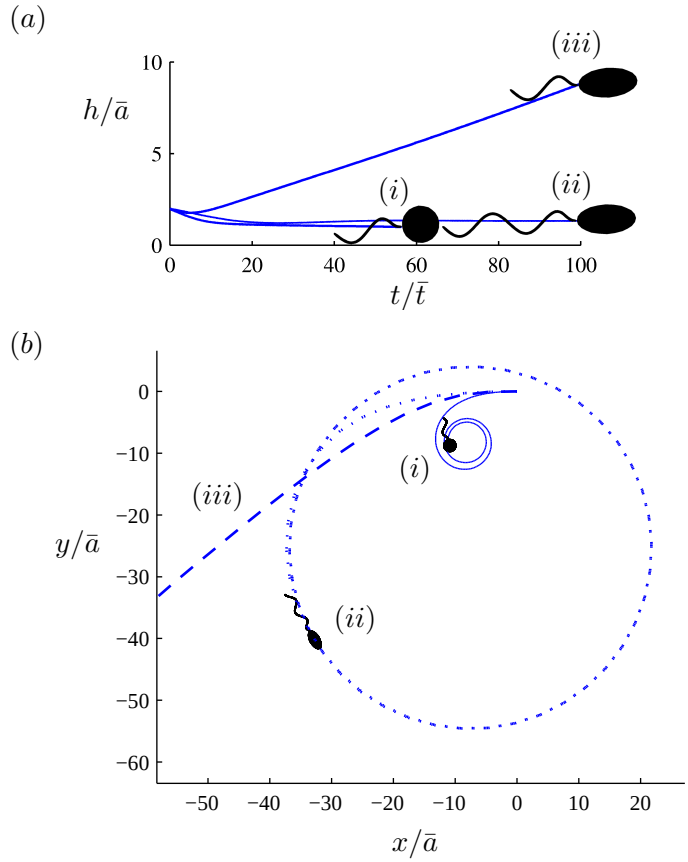

Figure 4.5: Examples of the three types of bacterial trajectories near plane surfaces, (i) descent into the wall, (ii) stable circular orbiting, and (iii) escape into the bulk medium. In (a), the junction height is plotted against time and the model bacteria shown to the scale of the junction height axis. The top-down view of the trajectories are shown in (b). The characteristic behaviour observed is consistent over a wide range of initial conditions and is determined by the shape of the bacterium. The cell body aspect ratios and flagellum lengths used in these examples are (i) $a_1^{\mathrm{B}}/a_2^{\mathrm{B}} = 1$, $L/\bar{a} = 5$; (ii) $a_1^{\mathrm{B}}/a_2^{\mathrm{B}} = 2$, $L/\bar{a} = 10$; and (iii) $a_1^{\mathrm{B}}/a_2^{\mathrm{B}} = 2$, $L/\bar{a} = 5$. The other parameter values used in these simulations were fixed at: $\lambda = \lambda_0 \approx 3.58$, $ak = 1$, $a^{\mathrm{T}}/\bar{a} = 0.05$, $k/k_E = 1$. λ_0 was chosen such that $N_\lambda = 2$ for $L/\bar{a} = 10$. Figure originally published by Shum et al. [114].

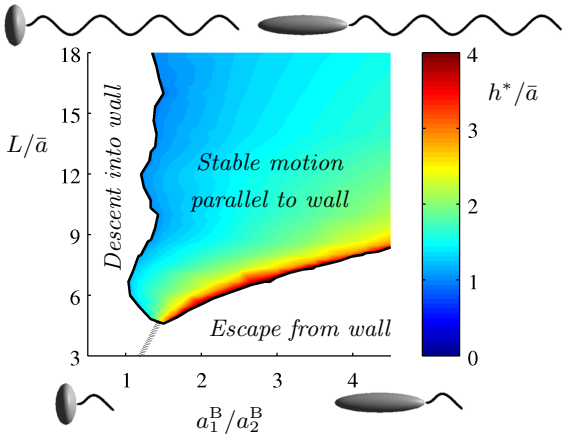

Figure 4.6: Phase diagram showing regions of descent, stable orbits and escape from walls as cell body aspect ratio and flagellum length are varied. The colour scale indicates non-dimensionalised stable height above wall, $h^*/\bar{a}$. The dotted line between the region of escape and the region of descent is only hypothesised as these parameters were not explored. Bacterium shapes are illustrated for the points at the four corners of parameter space. The fixed parameters are the same as those quoted for Fig. 4.5. Figure originally published by Shum et al. [114].

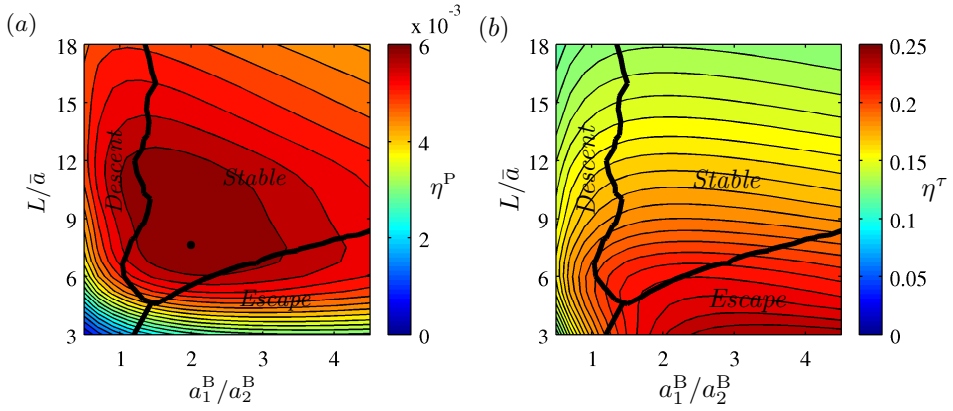

Figure 4.7: Free space (a) power efficiency and (b) torque efficiency with varying flagellar length and cell aspect ratio as in Fig. 3.3 with boundary behaviour from Fig. 4.6 overlaid. Thick lines separate regions where the behaviour of such swimmers near a plane boundary is characterised by stable orbits, escape from the wall, and descent into the influence of close-range surface interactions. As in Fig. 4.6, the boundary between the regions of escape and descent is only hypothesised as these parameters were not explored. A dot in (a) marks the location of the power optimum. Figure originally published by Shum et al. [114].

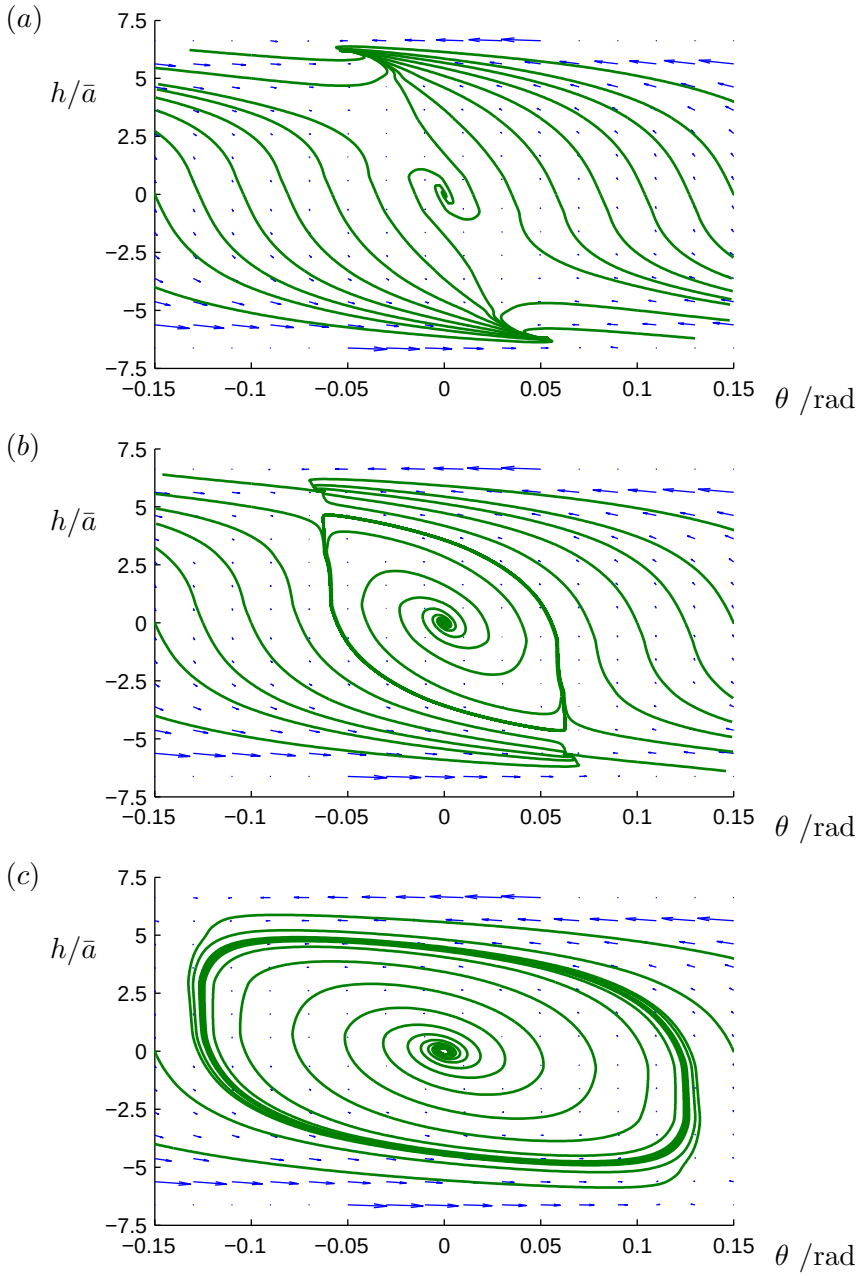

Figure 4.8: Phase plane diagrams for bacteria of flagellar length L swimming between parallel plates of separation $H/\bar{a} = 15$. (a) $L = 7.5\,\bar{a}$, (b) $L = 6.5\,\bar{a}$, and (c) $L = 5\,\bar{a}$. A bifurcation takes place over this range of parameters corresponding to the bifurcation seen in the half space geometry (Fig. 4.4). In all cases, the central point $(\theta = 0, h = 0)$ is an unstable steady state. In (a), there is practically global attraction to the stable states, of which there is one close to each plate. These stable points are absent in (c) and trajectories instead converge to a limit cycle that oscillates from one plate to the other. Case (b) is an intermediary, with some trajectories leading to the stable states and others attracted to the limit cycle.

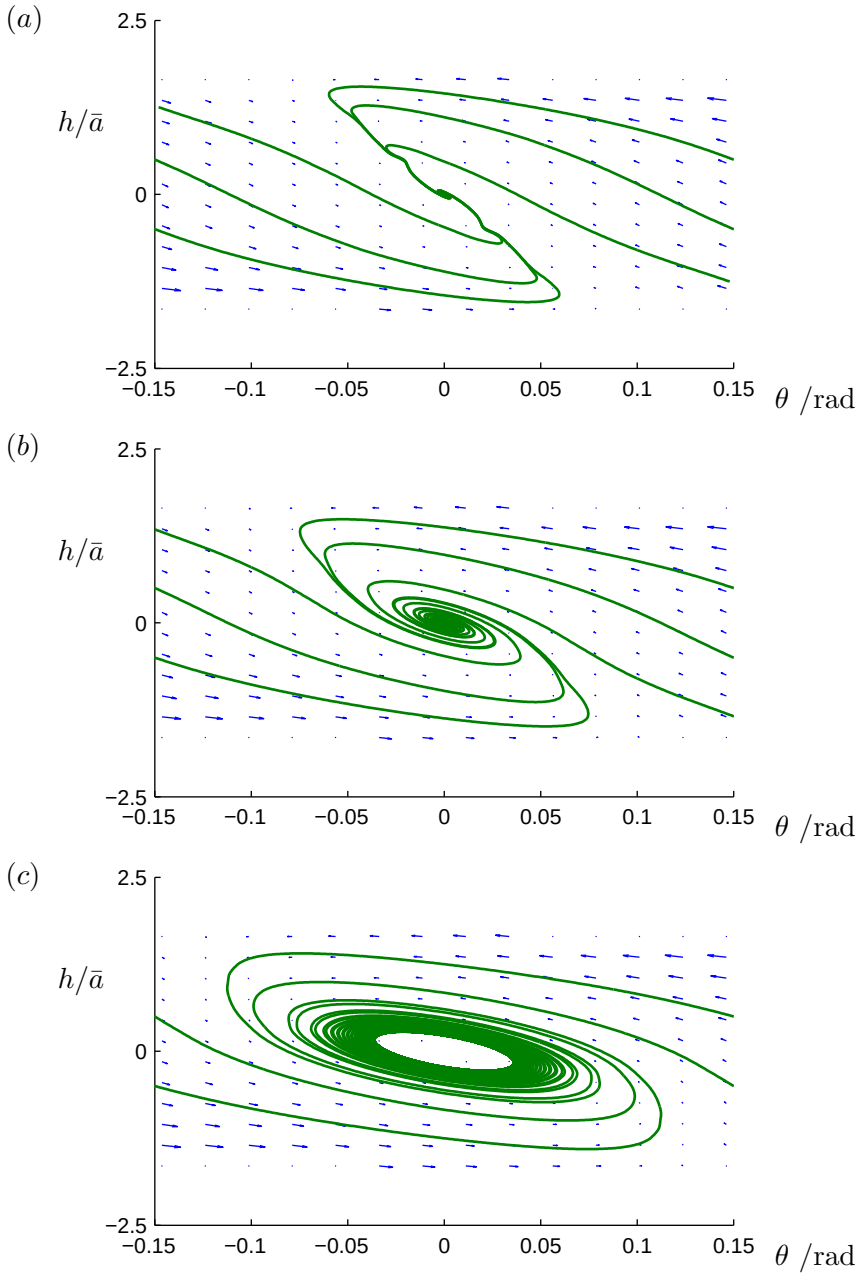

Figure 4.9: Phase plane diagrams for bacteria of flagellar length L swimming between parallel plates of separation $H/\bar{a} = 5$. (a) $L = 7.5\,\bar{a}$, (b) $L = 6.5\,\bar{a}$, and (c) $L = 5\,\bar{a}$. The narrow gap constrains the bacterium to swim in or close to the centre in all cases. However, the central configuration is only a stable state in (a). In both (b) and (c), limit cycles can be seen around this point but are greatly reduced compared with those in Fig. 4.8 where the plate separation is larger. Moreover, we observe that a bifurcation has taken place with the boundary accumulating swimmer, (a). Instead of having two stable points close to the plates and an unstable point in the centre, there is only a single, stable steady state when the plate separation is small.

behaviour is very sensitive and a small alteration can differentiate an escaper from a boundary accumulator. This geometry dependence could contribute to the variability in observed motion in populations of bacteria near surfaces, though chemotactic regulation or stochasticity of the motor and other processess not included in the current model may certainly be influential as well.

The phase plane diagrams indicate that the boundary accumulating steady state is stable enough that an instantaneous vertical perturbation as large as $2\,\bar{a}$, or about $1.4\,\mu$m, accompanied by a rotational perturbation of several degrees should eventually decay. However, depending on the shape of the swimmer, the steady state could be close enough to a separatrix that smaller perturbations can lead to escape from the wall. In a system with stochastic effects present, this would give rise to a different spatial distribution of the population; a much larger proportion would be far from the surface and the average residency time near walls would be much shorter.

While swimming near a surface, hydrodynamic considerations predict that the bacterium's trajectory will curve into circular arcs. In experiments, such tracks are usually observed but there have also been cases where the trajectories were found to have negligible curvature. *V. alginolyticus* has been reported to swim forwards in straight lines but make tight circular trajectories when swimming backwards [81]. From simulation results, the path curvature does depend on the flagellar shape, which may be slightly different when the swimming direction is reversed, and on separation distance but whether this can adequately explain the significant differences in motion observed remains to be addressed.

Since the radius of curvature of the paths of boundary accumulating bacteria depends on cell and flagellar geometry, it may be possible to estimate the size and shape of the bacterium from analysing its tracks. Alternatively, the bacteria may be sorted and separated according to the curvature of the paths that naturally arise when swimming close to a surface. This was the inspiration behind the technique

demonstrated by Hulme et al. [68], who used curved, branching channels to divert bacteria according to the path curvature that each cell could follow. Short cells were isolated from a varied population by passing through a succession of sorting junctions.

Between infinite, parallel walls, three types of long term behaviour are predicted by our model. The first is circular orbiting close to one of the walls, which is the same as boundary accumulation in a half space. This mode is observed when the gap between the walls is large. When the gap is sufficiently small, perhaps one or two body lengths, the trajectory becomes a straight line parallel to and midway between the walls. This change in behaviour has important consequences in both natural and artifical applications since circular swimming does not allow the bacterium to explore much space while straight trajectories take the bacterium to new locations. Bacteria may have a tendency to become trapped and accumulate on the walls of large chambers while passing directly through chambers of shallow depth, for example.

Furthermore, the predicted separation between the bacterium and the walls can be larger in the straight swimming case than in circular orbits. This suggests the somewhat counter-intuitive result that bacteria are less likely to adhere to a surface when they are between two closely separated plates than when the plates are further apart. If this is so, it may be possible to delay bacterial colonisation of tubes and channels such as catheters by dividing the structure into multiple parallel layers of thin channels or narrow tubes. However, once cells have started to attach, narrow passageways are likely to rapidly become blocked while larger channels would require a more substantial accumulation of matter. Details of the attachment process, experiments and simulations would be needed to explore this issue further.

A third type of motion is exhibited by boundary escaping bacteria, which oscillate gradually between the two walls while remaining nearly parallel to the walls. Because the swimmer spends little time in close proximity to either boundary, there is minimal curvature in the observed path compared with the circular paths of boundary

accumulating swimmers. Additionally, because of symmetry, any bending of the path due to proximity to one boundary is balanced by an opposite bending when the swimmer approaches the other wall. The projection of the trajectory onto a plane parallel to the plates, typical of observations under a microscope, would be a zigzag. We found no evidence of qualitative changes as the plate separation is varied. Because boundary escaping bacteria do not become trapped in circular orbits, they are better able to explore their environment compared with boundary accumulators.

We briefly refer to the result found by Ramia et al. [107] that a bacterial swimmer midway between two closely separated parallel plates has a slightly higher swimming speed compared with the free space case at the same motor rotation frequency. Maintaining the same rotation rate close to no-slip boundaries requires higher torque and power. It was therefore noted that the motor frequency, and hence swimming speed of the bacterium, may be lower in a thin gap between parallel plates than in unbounded fluid. However, evidence indicates that for free space swimming, the motors of some bacteria operate in the sloping regime of the motor torque–frequency curve [84], which was discussed in §1.2.1. This means that a heavier torque load may be met with little loss in the motor frequency. As a result, it may be possible that the swimming speed in narrow channels is as high or even higher than the speed in unbounded fluid.

In chapter 3, we found that the torque and power optimal geometries for swimming are not significantly affected by the presence of a plane boundary. This means that good free space swimmers are also able to swim well near surfaces. However, there is an important distinction between the torque optimum and the power optimum. Torque efficiency favours high cell body aspect ratios and short flagella, both of which tend to encourage boundary escape. As shown in Fig. 4.7 for the case of optimisation over the cell body aspect ratio and the flagellar length, the torque optimal bacterium escapes from surfaces while the power optimum swims in stable

orbits near surfaces. Interestingly, as noted in the discussion section of chapter 3, both power and torque optima had slightly lower numbers of helical turns and flagellar lengths, and slightly more elongated cell bodies near a surface than in unbounded fluid. These characteristics increase the stable separation height, potentially inducing surface escape. This illustrates the complexity of the problem of design; there is potentially a conflict between optimising some relevant measure of efficiency and achieving a required asymptotic behaviour near boundaries.

4.6 Summary

Ramia et al. [107] began BEM studies of the hydrodynamic effects of boundaries by considering motion of flagellated swimmers in a half space and between two parallel plates. However, simulations were limited to a single swimmer geometry using a spherical cell body and the analysis of swimming between parallel plates considered only the case of a swimmer positioned midway and parallel to the plates. We have greatly extended the analysis of boundary effects on swimmers by systematically varying the geometry of the model organism and using phase plane techniques to assess the behaviour of swimmers starting from a general position near a plane boundary or between parallel plates.

It was found that model swimmers can exhibit different types of interactions with surfaces depending on the precise shape of the cell body and flagellum. One class of swimmers is hydrodynamically attracted towards plane boundaries from great distances but repelled when the separation is too small. This gives them a preferred separation distance from walls, which was found to be of the order of the cell body length. When swimming at this steady distance, the bacterium follows a circular orbit. The accumulation of bacteria near surfaces and circular trajectories of these swimmers are commonly observed in experiments [51, 13].

However, a feature for which no conclusive experimental evidence has been found

is that under some circumstances, the model swimmers have a tendency to avoid boundaries. While the attraction of bacteria to surfaces is widely known and can be explained hydrodynamically by considering the force-dipolar far field of a "pusher" model swimmer (see e.g. Berke et al. [13]), the possibility of a systematic repulsion from walls has not previously been reported. This occurrence depends on morphology and is predicted to be more likely for bacteria with elongated cell bodies and short flagella. These characteristics can easily be induced for experimental verification, for example by shearing the flagellar filaments, which grow back gradually and would allow the dependence of boundary accumulation on flagellar length to be tracked.

The final group of swimmers, those that were neither deflected away from surfaces nor attracted to stable circular trajectories, descended into the wall irrespective of starting conditions such that close-range interactions must be taken into account. The subsequent dynamics are beyond the scope of our model and so we will not consider this class of swimmers in further chapters of this thesis.

It should be noted that this categorisation of boundary behaviour describes only the long-term, asymptotic state of the swimmers. A separate issue, which we examined in chapter 3, is the swimming speed or efficiency. A swimmer should only be considered a boundary accumulator if it approaches surfaces on a reasonable timescale, which will not happen if the swimming speed is very low. Depending on the factors limiting the speed of a bacterium, there may be a conflict between maximising the swimming speed and achieving a desired surface behaviour.

The type of motion that arises for a bacterium near a plane boundary also determines how the bacterium will swim in other confined environments. Boundary accumulating swimmers continue to swim in circular paths near a wall when a second, parallel wall is introduced but when the two walls are close together, the bacterium swims in straight trajectories midway between the plates. Boundary escaping bacteria will tend to "bounce" between the two plates irrespective of the separation gap and

the trajectories, viewed from above the plates, will appear as zigzags. In the following chapter, we will explore the types of behaviour that arise in another fluid geometry, the channel.

Chapter 5

Swimming in channels

To model swimming in simplified microfluidic devices, we look at rectangular channels as the geometry of the fluid environment. In this case, it is necessary to discretise the four walls of the channel and we require two position coordinates and two orientation angles to identify a given configuration of the axisymmetric swimmer within the channel. We choose the channel to be aligned with the x-axis and assume that the bacterium is facing the $-x$ direction, i.e. the major axis body vector, which points backwards, has x-component $e_{1x}^{\mathrm{B}} > 0$. Up to channel symmetry, the configuration is then specified by y^{B}, z^{B}, e_{1y}^{B} and e_{1z}^{B}. We rename these variables y, z, η and ζ respectively to shorten notation when referring to channel geometry configurations. The techniques we use to analyse channel dynamics are similar to those in the single and parallel plane cases of §4 except that it is now a four-dimensional ODE system of the form

$$\left.\begin{aligned} \dot{y}(t) &= f_y(y(t), z(t), \eta(t), \zeta(t)), \\ \dot{z}(t) &= f_z(y(t), z(t), \eta(t), \zeta(t)), \\ \dot{\eta}(t) &= f_\eta(y(t), z(t), \eta(t), \zeta(t)), \\ \dot{\zeta}(t) &= f_\zeta(y(t), z(t), \eta(t), \zeta(t)), \end{aligned}\right\} \tag{5.1}$$

where we again use phase-averaged dynamics, f_y, f_z, f_η and f_ζ, to approximate the long-timescale behaviour and remove dependence on the tail phase.

In this chapter we consider a prism of fluid bounded by walls at $y = \pm\frac{1}{2}H_y$

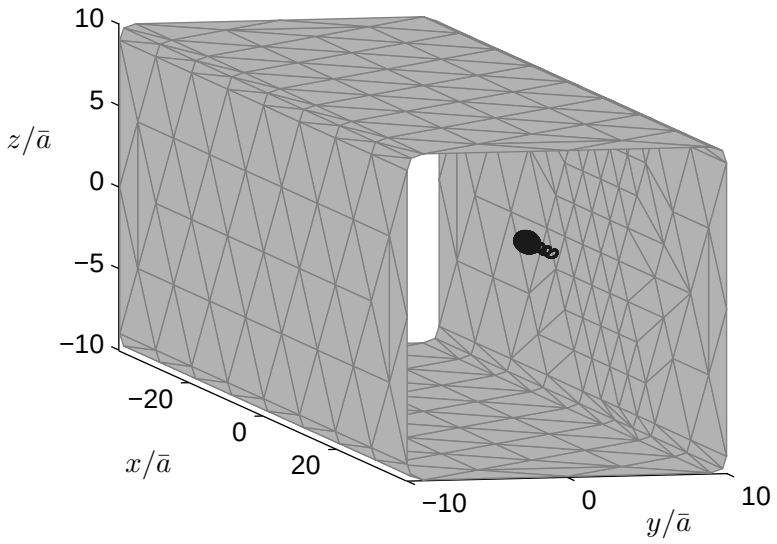

Figure 5.1: Visualisation of the mesh used for the BEM hydrodynamic model of bacterial swimming in a square channel. Because the far field of a force-free swimmer decays with the square of the distance relative to the size of the swimmer, accurate results can be obtained using a channel mesh extending only a few body lengths behind and ahead of the swimmer.

and $z = \pm\frac{1}{2}H_z$. The channel walls are discretised and meshed for the section in the vicinity of the swimmer. The x-extent of the meshed section covers 2–3 times the combined body and flagellum length ahead of and behind the swimmer, i.e., $|x - x^{\mathrm{B}}| \leq \frac{1}{2}L_x \approx 30\,\bar{a}$. This was shown to be a sufficient mesh to approximate the infinitely long channel (see appendix B). Additionally, the edges of the channels are rounded to maintain a continuously varying normal vector. This avoids singular solutions of the traction distribution, which may reduce accuracy of the numerical solution. An example of the mesh is shown in Fig. 5.1. Since the velocities are independent of the position along the axis of the channel, x, we will often view the projection of the trajectories in the y–z cross-sectional plane. In this view, the channel walls appear as "edges" and meet at "corners". To avoid confusion, we will only use the term "edge" to describe the region where two walls intersect even in the cross-sectional view.

First consider channels that are large compared with the volumetric radius of the cell body, $\bar{a}$, i.e. $H_y \gg \bar{a}$ and $H_z \gg \bar{a}$. We break down the behaviour by separately

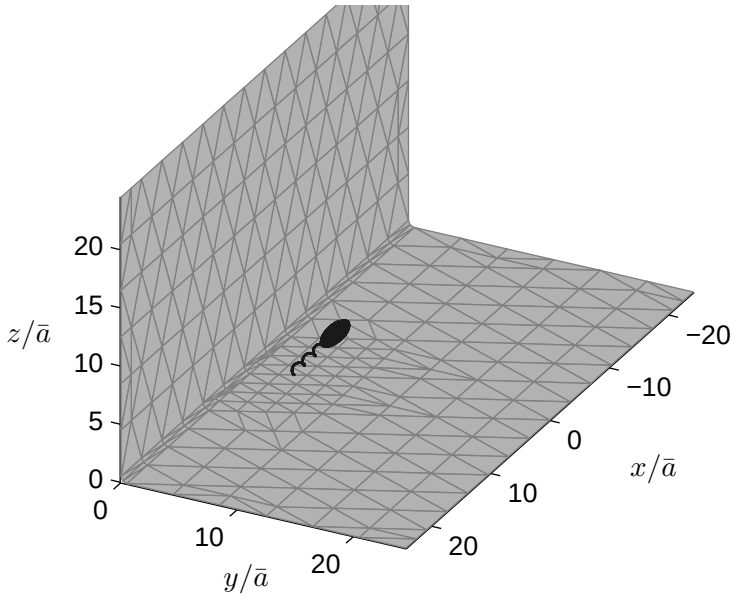

Figure 5.2: Visualisation of the mesh used for the BEM hydrodynamic model of bacterial swimming near an edge of an infinitely large square channel. Only the part of the channel within $25\,\bar{a}$ of the edge and within about $20\,\bar{a}$ behind and ahead of the bacterium is meshed.

considering different parts of the channel cross-section. Near the centre of the channel, wall effects are small so we expect trajectories to be straight. Close to a wall but far from the edges where two walls meet, the behaviour can be reduced to half space dynamics. This means that the bacterium is either deflected away from the wall or approaches and swims in a circular orbit. In the latter scenario, the circular trajectory may bring the swimmer close to the other channel walls depending on the starting conditions and the radius of curvature of the half space orbit compared with the channel width.

This presents a new situation in which the swimmer is at an edge, with two mutually perpendicular walls nearby. This is the scenario we must now numerically examine. We do this for one model bacterium that is known to escape from plane boundaries and for one that accumulates, using a channel-like domain mesh with only two walls, as illustrated in Fig. 5.2. We will subsequently investigate channels of finite width and height with all four walls in the vicinity of the swimmer, using the insight gained from the isolated edge geometry to aid in understanding the dynamics.

The two model swimmers we will use both have a cell body aspect ratio of 3. The boundary escaping bacterium has a flagellum completing two helical turns with a length $L/\bar{a} = 5$, while the flagellum of the boundary accumulating bacterium has length $L/\bar{a} = 7.5$ and completes about three helical turns. The preferred swimming height of the boundary accumulating swimmer near a plane surface is $h^*/\bar{a} = 1.27$, calculated using the techniques described in §4.

5.1 Methods for approximate trajectory analysis

5.1.1 Edges of large channels

We restrict our interest to the region within a distance of $15\,\bar{a}$, corresponding to about $10\,\mu$m for a bacterium comparable in size to *R. sphaeroides*, from both walls and compute the motor phase-averaged velocities (discussed in §3.5) on a sample of points in (y, z, η, ζ) phase space. Without loss of generality, we consider dynamics near the edge with $y = -\frac{1}{2}H_y$ and $z = -\frac{1}{2}H_z$. A coordinate system centred on the edge is more natural for this analysis so we introduce the variables $\bar{y} := y + \frac{1}{2}H_y$ and $\bar{z} := z + \frac{1}{2}H_z$.

Regular rectangular grids are highly unsuitable because velocities vary rapidly only in the vicinity of a wall and only with changes in position and orientation relative to this wall. In order to capture the interesting dynamics without excessive evaluations of the velocities, the phase space is subdivided into four regions by proximity to each wall using the following parameter bounds:

Region 1 $0.9 \le \bar{y} \le 2$, $0.9 \le \bar{z} \le 2$, $-0.1 \le \eta \le 0.06$, $-0.1 \le \zeta \le 0.06$

Region 2 $0.9 \le \bar{y} \le 2$, $2 \le \bar{z} \le 14$, $-0.1 \le \eta \le 0.06$, $-0.6 \le \zeta \le 0.6$

Region 3 $2 \le \bar{y} \le 14$, $0.9 \le \bar{z} \le 2$, $-0.6 \le \eta \le 0.6$, $-0.1 \le \zeta \le 0.06$

Region 4 $2 \le \bar{y} \le 14$, $2 \le \bar{z} \le 14$, $-0.6 \le \eta \le 0.6$, $-0.6 \le \zeta \le 0.6$

The spatial division of the channel into these regions is illustrated in Fig. 5.3. The bounds on the cell orientation in each region were chosen to reflect the observation that a bacterium pointing sharply towards a wall is unable to deflect away without collision. Similarly, the hydrodynamic effect of a wall is not strong enough to prevent a bacterium from swimming out of the region of interest if it is initially pointing sharply away from the wall. Furthermore, bearing in mind that the quantities $\bar{y}$ and $\bar{z}$ refer to the position of the cell body–flagellum junction and not to the point on the bacterium closest to the wall, large inclination angles would cause the cell body or flagellum to intersect the wall. Therefore, it is unnecessary to consider large angles of orientation towards or away from the walls.

Between 7 and 10 values of each parameter are chosen in each of the parameter ranges given above to sample the dynamics in each region. By interpolating between phase space evaluation points, we are able to efficiently approximate the ODE system (5.1). This is used to simulate a large number of trajectories starting from initial conditions generated in the following manner. For each region, we choose one of the region boundaries; top, bottom, left or right, as seen in the $\bar{y}$–$\bar{z}$ plane. An initial condition is set by generating a random point along this boundary and a random orientation. The variables η, ζ and the single randomly determined spatial variable are drawn from uniform distributions over the relevant parameter ranges.

We will use 100 random initial conditions on each region boundary and compute the trajectories up to a maximum time of $500\,\bar{t}$, where the timescale $\bar{t} = 16\pi^2\bar{a}^3\mu/\tau^{\mathrm{M}}$ is as discussed in §4.3. Trajectories might terminate before the prescribed end time if:

1. the trajectory approaches the imposed bounds of the parameter range for its region, or

2. interpolation is not possible due to absence of data.

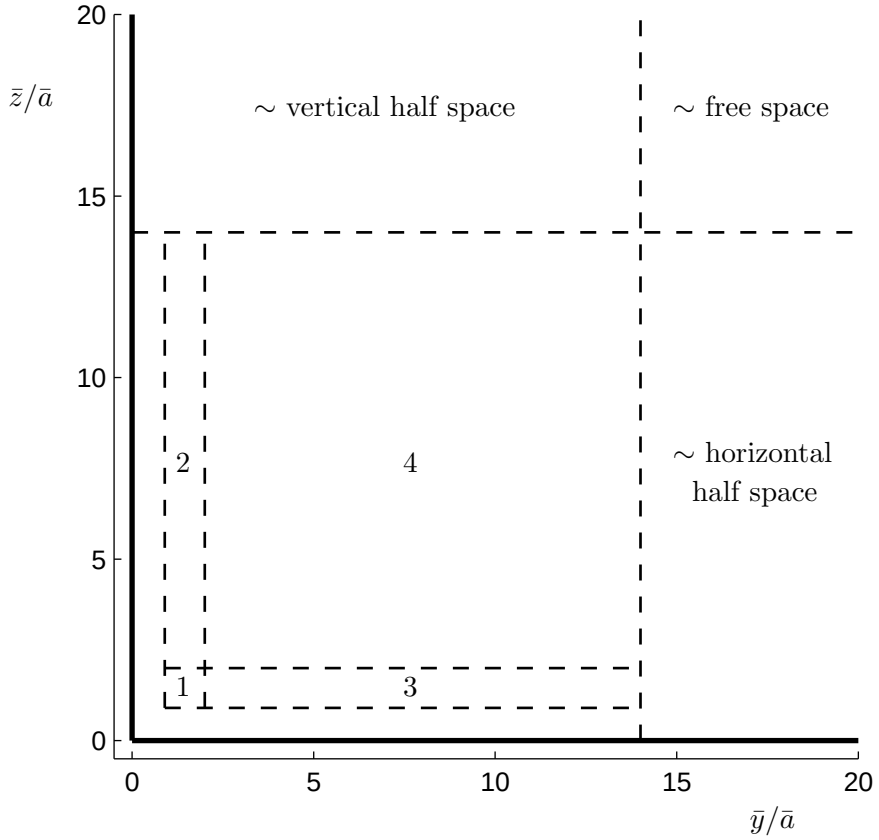

Figure 5.3: The breakdown of the channel by proximity to walls. This diagram concerns the space near the $\bar{y} = \bar{z} = 0$ edge of a channel of large cross-sectional extent. The vertical and horizontal walls at this edge are shown in thick, solid lines. Dashed lines indicate the division of the fluid space into Regions 1–4 and other regions that we do not explicitly analyse. The dynamics in the marked half space and free space regions can be inferred from previous work. The space between the walls and the enumerated regions is largely excluded because the finite volume occupied by the cell intersects or closely approaches the walls when the tracked junction position, $\mathbf{x}^{\mathrm{B}}$, is in this region.

The first situation indicates that either the swimmer has moved into a different region of the channel or the orientation angle has become too large, which we assume will lead to the bacterium exiting the current region in the direction it has turned to.

The second situation occurs because some combinations of the phase space variables correspond to configurations that intersect or come close to intersecting the channel walls. Interpolation is only possible if there are sufficient valid grid points surrounding the desired point. Given a fine enough grid, this will only be a problem when the trajectory approaches too closely to a wall and we therefore treat these events as collisions. In practice, with the grids that have been chosen, trajectories sometimes terminate at separation distances of about $0.3\,\bar{a}$. This is about half of the semi-minor axis of the cell body and is closer to the wall than typical boundary accumulating orbits. Nevertheless, trajectories that would only transiently reach this proximity may incorrectly be identified as a collision because of this grid effect.

We take note of how and where each trajectory terminates in order to infer the general or most likely behaviour of a swimmer in each of the separate regions. A trajectory is deemed to have exited on the left of a given region if:

1. it approached the lower bound of the $\bar{y}$ range for the region, the natural definition for leaving a bounded region, or

2. it collided with the left channel wall before reaching the lower bound of the $\bar{y}$ range, which is possible because of the orientation-dependent, finite y-extent of the swimmer, or

3. it approached the upper bound of the η range. This condition indicates that the swimmer is turning to strongly face the left wall ($\eta \equiv e_{1y}^{\mathrm{B}}$ increasing) and we assume that this will eventually lead to condition (1) or (2) above.

Corresponding conditions are used to determine instances of exiting through the top, bottom and right of the regions.

Conclusions based on the likelihood of each destination are only qualitative and should be drawn with care since the exact distribution of outcomes depends on the parameter ranges used and how the starting states are chosen, among other factors.

5.1.2 Channels of finite cross-section

Trajectories in channels of finite width and height are computed using the interpolation method with similar grids to those employed to analyse edge dynamics. The channel is subdivided into regions based on proximity to the walls and a suitably refined phase space grid is used for each region. By combining the grids from all regions, we can continue to simulate trajectories that pass from one region to another.

Initial conditions are drawn from a uniform random distribution in all four variables, $\bar{y}$, $\bar{z}$, η and ζ. Trajectories are computed up to a maximum time of $500\,\bar{t}$. To obtain a representative range of possible behaviour, we compute 200 such trajectories for each set of model parameters. Due to the symmetry of the channel geometry, it is not interesting to note which wall each trajectory collides with. Instead, we will analyse the distribution of trajectory durations. The effect of collisions is beyond the scope of the current model but may be as subtle as realigning the bacterium with the channel or as significant as trapping the cell in place, depending on electrostatic and biochemical interactions with the substrate. By investigating the frequency of close contact, we can determine how important the details of near-surface interactions might be.

It is possible that trajectories never collide with the channel walls, instead remaining in the interior. If stable steady states or periodic orbits exist, these would be evident upon examining the projections of trajectories in the cross-section of the channel. However, although we view the dynamics in this two-dimensional projection, the swimmer has a further two rotational degrees of freedom. Hence, it is not necessary for fixed points or periodic orbits to exist even if trajectories never

approach the bounding walls.

5.2 Simulated trajectories in channels

5.2.1 Trajectories in edges of large channels

The outcomes of simulated trajectories for a boundary accumulating cell are presented in tables 5.1–5.4. Wall effects are expected to be relatively weak in Region 4 so it is unsurprising that trajectories from the bulk fluid above and on the right pass through to the other region boundaries. There was one track that entered through the top and subsequently exited through the top, suggesting a strong deflection within this region. However, this can be explained by the fact that this particular trajectory curved upwards as it approached the left hand wall. The attraction close to walls can be inferred by observing that no trajectories entering from the bottom or left were found to exit through the respective opposite side of Region 4.

In Region 1, which is the region closest to both walls, there is a strong tendency for trajectories to exit through the right or through the bottom. In this region, the latter corresponds to collisions with the horizontal boundary. Hence, we infer that there is a strong attraction to the lower wall. However, collisions rarely occur for trajectories entering from Region 3 on the right; instead these trajectories are deflected back into Region 3, as are nearly all other non-colliding trajectories.

In Region 2, along the vertical wall, trajectories overwhelmingly leave through either the top or the bottom. This is consistent with the behaviour expected near a half space, neglecting the horizontal channel wall. Bacteria are attracted to the vertical wall, and hence do not often escape through the right hand boundary. Due to the chirality of the model swimmers, we expect the bacteria to swim in arcs in the right-handed sense about the normal vector of the wall pointing into the channel. This would lead to a strong bias for trajectories to exit through the top of Region 2 compared with the bottom. Indeed, the simulations showed this to be the case

(table 5.2), with the exception of trajectories originating from Region 1 below. These swimmers were influenced by the horizontal channel wall and had a high probability of being pulled back down, as discussed above.

Region 3 produced the most distinctive behaviour compared with known half space and free space dynamics. As expected, there was a strong attraction to the horizontal wall, indicated by the fact that very few of the simulated trajectories escaped through the top of this region. Consistently with the dynamics predicted in a half space neglecting the vertical wall, the majority of swimmers curved counter-clockwise, exiting to the left. It should be noted that, although it appears from table 5.3 that most trajectories entering at the left curve back and return, almost all of these are actually instances of the flagellum colliding with the left wall as the bacterium turns to the right, away from the wall. In any case, a significant proportion of trajectories from all origins lead left towards the edge region. However, we have already established that cells at the edge tend to swim to the right. This suggests the possibility of oscillatory motion between Region 1 and Region 3.

In fact, these observations are consistent with a unique feature of Region 3: trajectories can remain confined to this region over long timescales. It was possible to compute trajectories, starting from any of the boundaries of Region 3, up to the specified end time of $500\,\bar{t}$, which is more than 50 times longer than the longest track produced in Region 2, for comparison.

Examining the trajectories that endured until the end time, we found that these swimmers had become trapped in a stable periodic orbit oscillating in the y-direction but with a nearly constant vertical position comparable to the half space boundary accumulation height, as illustrated in Fig. 5.4. These oscillations brought the trajectories close to the border with Region 1, which is consistent with both the tendency for trajectories to leave Region 3 on the left and the apparent deflection in Region 1 of trajectories from the right back towards the right.

Table 5.1: Origin and destination distributions of trajectories in Region 1 of channel edges, where boundaries correspond to the following: Left – vertical wall; Bottom – horizontal wall; Right – Region 3; Top – Region 2. Interior – remains in Region 1.

Origin \ Destination	Left	Bottom	Right	Top	Interior
Left	19	55	22	4	0
Bottom	6	70	24	0	0
Right	0	3	97	0	0
Top	3	69	28	0	0
Total	28	197	171	4	0

Table 5.2: Origin and destination distributions of trajectories in Region 2 of channel edges, where boundaries correspond to the following: Left – vertical wall; Bottom – Region 1; Right – Region 4; Top – vertical half space. Interior – remains in Region 2.

Origin \ Destination	Left	Bottom	Right	Top	Interior
Left	1	20	0	79	0
Bottom	6	87	7	0	0
Right	0	34	6	60	0
Top	12	40	0	48	0
Total	19	181	13	187	0

Table 5.3: Origin and destination distributions of trajectories in Region 3 of channel edges, where boundaries correspond to the following: Left – Region 1; Bottom – horizontal wall; Right – horizontal half space; Top – Region 4. Interior – remains in Region 3.

Origin \ Destination	Left	Bottom	Right	Top	Interior
Left	90	4	0	0	6
Bottom	57	3	19	0	21
Right	88	6	0	1	5
Top	43	0	29	0	28
Total	278	13	48	1	60

Table 5.4: Origin and destination distributions of trajectories in Region 4 of channel edges, where boundaries correspond to the following: Left – Region 2; Bottom – Region 3; Right – horizontal half space; Top – vertical half space. Interior – remains in Region 4.

Origin \ Destination	Left	Bottom	Right	Top	Interior
Left	30	36	0	34	0
Bottom	26	44	30	0	0
Right	26	44	0	30	0
Top	40	22	37	1	0
Total	122	146	67	65	0

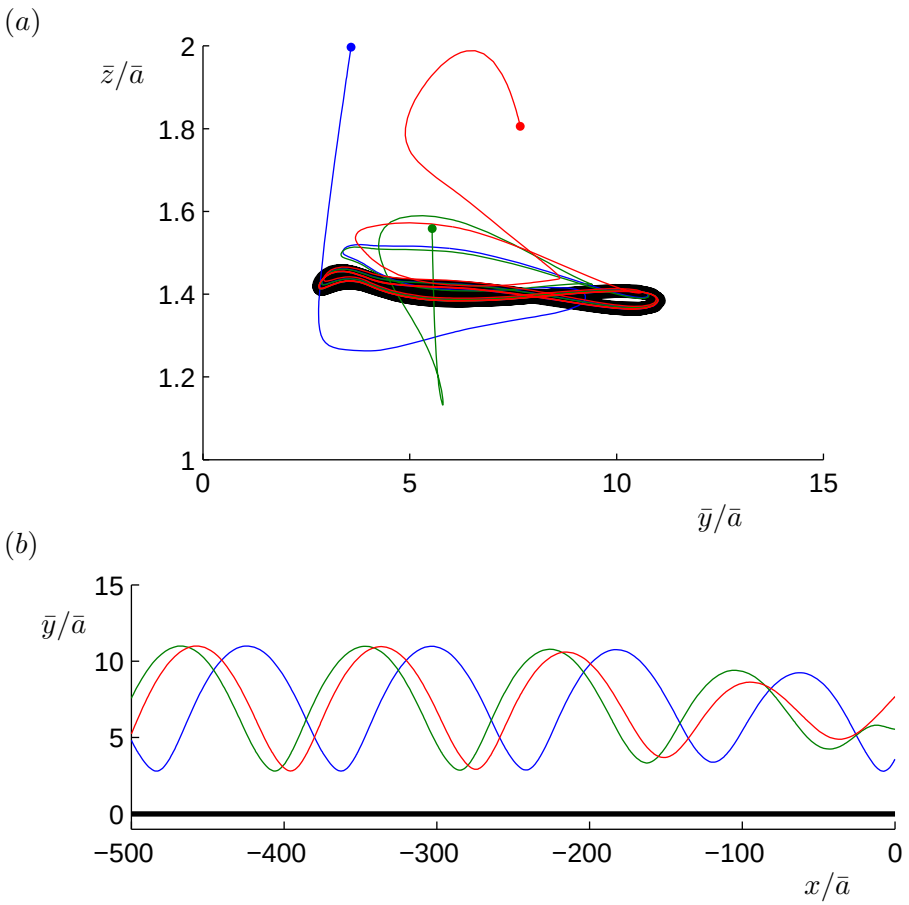

Figure 5.4: Three channel trajectories relaxing to an edge accumulating periodic orbit in (a) the cross-sectional view and (b) the top–down view, with starting points indicated by dots in (a). Only two of the channel walls were meshed, as described in §5.1.1, with the horizontal wall at height $\bar{z}/\bar{a} = 0$ and the vertical wall being the plane $\bar{y}/\bar{a} = 0$, indicated by a straight black line in (b). In both (a) and (b), the vertical scale is 10 times as fine as the horizontal scale to allow the structure of the orbit to be more clearly seen. The thick, black curve in (a) marks the periodic orbit, which is nearly constant in $\bar{z}$, reached by all three shown trajectories.

This periodic orbit was the only mode of behaviour found to persist in the vicinity of channel edges over such long timescales and we refer to this as edge accumulation. The asymmetry between the y- and z-directions is due to the chirality and rotation of the helical flagellum. Inverting the handedness of the flagellum and reversing the motor direction would result in the mirror image of the observed behaviour, i.e. vertical oscillations along the x–z wall.

5.2.2 Long-term behaviour in fully enclosed channels

We now return to the problem of swimming through channels bounded on all four sides. By combining knowledge from free space, half space, parallel plane and edge geometries, we can predict some possible long-timescale trajectories in channels:

1. straight down the axis of the channel, if the walls are sufficiently close together;
2. "bouncing" from wall to wall, if the swimmer is strongly deflected away from plane boundaries;
3. edge accumulation, if the swimmer is attracted to plane boundaries and the channel is large enough that behaviour is similar to the edge geometry case analysed above;
4. spiralling, or traversing each wall obliquely and switching to the next wall as an edge is encountered.

The first type of motion is the analogue of a half space boundary accumulating swimmer on a stable, straight path midway between two parallel plates. This is straightforward to investigate since it requires the central position aligned with the

channel to be a stable fixed point in the channel phase space. That is, we require

$$\left.\begin{aligned} f_y(y=0,z=0,\eta=0,\zeta=0)&=0,\\ f_z(y=0,z=0,\eta=0,\zeta=0)&=0,\\ f_\eta(y=0,z=0,\eta=0,\zeta=0)&=0,\\ f_\zeta(y=0,z=0,\eta=0,\zeta=0)&=0, \end{aligned}\right\} \tag{5.2}$$

and all of the eigenvalues of the Jacobian matrix to have negative real parts, where the Jacobian matrix is given by

$$\mathbf{J}^{\text{chan}} = \begin{bmatrix} \frac{\partial f_y}{\partial y} & \frac{\partial f_y}{\partial z} & \frac{\partial f_y}{\partial \eta} & \frac{\partial f_y}{\partial \zeta} \\ \frac{\partial f_z}{\partial y} & \frac{\partial f_z}{\partial z} & \frac{\partial f_z}{\partial \eta} & \frac{\partial f_z}{\partial \zeta} \\ \frac{\partial f_\eta}{\partial y} & \frac{\partial f_\eta}{\partial z} & \frac{\partial f_\eta}{\partial \eta} & \frac{\partial f_\eta}{\partial \zeta} \\ \frac{\partial f_\zeta}{\partial y} & \frac{\partial f_\zeta}{\partial z} & \frac{\partial f_\zeta}{\partial \eta} & \frac{\partial f_\zeta}{\partial \zeta} \end{bmatrix}. \tag{5.3}$$

The conditions (5.2) are satisfied due to the symmetry of the channel and model bacterium after phase-averaging. The partial derivatives can be estimated using finite difference formulas and the eigenvalues of $\mathbf{J}^{\text{chan}}$ found using the MATLAB function, `eigs`. This was performed for different bacterial shapes and different channel sizes but there was always at least one eigenvalue with positive real part and hence no examples were found to possess a stable central configuration (Fig. 5.5).

To observe the other predicted types of behaviour requires simulation of the ODE system over long timescales. Initial conditions were randomly generated and trajectories were computed using the interpolation techniques employed in the channel edge geometry. A variety of bacterial shapes and channel sizes were tested, continuing trajectories as long as necessary for long-term behaviour to be determined. A small selection of trajectories were compared with solutions of the full system.

We present the results beginning with a channel of square cross-section containing a half space boundary escaping bacterium. After transience, potentially periodic orbits could be identified by inspection. In appendix C we describe methods for verifying periodicity and for identifying distinct orbits from different trajectories.

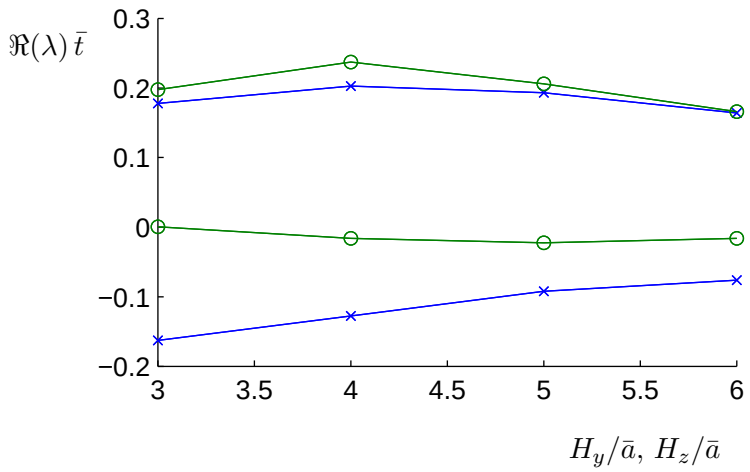

Figure 5.5: Real parts of the eigenvalues, λ, of the Jacobian matrix $\mathbf{J}^{\text{chan}}$ evaluated in the parallel, central position of a square channel as the width of the channel is varied. The eigenvalues are scaled by the rate $\bar{t}^{-1}$. In each case, two pairs of complex conjugate eigenvalues were found. The distinct real parts are plotted and marked with crosses for a boundary accumulator and with open circles for a boundary escaper. Since at least one pair of complex eigenvalues has positive real part, there is no evidence of stability of the central position within the parameter range tested.

Projections of these periodic orbits, as well as plots showing examples of evolution in the transient phase, are given in Fig. 5.6. Viewed in the channel cross-section, these orbits are approximately square with a slight rotational offset with respect to the channel walls. The orbits can be described as collections of relatively straight paths between adjacent channel walls, punctuated by abrupt deflections as each wall is encountered. This exemplifies the "bouncing" behaviour predicted for bacteria that are hydrodynamically repelled from surfaces. To validate the interpolation approximation, we compute a trajectory using both the approximate and the full method for the same starting conditions and find good agreement (Fig. 5.7).

There is some variation in the shape and symmetry of the stable orbit as we change the size of the channel. For square channels of width $20\,\bar{a}$ (Fig. 5.6), two distinct orbits can be obtained, both of order four rotational symmetry. When the channel width is increased to $30\,\bar{a}$ (Fig. 5.8), the orbits are reduced to rotational symmetry of order two. Furthermore, up to symmetry, only one periodic orbit could be found in this larger channel. Some channels of rectangular cross-section also give rise to a single periodic orbit of order two symmetry (Fig. 5.9). Intermediate channel sizes and aspect ratios have not been studied so a more detailed description of these symmetry breaking bifurcations cannot be given at present. It is interesting to note that in all periodic "bouncing" orbits, the bacterium progress around the channel in a counter-clockwise, or left-handed, sense.

Varying the dimensions of the channel also had an effect on how quickly the periodic state was approached. The quickest convergence was found for channels around $20\,\bar{a}$ in width but this is likely to depend on bacterial shape. In some channels, periodic orbits may take an impractically long time to emerge, as can be inferred from the number of transient "bounces" and the time or distance travelled between such events in examples such as Fig. 5.8 and Fig. 5.9.

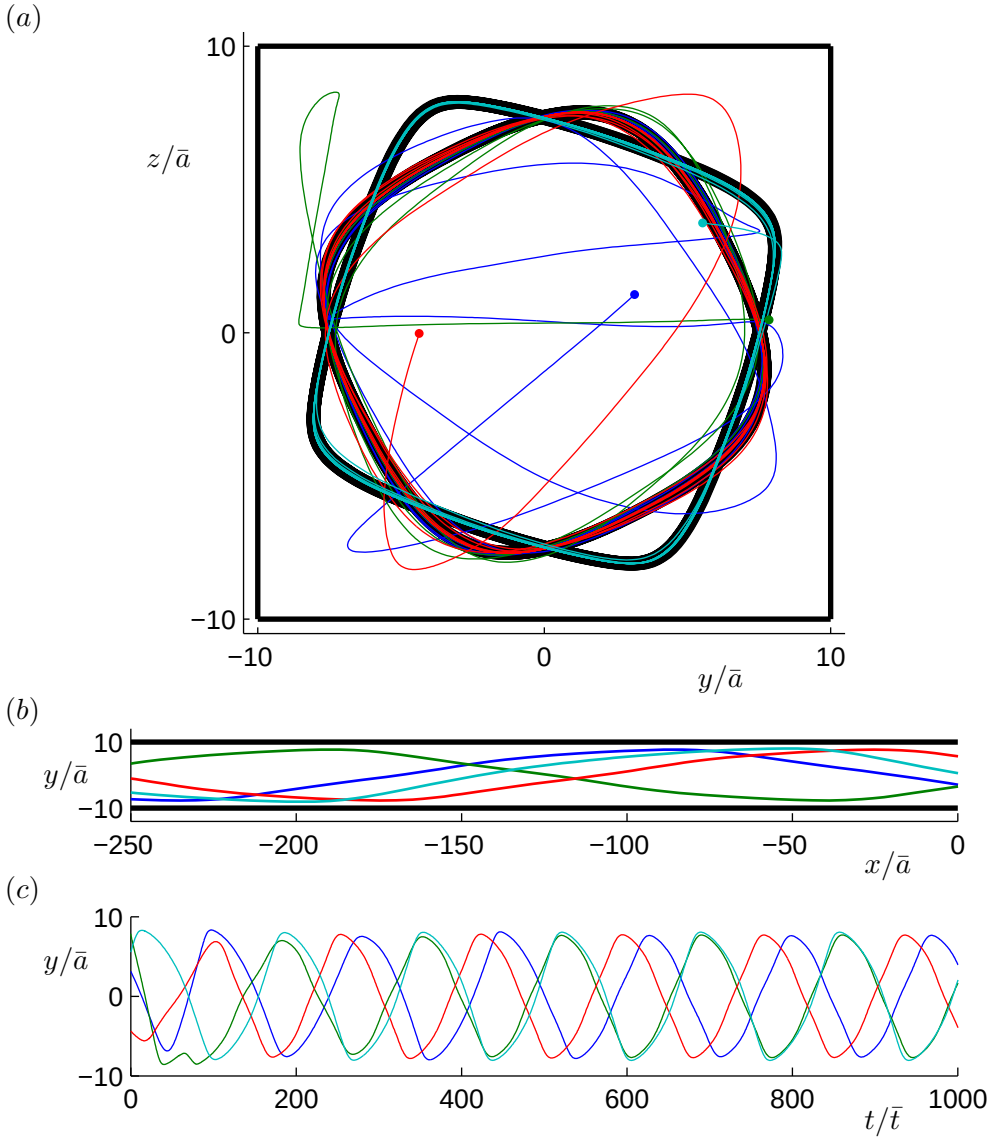

Figure 5.6: Relaxation to periodic orbits for a boundary escaping bacterium in a square channel of width $20\,\bar{a}$. (*a*) Thick, black curves indicate two periodic orbits in the cross-sectional view, while four sample trajectories that converge to these two states are shown in thinner curves of different colours. The initial conditions of these four trajectories are marked by dots. (*b*) Top–down view of channel showing the computed tracks once the bacteria have relaxed to periodic orbits. (*c*) Time series of the transient phase of the same trajectories in (*a*) and (*b*). Note that only a small proportion of random initial conditions evolve to a periodic orbit without colliding into walls so these are not representative of generic trajectories. The extent of the channel is marked with straight, black lines in (*a*) and (*b*).

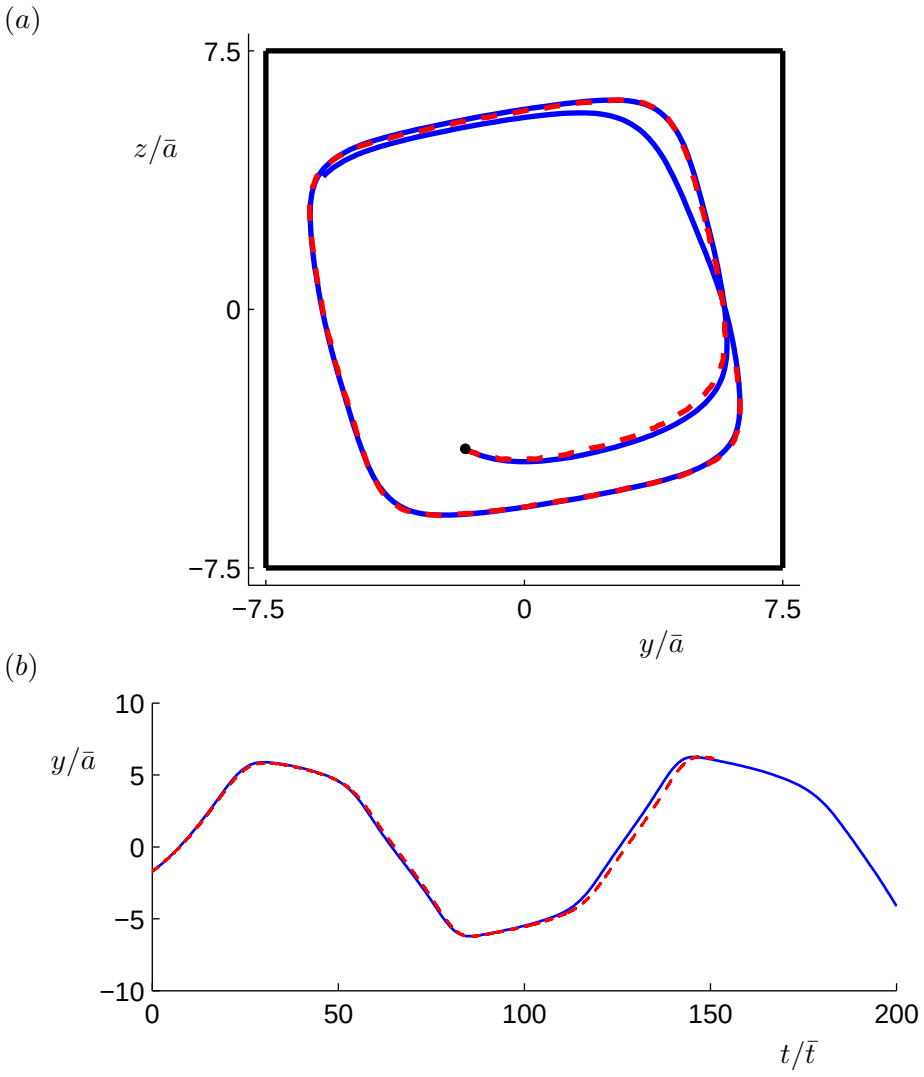

Figure 5.7: Comparison between approximate solution using the interpolation method (solid curves) and time stepping simulation of the full system (dashed curves) for a boundary escaping bacterium in a channel of size $H_y = H_z = 15\,\bar{a}$. (a) The cross-sectional view with the extent of the channel marked by straight, black lines and the starting point of the trajectory indicated by a dot. (b) The time series of the horizontal position, y.

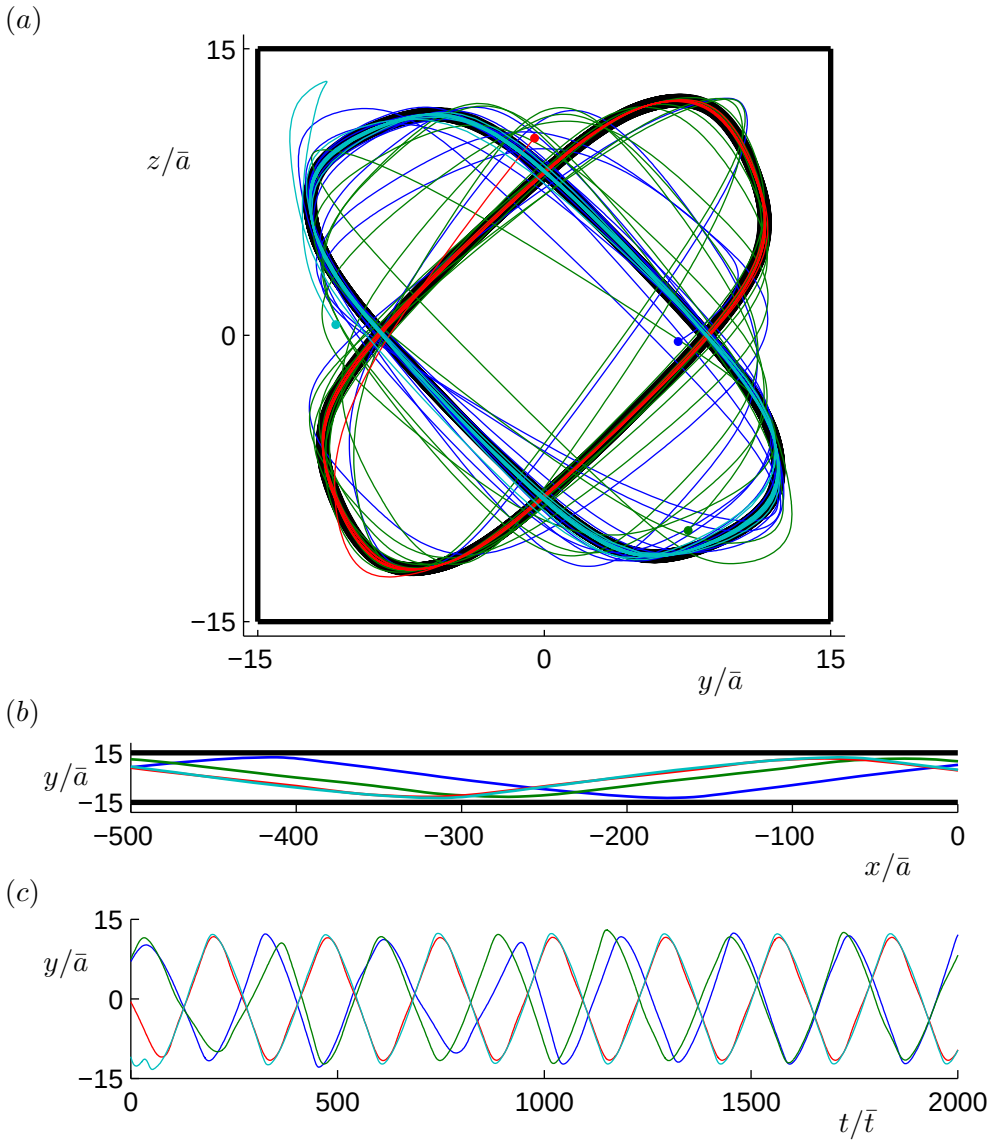

Figure 5.8: Relaxation to periodic orbits for a boundary escaping bacterium in a square channel of width $30\,\bar{a}$. (*a*) Thick, black curves indicate two periodic orbits in the cross-sectional view, while four sample trajectories that converge to these two states are shown in thinner curves of different colours. The initial conditions of these four trajectories are marked by dots. (*b*) Top–down view of channel showing the computed tracks once the bacteria have relaxed to periodic orbits. (*c*) Time series of the transient phase of the same trajectories in (*a*) and (*b*). The extent of the channel is marked with straight, black lines in (*a*) and (*b*).

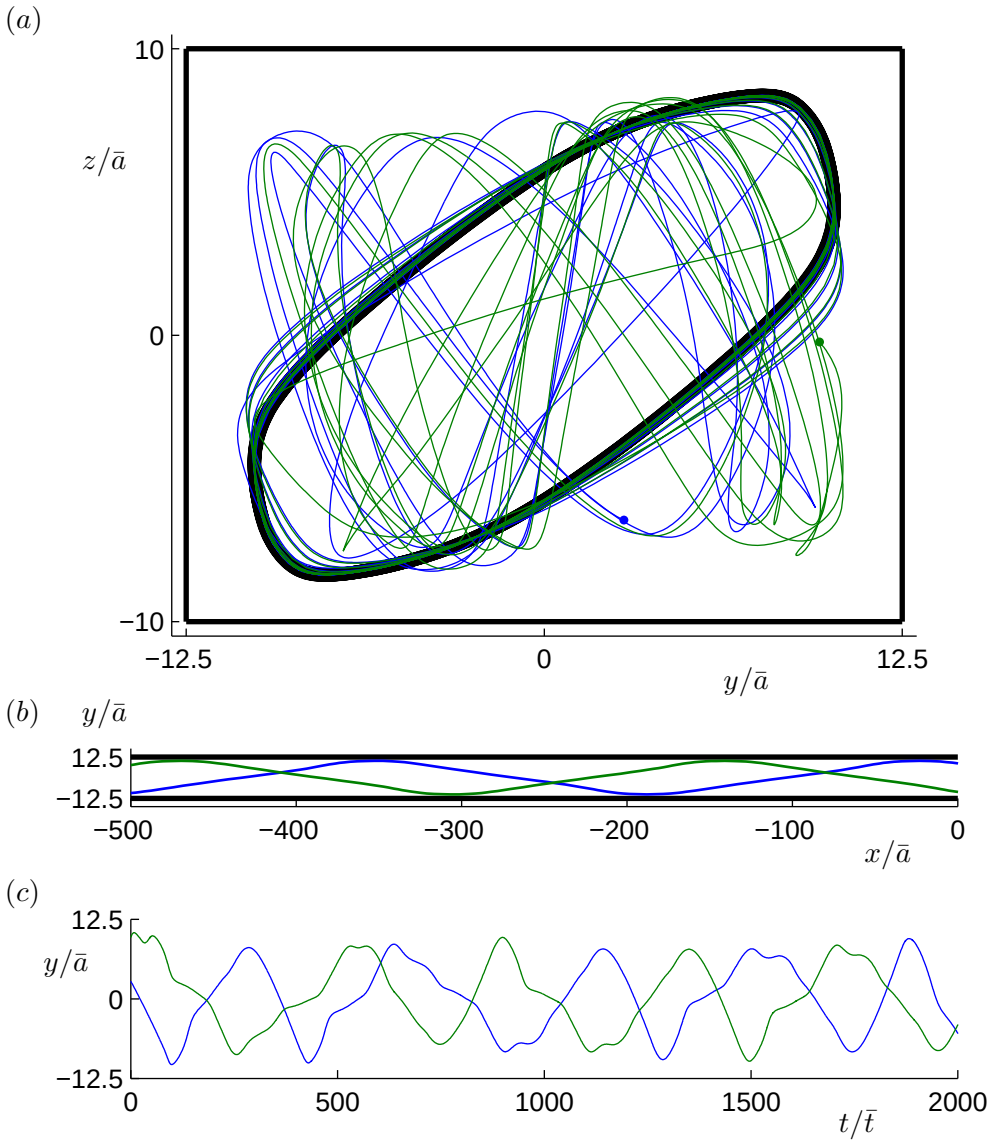

Figure 5.9: Relaxation to periodic orbits for a boundary escaping bacterium in a rectangular channel of size $H_y = 25\,\bar{a}$, $H_z = 20\,\bar{a}$. (*a*) A thick, black curve indicates the periodic orbit in the cross-sectional view, while two sample trajectories that converge to this state are shown in thin curves of different colours with the starting points marked by dots. (*b*) Top–down view of channel showing the computed tracks once the bacteria have relaxed to periodic orbits. (*c*) Time series of the transient phase of the trajectories in (*a*) and (*b*). The extent of the channel is marked with straight, black lines in (*a*) and (*b*).

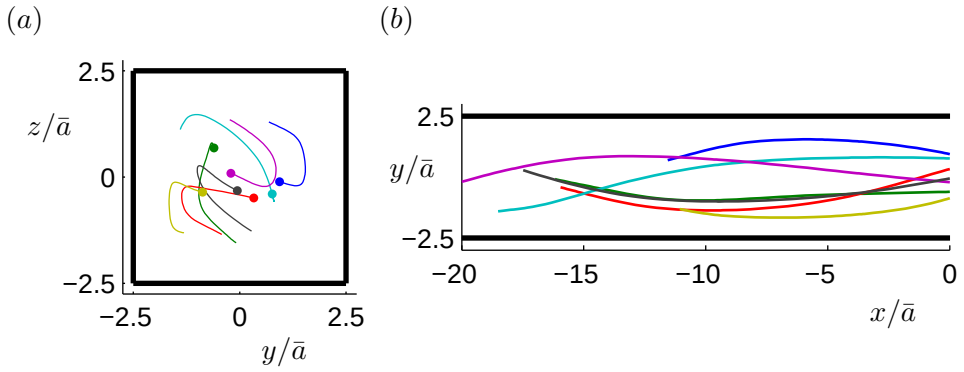

Figure 5.10: Sample trajectories for a boundary escaping bacterium in a square channel of width $5\,\bar{a}$ in (a) the cross-sectional view, and (b) the top–down view of channel. Collisions severely limit the extent of tracks. The extent of the channel is marked with straight, black lines.

In channels of small width, the swimmer quickly collided into the walls and no long-term behaviour was found, although the tendency to move in left handed spirals through the channel was still observable (Fig. 5.10). Of 200 trajectories simulated in a channel of width $5\,\bar{a}$, the longest track lasted until time $t = 24\,\bar{t}$ and spanned $34\,\bar{a}$ in the direction of the channel while the average track duration was under $6\,\bar{t}$.

We now discuss the behaviour of a model bacterium that exhibits boundary accumulation near a plane boundary. As argued previously, such a swimmer would migrate towards one of the channel walls and swim in approximately circular paths if the channel is large enough that the other walls may be neglected. We will not attempt to verify this behaviour, instead concentrating computational effort on the range of orientations $-0.6 \leq \eta, \zeta \leq 0.6$ to probe long-timescale travel along the axis of the channel, as was done in §5.1.1. A trajectory is illustrated in Fig. 5.11. Here we see the same edge accumulation behaviour that was described in §5.2.1. By symmetry, accumulation can occur near any of the four channel edges but always against the wall preceding the edge in the clockwise sense.

Edge accumulation is described by periodic oscillations towards and away from the edge but close to and approximately parallel to one of the walls. At the furthest

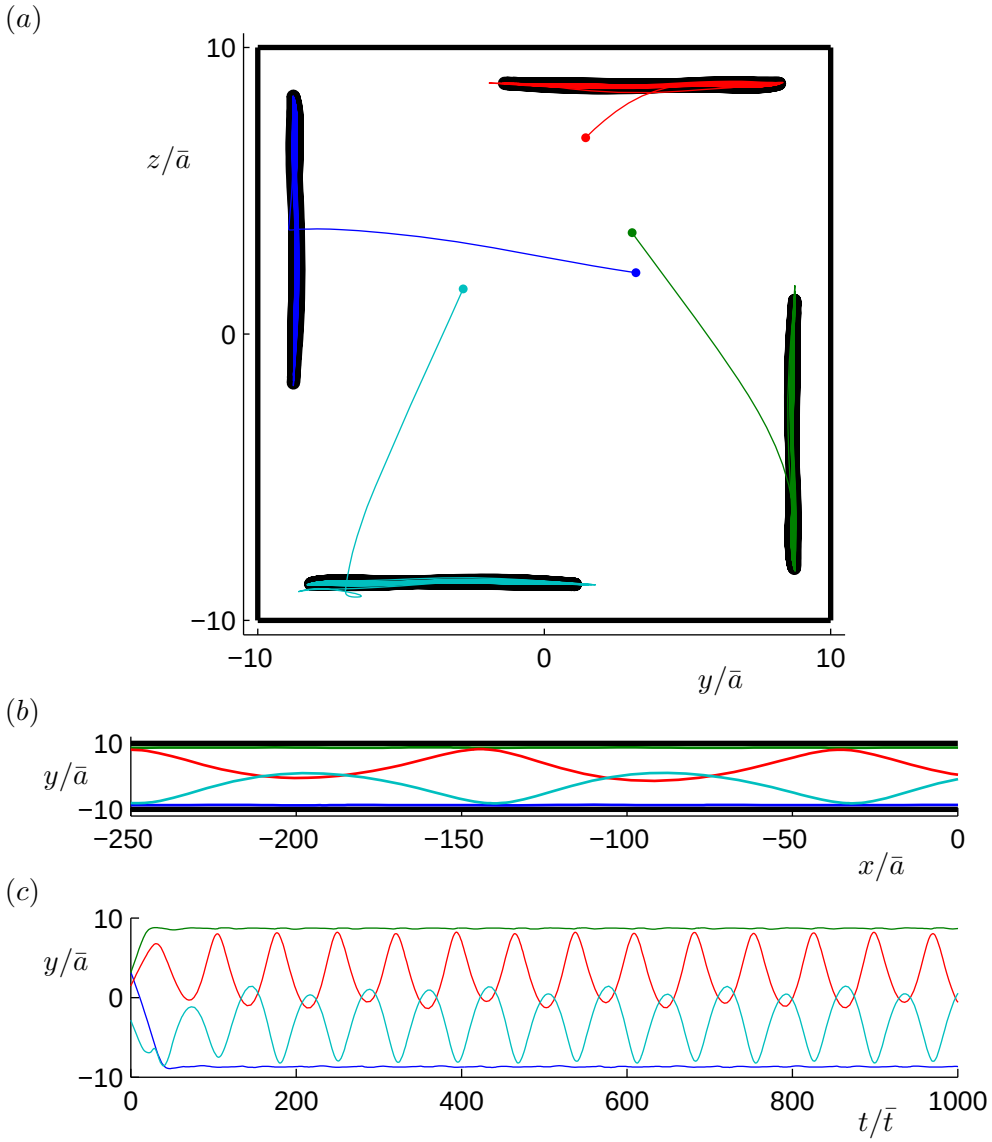

Figure 5.11: Relaxation to periodic orbits for a boundary accumulating bacterium in a square channel of width $20\,\bar{a}$. (a) Isolated, thick, black regions indicate the projections of the four periodic orbits in the cross-sectional view. These periodic orbits are related to each other by rotations about the axis of the channel. One trajectory that accumulates at each edge is shown in thin curves of different colours with starting points marked by dots. (b) Top–down view of channel showing the computed tracks once the bacteria have relaxed to periodic orbits. (c) Time series of the transient phase of the same trajectories in (a) and (b). The extent of the channel is marked with straight, black lines in (a) and (b).

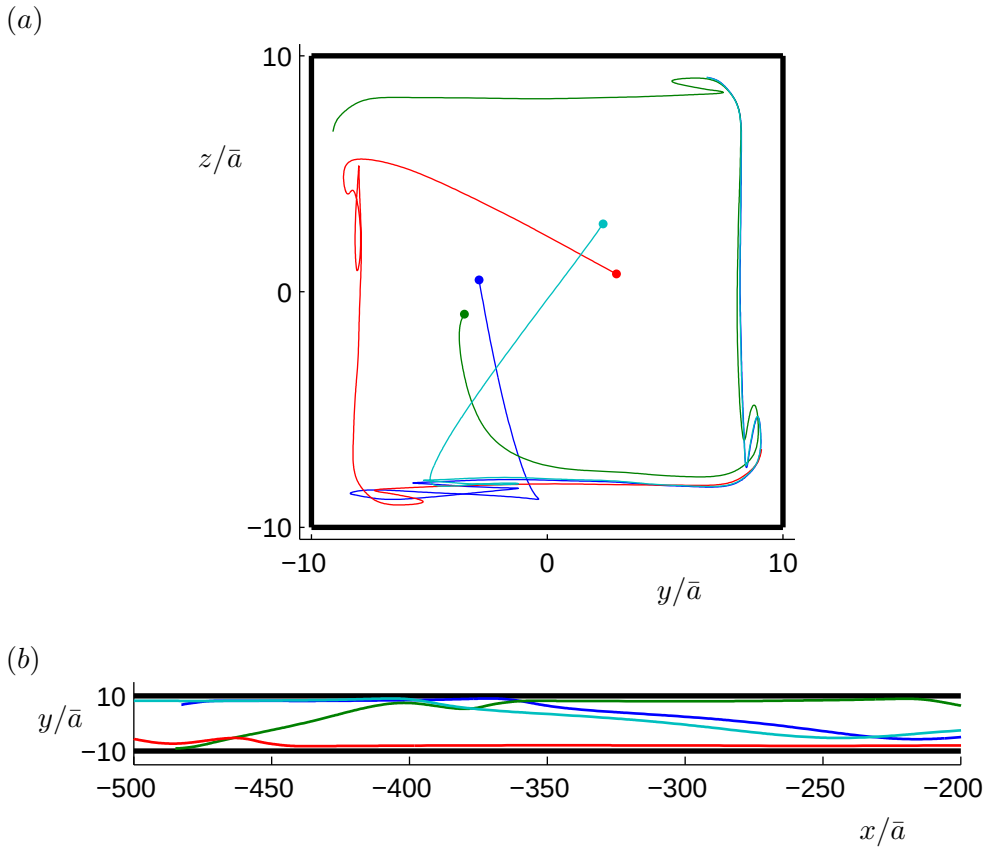

Figure 5.12: Behaviour of a boundary accumulating bacterium in a square channel of width $20\,\bar{a}$. (a) The projections in the channel cross-section of four trajectories starting from different initial conditions are shown in different colours. (b) Top–down view of the channel showing a section of the tracks in (a). The bacterium here has a flagellar length of $L/\bar{a} = 6.5$, which differs from the length $L/\bar{a} = 7.5$ used in all other presented examples of boundary accumulating swimmers in this section. The shorter length increases the preferred distance from walls, reducing close contact and allowing longer trajectories to be computed. Similar behaviour could be found in slightly smaller channels using the flagellar length $L/\bar{a} = 7.5$ but collisions could not be avoided at edges as they are in this figure. The extent of the channel is marked with straight, black lines.

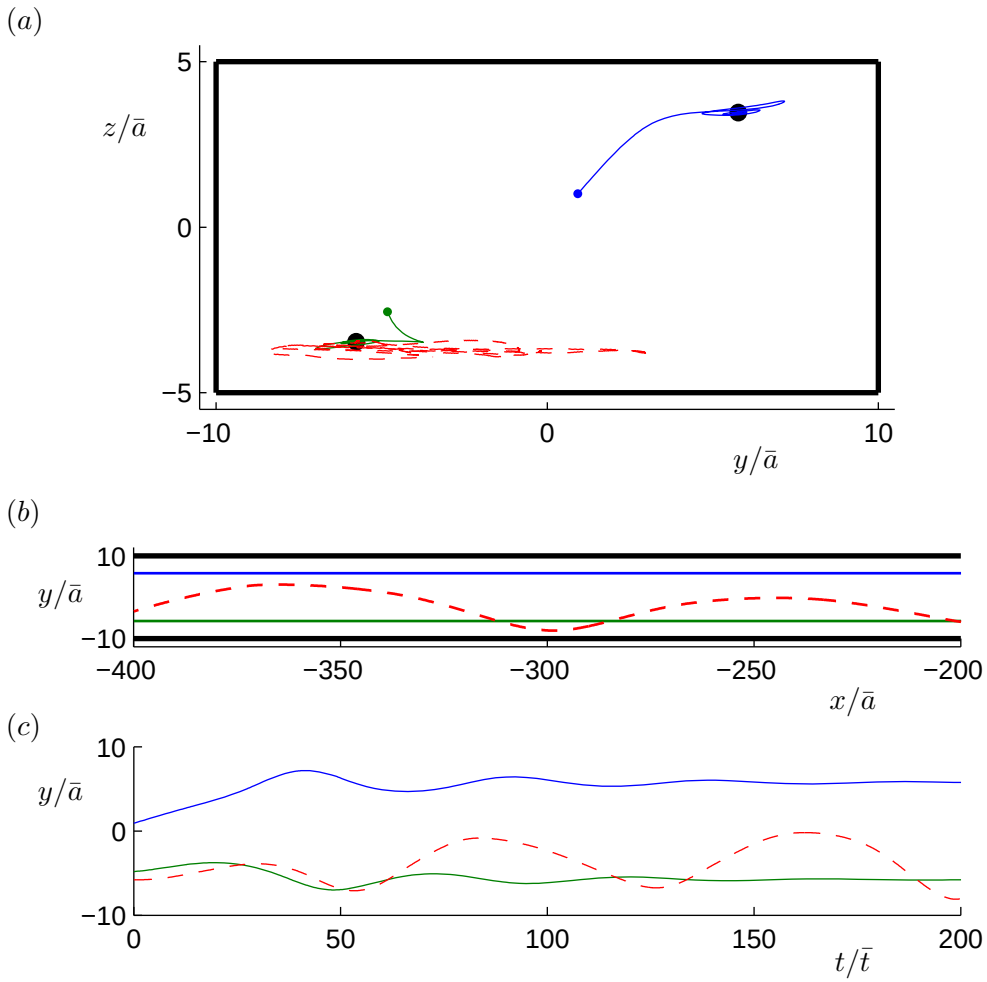

Figure 5.13: Relaxation to periodic orbits for a boundary accumulating bacterium in a channel of size $H_y = 20\,\bar{a}$, $H_z = 10\,\bar{a}$. (*a*) Large, black dots mark stable steady states in the cross-sectional view, while one trajectory that accumulates at each of these is shown in thinner, solid curves of different colours. The starting points of these trajectories are marked by dots. In addition, one trajectory computed using precise velocity evaluations rather than phase-averaged interpolation is shown in a dashed curve. (*b*) Top–down view of channel showing two computed tracks once the bacteria have relaxed to the steady states (solid lines) of the phase-averaged system and a solution of the full system (dashed curve). (*c*) Time series of the transient phase of the same trajectories in (*a*) and (*b*). The extent of the channel is marked with straight, black lines in (*a*) and (*b*).

point in the oscillation, the swimmer can be as far as 10 body radii from the edge. If the width of the channel is small enough, then the swimmer may be pulled towards the edge on the opposite side of the wall and begin edge accumulation there. This process can then repeat for the new edge so the bacterium cyclically transfers from edge to edge resulting in the pattern of behaviour shown in Fig. 5.12. There is a strong tendency for swimmers to approach the walls too closely as they turn around edges. Hence, simulations rarely span more than one or two edge turns. Nonetheless, assuming close-range surface interactions perturb the bacterium's path minimally, it can be imagined that the swimmer progresses as described from edge to edge, possibly with collisions at each turn. We refer to these trajectories as "wall-hugging spirals" in constrast to the "bouncing" or "wall-avoiding" spirals demonstrated by boundary escaping swimmers.

With rectangular channels, it is possible to choose dimensions such that edge accumulation is possible on one pair of parallel walls but not on the other. In this case, there will be two locations instead of four where the swimmer is likely to be found. Fig. 5.13 illustrates this in a case where the periodic orbit appears to be a fixed point with no oscillations. However, this fixed point behaviour may be an artifact of the phase-averaging and interpolation errors; a simulation of the full dynamics (also plotted in Fig. 5.13), without resorting to interpolation, displayed the same large amplitude oscillations parallel to the closest wall that was found in previous examples of edge accumulation.

Further decreasing one or both of the channel cross-sectional dimensions increases the tendency to collide into the walls and stable long-term behaviour is no longer exhibited. Where present, the edge accumulating orbits were found at distances $1.3\,\bar{a}$–$1.4\,\bar{a}$ from the nearest wall, only slightly greater than the computed half space accumulation height of $1.27\,\bar{a}$.

5.2.3 Average swimming speeds and durations

So far we have only discussed the forms of long-term trajectories that may arise in channels. We now investigate the effect that channel size has on the average speed at which cells progress in the direction of the channel, which we term the channel progression speed. It is difficult to estimate the channel progression speed of swimmers to be expected in an experiment because the instantaneous speed depends on the bacterium's position and therefore the average speed of a single swimmer over a trajectory depends on the path taken. Excluding stochastic effects, this means that the average speed over a given time interval depends on the initial condition of the ODE system. The average speed of a population of swimmers therefore depends on the distribution of initial conditions for bacteria entering the observed section of the channel, which in turn depends on events upstream. Without further information for specifying an appropriate distribution, we attempt the following two approaches:

1. consider uniformly distributed random configurations, and

2. assume sufficient time has been allowed for periodic states to be reached.

Starting from random configurations, we consistently find that a significant proportion of trajectories terminate before the preset end time of $500\,\bar{t}$, indicating collision events. We show the distributions of track durations in channels of varying sizes, with boundary accumulating and boundary escaping swimmers, in Fig. 5.14. There is a clear bimodal distribution in most cases. Either a collision occurs within about $100\,\bar{t}$ or the trajectory successfully reaches the target end time, indicating a good chance of attaining a periodic state.

With the boundary accumulating bacterium, there is a minimum channel size of about $17\,\bar{a}$ that allows long-term edge accumulation without collisions. The proportion of trajectories reaching time $t = 500\,\bar{t}$ appears to be greatest close to this critical point, decreasing slightly as the channel size increases further. This could

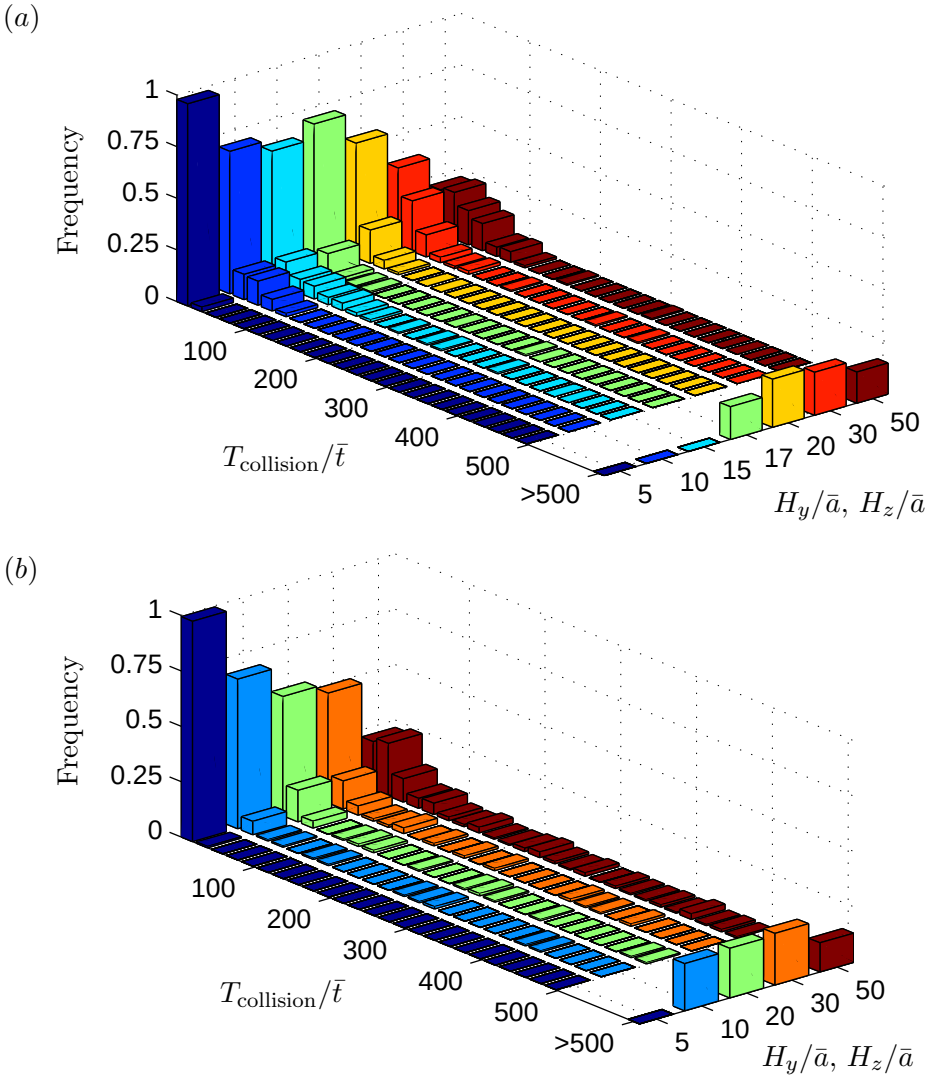

Figure 5.14: Histograms showing the frequency distributions of track durations, $T_{\text{collision}}$, for swimming in square channels of varying size. A total of 200 trajectories starting from random initial conditions were computed for each channel size with (a) a boundary accumulating swimmer, and (b) a boundary escaping swimmer. Most of the trajectories in the category for durations greater than $500\,\bar{t}$ evolve to periodic orbits and hence do not have finite track durations.

be explained by the greater possibility of deviating significantly from the channel alignment, and hence swimming into a boundary, after being attracted into a circular orbit along one of the walls. However, further tests would be required to verify this trend.

The results for boundary escaping bacteria are very similar in terms of the distributions of track durations. Collisions are unavoidable for channels as small as $5\,\bar{a}$ in width but for channel sizes of $10\,\bar{a}$ and above, the proportion of initial conditions that allow long trajectories is nearly constant. This critical size is significantly smaller than the critical channel size for edge accumulating bacteria. Slightly fewer trajectories longer than $500\,\bar{t}$ were found in the largest tested channel than in smaller channels but, again, further tests should be carried out to assess whether this is a significant effect.

We obtain the periodic orbits by extending the simulation timespan, as long as no collisions occur, until the y–z projection of the trajectory approaches a limit cycle by visual inspection, as in Fig. 5.4 or Fig. 5.6. As discussed in §5.2.2 and illustrated in Fig. 5.6, Fig. 5.8 and Fig. 5.9, boundary escaping swimmers can evolve to one of at most two distinct wall-avoiding spiral orbits while boundary accumulating swimmers, by symmetry of the square or rectangular channel, have at most two different edge environments for accumulating orbits. It is therefore straightforward to define the mean channel progression speeds of a population given time to relax to periodic states, assuming the distinct orbits are equally likely or that the speed associated with each orbit is similar enough that this is unimportant.

For boundary escaping bacteria in channels of width $10\,\bar{a}$, trajectories did not reach periodic orbits even after durations of $5000\,\bar{t}$, which is about one minute using physiological parameters for *V. alginolyticus*. However, although transience had not fully decayed, the mean speed in the direction of the channel axis was nearly constant for most of this duration and there was very little variation in this average progression

speed between trajectories. We therefore use these long trajectories in lieu of periodic orbits to estimate the "periodic orbit speed". It is not known if the periodic orbit is absent from this system or if it is present but the attraction of nearby trajectories to the orbit is weak enough that numerical errors prevent convergence.

Fig. 5.15 shows the variations of mean channel progression speeds with channel width comparing the periodic orbits with trajectories that terminated before time $t = 500\,\bar{t}$. It can be seen that the channel progression speed of periodic motion is more or less independent of channel size and only slightly lower than the expected swimming speed in a straight path through free space. However, since the swimmers that collide with the wall are likely to be more out of alignment with the channel axis, the mean progression speed of short trajectories was found to be 10–25% lower than that for periodic orbits. The trends were similar for both boundary accumulating and boundary escaping swimmers.

5.2.4 Discussion

Three distinct modes of long-term behaviour were displayed through model simulations of flagellated bacteria in channels of rectangular cross-section. Swimmers that have a tendency to escape from planar surfaces are also deflected from channel walls and fall into periodic orbits that resemble elastic collisions with each wall in turn. For the chosen boundary escaping swimmer, these periodic orbits were most readily observed in square channels of size $10\,\bar{a} \leq H_y = H_z \leq 20\,\bar{a}$. Collisions were more likely in smaller channels and relaxation to the periodic orbit took much longer in larger channels and rectangular channels. This suggests a specific, narrow range of channel sizes in which experimental verification of this predicted spiralling motion is most likely to be found.

However, regardless of the length of the transient period, roughly the same proportion of randomly initialised trajectories avoid collisions and tend to become

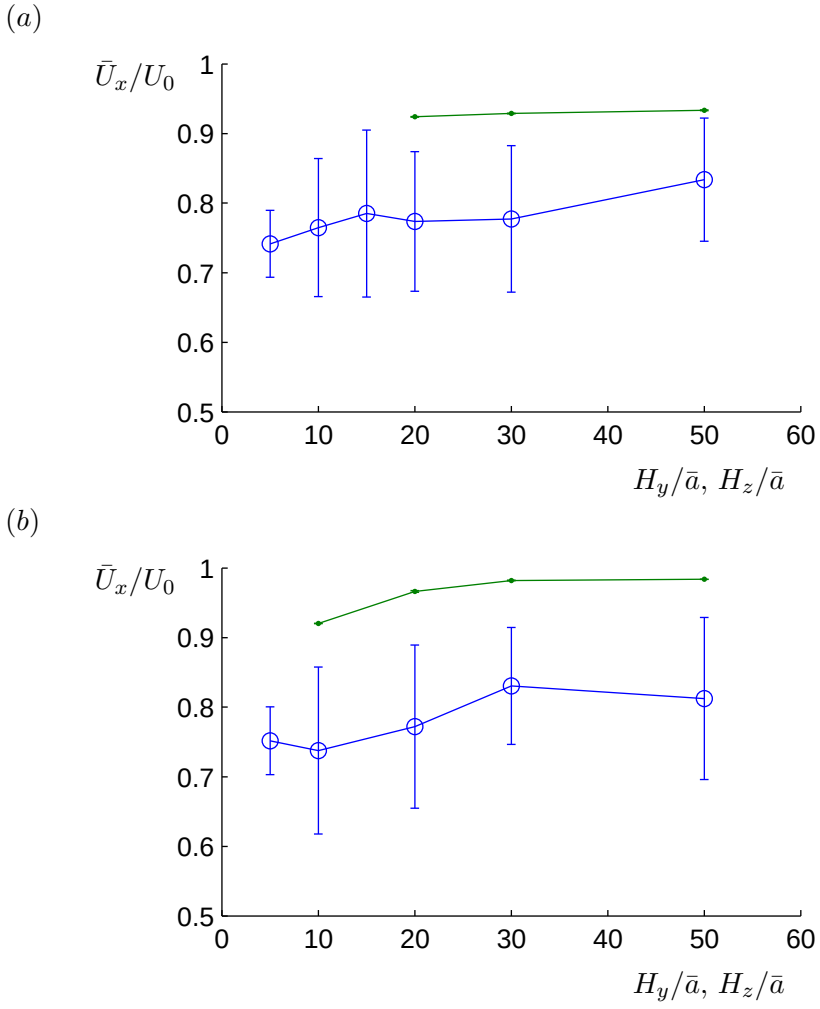

Figure 5.15: Average channel progression speeds, $\bar{U}_x$, in square channels of different sizes for (a) a boundary accumulating swimmer, and (b) a boundary escaping swimmer. Speeds of long-term trajectories are plotted with dots while the average speed of trajectories lasting less than $500\,\bar{t}$ before collision are marked with open circles. Error bars indicate the standard deviations computed from samples of 200 runs, combining both colliding and non-colliding trajectories. The speeds are expressed as fractions of the respective free space phase-averaged swimming speed, U_0, of the bacterium.

well aligned with the channel. The alignment can be explained by examining the phase plane diagram of the half space dynamics of boundary escapers in Fig. 4.4(c). Trajectories approaching a boundary with a wide range of angles tend to converge to a much narrower range of departure angles, inclined roughly 0–0.2 radians away from the plane. The effect should be the same in channels, provided that the cross-section is large enough that the swimmer effectively interacts with plane boundaries.

Furthermore, since collisions with a plane are determined by the angle of approach to the boundary, the size of the channel is relatively unimportant once interactions over most of the area of the channel walls can be approximated by half space dynamics. Although the initial position can affect which wall is encountered or whether the swimmer approaches an edge rather than a planar wall, it is largely the initial orientation that dictates whether or not a collision will take place. This explains why we might expect to find the same proportion of initial trajectories avoiding collisions in all large channels; this proportion corresponds to the fraction of orientations that are deflected from plane boundaries without collision.

Successive wall interactions bring the swimmer to an alignment angle of about 0.1 radians with respect to the channel axis. This results in a high average channel progression speed, independent of channel size, which is consistent with the simulation results for trajectories of long duration for boundary escaping swimmers (Fig. 5.15(b)).

Similar conclusions can be drawn for boundary accumulating swimmers, which manifest a different form of periodic behaviour, referred to as "edge accumulation". This requires a channel of at least a certain size, about twice the length of the combined cell body and helical flagellum. The channel progression speed in the edge accumulating orbit was independent of channel size and 10–20% higher than the average speed of colliding trajectories. As long as bacteria do not adhere when they interact closely with walls but simply reorientate to become more aligned with the surface, it is likely that most swimmers will become trapped in the periodic

orbits at edges. This is because a swimmer near the edge generally relaxes very quickly to a periodic orbit, due to the strong effect from nearby walls. In contrast, boundary escaping orbits keep the swimmer much further from the walls except when the bacterium momentarily approaches and is deflected from a wall. The long periods without wall interactions result in slow attraction to the periodic wall-avoiding spiral.

Edge accumulation can be made to take place only at two diagonally opposite edges of the channel by adjusting the width and height of the channel independently. This has an interesting implication for channels carrying bacteria in both directions. Assuming all of the bacteria remain in edge accumulating paths, the bacteria travelling in one direction will be found at two of the channel edges while bacteria travelling in the opposite direction will be found at the other two edges, as illustrated in Fig. 5.16. This means no collisions will occur between bacteria swimming in opposite directions, assuming sufficient spacing between adjacent edges. In contrast, square channels permit edge accumulation at all four edges so collisions between bacteria travelling in opposite directions are likely.

Empirical evidence reported by DiLuzio et al. [38] supports the edge accumulation behaviour predicted by the current numerical study. It was found that *E. coli* predominantly "swim on the right-hand side" of a thin, rectangular channel, that is, most of the bacteria swim closer to the bottom surface than to the top and, facing the direction of travel, the bacteria swim along the right-hand wall of the channel. The top–bottom asymmetry was due to a different material being used for the two surfaces; symmetry was restored when the same material was used on the top and bottom. In any case, the relevant observation from this study is that there is a strong preference for swimming along edges as opposed to more central positions in the channel. Note that preference was found for the bottom right edge while our simulations predict accumulation at the bottom left edge. This is simply because we have used a model bacterium with opposite chirality to that of the *E. coli* observed

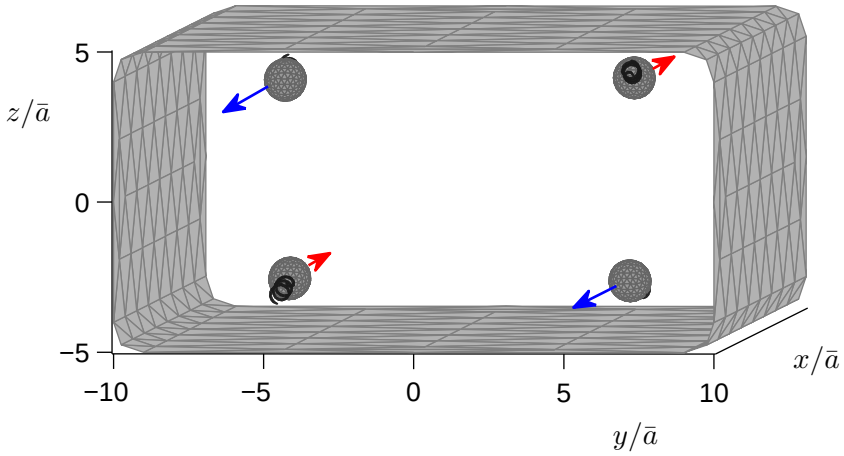

Figure 5.16: An example of how a population of bacteria in a rectangular channel might spontaneously separate into different regions according to the direction of travel. This effect is due to edge accumulation only being stable at two edges for a given swimming direction (Fig. 5.13).

in the experiment.

Another finding of the experimental work was that the left–right bias dropped significantly as the channel height was increased. As a possible explanation, it was suggested that the left–right bias is a direct result of the top–bottom asymmetry, from which it follows that the effect decreases as channel height increases since the hydrodynamic influence of walls decays with distance. The results of the current study offer the following possible contributing factor to the reduction in left–right asymmetry with larger channel heights. When the channel height is small, there are only two sites for edge accumulation; one on the top left and one on the bottom right. Hence, if most cells swim on the bottom, they will be seen on the right. As the channel height increases, it becomes possible for edge accumulation to occur at the other two edges. Consequently, bacteria on the bottom may be found either on the right or on the left, restoring the symmetry in the observed distribution.

The third type of long-term trajectory, referred to as a “wall-hugging spiral”,

also involves swimming along the surfaces of the channel walls. However, instead of remaining on one wall, the cell swims along the surface until it meets an edge, then turns around the edge and continues along the next wall. There are some significant differences between this and the spiral orbit of boundary escapers. In experiments, such as those reported by DiLuzio et al. [38] and Binz et al. [15], the channel is typically viewed from the top or bottom. In other words, videos show an x–y projection of the trajectory, often lacking information about the vertical position of the cells relative to the plane of focus. In this view, the wall-avoiding spiral trajectories appear as gradual oscillations from side to side whereas boundary accumulating bacteria stay very close to the channel walls. In the x–y projection, the wall-hugging spiral path alternates between straight segments down the channel and transitions from one side to the other.

As exhibited in Fig. 5.12, some unsteady motion will occur during the transition phase due to the edge accumulating effect inducing oscillations before the swimmer is pulled towards the opposite wall. Furthermore, unpredictable perturbations are likely because of the sensitive dynamics when the flagellum comes into close proximity with walls as the swimmer turns the channel edges. Therefore, the attachment and detachment of bacteria to the sides of a channel may appear random and noisy in an experiment, particularly at the detachment stage.

For this reason, as well as variability in morphology within a population, the predominantly observed behaviour will transition gradually from edge accumulation to wall-hugging spirals as the channel size is decreased. Channels of large width provide a wide barrier between two edges, reducing the likelihood of escaping from one and crossing over to the next. This means that edge accumulation is very stable and swimmers remain on one side of the channel, viewed in a top–down perspective (Fig. 5.11). As the channel width decreases, it becomes more probable that slight perturbations lead to escape from an edge accumulating orbit. Bacteria are observed

to cross from one side to the other more frequently (Fig. 5.12). This trend is strongly supported by the tracks of *S. marcescens* swimming through channels of various widths captured by Binz et al. [15].

The tendency to remain at channel edges may have implications for sustaining a population of bacteria in a channel. A large channel may contain plenty of dissolved nutrients required by the bacteria but if all of the bacteria remain at the edges, they could cause local depletion of nutrients. This will probably not be an issue for chemicals such as oxygen and sugars in a watery medium since the diffusion constant is of the order of $10^{-5}\,\mathrm{cm}^2\,\mathrm{s}^{-1}$ [44] and would allow molecules to spread across a 30 μm channel on a timescale of under one second. Diffusion is generally much slower in viscous fluids, however, so there may be naturally occurring or experimental situations in which localisation of the bacteria to edges can reduce nutrient uptake. In such cases, it may counter-intuitively be beneficial for the bacteria to swim in smaller channels, which encourage the swimmers to traverse the walls and pass through more of the channel fluid. Additionally, boundary escaping bacteria have an advantage in this respect as they explore a large portion of the channel cross-section, allowing them to utilise available nutrients throughout the channel.

5.3 Summary

The average velocity of a bacterium in a channel over the timescale of a motor revolution depends on its position within the cross-section and its orientation with respect to the walls. These yield four degrees of freedom and the dynamics can therefore be described by a four dimensional autonomous system of ODEs. We developed a method of analysing this sytem by interpolating pre-evaluated data. This is analogous to the technique used in the half space and between parallel plates, where the two dimensional dynamics were visualised in phase portrait diagrams and approximate trajectories computed using the MATLAB function, `streamline`. After

a suitable sampling of points throughout the state space, interpolation provides an efficient approximation to the dynamical system, allowing the behaviour to be assessed rapidly.

We identified two aspects that significantly influence the predicted behaviour of flagellated bacteria swimming in rectangular channels. One is the cross-sectional size and shape of the channel while the other is the type of behaviour of the bacterium near plane boundaries. The latter is in turn dependent on the cell and flagellum geometry but can broadly be divided into boundary accumulating swimmers, which are attracted into circular orbits near plane boundaries, and boundary escapers, which are repelled from surfaces.

Placed in channels of width and height around 15 μm and sufficient length, boundary accumulating bacteria are likely to become trapped in the edges of the channel cross-section, giving the appearance of swimming along the sides in the top–down view in typical microscopy experiments. Edge accumulation is stable in large channels but as the channel size is decreased, transitions from one edge to another would become more frequent due to reduced robustness of the edge swimming state with respect to perturbations in position and orientation.

By choosing a large channel width and small height, it is possible to induce edge accumulation on only two, diagonally opposite edges of the cross-section. This could be desirable for allowing bi-directional traffic of swimming bacteria in a channel since oppositely moving bacteria will confined to different edges and would therefore be less likely to inhibit one another.

In contrast, boundary escaping bacteria tend to "bounce" cyclically off all four walls, gradually falling into a distorted left handed helical orbit around the channel axis. The size and aspect ratio of the cross-section affect the time required for a periodic state to emerge as well as the shape of the periodic orbits but no qualitative difference in long-term behaviour was found in channels of different sizes. Compared

with channel trajectories of boundary accumulating bacteria, the orbits of boundary escaping bacteria are generally much further from the walls and can even pass near to the centre of the cross-section. Because of the relatively weak wall effect in the central region of channels, stochastic perturbations could prevent periodic motion from being apparent in experiments, especially in large channels.

These results have a number of implications for practical situations. For example, the attraction of boundary accumulating swimmers to edges of channels indicates that these are the most susceptible areas to biofilm initiation. A circular channel may therefore resist colonisation better than square or rectangular channels since there are no edges for bacteria to gather at. Flow through channels is also slowest at the edges due to the no-slip boundary condition. Although we have not investigated the effects of shear flow on bacterial dynamics, it can be hypothesised that edge accumulating bacteria would be less likely to be washed downstream by a background flow through the channel because the no-slip boundary condition weakens the flow at edges where the bacteria tend to swim.

Boundary escaping bacteria, on the other hand, have a tendency to cut across the central region of the channel where the background flow velocity is greatest. Therefore, a flow through the channel may be a suitable means of flushing out such swimmers and preventing biofilm formation.

The speed of travel through channels is expected to be largely constant over a wide range of channel sizes for both boundary accumulating and boundary escaping swimmers. As long as the channel is large enough to permit the oscillatory edge accumulation orbits, boundary accumulating bacteria are attracted to the edges and do not feel the hydrodynamic effect of the more distant walls and edges. Similarly, boundary escaping swimmers tend to align closely with the axis of the channel, whether or not a periodic orbit is attained. Hence, the average progression speed is almost independent of channel size for both types of swimmers.

In very large channels, however, it is possible that boundary accumulating bacteria will become trapped in circular orbits over a wall but far from edges. This would then prevent the swimmer from making any overall progress through the channel. The other extreme, very small channels, may also reduce the average progression speed since swimming along the centre of a channel is unstable, making collisions with the walls likely in such a confined space.

In chapter 4, we found that details of the bacterium's geometry are important to the precise trajectories near a single plane boundary. The same must also be true in channels but we have focussed on only two bacterial shapes to provide a qualitative account of the range of possible behaviours for boundary accumulating and escaping bacteria. Within each group, it is likely that perturbations of the shape can affect the quantitative details of the observed trajectories. For example, the average distance and amplitude of oscillation from each wall in an edge accumulating periodic orbit may vary with flagellum length and helical wavenumber. This should be considered when comparing numerical predictions with experiment.

Another possible source of error when applying our model to bacteria in channels is that we have restricted the motion of the flagellum to a rotation about a fixed axis with respect to the cell body. The presence of walls strongly confines and deflects the bacterial trajectories, especially for boundary accumulators, which have a tendency to swim near edges. It is plausible that the torque from the wall interacting with the front of the cell body or the end of the flagellum would cause some deformation from the assumed free space configuration of the swimmer. This motivates the work of the following chapter, which will allow some deformation of the cell body–flagellum alignment by treating the flagellar hook as an elastic rod.

Chapter 6

A model for flexible hooks

In this chapter we develop the bacterial model by including bending dynamics of the hook connecting the cell body to the rigid flagellar filament. The hook is modelled as a Kirchhoff rod, which is inextensible and unshearable. At timescales comparable with the motor frequency, inertia is negligible. We make the further simplification that viscous forces and moments acting on the hook are not important. These two approximations are justified in appendix A.

The theory of Kirchhoff rods is well-known and has been explored in detail by Kirchhoff and other authors [77, 78, 127]. We now briefly summarise a general kinematic description of a directed curve, which will represent the centreline of a rod, and the constitutive relations for the Kirchhoff model.

6.1 Curves and rods

A finite curve of length L can be defined by a vector-valued function $\mathbf{x}^0(s)$, where the spatial parameter $s \in [0, L]$ measures the arc length from one end of the curve. We define an associated right-handed, orthonormal, local director basis $\{\mathbf{d}_i^0(s),\, i = 1, 2, 3\}$ in such a way that the basis vectors are twice differentiable functions of arc length and time. The specification of the directors is not unique but may affect the dynamics once constitutive relations are imposed. If we allow this reference curve to deform, the evolution can be described by $\mathbf{x}(s, t)$, where s is the arc

length in the reference curve corresponding to a given material point of the deformed curve. The director basis of the deformed curve is $\{\mathbf{d}_i(s,t),\, i=1,2,3\}$.

We will use the convention of summation over indices $i=1,2,3$ where they appear twice in the same term. We also use primes to signify derivatives with respect to arc length and dots to signify time derivatives. At each point in time and along the rod, we can define a twist vector $\boldsymbol{\kappa}(s,t)=\kappa_i\mathbf{d}_i$ and a spin vector $\boldsymbol{\omega}(s,t)$ such that

$$\mathbf{d}_i' = \boldsymbol{\kappa}\times\mathbf{d}_i, \quad \dot{\mathbf{d}}_i = \boldsymbol{\omega}\times\mathbf{d}_i, \quad i=1,2,3. \tag{6.1}$$

Goriely & Tabor [58] showed algebraically that such vectors $\boldsymbol{\kappa}$ and $\boldsymbol{\omega}$ exist. This is because orthonormality of the directors implies that differentiable transformations, whether in s or in t, correspond to rotations. The derivative of a rotating vector can be written as a cross product with the rotation vector as given above. The evolution of the curve with respect to time is defined by (6.1) and the arc length derivative vector $\mathbf{v}:=\mathbf{x}'(s,t)$.

We consider a rod to be a three-dimensional object that is thin in two of the dimensions so that it approximately occupies the region of space within a distance r of a curve, where r is small compared with the length of the curve. More precisely, we define a material cross-section at the arc length s of the reference curve to be the set of points

$$\mathscr{C}^0(s) := \left\{\mathbf{X}^0(s,x_1,x_2)=\mathbf{x}^0(s)+x_1\mathbf{d}_1^0(s)+x_2\mathbf{d}_2^0(s)\,|\,(x_1,x_2)\in\mathscr{B}(s)\right\}, \tag{6.2}$$

for some simply connected region $\mathscr{B}(s)\subset\mathbb{R}^2$ that includes the origin. If the diameter of every $\mathscr{B}(s)$ is much smaller than the length of the curve, i.e., if

$$(x_1^2+x_2^2)^{1/2}/L \ll 1 \quad \forall\,(x_1,x_2)\in\mathscr{B}(s), \quad \forall\, s\in[0,L], \tag{6.3}$$

and no two cross-sections at different arc lengths intersect one another, then the union of all cross-sections of the reference curve forms the reference configuration of a rod. After a general deformation, the cross-section is given by

$$\mathscr{C}(s,t) := \{\mathbf{X}(s,x_1,x_2,t)=\mathbf{x}(s,t)+\mathbf{r}(s,x_1,x_2,t)\,|\,(x_1,x_2)\in\mathscr{B}(s)\}, \tag{6.4}$$

where $\mathbf{r}$ is a displacement from the centreline that depends on the original material position and the current deformation. We will now consider specific assumptions on the form of the displacement $\mathbf{r}$ and formulate a dynamic description of the rod through elastic constitutive relations.

6.2 The Kirchhoff rod

The Kirchhoff model is one of the simplest three-dimensional theories for elastic, rod-like objects. It is assumed that the rod is inextensible and unshearable. This means that cross-sections of the undeformed rod remain planar and normal to the local tangent upon deformation and s is now the arc length in both the deformed and the reference configuration. By convention, we take $\mathbf{d}_3$ to be the tangent vector, which now coincides with $\mathbf{v}$ due to inextensibility. Furthermore, it is assumed that there is no material deformation in the plane of the cross-section. The term describing the displacement of a point on the cross-section from the centreline then has a simple form, namely, $\mathbf{r}(s, x_1, x_2, t) = x_1\mathbf{d}_1(s,t) + x_2\mathbf{d}_2(s,t)$.

The stresses acting across each cross-section of the rod lead to a net force $\mathbf{n} = n_i\mathbf{d}_i$ and net moment $\mathbf{m} = m_i\mathbf{d}_i$. We follow the convention that these quantities are exerted by the side with greater s on the side with smaller s. Neglecting inertia and viscous stresses, force and moment balance considerations on a vanishingly short section of the rod lead to the equations (see reference [3] for more details)

$$\left.\begin{aligned} \mathbf{n}' &= \mathbf{0}, \\ \mathbf{m}' + \mathbf{d}_3 \times \mathbf{n} &= \mathbf{0}. \end{aligned}\right\} \tag{6.5}$$

We use a linear constitutive relation between the strain and the elastic moment in the rod. Assuming the rod is uniform and of circular cross-section and has no finite preferred curvature or torsion, the moment can be expressed as

$$\mathbf{m} = EI(\kappa_1\mathbf{d}_1 + \kappa_2\mathbf{d}_2 + \Gamma\kappa_3\mathbf{d}_3), \tag{6.6}$$

where E is the Young's modulus of the material, I is the moment of inertia of the cross-section and $\Gamma = GJ/EI$ is the ratio of twisting stiffness GJ to bending stiffness EI. Using this formula for the moment in (6.5), we find

$$\left.\begin{aligned} \kappa_1' &= \frac{1}{EI}(\mathbf{n}\cdot\mathbf{d}_2) - \kappa_2\kappa_3(\Gamma-1), \\ \kappa_2' &= -\frac{1}{EI}(\mathbf{n}\cdot\mathbf{d}_1) + \kappa_1\kappa_3(\Gamma-1), \\ \kappa_3' &= 0. \end{aligned}\right\} \tag{6.7}$$

Combined with the equations for $\mathbf{d}_i'$ in (6.1), we have a system of 12 ODEs for the 12 variables $\mathbf{d}_i, \kappa_i$, $i = 1, 2, 3$. Note that (6.6) means we can equivalently consider $\mathbf{m}$ instead of $\boldsymbol{\kappa}$. Hence, this can be solved as an initial value problem in the arc length parameter for a fixed time t if we are given the parameter $\mathbf{n}^{\mathrm{B}}(t) = \mathbf{n}(0,t)$ and the initial conditions $\mathbf{d}_i^{\mathrm{B}}(t) = \mathbf{d}_i(0,t)$ and $\mathbf{m}^{\mathrm{B}}(t) = \mathbf{m}(0,t)$. This is the well known Kirchhoff analogy, which states that the time-evolution of the body-fixed reference frame of a spinning top is governed by the same equations and is therefore equivalent to the variations along the arc length of the director basis of an elastic rod in equilibrium [77, 88].

By orthonormality of the directors, we have $\mathbf{d}_3 = \mathbf{d}_1 \times \mathbf{d}_2$. Additionally, the last equation of (6.7) immediately gives $\kappa_3(s) = \kappa_3(0)$. We therefore consider the reduced set of differential equations

$$\left.\begin{aligned} \mathbf{d}_1' &= \boldsymbol{\kappa}\times\mathbf{d}_1 = \kappa_3\mathbf{d}_2 - \kappa_2\mathbf{d}_3 \\ \mathbf{d}_2' &= \boldsymbol{\kappa}\times\mathbf{d}_2 = -\kappa_3\mathbf{d}_1 + \kappa_1\mathbf{d}_3 \\ \kappa_1' &= \frac{1}{EI}(\mathbf{n}\cdot\mathbf{d}_2) - \kappa_2\kappa_3(\Gamma-1), \\ \kappa_2' &= -\frac{1}{EI}(\mathbf{n}\cdot\mathbf{d}_1) + \kappa_1\kappa_3(\Gamma-1), \end{aligned}\right\} \tag{6.8}$$

which is still not independent because we have the constraints $\|\mathbf{d}_i\| = 1$, $i = 1, 2, 3$, and $\mathbf{d}_1\cdot\mathbf{d}_2 = 0$. By reformulating the directors in terms of Euler angles, it is possible to further reduce this to a set of equations for the five independent variables: κ_1, κ_2 and three Euler angles. This approach was followed by Goriely & Tabor [58] but leads to

significantly more complicated expressions. Instead, we numerically solve (6.8) using the fourth-order Runge-Kutta method and perform corrections after each step in arc length to ensure orthonormality constraints are satisfied. The corrections required at each step were found to be of the order of 10^{-11}. We are therefore confident that this method is accurate.

Once $\boldsymbol{\kappa}(s,t)$ and $\mathbf{d}_i(s,t)$, $i = 1,2,3$ are determined for time t, we can construct the centreline, and thus determine the shape of the rod, using the relation

$$\mathbf{x}'(s,t) = \mathbf{d}_3(s,t). \tag{6.9}$$

We will see how the initial conditions $\mathbf{d}_i^{\mathrm{B}}(t)$ and $\mathbf{m}^{\mathrm{B}}(t)$ and the parameter $\mathbf{n}^{\mathrm{B}}(t)$ are determined in §6.3 and §6.4.

We will apply these elastic rod equations to the bacterial hook, of length L^{H}. Since we will mainly be concerned with the end points $\mathbf{x}^{\mathrm{B}}$ and $\mathbf{x}^{\mathrm{T}}$ of the hook, where the cell body and flagellum are located, we write the solution to the rod equations symbolically as

$$\left.\begin{aligned}
\mathbf{x}^{\mathrm{T}} &= \mathbf{x}^{\mathrm{B}} + \mathbf{X}(\mathbf{d}_1^{\mathrm{B}}, \mathbf{d}_2^{\mathrm{B}}, \mathbf{d}_3^{\mathrm{B}}, \mathbf{n}^{\mathrm{B}}, \mathbf{m}^{\mathrm{B}}),\\
\mathbf{d}_1^{\mathrm{T}} &= \mathbf{D}_1(\mathbf{d}_1^{\mathrm{B}}, \mathbf{d}_2^{\mathrm{B}}, \mathbf{d}_3^{\mathrm{B}}, \mathbf{n}^{\mathrm{B}}, \mathbf{m}^{\mathrm{B}}),\\
\mathbf{d}_2^{\mathrm{T}} &= \mathbf{D}_2(\mathbf{d}_1^{\mathrm{B}}, \mathbf{d}_2^{\mathrm{B}}, \mathbf{d}_3^{\mathrm{B}}, \mathbf{n}^{\mathrm{B}}, \mathbf{m}^{\mathrm{B}}),\\
\mathbf{d}_3^{\mathrm{T}} &= \mathbf{D}_3(\mathbf{d}_1^{\mathrm{B}}, \mathbf{d}_2^{\mathrm{B}}, \mathbf{d}_3^{\mathrm{B}}, \mathbf{n}^{\mathrm{B}}, \mathbf{m}^{\mathrm{B}}),\\
\mathbf{m}^{\mathrm{T}} &= \mathbf{M}(\mathbf{d}_1^{\mathrm{B}}, \mathbf{d}_2^{\mathrm{B}}, \mathbf{d}_3^{\mathrm{B}}, \mathbf{n}^{\mathrm{B}}, \mathbf{m}^{\mathrm{B}}),
\end{aligned}\right\} \tag{6.10}$$

where we have shortened notation by defining $\mathbf{d}_i^{\mathrm{T}} := \mathbf{d}_i(L^{\mathrm{H}})$ and $\mathbf{m}^{\mathrm{T}} := \mathbf{m}(L^{\mathrm{H}})$. We set $\mathbf{d}_3^{\mathrm{B}} \equiv \mathbf{e}^{\mathrm{M}} \equiv \mathbf{e}_1^{\mathrm{B}}$ (see Fig. 6.1) while the initial choice of $\mathbf{d}_1^{\mathrm{B}}$ and $\mathbf{d}_2^{\mathrm{B}}$ is arbitrary within the constraints of orthonormality of the basis. The response functions $\mathbf{X}$, $\mathbf{D}_i$ and $\mathbf{M}$ depend on two intrinsic properties of the rod: the bend/twist ratio Γ and the scaled rigidity, also referred to as hook stiffness,

$$k^{\mathrm{H}} := \frac{EI}{\tau^{\mathrm{M}} L^{\mathrm{H}}}. \tag{6.11}$$

6.3 Bacterial dynamics with a Kirchhoff hook

The motion of the flagellum relative to the cell body is dictated by the changes in shape and orientation of the hook. If we write a point on the flagellum as

$$\mathbf{x}^0 = \mathbf{x}^{\mathrm{T}} + y_i\,\mathbf{d}_i^{\mathrm{T}}, \tag{6.12}$$

then the instantaneous velocity at $\mathbf{x}^0$ is given by

$$\begin{aligned}\mathbf{u}(\mathbf{x}^0) &= \dot{\mathbf{x}}^{\mathrm{T}} + y_i\,\dot{\mathbf{d}}_i^{\mathrm{T}} &(6.13)\\ &= (\dot{\mathbf{x}}^{\mathrm{B}} + \boldsymbol{\omega}^{\mathrm{B}} \times \mathbf{X} + \frac{\partial \mathbf{X}}{\partial \mathbf{n}^{\mathrm{B}}} \cdot \dot{\mathbf{n}}^{\mathrm{B}} + \frac{\partial \mathbf{X}}{\partial \mathbf{m}^{\mathrm{B}}} \cdot \dot{\mathbf{m}}^{\mathrm{B}}) + y_i\,\boldsymbol{\omega}^{\mathrm{T}} \times \mathbf{d}_i^{\mathrm{T}}, &(6.14)\end{aligned}$$

where $\boldsymbol{\omega}^{\mathrm{B}}$ is the spin vector at the body end of the hook. Taking this to be the sum of the cell body rotation vector and a spin rate around the motor axis, $\boldsymbol{\omega}^{\mathrm{B}} = \boldsymbol{\Omega}^{\mathrm{B}} + \omega^{\mathrm{M}}\mathbf{e}^{\mathrm{M}}$. We also write $\boldsymbol{\omega}^{\mathrm{T}} = \boldsymbol{\omega}^{\mathrm{B}} + \boldsymbol{\Omega}^{\mathrm{H}}$, where $\boldsymbol{\Omega}^{\mathrm{H}}$ is the spin vector of the flagellum end of the hook relative to the cell body end due to $\dot{\mathbf{n}}^{\mathrm{B}}$ and $\dot{\mathbf{m}}^{\mathrm{B}}$ satisfying

$$\frac{\partial \mathbf{D}_i}{\partial \mathbf{n}^{\mathrm{B}}} \cdot \dot{\mathbf{n}}^{\mathrm{B}} + \frac{\partial \mathbf{D}_i}{\partial \mathbf{m}^{\mathrm{B}}} \cdot \dot{\mathbf{m}}^{\mathrm{B}} = \boldsymbol{\Omega}^{\mathrm{H}} \times \mathbf{D}_i, \quad i = 1, 2, 3. \tag{6.15}$$

Since the filament is treated as a rigid body, the velocity at a point on the flagellum can be expressed as

$$\mathbf{u}(\mathbf{x}^0) = (\mathbf{U}^{\mathrm{B}} + \mathbf{U}^{\mathrm{T}}) + (\boldsymbol{\Omega}^{\mathrm{B}} + \boldsymbol{\Omega}^{\mathrm{T}}) \times \tilde{\mathbf{x}}, \quad \mathbf{x}^0 \text{ on the flagellum}, \tag{6.16}$$

where $\mathbf{U}^{\mathrm{B}}$ and $\boldsymbol{\Omega}^{\mathrm{B}}$ are the translational and rotational velocities respectively of the cell body, $\tilde{\mathbf{x}} = \mathbf{x}^0 - \mathbf{x}^{\mathrm{B}}$ is the displacement vector relative to the body–hook junction, and $\mathbf{U}^{\mathrm{T}}$ and $\boldsymbol{\Omega}^{\mathrm{T}}$ describe the instantaneous motion of the flagellum relative to the cell body. Comparing this with (6.13), we see that

$$\left.\begin{aligned}\mathbf{U}^{\mathrm{T}} &= \frac{\partial \mathbf{X}}{\partial \mathbf{n}^{\mathrm{B}}} \cdot \dot{\mathbf{n}}^{\mathrm{B}} + \frac{\partial \mathbf{X}}{\partial \mathbf{m}^{\mathrm{B}}} \cdot \dot{\mathbf{m}}^{\mathrm{B}} + \boldsymbol{\Omega}^{\mathrm{T}} \times (\mathbf{x}^{\mathrm{B}} - \mathbf{x}^{\mathrm{T}}),\\ \boldsymbol{\Omega}^{\mathrm{T}} &= \omega^{\mathrm{M}}\mathbf{e}^{\mathrm{M}} + \boldsymbol{\Omega}^{\mathrm{H}}.\end{aligned}\right\} \tag{6.17}$$

The partial derivatives $\partial\mathbf{X}/\partial\mathbf{n}^{\mathrm{B}}$, $\partial\mathbf{X}/\partial\mathbf{m}^{\mathrm{B}}$, $\partial\mathbf{D}_i/\partial\mathbf{n}^{\mathrm{B}}$ and $\partial\mathbf{D}_i/\partial\mathbf{m}^{\mathrm{B}}$ can be computed using a finite difference formula. Noting (6.15), we can write $\mathbf{U}^{\mathrm{T}}$ and $\boldsymbol{\Omega}^{\mathrm{T}}$ as linear functions of the unknown velocities $\dot{\mathbf{n}}^{\mathrm{B}}$, $\dot{\mathbf{m}}^{\mathrm{B}}$ and ω^{M}.

By considering the cell body and the flagellum as separate bodies in the fluid, we have the force and moment balance equations

$$\left.\begin{aligned} \int_B \mathbf{f}\,\mathrm{d}S + \mathbf{F}^{\mathrm{B}} = \mathbf{0}, \quad \int_B \tilde{\mathbf{x}} \times \mathbf{f}\,\mathrm{d}S + \boldsymbol{\tau}^{\mathrm{B}} = \mathbf{0}, \\ \int_T \mathbf{f}\,\mathrm{d}S + \mathbf{F}^{\mathrm{T}} = \mathbf{0}, \quad \int_T \tilde{\mathbf{x}} \times \mathbf{f}\,\mathrm{d}S + \boldsymbol{\tau}^{\mathrm{T}} = \mathbf{0}, \end{aligned}\right\} \tag{6.18}$$

where $\mathbf{F}^{\mathrm{B}}$ and $\boldsymbol{\tau}^{\mathrm{B}}$ are the forces and moments exerted on the cell body by the hook, $\mathbf{F}^{\mathrm{T}}$ and $\boldsymbol{\tau}^{\mathrm{T}}$ are the forces and moments exerted on the flagellum by the hook, and B and T denote the surfaces of the cell body and the flagellum respectively. The forces and torques acting on the cell body and flagellum are exactly those from the boundary conditions of the Kirchhoff hook. We therefore have the equations

$$\left.\begin{aligned} \mathbf{F}^{\mathrm{B}} = \mathbf{n}^{\mathrm{B}}, \quad \boldsymbol{\tau}^{\mathrm{B}} = \mathbf{m}^{\mathrm{B}}, \\ \mathbf{F}^{\mathrm{T}} = -\mathbf{n}^{\mathrm{B}}, \quad \boldsymbol{\tau}^{\mathrm{T}} = -\mathbf{m}^{\mathrm{T}} - (\mathbf{x}^{\mathrm{T}} - \mathbf{x}^{\mathrm{B}}) \times \mathbf{n}^{\mathrm{B}} = -\mathbf{m}^{\mathrm{B}}, \end{aligned}\right\} \tag{6.19}$$

relating the hook configuration to the force and torque balance conditions (6.18).

To enforce a prescribed motor torque, we use the condition $\mathbf{e}^{\mathrm{M}} \cdot \boldsymbol{\tau}^{\mathrm{B}} = -\tau^{\mathrm{M}}$, which is equivalent to the rod condition $m_3^{\mathrm{B}} = -\tau^{\mathrm{M}}$ since $\mathbf{e}^{\mathrm{M}} = \mathbf{d}_3^{\mathrm{B}}$. This means that we are fixing $\dot{m}_3^{\mathrm{B}} = 0$. The other components of torque and force are obtained by time stepping, which will be discussed in §6.4. At a given time t we have the values of $\mathbf{x}^{\mathrm{B}}$, $\mathbf{d}_i^{\mathrm{B}}$, $\mathbf{n}^{\mathrm{B}}$ and $\mathbf{m}^{\mathrm{B}}$. From these we can compute $\mathbf{x}^{\mathrm{T}}$ and $\mathbf{d}_i^{\mathrm{T}}$, giving us the configuration of the flagellar filament.

For a BEM mesh with N collocation nodes, we have a system of $3N$ boundary integral equations (2.25) and 12 additional equations from the force and torque balance considerations (6.18). The unknowns at a given time are the $3N$ viscous traction components on the surface mesh, the 6 body velocities $\mathbf{U}^{\mathrm{B}}$ and $\boldsymbol{\Omega}^{\mathrm{B}}$, the 5 rates of change of hook force and moment $\dot{\mathbf{n}}^{\mathrm{B}}$, $\dot{m}_1^{\mathrm{B}}$ and $\dot{m}_2^{\mathrm{B}}$, and the motor frequency ω^{M}. This means that there are $3N + 12$ unknowns and an equal number of equations, which we solve as for the rigid hook model of bacterial swimming in previous chapters.

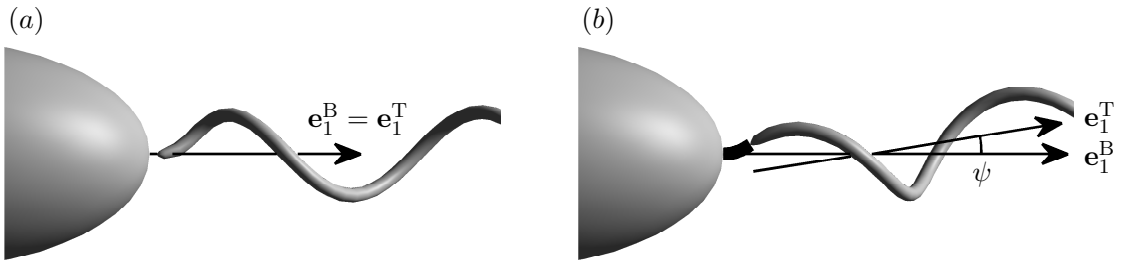

Figure 6.1: Comparison between (a) the rigid hook model and (b) the current, flexible hook. The alignment angle between the body axis, $\mathbf{e}_1^{\mathrm{B}}$, and the flagellum axis, $\mathbf{e}_1^{\mathrm{T}}$, is denoted ψ. Since the shapes of the flagella differ near the cell body, the rigid model is not simply the limiting case where stiffness is taken to be very large in the flexible hook model. In both models we assume the motor axis is aligned with the major axis of the cell, i.e. $\mathbf{e}^{\mathrm{M}} = \mathbf{e}_1^{\mathrm{B}}$.

Table 6.1: Parameters used for bacterial swimmers in this chapter. Bacterial shape B is based on parameters for the monotrichous bacterium, *R. sphaeroides*, estimated from Armitage et al. [5]. See §3.1 for descriptions of variables and Fig. 6.2 for illustrations of the two swimmers.

Shape	$\lambda/\bar{a}$	$L/\bar{a}$	ak	$a_1^{\mathrm{B}}/a_2^{\mathrm{B}}$	$L^{\mathrm{H}}/\bar{a}$	$a^{\mathrm{T}}/\bar{a}$
A	2.0	10.0	1.0	2.0	0.2	0.05
B	1.8	7.4	1.0	1.6	0.2	0.02

The geometrical differences between the rigid hook model and the new, Kirchhoff model are shown in Fig. 6.1. An important distinction is that we no longer employ the helical amplitude envelope described in §3.1. The flagellar filament is purely helical.

We will present results in this chapter using two sets of parameters for the shape of the bacterial cell body and flagellum. We refer to the first as shape A and use this wherever the shape is otherwise not specified. The second shape, B, uses parameters estimated for *R. sphaeroides* [5]. The key parameters are listed in table 6.1 and the shapes of the bacteria are shown in Fig. 6.2. Both of these shapes give rise to boundary accumulating behaviour near a single no-slip plane boundary when the parameters are used in the rigid hook model.

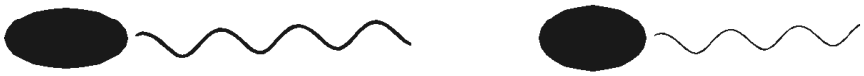

Figure 6.2: Illustrations of bacterial shape A (left) and B (right). See table 6.1 for geometry parameters used.

.

6.4 Hook behaviour in free space

In principle, the predictor–corrector method employed in the preceding chapters could also be used to track the motion of the model bacterium with a flexible hook. However, the elastic dynamics of the hook introduce a very short timescale compared with the motor revolution, making the system of equations stiff. In order to avoid using prohibitively short time steps, an implicit rule must be used for time stepping. It was found that good results can be achieved by using the backward Euler integration rule for time stepping the hook force, $\mathbf{n}^{\mathrm{B}}$, and the trapezoidal rule for the other quantities. The trapezoidal rule, being a second order method, allows more accurate tracking while the backward Euler method is more effective at damping numerical errors.

The configuration of the bacterium is updated during time stepping as follows. Given the velocities $\mathbf{U}^{\mathrm{B}}$, $\boldsymbol{\Omega}^{\mathrm{B}}$, $\dot{\mathbf{n}}^{\mathrm{B}}$, $\dot{\mathbf{m}}^{\mathrm{B}}$ and ω^{M}, the entire swimmer is moved to its new position in the manner described in §3.3. The final step of incrementing the flagellar phase is performed by rotating the hook director basis $\{\mathbf{d}_i^{\mathrm{B}}\}$ by the angle $\omega^{\mathrm{M}}\delta t$ about the motor axis $\mathbf{e}^{\mathrm{M}}$. The force and moment $\mathbf{n}^{\mathrm{B}}$ and $\mathbf{m}^{\mathrm{B}}$ exerted on the body by the hook are incremented $\dot{\mathbf{n}}^{\mathrm{B}}\delta t$ and $\dot{\mathbf{m}}^{\mathrm{B}}\delta t$ respectively, which then allows computation of $\mathbf{x}^{\mathrm{T}}$ and $\{\mathbf{d}_i^{\mathrm{T}}\}$. Finally, the flagellum filament is repositioned as a rigid extension of the tip of the hook.

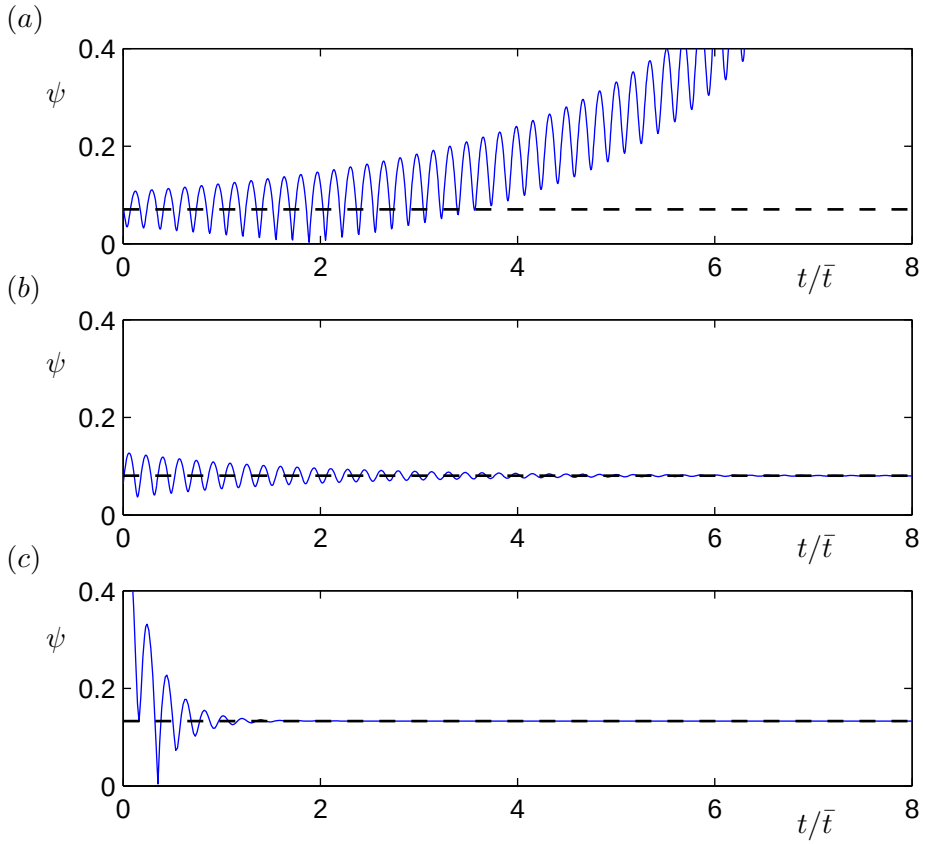

Figure 6.3: Evolution of alignment angle ψ showing transient hook behaviour at different levels of stiffness. The steady state alignment angles are plotted as dashed lines (see Fig. 6.5). (a) $k^{\mathrm{H}} = 0.4$, (b) $k^{\mathrm{H}} = 0.5$, (c) $k^{\mathrm{H}} = 1$. Time is non-dimensionalised by the timescale $\bar{t} = 16\pi^2\bar{a}^3\mu/\tau^{\mathrm{M}}$, where $\bar{a}$ is the body's volumetric radius, μ is the dynamic viscosity of the fluid and τ^{M} is the magnitude of the motor torque.

Starting from nearly straight hooks, one of the observed outcomes of time stepping simulations in unbounded fluid is that the hook approaches a steady state. This means that the hook force and moment converge to stable values after which the flagellum simply rotates with some angular rate ω^{M} about the motor axis. In other simulations, the oscillations in alignment between the cell body and flagellum grow until the hook curvature becomes too large for the scope of the current model. Examples of these hook dynamics are given in Fig. 6.3 and corresponding swimmers are shown at various times during a run in Fig. 6.4.

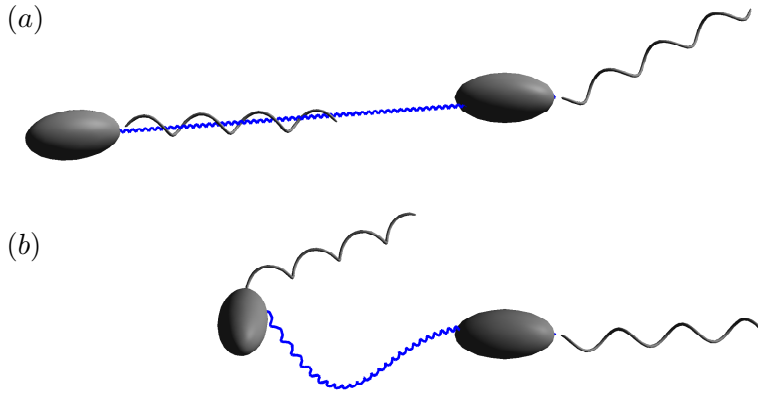

Figure 6.4: Exemplar swimmers (a) with a stable hook state and (b) with an unstable steady hook state. The initial configurations (right) are out of equilibrium but a steady state is soon reached in the stable case. The paths of the junction point $\mathbf{x}^{\mathrm{B}}$ are shown as solid curves. The trajectories correspond to cases (c) and (a) respectively from Fig. 6.3.

Further details of the dynamics and how the stiffness of the hook affects the resulting motion can be obtained by analysing the steady hook state using linear stability theory.

6.5 Steady states of the hook

Since we will only consider swimmers with an axisymmetric cell body, in unbounded fluid the velocities in the reference frame of the hook are independent of the rotational phase of the body relative to the hook. In this basis, the velocities depend only on the instantaneous shape of the hook, which is determined by $\mathbf{n}^{\mathrm{B}}$ and $\mathbf{m}^{\mathrm{B}}$. Thus, we can write

$$\mathbf{v} = \mathscr{F}(\mathbf{n}^{\mathrm{B}}, \mathbf{m}^{\mathrm{B}}), \tag{6.20}$$

where $\mathbf{v}$ can describe any of the velocities written in the hook basis, such as the translational velocity of the swimmer, and $\mathscr{F}$ is a function that we are able to numerically evaluate by solving the BEM problem. Consider the case where $\mathbf{v}$ is the vector of time derivatives of the hook forces and moments. Then the roots of the

function $\mathscr{F}$ are the steady states of the hook, $\mathbf{n}^{\mathrm{B}*}$ and $\mathbf{m}^{\mathrm{B}*}$. The stability of this state is given by the eigenvalues of the matrix of partial derivatives of $\mathscr{F}$. We denote the real part of the eigenvalue with the greatest real part by Λ. The steady state is stable if $\Lambda < 0$ and unstable if $\Lambda > 0$.

We use Newton's method to locate the steady states. Convergence using this method usually requires a good initial estimate of $\mathbf{n}^{\mathrm{B}*}$ and $\mathbf{m}^{\mathrm{B}*}$. This may come from a known steady state of a similar swimmer or from simulating the transient dynamics of the hook until an equilibrium is reached. Once a steady state is found, the Jacobian matrix can be computed using finite difference formulas.

The response of the steady state as the hook stiffness is gradually varied is plotted in Fig. 6.5. We find that below a critical value of hook stiffness $k^{\mathrm{H}} \approx 0.5$, the steady state is unstable. In these cases, the hook forces and torques diverge, resulting in highly deformed hook shapes for which the present Kirchhoff model is inadequate. In an intermediate range of hook stiffness, the flagellum is well aligned with the axis of the body and the swimming speed is close to that calculated for the corresponding bacterium in the rigid hook model. However, for high values of hook stiffness, there is a significant misalignment between the body and flagellum due to the hook being nearly straight. This leads to much lower swimming speeds as there is more oscillatory, lateral motion. A sharp jump in the stability measure, Λ, can be seen at $k^{\mathrm{H}} \approx 2$, which coincides with the transition from the strong to the poor swimming regime.

6.5.1 Bend/twist ratio

The bend/twist ratio Γ determines the relative tendency for a structure to bend or twist. This ratio is also related to the Poisson ratio ν by the formula $\Gamma = 1/(1+\nu)$. In particular, $\Gamma = 2/3$ corresponds to an incompressible material and $\Gamma = 1$ means that there is no transverse strain when the material is stretched in one direction. The value for most common materials lies between these limits. However, simulations of

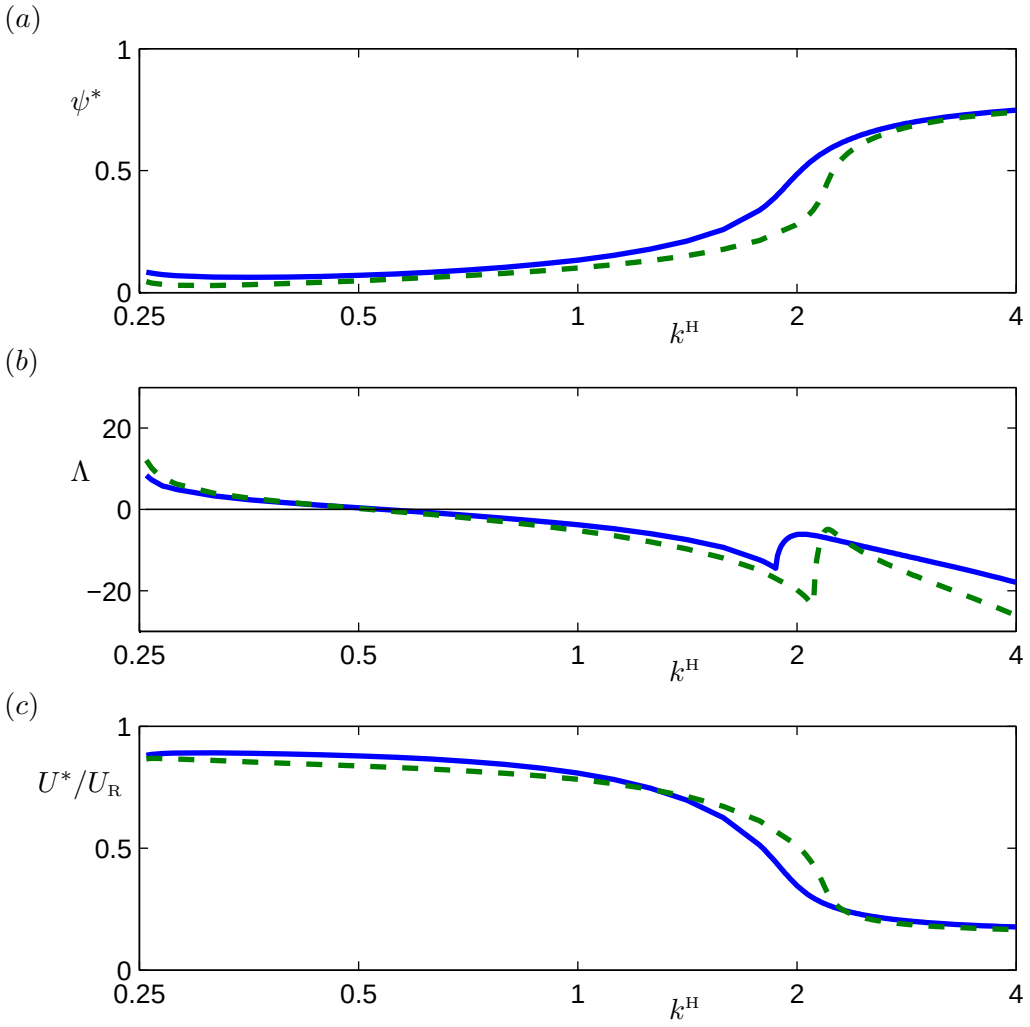

Figure 6.5: Variations in steady state (a) alignment angle, (b) stability and (c) swimming speed with hook stiffness. Solid curves indicate data for bacterial shape A while dashed curves correspond to shape B. Swimming speeds in (c) are plotted relative to the speeds, U_{R}, calculated using the previous rigid hook model with the equivalent geometrical parameters.

the hook structure have given an estimated value of $\Gamma \approx 20$ [48]. Using our model, we found differences of no more than 0.002% in alignment angle and swimming speed while varying Γ from 0.5 to 32. This insensitivity is due to the fact that Γ characterises the resistance to twisting deformations. Changing this parameter simply alters the rate of twisting of the transverse hook directors around the tangent vector with respect to arc length without affecting the geometrical curvature of the centreline. We use the value $\Gamma = 1$ in all of the results presented.

6.5.2 Hook length

For a constant rigidity, increasing the length of the hook leads to gradual but non-monotonic changes in swimming speed and alignment angle (Fig. 6.6). Experimental measurements indicate that wild-type bacterial strains have hooks roughly 100 nm long. We varied the simulated hook length from the equivalent of 35 nm to 700 nm and found that the free space swimming speed and cell body–flagellum alignment angle varied by no more than 10%. However, this does not indicate that hook length

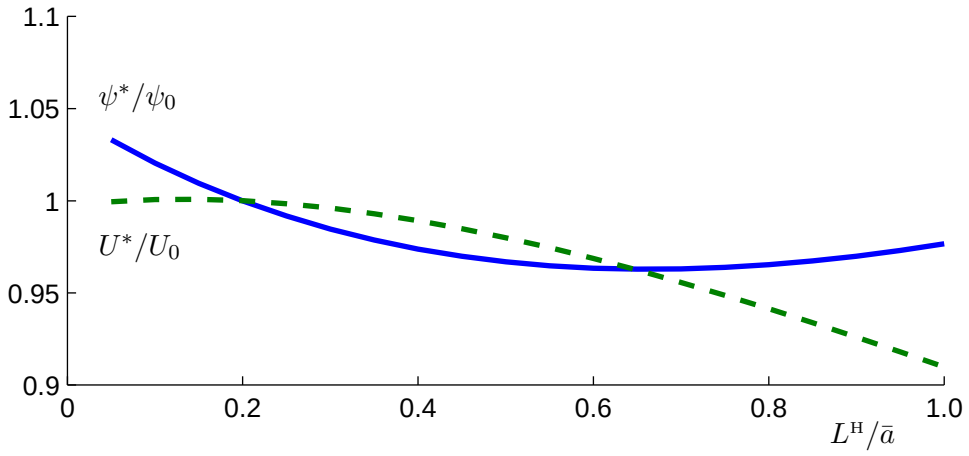

Figure 6.6: Variations in alignment angle (solid curve) and swimming speed (dashed curve) with hook length $L^{\mathrm{H}}/\bar{a}$. The lengthscale $\bar{a}$ is the volumetric radius of the cell body and the alignment angles and swimming speeds are shown normalised by the values ψ_0 and U_0 respectively for our standard swimmer A with hook length $L^{\mathrm{H}}/\bar{a} = 0.2$.

regulation is unnecessary in bacteria since the hook rigidity, $k^{\mathrm{H}} := EI/(\tau^{\mathrm{M}} L^{\mathrm{H}})$, is inversely proportional to its length and we have seen that hook rigidity has a significant effect on swimming motion.

6.5.3 Boundary accumulation

By simulating the same swimmer in a half space fluid domain, we now explore the effect of hook flexibility on near-surface swimming. This is more complicated to precisely analyse because the instantaneous dynamics depend on the distance and orientation relative to the wall as well as the forces and torques on the hook. Allowing the initial transient period to pass, we still observe steady motion at a constant distance from the wall for some values of hook stiffness (Fig. 6.7). However, instead of the constant hook state found in free space, we find oscillations on the timescale of the motor revolution as the boundary disrupts the invariance with respect to motor phase.

We also note that the stable near-surface orbit is very sensitive to hook stiffness and that there is a non-trivial relationship between the two. The boundary behaviour for bacterial shape A is summarised in Fig. 6.8. At an intermediate value of stiffness, $k^{\mathrm{H}} = 1$, the flagellum is well aligned with the body and the free space behaviour is very similar to that of the model swimmer with a rigid hook analysed in previous chapters. In a half space, there is minimal perturbation of the free space steady hook alignment and the boundary accumulation is similar to the behaviour of the rigid hook model swimmer.

Increasing the hook stiffness from $k^{\mathrm{H}} = 1$ decreases the accumulation height slightly until the critical point that we observed in free space at which the alignment angle becomes large and the swimmer tends to "wobble" significantly. This causes a larger fluctuation in junction height above the wall, seen in Fig. 6.8, as well as a slightly increased average height.

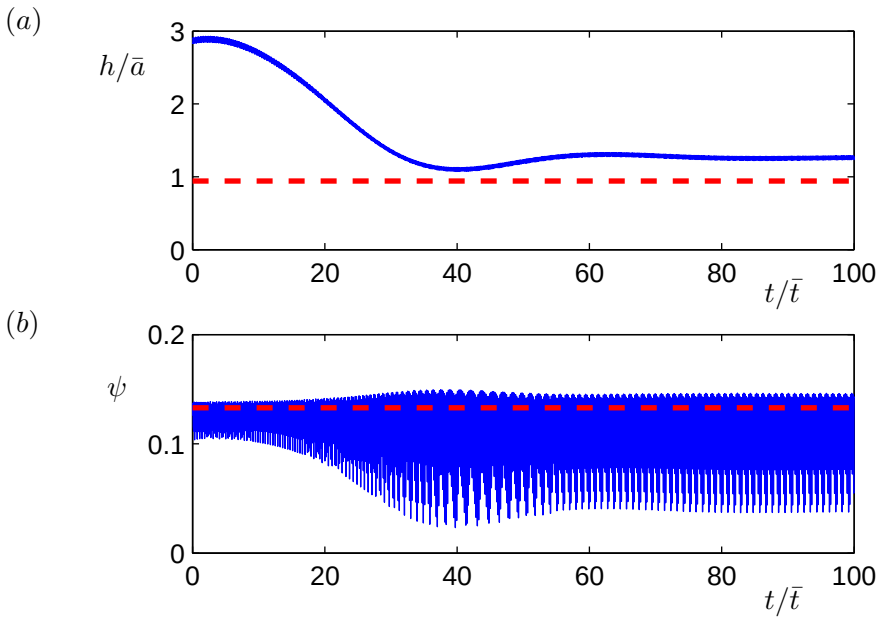

Figure 6.7: Time series of (a) junction height, h, and (b) hook alignment angle, ψ, as a bacterium with hook stiffness $k^{\mathrm{H}} = 1$ approaches a stable orbit above a plane boundary. The stable accumulation height of the rigid hook model equivalent, $h^*/\bar{a} \approx 0.94$ is indicated by a horizontal dashed line in (a) and the value of the stable alignment angle $\psi^* \approx 0.13$ in free space is marked by a horizontal dashed line in (b).

If we instead decrease the hook stiffness from the value $k^{\mathrm{H}} = 1$, we find the stable accumulation height increases gradually before dropping rapidly below about $k^{\mathrm{H}} = 0.65$. By $k^{\mathrm{H}} = 0.6$ we could no longer find a stable boundary accumulating trajectory as the swimmer had a strong tendency to swim into the wall. Close to this critical stiffness, an increase in the alignment angle relative to the free space stable alignment can be observed. This is reminiscent of the loss of stability of the steady hook configuration seen in free space at around $k^{\mathrm{H}} = 0.5$ (Fig. 6.5). The wall may have a destabilising effect on the hook by exerting additional stresses on the flagellum, causing the alignment angle to grow at hook stiffnesses slightly higher than the free space critical point.

This pattern of near-boundary behaviour does not seem to be universal, that is,

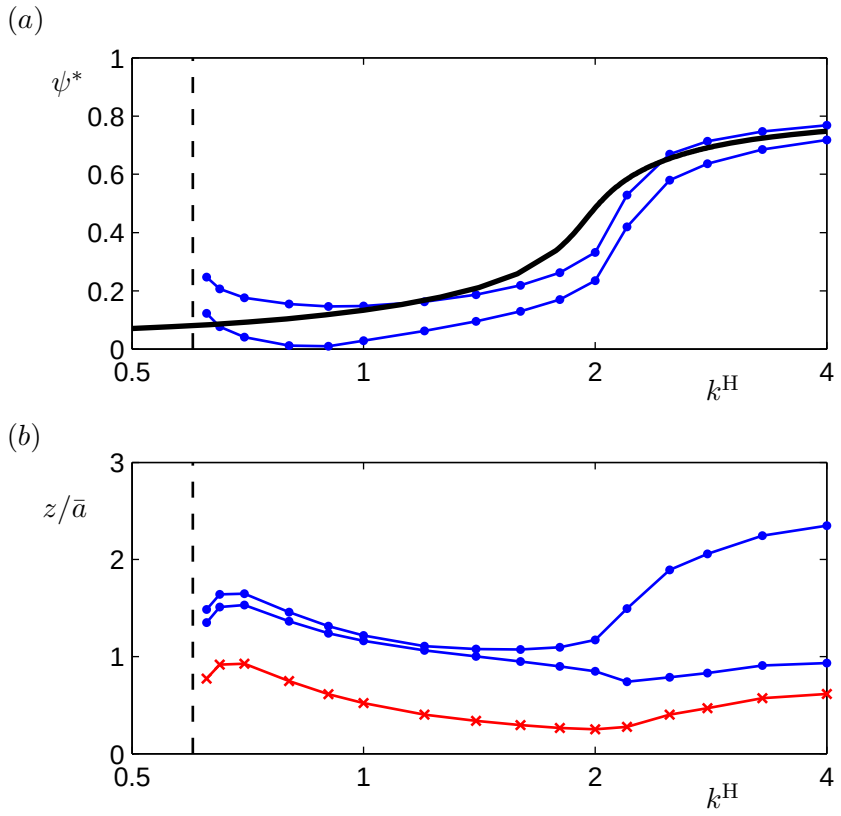

Figure 6.8: Swimming behaviour of bacterial shape A near a plane boundary with varying hook stiffness. (a) Curves marked with dots indicate the minimum and maximum alignment angles observed after transience compared with the free space stable angle shown by the unmarked, thick curve. (b) The minimum and maximum swimming heights over a revolution of the motor during stable boundary swimming after transience (curves marked with dots) and the minimum separation distance between the wall and the swimmer (curve marked with crosses). Using the rigid hook model, this swimmer would have a stable swimming height of $h^*/\bar{a} \approx 0.94$. The dashed lines on the left hand side mark the stiffness value for which the swimmer was found to collide with the wall below and no boundary accumulating trajectory could be obtained.

other swimmer shapes have different responses to variations in hook stiffness. With bacterial shape B, stable orbits were found for a much narrower range in stiffness, as shown in Fig. 6.9. Throughout the intermediate range of stiffness, a similar trend to that with shape A was observed: the stable height increased with decreasing stiffness. However, the change was very abrupt near $k^{\mathrm{H}} = 1$ and trajectories failed to remain close to the wall when values $k^{\mathrm{H}} \leq 0.975$ were used. Similarly, trajectories consistently deflected away from the boundary when values $k^{\mathrm{H}} \geq 2.5$ were tested. This swimmer appeared to transition from a boundary accumulator at intermediate values of hook stiffness to a boundary escaper when the stiffness was too low or too high.

Two boundary accumulating trajectories for bacterial shape A are shown in Fig. 6.10. One swimmer has hook stiffness $k^{\mathrm{H}} = 0.7$, which is close to the lower limit for stable boundary accumulation, and the other has stiffness $k^{\mathrm{H}} = 2$, just at the onset of "wobbling" motion. In addition to the difference in accumulation height, we can see a significant change in the curvature of the circular paths resulting purely from the change in hook stiffness.

6.6 Discussion

Our results suggest that hook flexibility may be an important factor in determining swimming dynamics of bacteria. We found a sharp transition from effective swimming to inefficient "wobbling", which occurs when the hook is too rigid to allow the helical flagellum to be aligned with the body for effective propulsion. This behaviour occurs because the hook is naturally straight and is less likely to bend at high rigidities. The hook attaches to the flagellar filament with a continuous tangent but since the tangent to the helical filament is not in the direction of the helix axis, the flagellum rotates about an axis that is not close to its natural axis, causing large wobbling motion and low mean speed.

A hook that is too flexible might also hinder swimming, according to our

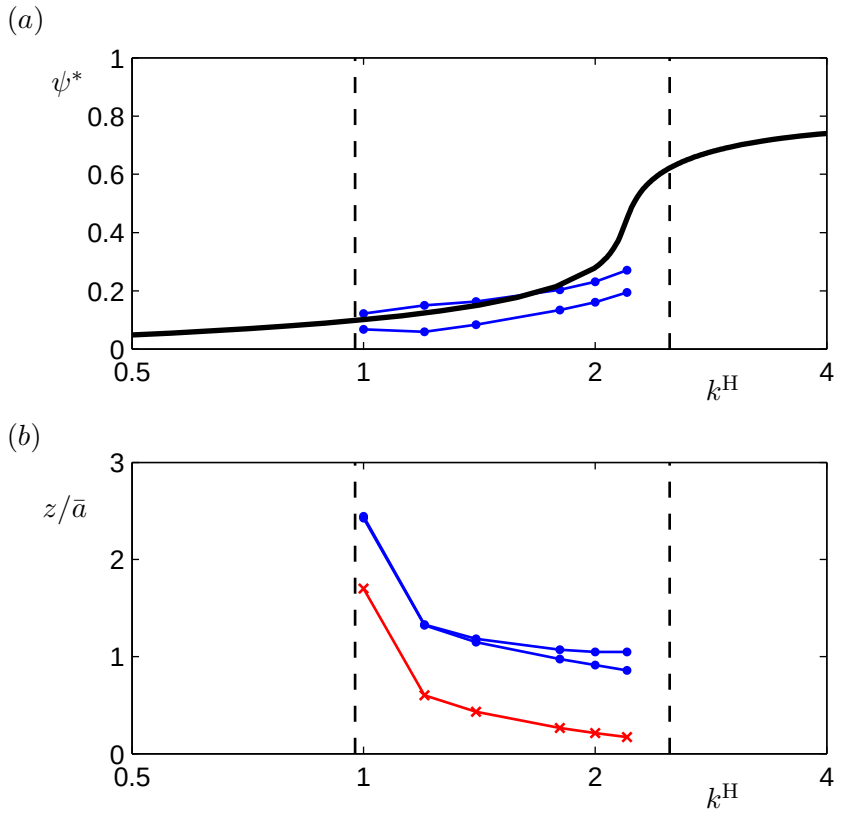

Figure 6.9: Swimming behaviour of bacterial shape B near a plane boundary with varying hook stiffness. (a) Curves marked with dots indicate the minimum and maximum alignment angles observed after transience compared with the free space stable angle shown by the unmarked, thick curve. (b) The minimum and maximum swimming heights over a revolution of the motor during stable boundary swimming after transience (curves marked with dots) and the minimum separation distance between the wall and the swimmer (curve marked with crosses). Using the rigid hook model, this swimmer would have a stable swimming height of $h^*/\bar{a} \approx 0.92$. The dashed lines on the left and right hand sides mark stiffness values for which the swimmer was found to escape from the wall and no boundary accumulating trajectory could be obtained.

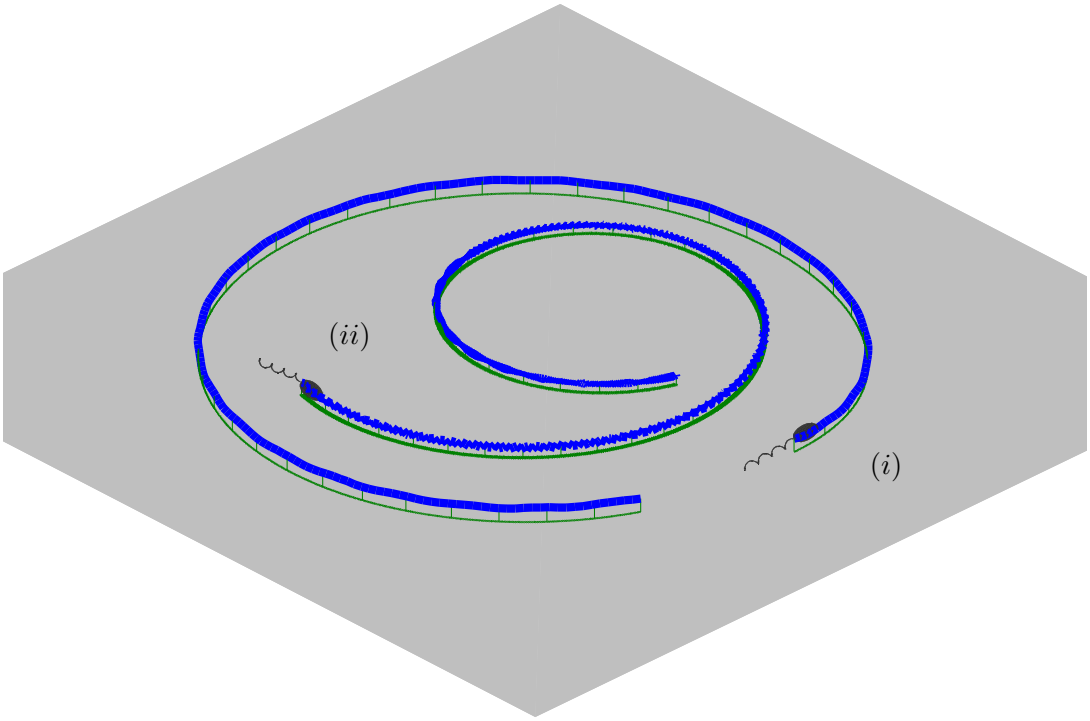

Figure 6.10: Trajectories of two geometrically identical swimmers near plane boundaries. Swimmer (i) has hook stiffness $k^{\mathrm{H}} = 0.7$ and swimmer (ii) has hook stiffness $k^{\mathrm{H}} = 2$. The 3-D trajectories are shown in thick, blue curves while projections of the trajectories onto the x–y plane are shown in thin, green curves. The heights of the swimmers above the wall are also indicated at regular time intervals by vertical lines from the x–y plane. The bacteria are shown at their respective starting positions. Note the much smaller radius of curvature of swimmer (ii) once the steady circular orbit is reached.

simulation results. Below a threshold stiffness, we found that the hook force and torque would suddenly undergo rapid changes (data not shown) characteristic of dynamical instabilities. Buckling of beams and rods is very interesting and has been extensively studied in other contexts [58, 129, 124]. However, the current model does not aim to probe this complex phenomenon. We simply suggest that buckling and unsteady behaviour of the hook could be detrimental to effective swimming.

While hook flexibility is clearly necessary in peritrichous bacteria, where many filaments must wrap around the cell body to join a flagellar bundle, it is not understood what role hook flexibility has in monotrichous species. Analysis of several species revealed that hooks from monotrichous and peritrichous bacteria have similar stiffnesses [110]. From the results we have shown, there may be a bounded range of hook stiffnesses allowing good swimming performance in monotrichous bacteria. Using available parameter data, the physiological stiffness can be estimated at $k^{\mathrm{H}} \sim 0.1$–1, the upper portion of which matches well with our computed regime of effective swimmers. However, comparisons must be made with care as comprehensive experimental data has not been collected for *R. sphaeroides* or any other suitable species. It is uncertain how accurate elastic moduli from other species would be as estimates for *R. sphaeroides*, which is known to have a number of unusual characteristics, including a naturally straight hook that our model assumes.

Using a modification of the method described in this chapter, one could examine the dynamics of bacteria with naturally curved hooks. Depending on the preferred curvature, there could be a much less restrictive upper bound on hook stiffness since body–flagellum alignment would require less deformation of the hook.

Authors [128] have noted that the motility of flagellated bacteria is sensitive to hook length. Mutants that grow abnormally long hooks have an impaired ability to swim. Our simulations showed only a modest variation in swimming behaviour with hook length for a given stiffness. However, hook stiffness is inversely

proportional to hook length so we would expect long hooks of mutants to have decreased stiffness. We found that decreasing stiffness leads to better swimming speeds, seeming to contradict empirical evidence. However, dynamical instabilities arise below a threshold, providing a possible mechanical explanation for the need to regulate the hook length.

Away from extremes of hook rigidity, there is little qualitative difference between the rigid hook model and the current model in unbounded fluid, where we find that the hook quickly enters a steady state and therefore becomes indistinguishable from rigid to an observer. The main difference is that the shape of the connecting hook is found through elastic rod equations rather than approximated by the growing helical amplitude of the rigid hook model. Another difference is that the tail axis is not perfectly aligned with the body axis. This causes a slight "wobble" in the swimming motion of the bacterium, which is frequently observed under the microscope. This "wobble" is also present in the rigid hook model but is of much smaller magnitude and not readily discernible in simulation movies.

Although there does not appear to be significant perturbations in the hook as the swimmer approaches a boundary, we find that boundary accumulation is very sensitive to hook flexibility. In some cases there may be abrupt transitions from boundary accumulating to boundary escaping behaviour. Even within the range of stable surface swimming, changes in hook stiffness affect the steady state separation between the wall and the swimmer. The variations in stable swimming height are not always monotonic and can appear modest, between about $h^*/\bar{a} = 1$ and $h^*/\bar{a} = 1.5$ for shape A. A larger range, $h^*/\bar{a} = 1$ to $h^*/\bar{a} = 2.5$, was found for shape B.

However, in terms of separation distances, the effect of hook stiffness is actually substantial. Since h^* is measured from the wall to the cell body–hook junction, the gap between the wall and the closest point on the swimmer is considerably smaller. As shown in Fig. 6.9, these stable swimming heights translate to minimum separations

that vary from $0.07\,\bar{a}$ to $1.6\,\bar{a}$ as the stiffness is altered. The lower figure amounts to about 50 nm, which, depending on the substrate, could make the bacterium susceptible to close range surface interactions. At the other end of the range, $1.6\,\bar{a}$ is over 1 μm at the lengthscale of *R. sphaeroides* and well beyond the range of likely surface forces.

Thus, hook flexibility could alter the likelihood of close range surface interactions as well as the tendency to accumulate near surfaces at all. The changes in preferred separation also have a significant impact on the strength of hydrodynamic wall interactions and hence the radius of curvature of the circular orbit, as evident in Fig. 6.10. Along with the details of the bacterium's shape, such as cell body aspect ratio and flagellum length, hook stiffness is an important factor in determining the swimming behaviour near boundaries.

6.7 Conclusions

Many aspects of the role of bacterial hooks are not yet fully understood. It is accepted that the flexibility of the hook is important to peritrichous bacteria, which require the flagellar filaments all over the cell body to point backwards and form a bundle for propulsion. The benefits offered to monotrichous bacteria are less clear. Indeed, through simulations of monotrichous bacteria with flexible hooks, we find that the hook usually relaxes to a steady shape for swimmers in unbounded fluid. In this state, the motion is indistinguishable from the case where the the hook is rigid so there appears to be no need for flexibility. This supports the common assumption that the hook is rigid in mathematical and numerical models as long as steady swimming motion is being considered.

However, it is precisely the flexibility of the hook that allows the correct shape to be attained. A stiff hook would not permit the attached helical filament to align with the principal axis of the cell body and therefore swimming would be impeded. On

the other hand, if the hook is too flexible compared with the torque exerted by the motor, the required hook shape cannot be maintained and the flagellum again loses alignment with the cell body. Hence, our simulations indicate lower and upper bounds on the hook stiffness suitable for a swimming bacterium. These bounds are geometry dependent but are of a similar order of magnitude to estimates of physiological hook stiffness.

It has been observed that hook length regulation is important to achieving motility. This can be explained by the lower and upper bounds on hook stiffness described above, since increasing the length of an elastic rod decreases the stiffness of the overall structure. If we instead maintain the same effective hook stiffness but change the hook length, we find only slight variations in the resulting swimming speed.

Near plane boundaries, the flexibility of hooks can have further consequences. Our model treating the bacterial hook as an elastic rod was able to exhibit the same boundary accumulation trajectories that have been predicted using model swimmers with rigid hooks, such as those in the preceding chapters of this thesis. However, the stiffness of the hook influences the resulting behaviour near boundaries. Depending on bacterial geometry, there may be transitions between boundary colliding, boundary accumulating and boundary escaping behaviour within the span of hook stiffness suitable for swimming.

Since the hook stiffness is defined relative to the motor torque, we deduce that the viscosity of the medium may alter the behaviour of the hook and consequently the boundary accumulation of the cell. This is because the exerted motor torque varies with the frequency. Depending on the location of intersection between the motor torque–frequency curve and the flagellum load curve, increasing the fluid viscosity may result in a decrease in frequency and simultaneous increase in motor torque, which would effectively reduce the hook stiffness.

We also conclude that it may be possible to dynamically control boundary

accumulation by adjusting the motor activity in a fixed medium. When the torque is high, the relative hook stiffness is low. Using parameters based on *R. sphaeroides*, lowering the hook stiffness was found to cause the swimmer to escape from the wall. This effect could be of interest to engineers of artificial flagellated micro-swimmers.

Most bacteria are unlikely to have sufficient motor control to regulate boundary accumulation in this way but *R. sphaeroides* is known to have a variable-speed motor [96]. Modulation of motor speed, which is linked to motor torque, could result in substantial changes in the hook shape and dynamics, with the possibility of not only inducing boundary escape but also unpredictable reorientation, or tumbling, resulting from the elastic instability seen when the stiffness is sufficiently low. This would be an interesting area of further investigation.

Chapter 7

Discussion and future work

7.1 Discussion

In this thesis we have presented simulation results related to the propulsion of flagellated bacteria and the dynamics of bacteria in confined fluid environments. We now discuss the implications of our key findings, with particular attention to: comparisons with other approaches to modelling, understanding the circumstances that make surface colonisation by bacteria likely, guiding the designs of microfluidic devices containing bacteria and designing artificial flagellated micro-swimmers.

7.1.1 Swimming efficiency

Calculating power and torque efficiency of swimmers with different cell and flagellum shapes, we found that torque efficiency favoured more elongated cell bodies and shorter flagella with smaller helical amplitude compared with power efficiency. Optima of these two criteria were fairly broad, however, making efficient swimming robust to variability in the precise shape of a bacterium. Although we cannot conclusively link real bacterial examples to either optimisation criterion, the contrast between the two optima highlights the necessity to specify the most appropriate objective function. In designing a swimmer, considerations such as motor performance, power source and intended duration of operation would determine the factors that are important for optimisation.

7.1.2 Swimming near surfaces

Three classes of behaviour emerged from simulations of swimming near a plane boundary: bacteria can be attracted towards walls to the point of collision, approach walls from afar but settle at a stable distance of the order of a body length from the wall, or show a strong tendency to swim away from walls. By systematically varying many of the parameters determining the shape of the swimmer, we found that boundary behaviour was particularly sensitive to the aspect ratio of the cell body and the length of the flagellum. Changes in these parameters can affect whether bacteria accumulate or escape from surfaces, with abrupt transitions near critical points.

For this reason, it can be important to use accurate parameter values in models; the spherical cell body commonly used for its mathematical simplicity has a strong tendency to swim into surfaces, while an elongated cell more accurately resembles rod-shaped bacteria and is able to swim at a steady distance from boundaries. As a consequence, models that treat bacteria as "pusher" point force dipoles in a fluid require adjustment based on cell and flagellum shape to correctly capture the dynamics even at moderate and far distances from a boundary.

The effect of swimmer geometry on boundary behaviour must also be considered when designing an artificial micro-swimmer; for example, swimmers with spherical bodies will not be able to swim effectively in the presence of surfaces.

The behaviour of a bacterium near a plane boundary is intimately linked with the expected behaviour in other fluid domains. For example, boundary escaping bacteria tend to "bounce" with shallow incidence angles between two parallel plates while the projection of the trajectory onto the plane is nearly straight. By contrast, boundary accumulating bacteria execute circular orbits close to one plate except when the plate separation is very small, in which case they also swim in straight paths. In channels, bacteria either tend to swim along the edges, occasionally crossing from one edge to another depending on channel dimensions, or swim predominantly

through the central region of the channel, deflecting whenever a wall is approached. These characteristics correspond to swimmers that accumulate or escape from plane boundaries respectively.

Our results have given many testable predictions for factors that influence the expected distribution of bacteria in a particular environment, which is important for understanding when and where surface adhesion leading to biofilm formation might be more likely to take place. For instance, it is predicted that shorter cell bodies and longer flagella encourage bacteria to swim in close proximity to surfaces, facilitating adhesion. Edges are particularly attractive to boundary accumulating bacteria so these locations would be the most vulnerable to surface colonisation within a fluid channel. However, the width and height of channels can be chosen so that streams of bacteria moving in opposite directions are naturally separated into different edges of the channel. This reduces collisions between cells, increasing the average rate of flow of cells and reducing the the risk of adhesion due to cells being driven into channel walls by the impact.

Boundary accumulation properties can be exploited to separate cells in a population by size and shape. This has already been demonstrated by Hulme et al. [68]. The design of microfabricated channels for manipulating bacteria can be aided by the findings of our simulations of swimming in channels and between parallel plates. For example, the circular swimming induced in boundary accumulating bacteria between widely separated plates can be used to effectively randomise the swimming direction, assuming the bacteria eventually escape from such an orbit. We can also attempt to control the flow direction by constructing a channel so that the cells are separated into different edges according to their direction. Bacteria travelling against the desired direction could then be "skimmed off" and rerouted by branching channels, similar to those used by Hulme.

7.1.3 Effect of hook stiffness

In our model, which assumes a naturally straight hook connected to a rigid helical flagellar filament, there was a range of hook rigidities that permitted effective swimming motion, roughly coinciding with physiological estimates. This suggests explanations for the observed flexibility of hooks in monotrichous bacteria as well as reasons for the tight regulation of hook length.

Within the bounds of hook stiffness for effective swimming, the hook was found to relax to a steady shape during free space swimming with the helical flagellum trailing behind the cell body in the familiar manner. The subsequent motion can equivalently arise from a model assuming a completely rigid hook, thereby validating this assumption at least in unbounded fluid or when the deviation from the unbounded case is small.

The stiffness of the flagellar hook was shown to be influential to the behaviour of swimmers near boundaries. The relationship has not yet been completely determined but our results indicate that increasing the rigidity generally leads to stronger boundary attraction. Since reducing the motor torque has the same effect as increasing hook stiffness, apart from a rescaling of time, this suggests a way to induce an escape from or attraction to boundaries in artificial swimmers. There may also be relevance to the behaviour of certain bacterial species, such as *R. sphaeroides*, which have variable-speed motors [96].

7.2 Future work

We have attempted to focus on practical, observable issues regarding bacterial locomotion and behaviour near surfaces. Consequently, many of the results we have obtained from simulation lend themselves to experimental verification. Since boundary accumulation is an inherently three-dimensional problem, conventional 2-D microscopy is of limited use. However, there are techniques available for tracking

the 3-D motion of micro-organisms. Holographic microscopy is an example and recent advances have demonstrated the ability to simultaneously track the three-dimensional movement of thousands of cells, about 6–10 μm in length, in a dense suspension [112]. Data was recorded at a rate of 120 frames per second and digitally reconstructed two-dimensional images could achieve resolutions of just under 1 μm. Although a significant improvement is required before the flagella can be imaged with this technique, it is quite reasonable to use holographic microscopy to track the motion of bacterial cell bodies. This would allow numerical predictions such as separation distances from surfaces, spiralling trajectories and edge accumulation in channels to be tested *in vitro*.

The current model for bacterial propulsion can be used with little or no modification to analyse many more scenarios of relevance to microfluidics or biomedicine. The attraction of bacteria to channel edges may suggest that circular channels would be less susceptible to surface colonisation, due to the lack of edges. However, bacterial encrustation is known to be a widespread problem in ureteral stents and catheters, which are of circular cross-section. It may be fruitful to investigate swimming in cylinders using numerical simulation. In such situations, it is reasonable to suggest that preventing bacteria from entering the channels would be beneficial. Hence, the interface between a more open chamber and a channel opening would be an interesting environment to explore.

A natural extension to swimming in channels, especially in light of the relevance to bacterial colonisation of catheters, is to investigate the effect of background shear flows. Experiments on *E. coli* swimming in flow cells indicated a tendency to swim in the upstream direction [65]. The hydrodynamic cause of this would be elucidated by numerical simulation.

We have considered parallel plates and channels but in practice these geometries will not continue infinitely. One more environment should be analysed in order to

complete our understanding of swimming in a basic microfluidic device; a corner where three mutually perpendicular walls meet. This is an important part of bacterial dynamics in microdevices where, for example, there might be a number of cuboidal chambers connected by channels. It is difficult to imagine anything other than collisions occurring when a bacterium swims into a corner so close-range bacterium–wall forces will probably be critical. Substantial deformations of the flagellar hook and filament may be expected as well, but to consider the latter would require a significant extension of the model.

Including elastic deformations of the filament would be important for other investigations, such as the bundling of flagella in peritrichous bacteria. This has already begun to receive attention [126, 47] but is a complex topic, made more so by numerous polymorphisms. Elasticity is an integral part of tumbling and its monotrichous counterparts, motor stops and reversals, which have evolved as different means to the common goal of reorientating the cell. Through simulation, we may be able to learn what the implications of these mechanisms for reorientation are and why different bacteria employ different methods. Since reorientation is linked with search strategies, this can give insight into statistical descriptions of chemotaxis and how this process changes close to a substrate, for example.

Our model for incorporating the elastic effects of hook bending with fluid–surface interactions can also be used to investigate dynamics of tethered bacterium cells. Many authors have examined the properties of the bacterial motor, hook and flagellum by rotating cells that are bound to a substrate by their flagellum filaments [19, 12, 14]. Hashimoto et al. [62] recognised that complicated dynamics may arise as the cell body rotates and changes orientation in close proximity to the substrate. Although we have so far neglected short-ranged cell–surface interactions, the boundary element method is well suited for simulating tethered cells and could be used to verify or correct estimates of forces and torques in such systems. It would also be possible to

explore what effect hook flexibility has on such estimates obtained from experimental observation.

The detailed method we have employed for simulating the motion of individual bacteria is unsuited for scaling to populations of swimmers. Since many practical applications will involve a large number of bacteria, it is of interest to develop population scale models of bacterial dynamics. Representing each swimmer by a force dipole seems to be an appealing approach to solving the dynamics of many interacting cells but the dipole flow field is only accurate in the dilute suspension limit and in this case, noise from Brownian rotation and stochasticity of the motor activity dominate over hydrodynamic swimmer–swimmer interactions [40]. The boundary element method offers one solution for accurately describing interactions between swimmers of the order of microns apart, which could then be incorporated into population level models of denser populations, ultimately including effects such as chemotaxis, background flows and boundaries.

Appendix A

Swimmer geometry and parameters

The geometrical model for our swimming bacterium is illustrated in Fig. A.1 with the relevant parameters described in table A.1. The values of key geometrical parameters used in studies throughout the thesis are listed in table A.2. We now consider physiological estimates for hook dimensions and rigidity to show that the flagellar hook can be treated as quasi-static on the timescale of motor revolutions in our model for elastic hook dynamics (chapter 6).

The quasi-static bacterial hook

Given that the Kirchhoff rod model is a suitable description for the bacterial hook (see chapter 6), we aim to show that the viscous stresses acting over the surface of the bacterial hook as well as the linear and angular momenta of the hook are subdominant on the $T = 10^{-3}\,\mathrm{s}$ timescale of motor revolutions. In other words, the shape of the hook is governed by the static rod equations with no distributed load.

We begin with the equations for a Kirchhoff rod as presented in chapter 6 but including a distributed force per unit length, $\mathbf{f}$, torque per unit length, $\mathbf{l}$, and the rates of change of linear and angular momenta. The equations of motion for such a

rod are [3]

$$\mathbf{n}' + \mathbf{f} = \rho A \ddot{\mathbf{x}}, \tag{A.1}$$

$$\mathbf{m}' + \mathbf{d}_3 \times \mathbf{n} + \mathbf{l} = \rho I(\mathbf{d}_1 \times \ddot{\mathbf{d}}_1 + \mathbf{d}_2 \times \ddot{\mathbf{d}}_2) \tag{A.2}$$

where ρ is the mass density, A is the cross-sectional area, I is the second moment of area of the circular cross-section and $\boldsymbol{\omega}$ is the spin vector satisfying (6.1). We assume the hook is of the same density as the surrounding medium and take this to be $\rho = 1000\,\mathrm{kg\,m^{-3}}$. For a cylindrical hook of radius $r = 10\,\mathrm{nm}$, the inertial term in (A.1) is of magnitude $\rho\pi r^2 \ddot{\mathbf{x}} \sim 10^{-7} X\,\mathrm{N\,m^{-2}}$, where X is the characteristic variation in position of a point on the hook.

The forcing term $\mathbf{f}$ is the total viscous force per unit length acting on the surface of the hook. Using the resistive force theory approximation, this term scales as $f \sim \mu\dot{x} \sim X\,\mathrm{N\,m^{-2}}$. We see that inertia is negligible compared with viscous drag on the timescale of interest. This reduces (A.1) to

$$\mathbf{n}'(s) = -\mathbf{f}(s). \tag{A.3}$$

Since the flagellar filament is also inertialess, balance of linear momentum yields the boundary condition at the filament end of the hook $\mathbf{n}(L^{\mathrm{H}}) = \mathbf{F}^{\mathrm{fil}}$, where $\mathbf{F}^{\mathrm{fil}}$ is the net viscous drag force acting on the flagellar filament. Assuming the viscous drag per unit length is of the same order of magnitude throughout the length of the hook and flagellar filament, we can write the solution of (A.3) as

$$\mathbf{n}(s) = \mathbf{F}^{\mathrm{fil}}(1 + O(L^{\mathrm{H}}/L)), \tag{A.4}$$

where L is the length of the flagellar filament. The hook is of length $L^{\mathrm{H}} = 100\,\mathrm{nm}$ while the filament can be $10\,\mu\mathrm{m}$ long. Therefore, we can make the approximation that $\mathbf{n}$ is constant along the hook, implying that the viscous drag force, $\mathbf{f}$, is negligible.

The angular momentum term on the right-hand side of A.2 is of the order $\rho r^4/T^2 = 10^{-23}\,\mathrm{N}$. The viscous torque per unit length acting on a cylinder rotating

with angular frequency $\omega = 2\pi/T$ scales as $l \sim 4\pi\mu r^2\omega \approx 10^{-14}\,\mathrm{N}$ [129], which dominates over the angular momentum. This reduces (A.2) to

$$\mathbf{m}'(s) = -\mathbf{d}_3(s) \times \mathbf{n}(s) - \mathbf{l}(s). \tag{A.5}$$

Integrating $\mathbf{l}$ along the rod gives a maximum contribution to the contact moment of order $L^{\mathrm{H}}\, l \sim 10^{-21}\,\mathrm{N\,m}$. This is much smaller than the torque generated by the bacterial motor, $m(0) \sim 10^{-18}\,\mathrm{N\,m}$. Hence, we can neglect the viscous torques acting over the surface of the hook. This yields the static rod equations with no distributed forces or torques.

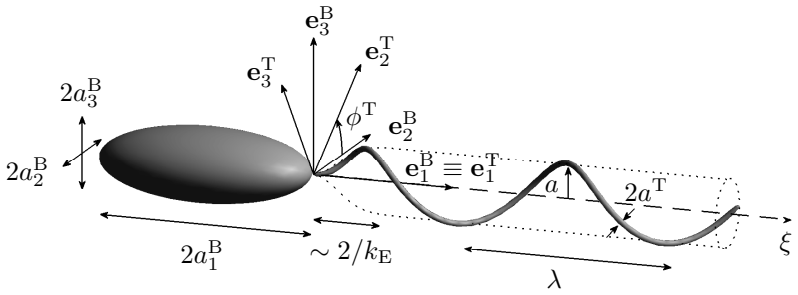

Figure A.1: Illustration of model bacterium in the body reference frame (repeated from Fig. 3.1 for convenience). Refer to table A.1 and §3.1 for further details.

Table A.1: Parameters related to geometry and configuration of the bacterium.

Symbol	Interpretation	Further information
a	amplitude of helical tail	Fig. A.1
a_1^{B}	polar radius of cell body	Fig. A.1
$a_2^{\mathrm{B}}, a_3^{\mathrm{B}}$	equatorial radius of cell body	Fig. A.1; only spheroidal cell bodies considered ($a_2^{\mathrm{B}} = a_3^{\mathrm{B}}$)
$\bar{a}$	volumetric radius of cell body	$\approx 0.7\,\mu\mathrm{m}$ for *R. sphaeroides* [115]
a^{T}	radius of cylindrical tail filament	Fig. A.1
$\mathbf{e}_1^{\mathrm{B}}, \mathbf{e}_2^{\mathrm{B}}, \mathbf{e}_3^{\mathrm{B}}$	body-fixed frame directors	Fig. A.1
$\mathbf{e}_1^{\mathrm{T}}, \mathbf{e}_2^{\mathrm{T}}, \mathbf{e}_3^{\mathrm{T}}$	flagellum-fixed frame directors	§3.1
k	wavenumber of helix	$k = 2\pi/\lambda$
k_{E}	tail amplitude envelope growth rate	Fig. A.1; §3.1
L	curvilinear length of flagellum	
L^{H}	length of flagellar hook	chapter 6
λ	wavelength of helical tail	Fig. A.1
N_λ	number of turns on tail	
ϕ^{T}	tail phase relative to cell body	$\dot{\phi}^{\mathrm{T}} = \Omega^{\mathrm{T}}$
$\mathbf{x}^{\mathrm{B}}$	cell body–hook junction position	§3.1

Table A.2: Base parameter values used in simulations. Where the rigid hook model is used, L^{H} is simply the length of the gap between the cell body and the meshed flagellum filament. In all cases we use the helical pitch angle $ak = 1$.

Shape	N_λ	$\lambda/\bar{a}$	$L/\bar{a}$	$a_1^{\mathrm{B}}/a_2^{\mathrm{B}}$	$a^{\mathrm{T}}/\bar{a}$	$L^{\mathrm{H}}/\bar{a}$	Hook model	Reference
Base	2.0	3.6	10.0	2.0	0.05	0.02	Rigid	chapter 4
Accumulator	3.0	1.8	7.5	3.0	0.05	0.10	Rigid	chapter 5
Escaper	2.0	1.8	5.0	3.0	0.05	0.10	Rigid	chapter 5
A	3.5	2.0	10.0	2.0	0.05	0.20	Kirchhoff	chapter 6
B	3.0	1.8	7.4	1.6	0.02	0.20	Kirchhoff	chapter 6

Appendix B

Convergence of numerical methods

We present the following tests for the validation of our numerical implementation of the boundary element method:

1. Fig. B.1 – the translational velocity of a sphere moving through unbounded fluid under a constant force,
2. Fig. B.2 – the translational velocity of a sphere moving in a half space under a constant force normal to the plane boundary,
3. Fig. B.3 – the instantaneous translational velocity of a model bacterium in free space,
4. Fig. B.4 – the swimming speed using different flagellar geometries, and
5. Fig. B.5 – the instantaneous velocity of a model bacterium in a square channel.

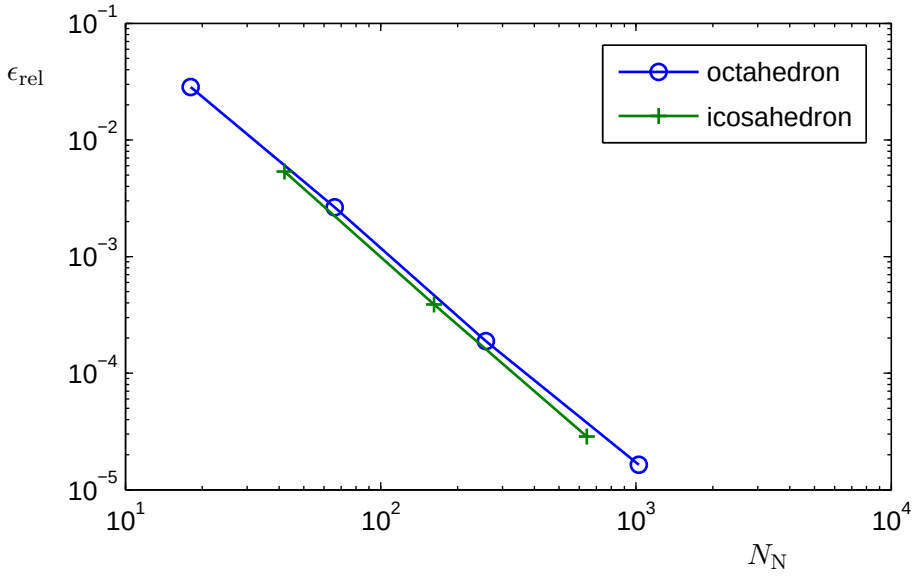

Figure B.1: Convergence of the BEM with increasing mesh refinement for a sphere of radius $\bar{a}$ translating in free space under a prescribed force $\mathbf{F}$. The relative error is defined as $\epsilon_{\mathrm{rel}} := \|\mathbf{U} - \mathbf{U}_0\|/\|\mathbf{U}_0\|$, where $\mathbf{U}$ is the computed velocity and $\mathbf{U}_0 = \mathbf{F}/(6\pi\mu\bar{a})$ is the analytical velocity determined by the formula for Stokes' drag. The two sets of data correspond to an octahedral and an icosahedral arrangement of mesh nodes before refinement. We generally use the second icosahedral level of refinement in simulations of swimming bacteria.

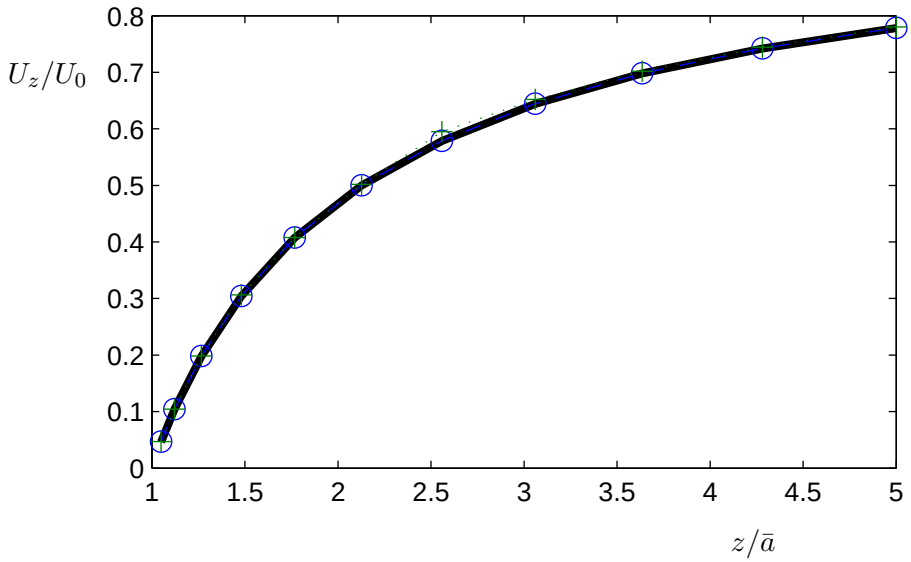

Figure B.2: Comparison of the BEM with analytical result for a sphere of radius $\bar{a}$ translating under a prescribed force $\mathbf{F}$ towards a no-slip plane boundary at $z/\bar{a} = 0$. The vertical speed U_z is computed using the half space Green's function (dashed curve marked with open circles) and by explicitly meshing a portion of the boundary of size $20\,\bar{a} \times 20\,\bar{a}$ underneath the sphere (dotted curve marked with crosses). An analytical expression for the correction factor to Stokes' drag due to the presence of a plane boundary was given by Brenner [23]. This gives us the analytical speed of the sphere, shown with a solid, unmarked curve. Elements of the sphere mesh are adaptively refined based on proximity to the wall and likewise the elements on the wall are refined based on proximity to the sphere.

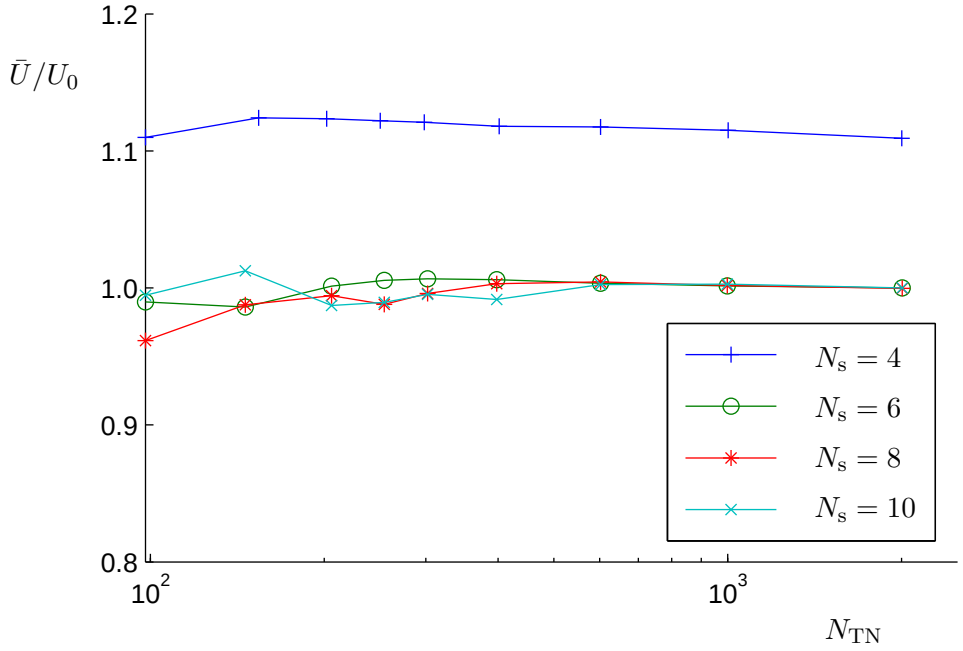

Figure B.3: Convergence of the BEM for a bacterium swimming in free space using different levels of flagellum mesh refinement determined by the mesh parameters N_{s} and N_{TN}, described in §3.1. The progressive speed, $\bar{U}$, is defined in §3.5 and is scaled by the value U_0 at the highest refinement level with $N_{\mathrm{s}} = 10$. Reliable results are achieved with $N_{\mathrm{s}} \geq 6$ and $N_{\mathrm{TN}} \geq 200$ for this swimmer geometry, which is described by the parameters: $a_1^{\mathrm{B}}/a_2^{\mathrm{B}} = 1.4$, $N_\lambda = 1.5$, $L/\bar{a} = 10$, $ak = 1$, $a^{\mathrm{T}}/\bar{a} = 0.05$. The interpretations of model geometry parameters are summarised in appendix A.

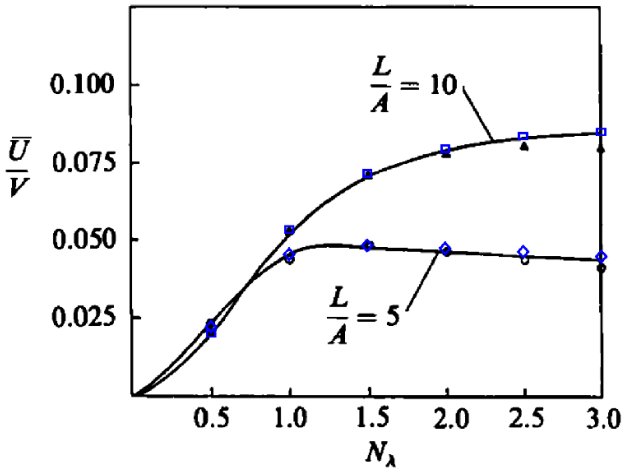

Figure B.4: Comparison of results using the rigid hook model of this thesis, abbreviated (S), the BEM of Phan-Thien et al. [99], abbreviated (P), and the SBT analysis of Higdon [64], abbreviated (H). $\bar{U}/V$ is the progressive speed non-dimensionalised by the linear wavespeed of the flagellum. The radius of the spherical cell body considered for this data set is denoted by $A \equiv \bar{a}$. The solid curves are predictions from (H). On the curve labelled $L/A = 5$, the solutions of (P) are represented by open circles while diamonds show the results of (S). On the curve labelled $L/A = 10$, the results of (P) are marked by closed triangles while those of (S) are open squares. This figure was reproduced with permission from reference [99] with new data overlaid.

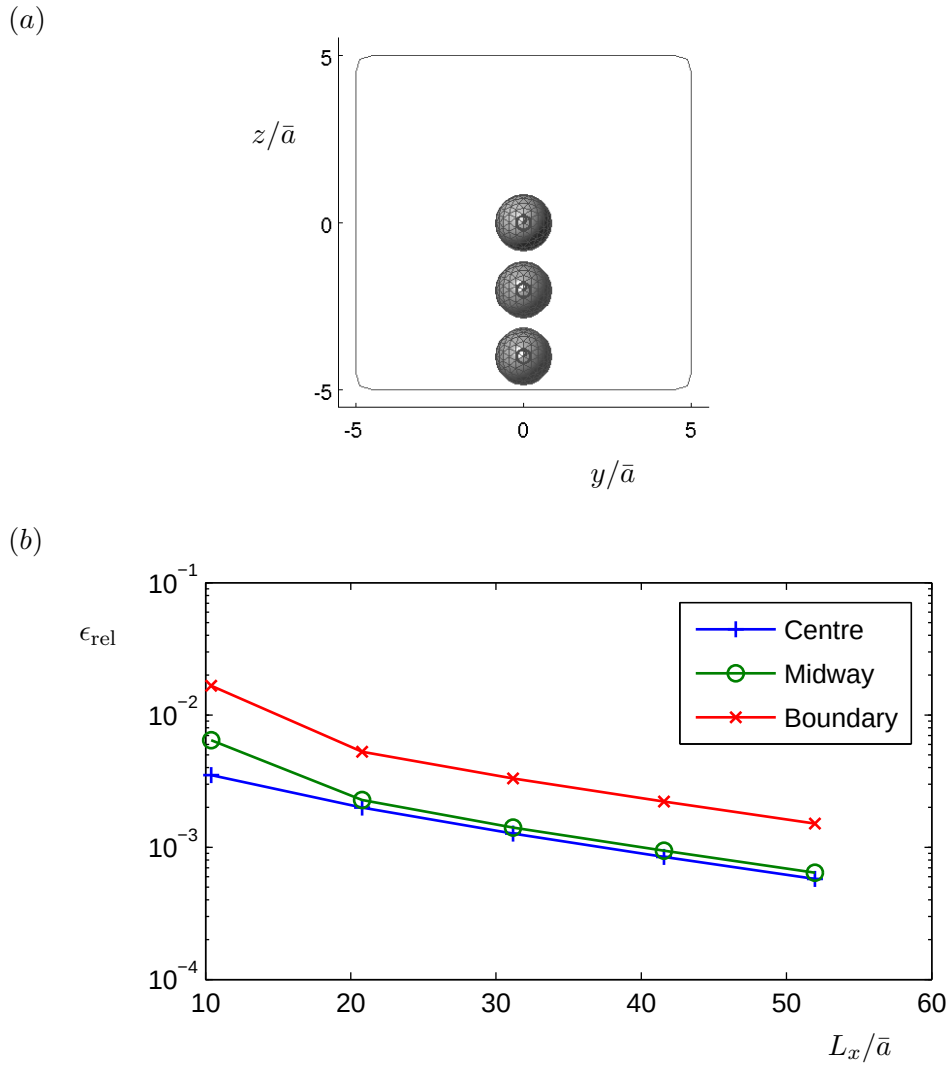

Figure B.5: Convergence of the swimming velocity for a bacterium in a channel as the length of the meshed channel section, L_x, is varied. The channel has dimensions $H_y = H_z = 10\,\bar{a}$ and the bacterium is aligned with the channel and placed at $y/\bar{a} = 0$ with three different heights: $z/\bar{a} = 0$ ("centre"), $z/\bar{a} = -2$ ("midway") and $z/\bar{a} = -4$ ("boundary") as illustrated in (a). The relative error is defined as $\epsilon_{\text{rel}} := \|\mathbf{U} - \mathbf{U}_0\|/\|\mathbf{U}_0\|$, where $\mathbf{U}$ is the computed instantaneous velocity and $\mathbf{U}_0$ is the instantaneous velocity in the case of the greatest meshed channel section length, $L_x = 100\,\bar{a}$.

Appendix C

Analysis of potentially periodic trajectories

We describe methods for quantifying the periodicity of a swimmer trajectory and comparing periodic trajectories to distinguish between distinct periodic orbits. We first consider the one-dimensional time series $\{x_i,\ i = 1, 2, ..., N_{\text{data}}\}$ before extending this to multi-dimensional trajectories from swimming in channels in chapter 5. The techniques may also be applied to a general time series showing periodicity.

C.1 Identifying periodicity in a one-variable time series

Suppose that the data point x_i is taken at time t_i, $i = 1, 2, ..., N_{\text{data}}$ where it can be assumed that the time points are monotonically increasing. We define $x : [t_1, t_{N_{\text{data}}}] \to \mathbb{R}$ to be the cubic spline interpolant of the data set. Then $x(t)$ is an approximation to the continuous system that we have sampled at the discrete times t_i, and in particular satisfies

$$x_i = x(t_i), \quad i = 1, 2, ..., N_{\text{data}}. \tag{C.1}$$

We resample a portion of the data at N regularly spaced time points by defining

$$\tilde{t}_j := \tilde{t}_0 + (j-1)\Delta T/N, \quad \tilde{x}_j := x(\tilde{t}_j), \quad j = 1, 2, ..., N, \tag{C.2}$$

where $\tilde{t}_0 \geq t_1$ and $\tilde{t}_0 + \Delta T \leq t_{N_{\text{data}}}$.

The discrete Fourier transform of the resampled data is defined by

$$\tilde{X}_k = \sum_{j=1}^{N} \tilde{x}_j \mathrm{e}^{-2\pi i(j-1)(k-1)/N}, \quad k = 1, 2, ..., N, \tag{C.3}$$

and the data can be reconstructed from the discrete Fourier transform through the inverse discrete Fourier transform formula,

$$\tilde{x}_j = \frac{1}{N} \sum_{k=1}^{N} \tilde{X}_k \mathrm{e}^{2\pi i(j-1)(k-1)/N}, \quad j = 1, 2, ..., N, \tag{C.4}$$

where $i = \sqrt{-1}$. The discrete Fourier transform represents the data as a combination of periodic modes of discrete frequencies [20]. The periodogram is defined as

$$I_k := N|\tilde{X}_k|^2, \tag{C.5}$$

where $|\tilde{X}_k|$ denotes the modulus of the complex number $\tilde{X}_k$, and indicates the relative strength of the contribution from mode k, which is associated with the Fourier frequency $k/\Delta T$.

If $\{\tilde{x}_j\}$ is an exactly periodic data set with period τ and contains an integer number N_τ of periods, i.e.,

$$\Delta T = \tau N_\tau, \tag{C.6}$$

then any contributing Fourier mode must have a frequency that is an integer multiple of $N_\tau/\Delta T$. In other words, $I_k > 0$ only if k is a multiple of N_τ. We will choose the length of the data sample, N, to be divisible by $2N_\tau$ and define

$$N_t := N/N_\tau, \tag{C.7}$$

which is an even number. Conversely, if the periodogram is zero for all modes that are not multiples of N_τ, then the data is periodic and τ is an integer multiple of the period. We can therefore test the assumption that τ is an integer multiple of the period by computing the relative contributions from modes that are non-multiples of N_τ,

$$\varepsilon_{\tau,N_\tau} := \frac{1}{I}\left(I - \sum_{n=1}^{N_t} I_{nN_\tau}\right), \quad I := \sum_{k=1}^{N} I_k, \tag{C.8}$$

where the subscripts τ and N_τ on the error $\varepsilon_{\tau,N_\tau}$ indicate that the result depends on the choice of τ and N_τ since these determine the time points $\{\tilde{t}_j\}$ of the sampled data through definition (C.3) and the assumption (C.6).

If the data is periodic but the frequency is not precisely a Fourier frequency, then the periodogram may be non-zero for modes that do not correspond to oscillation frequencies of the data. This is known as leakage and means that the data has not been separated into its natural component frequencies [20]. In order to best determine the periodicity of the given data set $\{x_i\}$, we minimise (C.8) with respect to τ. That is, we fix N_τ and adjust the sample span ΔT, and hence the assumed period $\tau \equiv \Delta T/N_\tau$, to minimise the error ε. This is achieved using the MATLAB function `fminbnd`, which locates a minimum of a function within specified bounds. These bounds are selected by inspection of the data.

C.2 Periodicity of channel trajectories

Numerical solution of the ODE system governing the phase-averaged bacterial dynamics in a channel gives the data

$$t_i,\ \mathbf{x}_i = (y_i, z_i, \eta_i, \zeta_i), \quad i = 1, 2, ..., N_{\text{data}}. \tag{C.9}$$

We write $x_i^1 = y_i$, $x_i^2 = z_i$, $x_i^3 = \eta_i$ and $x_i^4 = \zeta_i$. The solution typically passes through a transient stage but may eventually show regularity and potential periodicity. Once a candidate for periodic behaviour has been determined, we use the technique described in §C.1 except that we consider the discrete Fourier transform of each time series $\{\mathbf{x}_i^m\}$, $m = 1, 2, 3, 4$. Denoting the periodogram for component m by I_k^m, the error defined in (C.8) is replaced by the mean of the errors in each component,

$$\varepsilon_{\tau,N_\tau} := \frac{1}{4}\sum_{m=1}^{4}\left(1 - \frac{1}{I^m}\sum_{n=1}^{N_t} I_{nN_\tau}^m\right), \quad I^m := \sum_{k=1}^{N} I_k^m. \tag{C.10}$$

This is then minimised in the same way as before to determine the best estimate for the period τ. We choose the starting point of the resampled data, $\tilde{t}_0$, such that

the final time, $\tilde{t}_N$, is close to the upper limit of the given data, $t_{N_{\text{data}}}$. This selects the final segment of computed data so that transient effects should be minimised. We use the value $N_\tau = 5$ and set a threshold $\varepsilon_{\text{tol}} = 0.05$ for the error, below which we consider the trajectory to have reached a periodic orbit. An example application of this test is shown in Fig. C.1.

We define the (eventual) periodic orbit of a trajectory to be the first N_t points of the time series $\{\tilde{\mathbf{x}}_j\}$ of minimal period that satisfies the condition

$$\varepsilon_{\tau,N_\tau} < \varepsilon_{\text{tol}}. \tag{C.11}$$

This reduced data set, denoted $\{\hat{\mathbf{x}}_j\} \equiv \{\tilde{\mathbf{x}}_j,\, j = 1, 2, ..., N_t\}$, contains one period of the trajectory by construction. By reducing the size of this set to one period, the discrete Fourier transform will include only modes that are harmonics of the fundamental frequency.

C.3 Comparing periodic orbits

A periodic orbit can be shifted in time without changing its characteristics. We therefore consider two periodic orbits to be equivalent if they are equal up to a phase difference. In particular, the periodograms of the two orbits must agree. If the discrete Fourier transform of the mth variable of a periodic orbit p is $\{\hat{X}_k^{m,p}\}$ and the corresponding periodogram is $I_k^{m,p}$, then for two orbits p and q, the difference in the periodograms of the discrete Fourier transforms can be quantified by

$$\varepsilon_I^{p,q} := \frac{1}{4}\sum_{m=1}^{4}\sqrt{\frac{\sum_{k=1}^{N_t}(I_k^{m,p} - I_k^{m,q})^2}{\sum_{k=1}^{N_t}(\bar{I}_k^{m,p,q})^2}}, \tag{C.12}$$

where we define the average periodogram by

$$\bar{I}_k^{m,p,q} := \frac{I_k^{m,p} + I_k^{m,q}}{2}. \tag{C.13}$$

The phase, or argument, of the complex number $\tilde{X}_k^{m,p}$ is denoted $\varphi_k^{m,p}$. If the two samples p and q are equivalent up to a phase difference, then the phase difference,

$$\delta\varphi_k^{m,p,q} := \varphi_k^{m,q} - \varphi_k^{m,p}, \text{ mod } T_k, \quad k = 1, 2, ..., N_t, \tag{C.14}$$

should be independent of m. The T_k term in this expression is the period of oscillation of mode m given by

$$T_1 = \pi, \quad T_k = 2\pi/(k-1), \quad k = 2, 3, ..., N_t. \tag{C.15}$$

The $k = 1$ term is defined separately because this mode corresponds to a constant term. The phase for this mode only takes the values 0 or π, depending on the sign of $\tilde{X}_1$, hence the phase difference is either 0 or π. Since T_k represents the maximum possible phase difference between corresponding modes of two signals, we define $T_1 = \pi$. We may neglect modes $k > (N_t/2 + 1)$ since these are equivalent to the oscillation modes $k < (N_t/2 + 1)$. The weighted average phase difference with respect to m, using the average periodogram to weight each term, is defined as

$$\overline{\delta\varphi}_1^{p,q} := 0, \quad \overline{\delta\varphi}_k^{p,q} := \frac{\sum_{m=1}^{4} \delta\varphi_k^{m,p,q} \cdot \bar{I}_k^{m,p,q}}{\sum_{m=1}^{4} \bar{I}_k^{m,p,q}}, \quad k = 2, 3, ..., N_t/2 + 1, \tag{C.16}$$

where the case $k = 1$ is given the value $\overline{\delta\varphi}_1^{p,q} = 0$ so that the error defined below will penalise any phase difference in the first mode, which corresponds to a mismatch in sign of $\tilde{X}_1^{m,p}$ compared with $\tilde{X}_1^{m,q}$.

We measure the deviation of the phase differences from the mean, weighted by the average periodograms and by the mode frequency, using the following formula:

$$\varepsilon_\varphi^{p,q} := \frac{1}{4} \sum_{m=1}^{4} \sqrt{\frac{\sum_{k=1}^{N_t/2+1} \left(\frac{\delta\varphi_k^{m,p,q} - \overline{\delta\varphi}_k^{p,q}}{T_k} \right)^2 \cdot \bar{I}_k^{m,p,q}}{\sum_{k=1}^{N_t/2+1} \bar{I}_k^{m,p,q}}}. \tag{C.17}$$

Imposing a threshold of $\varepsilon_{\text{tol}} = 0.05$, we say that the periodic orbits p and q are equivalent (up to a phase difference) if

$$\varepsilon_I^{p,q} < \varepsilon_{\text{tol}} \text{ and } \varepsilon_\varphi^{p,q} < \varepsilon_{\text{tol}}, \tag{C.18}$$

and the phase difference is $\overline{\delta\varphi}^{p,q}$. Note that with this notion of equivalence, two periodic orbits extracted from the same trajectory will, in principle, be equivalent.

Due to rotational symmetry of the channel cross-section, two periodic orbits that are distinct in this sense may be related to one another by a rotation. A rotation of the coordinate system by an angle θ about the axis of the channel corresponds to the transformation of the time series

$$\mathbf{x}_i \to \mathbf{R}(\theta)\mathbf{x}_i, \quad \mathbf{R}(\theta) = \begin{bmatrix} \cos\theta & -\sin\theta & 0 & 0 \\ \sin\theta & \cos\theta & 0 & 0 \\ 0 & 0 & \cos\theta & -\sin\theta \\ 0 & 0 & \sin\theta & \cos\theta \end{bmatrix}, \; i = 1, 2, ..., N_{\text{data}}. \tag{C.19}$$

In a square channel, there is order four symmetry, admitting rotations by multiples of $\pi/2$. In rectangular channels with order two rotational symmetry, the trajectories may be rotated by π about the channel axis. Periodic orbits p and q are the same up to channel symmetry if orbit p is equivalent up to a phase difference to some allowed rotation of orbit q.

To illustrate this method of comparing trajectories, we present the results for trajectories in two channels. The first case is a boundary escaping swimmer in a square channel of width $20\,\bar{a}$ (Fig. C.2(a)). The errors in comparing a periodic orbit $\{\tilde{\mathbf{x}}_j\}$ with the rotated copies of the same data are given in table C.1. The low errors indicate that the periodic orbit is equivalent to its rotations, therefore this orbit has rotational symmetry of order four.

In contrast, table C.2 shows large errors between an orbit and its rotations by odd multiples of $\pi/2$. These orbits are for boundary escaping swimmers in a square channel of width $30\,\bar{a}$, illustrated in Fig. C.2(b). We conclude that these orbits have rotational symmetry of order two.

Finally, we compare orbits obtained from different trajectories in table C.3. The errors suggest that trajectory p is equivalent to trajectories q_2, q_3 and q_4 but distinct from q_1. Indeed, as shown in Fig. C.2(a), p (coloured curves) does not overlap with q_1 (black curve).

Table C.1: Errors in the periodogram and phase difference between a time series p and its rotations q. See Fig. C.2(a).

	$\mathbf{R}(\pi/2)\{\tilde{\mathbf{x}}_j^p\}$	$\mathbf{R}(\pi)\{\tilde{\mathbf{x}}_j^p\}$	$\mathbf{R}(3\pi/2)\{\tilde{\mathbf{x}}_j^p\}$	$\mathbf{R}(2\pi)\{\tilde{\mathbf{x}}_j^p\}$
$\varepsilon_I^{p,q}$	0.005	0.000	0.005	0.000
$\varepsilon_\varphi^{p,q}$	0.002	0.000	0.002	0.000

Table C.2: Errors in the periodogram and phase difference between a time series p and its rotations q. See Fig. C.2(b).

	$\mathbf{R}(\pi/2)\{\tilde{\mathbf{x}}_j^p\}$	$\mathbf{R}(\pi)\{\tilde{\mathbf{x}}_j^p\}$	$\mathbf{R}(3\pi/2)\{\tilde{\mathbf{x}}_j^p\}$	$\mathbf{R}(2\pi)\{\tilde{\mathbf{x}}_j^p\}$
$\varepsilon_I^{p,q}$	0.136	0.000	0.136	0.000
$\varepsilon_\varphi^{p,q}$	0.104	0.000	0.104	0.000

Table C.3: Pairwise errors in the periodogram and phase difference between time series from different trajectories p and q. Trajectories p and q_1 correspond to the plotted orbits in Fig. C.2(a).

	$\{\tilde{\mathbf{x}}_j^{q_1}\}$	$\{\tilde{\mathbf{x}}_j^{q_2}\}$	$\{\tilde{\mathbf{x}}_j^{q_3}\}$	$\{\tilde{\mathbf{x}}_j^{q_4}\}$
$\varepsilon_I^{p,q}$	0.140	0.001	0.006	0.001
$\varepsilon_\varphi^{p,q}$	0.251	0.001	0.005	0.002

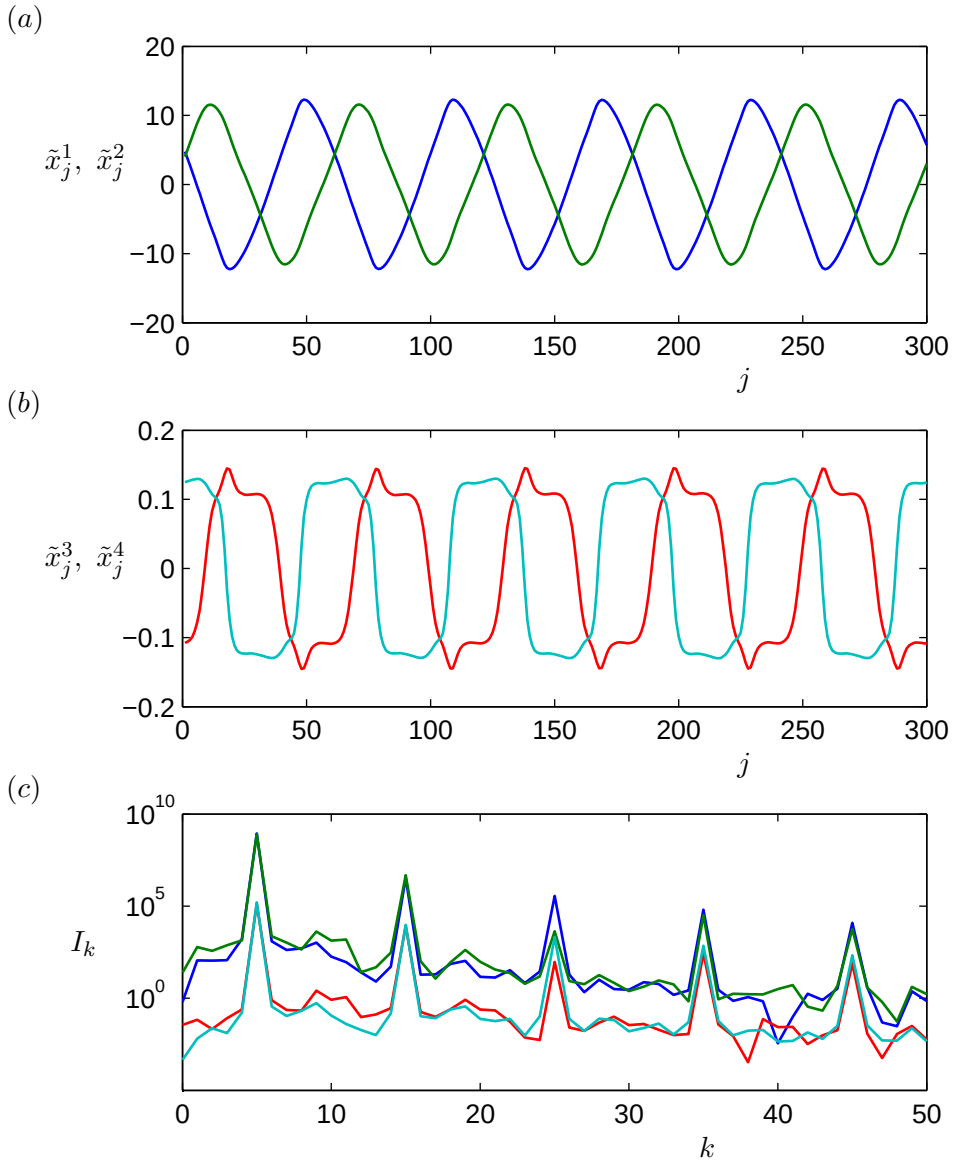

Figure C.1: A periodic orbit found for a trajectory in a square channel of size $30\,\bar{a}$ (see Fig. 5.8). (*a*) Time series of $\tilde{x}_j^1 \equiv \tilde{y}_j$ (blue curve) and $\tilde{x}_j^2 \equiv \tilde{z}_j$ (green curve), (*b*) $\tilde{x}_j^3 \equiv \tilde{\eta}_j$ (cyan curve) and $\tilde{x}_j^4 \equiv \tilde{\zeta}_j$ (red curve). (*c*) Periodograms I_k of the discrete Fourier transform for each of the components of the trajectory. Colours correspond to the curves in (*a*) and (*b*) and the vertical scale is logarithmic. Strong peaks are evident at some multiples of the fundamental frequency $k = N_\tau = 5$ and the error computed for this data set was $\varepsilon_{\tau,N_\tau} = 2.5 \times 10^{-5}$.

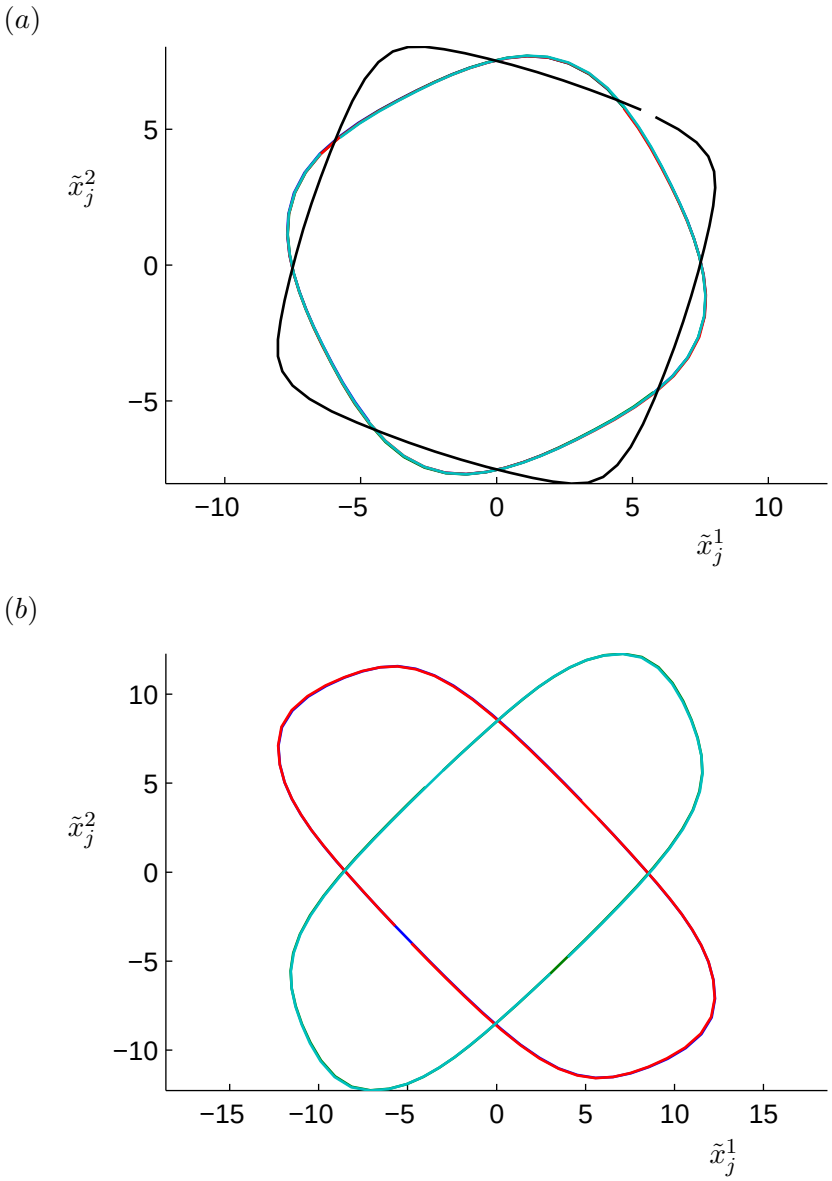

Figure C.2: Comparison of periodic orbits from different trajectories and evaluation of rotational symmetry. (a) A periodic orbit and its three rotational images are plotted (all lying under the cyan curve) for a boundary escaping swimmer in a square channel of width $20\,\bar{a}$. The periodic orbit of another trajectory is also plotted (black curve). (b) A periodic orbit and its three rotational images are plotted for a boundary escaping swimmer in a square channel of width $30\,\bar{a}$. This orbit has rotational symmetry of order two.

Bibliography

[1] M. Abramowitz and I. A. Stegun, editors. *Handbook of mathematical functions with formulas, graphs, and mathematical tables*. Dover, New York, 1964.

[2] F. Alouges, A. DeSimone, and L. Heltai. Numerical strategies for stroke optimization of axisymmetric microswimmers. *Math. Mod. Meth. Appl. S.*, 21:361–387, 2011.

[3] S. S. Antman. *Nonlinear problems of elasticity*. Springer, 2nd edition, 2005.

[4] J. P. Armitage and R. M. Macnab. Unidirectional, intermittent rotation of the flagellum of *Rhodobacter sphaeroides*. *J. Bacteriol.*, 169:514–518, 1987.

[5] J. P. Armitage, T. P. Pitta, M. A.-S. Vigeant, H. L. Packer, and R. M. Ford. Transformations in flagellar structure of *Rhodobacter sphaeroides* and possible relationship to changes in swimming speed. *J. Bacteriol.*, 181:4825–4833, 1999.

[6] P. K. Banerjee and R. Butterfield. *Boundary element methods in engineering science*. McGraw–Hill, London, 1981.

[7] E. Barta and N. Liron. Slender body interactions for low Reynolds numbers—Part I: Body-wall interactions. *SIAM J. Appl. Math.*, 48:992–1008, 1988.

[8] G. K. Batchelor. Slender-body theory for particles of arbitrary cross-section in Stokes flow. *J. Fluid Mech.*, 44:419–440, 1970.

[9] G. K. Batchelor. The stress system in a suspension of force-free particles. *J. Fluid Mech.*, 41:545–570, 1970.

[10] H. C. Berg. http://www.rowland.harvard.edu/labs/bacteria/index_movies.html.

[11] H. C. Berg and L. Turner. Chemotaxis of bacteria in glass capillary arrays. *Escherichia coli*, motility, microchannel plate, and light scattering. *Biophys. J.*, 58:919–930, 1990.

[12] H. C. Berg and L. Turner. Torque generated by the flagellar motor of *Escherichia coli*. *Biophys. J.*, 65:2201–2216, 1993.

[13] A. P. Berke, L. Turner, H. C. Berg, and E. Lauga. Hydrodynamic attraction of swimming microorganisms by surfaces. *Phys. Rev. Lett.*, 101:038102, 2008.

[14] R. M. Berry, L. Turner, and H. C. Berg. Mechanical limits of bacterial flagellar motors probed by electrorotation. *Biophys. J.*, 69:280–286, 1995.

[15] M. Binz, A. P. Lee, C. E., and D. V. Nicolau. Motility of bacteria in microfluidic structures. *Microelectron. Eng.*, 87:810–813, 2010.

[16] S. A. Biondi, J. A. Quinn, and H. Goldfine. Random motility of swimming bacteria in restricted geometries. *AIChE Journal*, 44:1923–1929, 1998.

[17] J. R. Blake. A note on the image system for a stokeslet in a no-slip boundary. *Proc. Camb. Phil. Soc.*, 70:303–310, 1971.

[18] J. R. Blake. Singularities of viscous flow. Part II: Applications to slender body theory. *J. Eng. Math.*, 8:113–124, 1974.

[19] S. M. Block, D. F. Blair, and H. C. Berg. Compliance of bacterial flagella measured with optical tweezers. *Nature*, 338:514–518, 1989.

[20] P. Bloomfield. *Fourier analysis of time series: an introduction.* Wiley-Interscience, New York, 2004.

[21] C. A. Brebbia. *The boundary element method for engineers.* Pentech Press/Halstead Press, 1978.

[22] C. Brennen and H. Winet. Fluid mechanics of propulsion by cilia and flagella. *Annu. Rev. Fluid Mech.*, 9:339–398, 1977.

[23] H. Brenner. The slow motion of a sphere through a viscous fluid towards a plane surface. *Chem. Eng. Sci.*, 16:242–251, 1961.

[24] T. T. Bringley and C. S. Peskin. Validation of a simple method for representing spheres and slender bodies in an immersed boundary method for stokes flow on an unbounded domain. *J. Comput. Phys.*, 227:5397–5425, 2008.

[25] M. T. Cabeen and C. Jacobs-Wagner. Bacterial cell shape. *Nat. Rev. Microbiol.*, 3:601–610, 2005.

[26] C. R. Calladine. Construction of bacterial flagella. *Nature*, 255:121–124, 1975.

[27] C.V. Camp and G.S. Gipson. Overhauser elements in boundary element analysis. *Mathematical and Computer Modelling*, 15:59–69, 1991.

[28] S. Chattopadhyay and X.-L. Wu. The effect of long-range hydrodynamic interaction on the swimming of a single bacterium. *Biophys. J.*, 96:2023–2028, 2009.

[29] A. H.-D. Cheng and D. T. Cheng. Heritage and early history of the boundary element method. *Eng. Anal. Bound. Elem.*, 29:268–302, 2005.

[30] A. T. Chwang and T. Y. Wu. A note on the helical movement of micro-organisms. *Proc. R. Soc. Lond. Ser. B*, 178:327–346, 1971.

[31] C. J. Coakley and M. E. J. Holwill. Propulsion of micro-organisms by three-dimensional flagellar waves. *J. Theor. Biol.*, 35:525–542, 1972.

[32] J. W. Costerton, K. J. Cheng, G. G. Geesey, T. I. Ladd, J. C. Nickel, M. Dasgupta, and T. J. Marrie. Bacterial biofilms in nature and disease. *Annu. Rev. Microbiol.*, 41:435–464, 1987.

[33] R. G. Cox. The motion of long slender bodies in a viscous fluid part 1. general theory. *J. Fluid Mech.*, 44:791–810, 1970.

[34] N. C. Darnton and H. C. Berg. Force-extension measurements on bacterial flagella: triggering polymorphic transformations. *Biophys. J.*, 92:2230–2236, 2007.

[35] M. L. DePamphilis and J. Adler. Attachment of flagellar basal bodies to the cell envelope: specific attachment to the outer, lipopolysaccharide membrane and the cyoplasmic membrane. *J. Bacteriol.*, 105:396–407, 1971.

[36] M. L. DePamphilis and J. Adler. Fine structure and isolation of the hook-basal body complex of flagella from escherichia coli and bacillus subtilis. *J. Bacteriol.*, 105:384–395, 1971.

[37] D. J. DeRosier. The turn of the screw: The bacterial flagellar motor. *Cell*, 93:17–20, 1998.

[38] W. R. DiLuzio, L. T., M. Mayer, P. Garstecki, D. B. Weibel, H. C. Berg, and G. M. Whitesides. *Escherichia coli* swim on the right-hand side. *Nature*, 435:1271–1274, 2005.

[39] R. N. Doetsch. Some speculations accounting for the movement of bacterial flagella. *J. Theor. Biol.*, 11:411–417, 1966.

[40] K. Drescher, J. Dunkel, L. H. Cisneros, S. Ganguly, and R. E. Goldstein. Fluid dynamics and noise in bacterial cell-cell and cell-surface scattering. *Proc. Natl. Acad. Sci. USA*, 108:10940–10945, 2011.

[41] K. Drescher, R. E. Goldstein, N. Michel, M. Polin, and I. Tuval. Direct measurement of the flow field around swimming microorganisms. *Phys. Rev. Lett.*, 105:168101, 2010.

[42] J. E. Duddridge, C. A. Kent, and J. F. Laws. Effect of surface shear stress on the attachment of *Pseudomonas fluorescens* to stainless steel under defined flow conditions. *Biotechnol. Bioeng.*, 24:153–164, 1982.

[43] D. A. Dunavant. High degree efficient symmetrical gaussian quadrature rules for the triangle. *Int. J. Numer. Meth. Eng.*, 21:1129–1148, 1985.

[44] D. B. Dusenbery. Minimum size limit for useful locomotion by free-swimming microbes. *Proc. Natl. Acad. Sci. USA*, 94:10949–10954, 1997.

[45] M. Feldman, R. Bryan, S. Rajan, L. Scheffler, S. Brunnert, H. Tang, and A. Prince. Role of flagella in pathogenesis of *Pseudomonas aeruginosa* pulmonary infection. *Infect. Immun.*, 66:43–51, 1998.

[46] H.-C. Flemming. Biofouling in water systems–cases, causes and countermeasures. *Appl. Microbiol. Biotechnol.*, 59:629–640, 2002.

[47] H. Flores, E. Lobaton, S. Mendez-Diez, S. Tlupova, and R. Cortez. A study of bacterial flagellar bundling. *Bull. Math. Biol.*, 67:137–168, 2005.

[48] T. C. Flynn and J. Ma. Theoretical analysis of twist/bend ratio and mechanical moduli of bacterial flagellar hook and filament. *Biophys. J.*, 86:3204–3210, 2004.

[49] N. R. Francis, G. E. Sosinsky, D. Thomas, and D. J. DeRosier. Isolation, characterization and structure of bacterial flagellar motors containing the switch complex. *J. Mol. Biol.*, 235:1261–1270, 1994.

[50] B. M. Friedrich, I. H. Riedel-Kruse, J. Howard, and F. Jülicher. High-precision tracking of sperm swimming fine structure provides strong test of resistive force theory. *J. Exp. Biol.*, 213:1226–1234, 2010.

[51] P. D. Frymier, R. M. Ford, H. C. Berg, and P. T. Cummings. Three-dimensional tracking of motile bacteria near a solid planar surface. *Proc. Natl. Acad. Sci. USA*, 92:6195–6199, 1995.

[52] M. Fujii, S. Shibata, and S.-I. Aizawa. Polar, peritrichous, and lateral flagella belong to three distinguishable flagellar families. *J. Mol. Biol.*, 379:273–283, 2008.

[53] T. Fujita and T. Kawai. Optimum shape of a flagellated microorganism. *JSME Int. J. Ser. C*, 44:952–957, 2001.

[54] H. Gadêlha, E. A. Gaffney, D. J. Smith, and J. C. Kirkman-Brown. Nonlinear instability in flagellar dynamics: a novel modulation mechanism in sperm migration? *J. R. Soc. Interface*, 7:1689–1697, 2010.

[55] P. Galajda, J. Keymer, P. Chaikin, and R. Austin. A wall of funnels concentrates swimming bacteria. *J. Bacteriol.*, 189:8704–8707, 2007.

[56] S. F. Goldstein. Asymmetric waveforms in echinoderm sperm flagella. *J. Exp. Biol.*, 71:157–170, 1977.

[57] B. González-Pedrajo, T. Ballado, A. Campos, R. E. Sockett, L. Camarena, and G. Dreyfus. Structural and genetic analysis of a mutant of *Rhodobacter sphaeroides* WS8 deficient in hook length control. *J. Bacteriol.*, 179:6581–6588, 1997.

[58] A. Goriely and M. Tabor. Nonlinear dynamics of filaments i. dynamical instabilities. *Physica D: Nonlinear Phenomena*, 105:20–44, 1997.

[59] T. Goto, S. Masuda, K. Terada, and Y. Takano. Comparison between observation and boundary element analysis of bacterium swimming motion. *JSME Int. J. Ser. C*, 44:958–963, 2001.

[60] J. Gray and G. J. Hancock. The propulsion of sea-urchin spermatozoa. *J. Exp. Biol.*, 32:802–814, 1955.

[61] G. J. Hancock. The self-propulsion of microscopic organisms through liquids. *Proc. R. Soc. Lond. Ser. A*, 217:96–121, 1953.

[62] M. Hashimoto, T. Mashimo, T. Hirano, S. Yamaguchi, and S.-I. Aizawa. Functional roles of the hook in a rotating tethered cell. *J. Mol. Biol.*, 375:367–375, 2008.

[63] J. J. L. Higdon. A hydrodynamic analysis of flagellar propulsion. *J. Fluid Mech.*, 90:685–711, 1979.

[64] J. J. L. Higdon. The hydrodynamics of flagellar propulsion: helical waves. *J. Fluid Mech.*, 94:331–351, 1979.

[65] J. Hill, O. Kalkanci, J. L. McMurry, and H. Koser. Hydrodynamic surface interactions enable escherichia coli to seek efficient routes to swim upstream. *Phys. Rev. Lett.*, 98:068101, 2007.

[66] T. Hirano, S. Yamaguchi, K. Oosawa, and S. Aizawa. Roles of FliK and FlhB in determination of flagellar hook length in *Salmonella typhimurium*. *J. Bacteriol.*, 176:5439–5449, 1994.

[67] C.-Y. Hsu and R. Dillon. A 3d motile rod-shaped monotrichous bacterial model. *Bull. Math. Biol.*, 71:1228–1263, 2009.

[68] S. E. Hulme, W. R. DiLuzio, S. S. Shevkoplyas, L. Turner, M. Mayer, H. C. Berg, and G. M. Whitesides. Using ratchets and sorters to fractionate motile cells of *Escherichia coli* by length. *Lab on a Chip*, 8:1888–1895, 2008.

[69] M. S. Ingber and A. A. Mammoli. A comparison of integral formulations for the analysis of low Reynolds number flows. *Eng. Anal. Bound. Elem.*, 23:307–315, 1999.

[70] T. Ishikawa and M. Hota. Interaction of two swimming paramecia. *J. Exp. Biol.*, 209:4452–4463, 2006.

[71] R. E. Johnson. An improved slender-body theory for Stokes flow. *J. Fluid Mech.*, 99:411–431, 1980.

[72] R. E. Johnson and C. J. Brokaw. Flagellar hydrodynamics. a comparison between resistive-force theory and slender-body theory. *Biophys. J.*, 25:113–127, 1979.

[73] C. Josenhans and S. Suerbaum. The role of motility as a virulence factor in bacteria. *Int. J. Med. Microbiol.*, 291:605–614, 2002.

[74] D. F. Katz. On the propulsion of micro-organisms near solid boundaries. *J. Fluid Mech.*, 64:33–49, 1974.

[75] D. F. Katz, J. R. Blake, and S. L. Paveri-Fontana. On the movement of slender bodies near plane boundaries at low Reynolds number. *J. Fluid Mech.*, 72:529–540, 1975.

[76] J. B. Keller and S. I. Rubinow. Swimming of flagellated microorganisms. *Biophys. J.*, 16:151–170, 1976.

[77] G. Kirchhoff. Über das Gleichgewicht und die Bewegung eines unendlich dünnen elastischen Stabes. *J. reine angew. Math.*, 1859:285–313, 1859.

[78] G. R. Kirchhoff. *Vorlesungen über mathematische Physik. Mechanik, Vorl. 28.* BG Teubner, 1876.

[79] J. D. Klein, A. R. Clapp, and R. B. Dickinson. Direct measurement of interaction forces between a single bacterium and a flat plate. *J. Colloid Interface Sci.*, 261:379–385, 2003.

[80] K. Kobayashi, T. Saitoh, D. S H Shah, K. Ohnishi, I. G. Goodfellow, R. E. Sockett, and S-I. Aizawa. Purification and characterization of the flagellar basal body of *Rhodobacter sphaeroides*. *J. Bacteriol.*, 185:5295–5300, 2003.

[81] S. Kudo, N. Imai, M. Nishitoba, S. Sugiyama, and Y. Magariyama. Asymmetric swimming pattern of *Vibrio alginolyticus* cells with single polar flagella. *FEMS Microbiol. Lett.*, 242:221–225, 2005.

[82] E. Lauga, W. R. DiLuzio, G. M. Whitesides, and H. A. Stone. Swimming in circles: motion of bacteria near solid boundaries. *Biophys. J.*, 90:400–412, 2006.

[83] G. Li, L.-K. Tam, and J. X. Tang. Amplified effect of Brownian motion in bacterial near-surface swimming. *Proc. Natl. Acad. Sci. USA*, 105:18355–18359, 2008.

[84] G. Li and J. X. Tang. Low flagellar motor torque and high swimming efficiency of *Caulobacter crescentus* swarmer cells. *Biophys. J.*, 91:2726–2734, 2006.

[85] J. Lighthill. Flagellar hydrodynamics. the John von Neumann lecture. *SIAM Rev.*, 18:161–230, 1976.

[86] N. Liron and S. Mochon. Stokes flow for a stokeslet between two parallel flat plates. *J. Eng. Math.*, 10:287–303, 1976.

[87] M. A. Lock, R. R. Wallace, J. W. Costerton, R. M. Ventullo, and S. E. Charlton. River epilithon: Toward a structural-functional model. *Oikos*, 42:10–22, 1984.

[88] A. E. H. Love. *A treatise on the mathematical theory of elasticity.* Dover, New York, 4th edition, 1944.

[89] Y. Magariyama, M. Ichiba, K. Nakata, K. Baba, T. Ohtani, S. Kudo, and T. Goto. Difference in bacterial motion between forward and backward swimming caused by the wall effect. *Biophys. J.*, 88:3648–3658, 2005.

[90] Y. Magariyama, S. Sugiyama, K. Muramoto, I. Kawagishi, Y. Imae, and S. Kudo. Simultaneous measurement of bacterial flagellar rotation rate and swimming speed. *Biophys. J.*, 69:2154–2162, 1995.

[91] J. G. Mitchell. The energetics and scaling of search strategies in bacteria. *Am. Nat.*, 160:727–740, 2002.

[92] R. Mittal and G. Iaccarino. Immersed boundary methods. *Annu. Rev. Fluid Mech.*, 37:239–261, 2005.

[93] K. Namba and F. Vonderviszt. Molecular architecture of bacterial flagellum. *Q. Rev. Biophys.*, 30:1–65, 1997.

[94] D. V. Nicolau, K. Burrage, D. V. Nicolau, and P. K. Maini. 'extremotaxis': computing with a bacterial-inspired algorithm. *Biosystems*, 94:47–54, 2008.

[95] G. O'Toole, H. B. Kaplan, and R. Kolter. Biofilm formation as microbial development. *Annu. Rev. Microbiol.*, 54:49–79, 2000.

[96] H. L. Packer, H. Lawther, and J. P. Armitage. The *Rhodobacter sphaeroides* flagellar motor is a variable-speed rotor. *FEBS Lett.*, 409:37–40, 1997.

[97] C. S. Peskin. Flow patterns around heart valves: A numerical method. *J. Comput. Phys.*, 10:252 – 271, 1972.

[98] C. S. Peskin. The immersed boundary method. *Acta Numerica*, 11:479–517, 2002.

[99] N. Phan-Thien, T. Tran-Cong, and M. Ramia. A boundary-element analysis of flagellar propulsion. *J. Fluid Mech.*, 184:533–549, 1987.

[100] T. Pilizota, M. T. Brown, M. C. Leake, R. W. Branch, R. M. Berry, and J. P. Armitage. A molecular brake, not a clutch, stops the *Rhodobacter sphaeroides* flagellar motor. *Proc. Natl. Acad. Sci. USA*, 106:11582–11587, 2009.

[101] H. L. Pina, J. L. M. Fernandes, and C. Brebbia. Numerical integration formulae over triangles and squares with a l/r singularity. *Appl. Math. Model.*, 5:209–211, 1981.

[102] H. Power. The completed double layer boundary integral equation method for two-dimensional Stokes flow. *IMA J. Appl. Math.*, 51:123–145, 1993.

[103] H. Power and G. Miranda. Second kind integral equation formulation of Stokes' flows past a particle of arbitrary shape. *SIAM J. Appl. Math.*, 47:689–698, 1987.

[104] C. Pozrikidis. *Boundary integral and singularity methods for linearized viscous flow.* Cambridge University Press, New York, 1992.

[105] C. Pozrikidis. *A Practical Guide to Boundary Element Methods with the Software Library BEMLIB.* Chapman & Hall/CRC, 2002.

[106] W. H. Press, S. A. Teukolsky, W. T. Vetterling, and B. P. Flannery. *Numerical Recipes in Fortran 77: The Art of Scientific Computing.* Cambridge University Press, 1996.

[107] M. Ramia, D. L. Tullock, and N. Phan-Thien. The role of hydrodynamic interaction in the locomotion of microorganisms. *Biophys. J.*, 65:755–778, 1993.

[108] J. M. Schierholz and J. Beuth. Implant infections: a haven for opportunistic bacteria. *J. Hosp. Infect.*, 49:87–93, 2001.

[109] K. E. Schreiner. The helix as propeller of microorganisms. *J. Biomech.*, 4:73–83, 1971.

[110] A. Sen, R. K. Nandy, and A. N. Ghosh. Elasticity of flagellar hooks. *J. Electron Microsc.*, 53:305–309, 2004.

[111] S. H. Shah, T. Perehinec, S. M. Stevens, S.-I. Aizawa, and R. E. Sockett. The flagellar filament of *Rhodobacter sphaeroides*: pH-induced polymorphic transitions and analysis of the fliC gene. *J. Bacteriol.*, 182:5218–5224, 2000.

[112] J. Sheng, E. Malkiel, J. Katz, J. E. Adolf, and A. R. Place. A dinoflagellate exploits toxins to immobilize prey prior to ingestion. *Proc. Natl. Acad. Sci. USA*, 107:2082–2087, 2010.

[113] J. L. Sherwood, J. C. Sung, R. M. Ford, E. J. Fernandez, J. E. Maneval, and J. A. Smith. Analysis of bacterial random motility in a porous medium using magnetic resonance imaging and immunomagnetic labeling. *Environ. Sci. Technol.*, 37:781–785, 2003.

[114] H. Shum, E. A. Gaffney, and D. J. Smith. Modelling bacterial behaviour close to a no-slip plane boundary: the influence of bacterial geometry. *Proc. R. Soc. A*, 466:1725–1748, 2010.

[115] P. M. Slovak, G. H. Wadhams, and J. P. Armitage. Localization of MreB in *Rhodobacter sphaeroides* under conditions causing changes in cell shape and membrane structure. *J. Bacteriol.*, 187:54–64, 2005.

[116] D. J. Smith, E. A. Gaffney, J. R. Blake, and J. C. Kirkman-Brown. Human sperm accumulation near surfaces: a simulation study. *J. Fluid Mech.*, 621:289–320, 2009.

[117] R. E. Sockett and J. P. Armitage. Isolation, characterization, and complementation of a paralyzed flagellar mutant of *Rhodobacter sphaeroides* WS8. *J. Bacteriol.*, 173:2786–2790, 1991.

[118] Y. Sowa and R. M. Berry. Bacterial flagellar motor. *Q. Rev. Biophys.*, 41:103–132, 2008.

[119] Y. Sowa, H. Hotta, M. Homma, and A. Ishijima. Torque–speed relationship of the Na^+-driven flagellar motor of *Vibrio alginolyticus*. *J. Mol. Biol.*, 327:1043–1051, 2003.

[120] S. E. Spagnolie and E. Lauga. Comparative hydrodynamics of bacterial polymorphism. *Phys. Rev. Lett.*, 106:058103, 2011.

[121] S. V. Srigiriraju and T. R. Powers. Continuum model for polymorphism of bacterial flagella. *Phys. Rev. Lett.*, 94:248101, 2005.

[122] J. Stoer and R. Bulirsch. *Introduction to numerical analysis*, volume 12. Springer Verlag, 2002.

[123] V. Torsvik, R. Sørheim, and J. Goksøyr. Total bacterial diversity in soil and sediment communities—a review. *J. Ind. Microbiol. Biot.*, 17:170–178, 1996.

[124] G. H. M. van der Heijden, S. Neukirch, V. G. A. Goss, and J. M. T. Thompson. Instability and self-contact phenomena in the writhing of clamped rods. *Int. J. Mech. Sci.*, 45:161–196, 2003.

[125] M. A.-S. Vigeant, R. M. Ford, M. Wagner, and L. K. Tamm. Reversible and irreversible adhesion of motile *Escherichia coli* cells analyzed by total internal reflection aqueous fluorescence microscopy. *Appl. Environ. Microbiol.*, 68:2794–2801, 2002.

[126] N. Watari and R. G. Larson. The hydrodynamics of a run-and-tumble bacterium propelled by polymorphic helical flagella. *Biophys. J.*, 98:12–17, 2010.

[127] A. B. Whitman and C. N. DeSilva. An exact solution in a nonlinear theory of rods. *J. Elasticity*, 4:265–280, 1974.

[128] A. W. Williams, S. Yamaguchi, F. Togashi, S. I. Aizawa, I. Kawagishi, and R. M. Macnab. Mutations in fliK and flhB affecting flagellar hook and filament assembly in *Salmonella typhimurium*. *J. Bacteriol.*, 178:2960–2970, 1996.

[129] C. W. Wolgemuth, T. R. Powers, and R. E. Goldstein. Twirling and whirling: Viscous dynamics of rotating elastic filaments. *Phys. Rev. Lett.*, 84:1623–1626, 2000.

[130] K. D. Young. The selective value of bacterial shape. *Microbiol. Mol. Biol. Rev.*, 70:660–703, 2006.